

UC San Diego

UC San Diego Electronic Theses and Dissertations

Title

Semi-Lagrangian Float Motion and Observing System Design

Permalink

<https://escholarship.org/uc/item/2jt5p0q2>

Author

Chamberlain, Paul McNab

Publication Date

2022

Peer reviewed|Thesis/dissertation

UNIVERSITY OF CALIFORNIA SAN DIEGO

Semi-Lagrangian Float Motion and Observing System Design

A dissertation submitted in partial satisfaction of the
requirements for the degree Doctor of Philosophy

in

Oceanography

by

Paul McNab Chamberlain

Committee in charge:

Lynne Talley, Chair
Cathy Constable
Bruce Cornuelle
Sarah Gille
Matthew Mazloff
Armin Schwartzman

2022

Copyright

Paul McNab Chamberlain, 2022

All rights reserved.

The Dissertation of Paul McNab Chamberlain is approved, and it is acceptable in quality and form for publication on microfilm and electronically.

University of California San Diego

2022

EPIGRAPH

Got out of town on a boat,
Going to Southern Islands.

Crosby, Stills, and Nash

TABLE OF CONTENTS

Dissertation Approval Page	iii
Epigraph	iv
Table of Contents	v
List of Figures	viii
List of Tables	xv
Acknowledgements	xvi
Vita	xviii
Abstract of the Dissertation	xix
Introduction	1
Chapter 1 Observing the ice-covered Weddell Gyre with profiling floats: position uncertainties and correlation statistics	6
1.1 Abstract	6
1.2 Introduction	7
1.3 Float Data and Model Output	11
1.3.1 Satellite-tracked Argo floats	11
1.3.2 RAFOS-enabled Argo floats	13
1.3.3 SOSE Particle Release Simulations	16
1.3.4 SOSE Air-Sea Fluxes	17
1.3.5 Float Velocity Comparisons	18
1.4 Position Uncertainty Estimate	20
1.4.1 Methods	20
1.4.2 Results	23
1.4.3 Discussion	26
1.4.3.1 Quadratic form of position uncertainty	26
1.4.3.2 Application to ice-covered regions other than the Weddell Gyre	29
1.5 Temperature, Salinity, and Air-Sea Flux Spatial Correlation and Uncertainty ...	30
1.5.1 Methods	31
1.5.1.1 Temperature and Salinity Correlation Length Scales	31
1.5.1.2 Temperature and Salinity Flux Correlation Length Scales	33
1.5.1.3 Uncertainty Field and Representation Error Calculation	34
1.5.2 Results	35
1.5.2.1 Temperature and salinity correlation scales and total error	35
1.5.2.2 Air-sea fluxes and spatial correlation scales	37

1.5.2.3	Salinity and Temperature Error as a Function of Position Loss Time	39
1.6	Conclusions	41
1.7	Acknowledgements	43
Chapter 2	Acoustic Float Tracking with the Kalman Smoother	60
2.1	Abstract	60
2.2	Introduction	61
2.3	Data	65
2.3.1	Core Argo	65
2.3.2	Acoustically-tracked floats	66
2.3.3	DIMES floats	68
2.3.4	Weddell Sea floats	68
2.3.5	Ancillary Data	69
2.4	Numerical Particle Tracking Experiment	69
2.5	Methods	71
2.5.1	Kalman Forward Filter	72
2.5.2	Kalman Smoother	76
2.5.3	Regularizations	77
2.5.4	Preprocessing	78
2.5.5	Tuning Experiment	79
2.6	Results	81
2.6.1	Particle Release Experiment	82
2.6.2	DIMES Intercomparison	84
2.6.3	Weddell Sea Floats	87
2.7	Discussion	88
2.8	Conclusion	90
2.9	Acknowledgements	91
Chapter 3	Using existing Argo trajectories to statistically predict future float positions with a Transition Matrix	114
3.1	Abstract	114
3.2	Introduction	115
3.3	Data	119
3.4	Methods	120
3.5	Results and Discussion	125
3.5.1	Bias and Uncertainty Quantification	126
3.5.2	Argo Array Prediction	128
3.5.3	Estimating Future Array Density from Float Deployments Along Set Ship Tracks	129
3.5.4	Iridium vs. Argos System Communications	130
3.5.5	BGC Argo Sampling Predictions	131
3.5.6	SOSE Comparison	133
3.6	Conclusion	134

3.7	Acknowledgements	135
Chapter 4	The Performance of Present, Future, and Optimal Argo Infrastructure	156
4.1	Abstract	156
4.2	Introduction	157
4.3	Data	162
4.3.1	Argo float data	162
4.3.2	Biogeochemical Model	162
4.3.3	Transition Matrix	163
4.4	Methods	163
4.4.1	Objective Mapping	165
4.4.2	Variance Scaling	168
4.4.3	Localization	169
4.4.4	Variance Constrained by Static Argo Arrays	171
4.4.5	The Transition Matrix and Variance Constrained by Future Argo Arrays	173
4.4.6	Optimal Array Design	174
4.5	Results	176
4.5.1	Estimates of Variance Constrained by the Current Argo Float Array	176
4.5.2	Estimates of Variance Constrained by Monte-Carlo Distributions	177
4.5.3	Estimates of Variance Constrained by Future Argo Floats	177
4.5.4	Optimal Array Design	179
4.6	Discussion	180
4.6.1	Expected Error Variance Structure	180
4.6.2	Optimal Array Recommendations	182
4.7	Conclusion	183
4.8	Appendix	184
4.8.1	Comparison of Spatial Distribution of Sum of Variances	184
4.8.2	Impact of scaling on the data	186
4.8.3	Total Variance Before Observation	186
4.9	Acknowledgements	187
	Bibliography	208

LIST OF FIGURES

Figure 1.	Figure from Wong et al., 2019: Total number of profiles with temperature and salinity (A) World Ocean Database 2013 with updates from January 2018. (B) Profiles collected by Argo up to January 2019.	5
Figure 1.1.	All interpolated Argo float positions in the Southern Ocean.	45
Figure 1.2.	Histogram of Total Interpolated Position Time (TIPT) for all Antarctic and Weddell Sea Argo floats.	46
Figure 1.3.	(a) Satellite-tracked Argo float positions, (b) acoustically tracked positions of RAFOS enabled Argo floats, and (c) 240 SOSE particle tracks of particle release experiment (1000 particles total) in the Weddell Sea.	47
Figure 1.4.	(a) WMO ID Float 5901717 float track in the Weddell Sea. (b) Potential temperature and (c) Salinity for WMO ID float 5901717.	48
Figure 1.5.	(a) Normalized probability density function of float speeds from 3 datasets; (b) Mean acoustically derived speed minus mean interpolated speed for all periods of Total Interpolated Position time in the RAFOS-enabled float dataset.	49
Figure 1.6.	Selected float track data for RAFOS, Satellite, and SOSE particle datasets. Actual trajectories are compared with PV interpolation and linear interpolation.	50
Figure 1.7.	Position uncertainty as a function of interpolated position time (IPT), based on the difference between the actual track and the linear and potential vorticity interpolations of the track.	51
Figure 1.8.	Spatial distribution of linear interpolation uncertainty minus PV interpolation uncertainty (km/day) of SOSE data withholding experiment.	52
Figure 1.9.	Temperature correlation and total error as a function of latitude-longitude and PV distance and depth at 90% confidence.	53
Figure 1.10.	Salinity correlation and total error as a function of latitude-longitude and PV distance and depth at 90% confidence.	54
Figure 1.11.	Temperature correlation and total error as a function of latitude-longitude and PV distance and density at 90% confidence.	55
Figure 1.12.	Salinity correlation and total error as a function of latitude-longitude and PV distance and density at 90% confidence.	56

Figure 1.13.	Comparison of RAFOS-enabled float and interpolated Argo float for float WMO5901717. (a) Map of tracks. (b) Surface heat flux and (c) surface salinity flux along the RAFOS-enabled and interpolated Argo float tracks.	57
Figure 1.14.	Spatial correlation of surface fluxes from SOSE for (a) heat (b) buoyancy, and (c) salinity, for winter (May 15 - September 15), summer (November 15 - March 15), and year round.	58
Figure 1.15.	(a) Salinity and (b) temperature error in the Weddell Sea as a function of depth and time of position loss.	59
Figure 2.1.	Bathymetry and sound source locations for the a) Drake Passage and b) Weddell Sea. Distribution of the number of sources heard in the acoustic record for the c) DIMES experiment and the d) Weddell Sea, respectively.	93
Figure 2.2.	Cartoon of Kalman Smoother acoustic tracking scheme. Red dots represent sound source locations. Red arcs represent lines of position from ranging data observed on the float.	98
Figure 2.3.	Example of acoustic tracking from Float 5901718 in the Weddell Sea.	99
Figure 2.4.	Flow chart describing the Kalman Smoother calculation. Light blue shading represents calculations in forward time, dark blue shading represents calculations in reverse time. Yellow boxes represent initial timesteps, orange boxes represent the Forecast, and green boxes represent the Analysis.	100
Figure 2.5.	Example trajectory reconstruction of particle release experiment. The true particle trajectory is represented by yellow diamonds with trajectories estimated from Least Squares, Kalman Filter, and Kalman Smoother. Red circles represent sound source locations.	101
Figure 2.6.	Trajectory error for numerical simulation for Kalman Smoother, Kalman filter, and Least-Squares algorithm for varying percent of GPS positioning.	102
Figure 2.7.	Trajectory error for numerical simulation for Kalman Smoother, Kalman filter, and Least-Squares algorithm for varying quality of acoustic positioning.	103
Figure 2.8.	Trajectory error for numerical simulation for Kalman Smoother, Kalman Filter, and Least-Squares algorithm for varying quantity of acoustic positioning.	104

Figure 2.9.	a) Sensitivity of DIMES experiment Data Misfit to changes in Position Process Noise, Velocity Process Noise, $f H^{-1}$ Contour Noise, and Geostrophic Streamline Noise at various values. b) Minimum cost overall Weddell Sea tuning runs while varying λ from 0 to 100.	105
Figure 2.10.	Comparison of Kalman Smoother and ARTOA trajectories for DIMES floats a) 808, b) 853, c) 854, d) 802.	106
Figure 2.11.	TOA error for Kalman Smoother tracking of the DIMES experiment, Weddell Sea dataset by days since last positioned.	107
Figure 2.12.	Mean TOA error for Kalman Smoother tracking of the DIMES experiment, and Weddell Sea dataset by percent of trajectory which was acoustically tracked.	108
Figure 2.13.	a) Histogram of misfit of trajectory with available acoustic ranging for ARTOA and Kalman Smoother. b) Histogram of trajectory difference between Kalman Smoother and ARTOA trajectories. c) Speed histogram for ARTOA trajectories and Kalman Smoother trajectories.	109
Figure 2.14.	TOA error for Kalman Smoother tracking of the DIMES experiment, Weddell Sea dataset for the number of discrete sound sources heard.	110
Figure 2.15.	Trajectories of 22 previously untracked Weddell Sea RAFOS-enabled Argo floats. a) GPS positions and Satellite Linear Interpolations as provided by the Argo Global Data Assembly Center, which does not include acoustic tracking. b) Kalman Smoother estimate of true trajectories.	111
Figure 2.16.	a) Sensitivity of Weddell Sea experiment Data Misfit to changes in Position Process Noise, Velocity Process Noise, $f H^{-1}$ Contour Noise, and Geostrophic Streamline Noise at various values. b) Minimum cost overall Weddell Sea tuning runs while varying λ from 0 to 100.	112
Figure 2.17.	a) Histogram of TOA misfit of reconstructed Weddell Sea trajectories with available acoustic ranging. b) Histogram of calculated Weddell Sea trajectory speeds.	113
Figure 3.1.	a) Historical Argo trajectories off Cape Agulhas. b) Example of float prediction website (https://argovis.colorado.edu/ng/covar) for float in same region.	137
Figure 3.2.	Cartoon of Transition Matrix calculation for an arbitrary Cell _{blue} . Total probability for each element of the Transition Matrix will equal the total number of transitions within a grid cell divided by the total number of transitions in the dataset.	138

Figure 3.3.	Initial deployment locations for all Argo floats in the dataset, using both Argos System and Iridium communications.	139
Figure 3.4.	Examples of $2^\circ \times 2^\circ$ 180 day transition probabilities for (a) 180 day Transition Matrix, and (b) 30 day Transition Matrix multiplied by itself 5 times. Difference in the (c) first and (d) second statistical moment of Transition Matrices of various timesteps and Transition Matrix with 180 day timestep.	140
Figure 3.5.	180 day transition probabilities for (a) $2^\circ \times 2^\circ$ and (b) $4^\circ \times 4^\circ$ degree Transition Matrix. (c) Difference in mean transition between $1^\circ \times 1^\circ$ Transition Matrix and reduced resolution transition matrices derived from $1^\circ \times 1^\circ$ transition statistics. (d) Standard error of transition matrices.	141
Figure 3.6.	Standard error for (a) $2^\circ \times 2^\circ$ degree Transition Matrix and (b) $4^\circ \times 4^\circ$ degree Transition Matrix at 90 day timestep.	142
Figure 3.7.	Transition density based on global Argo trajectories binned in $2^\circ \times 2^\circ$ degree grid cells with a 90 day timestep.	143
Figure 3.8.	(a) Mean transition and (b) variance ellipse based on $2^\circ \times 2^\circ$ binned 90 day timestep Transition Matrix.	144
Figure 3.9.	Mean Lagrangian pathways for Argo floats at each step in 12 step Markov Chain derived from $2^\circ \times 2^\circ$ grid cell 90 day timestep Transition Matrix. ...	145
Figure 3.10.	(a) Current and (b) one year prediction of density of Core Argo array.	146
Figure 3.11.	(a) One year and (b) two year predictions of density of Core Argo array in the Pacific Ocean.	147
Figure 3.12.	(a) One year and (b) two year predictions of array density of Core Argo array in the Atlantic Ocean.	148
Figure 3.13.	(a) One year and (b) two year predictions of array density of Core Argo array in the Southern Ocean.	149
Figure 3.14.	180 day projection of (a) SOCCOM and (b) Argo arrays measure of survivability.	150
Figure 3.15.	Chance of observation for floats deployed in each gridcell along ship tracks of GO-SHIP cruises organized for the next 5 years.	151
Figure 3.16.	Comparison of future array density for (a) Argos System and (b) Iridium communications derived transition matrices at $2^\circ \times 3^\circ$ grid resolution and 180 day timestep. Transition matrices were propagated forward 8 years with initial array containing one float in each gridcell.	152

Figure 3.17.	Chance of (a) any observation within the next year and (b) seasonal observation within the next year of temperature and salinity sensor equipped Argo floats.	153
Figure 3.18.	Chance of any observation within the next year of (a) oxygen sensor equipped Argo floats, (b) chlorophyll sensor equipped Argo floats, (c) pH sensor equipped Argo floats.	154
Figure 3.19.	Difference of standard deviation around the mean of SOSE and Argo derived matrices for (a) $1^\circ \times 2^\circ$ and (b) $4^\circ \times 6^\circ$ grid cells with 180 day timestep.	155
Figure 4.1.	a) Map of May, 2021 snapshot Core and BGC Argo floats and b) example of random BGC float locations. Green dots are Core Argo floats, blue dots are BGC floats.	188
Figure 4.2.	Global Climate Model (CM4) correlation maps of a) chlorophyll and oxygen and b) temperature and oxygen at a depth of 100 m.	189
Figure 4.3.	(a-d) Maps of standard deviation of a) chlorophyll, b) oxygen, c) CO ₂ flux, d) salinity. e) Monthly mean and anomaly from annual mean normalized by standard deviation: chlorophyll, oxygen, pH, and salinity at 40°S, 20°W.	190
Figure 4.4.	(a and b) CM4 maps of eigenvectors of spatial surface pH covariance for a) the gravest mode and b) the 7 th eigenmode. (c and d) 72 month subsets of eigenvectors of temporal surface pH covariance for c) the gravest mode and d) the 7 th eigenmode.	191
Figure 4.5.	(a and b) CM4 maps of eigenvectors of spatial pH covariance for a) the gravest mode at 100 m depth and b) the gravest mode at 1000 m depth. (c and d) 72 month subsets of eigenvectors of temporal pH covariance for c) the gravest mode at 100 m depth and d) the gravest mode at 1000 m depth.	192
Figure 4.6.	Two year prediction of array density of global Core Argo array.	193
Figure 4.7.	a) Flowchart of optimal deployment locations and b) organization of variance products.	194
Figure 4.8.	Scaled pH formal mapping error (FME) of existing core and BGC Argo float array taken from May, 2021 snapshot at a) the surface and b) 1000 meters.	195
Figure 4.9.	Zonal average formal mapping error (FME) of existing Argo core and BGC float array at all depths of a) temperature, b) salinity, c) pH, d) chlorophyll, and e) oxygen.	196

Figure 4.10.	Zonal average covariance of the expected error (CEE) of existing Argo core and BGC float array at all depths, of a) temperature, b) salinity, c) pH, d) chlorophyll, and e) oxygen.	197
Figure 4.11.	Average formal mapping error (FME) of randomly distributed Argo floats of increasing density, and covariance of the expected error for 1000 BGC floats. l) Depth averaged FME by variable for increasing float density. m) Variable averaged FME for upper and lower ocean.....	198
Figure 4.12.	Scaled surface pH formal mapping error (FME) of the Argo float array of May, 2021, projected at a) one and b) two years into the future assuming floats are not replenished.	199
Figure 4.13.	Global average of the covariance of the expected error (CEE) of the existing core and BGC Argo float array and formal mapping error (FME) of the predicted Argo array at all depths for temperature, salinity, pH, chlorophyll, and oxygen	200
Figure 4.14.	a) Formal mapping Error (FME) and tracklines of 2 hypothetical floats deployed along the P1 GO-SHIP line 48 months after deployment. b-f) Difference of float 1 and float 2 Expected Error Variance for BGC variables.	201
Figure 4.15.	a) Map of the optimal distribution of 1000 BGC Argo floats with a grid spacing of approximately 6° in latitude and longitude. b) Histogram of zonally binned optimal array. c) Histogram of meridionally binned optimal array.	202
Figure 4.16.	a) Relative unconstrained variance of randomly distributed 1000 float arrays and the optimal 1000 float array with Gaussian noise added to the CEE at varying signal to noise ratios. b) Unconstrained variance of randomly distributed and optimal float arrays of increasing distributions.	203
Figure 4.17.	a,c,e,g,i) Raw CM4 time series in the Black Sea (location of very high variance) and b,d,f,h,j) raw CM4 time series in the western tropical Pacific (location of very low variance of temperature, salinity, pH, chlorophyll, and oxygen respectively). Mean removed from both timeseries.	204
Figure 4.18.	Sum of total variance at 4 depth levels considered in optimal array where individual variables are a) scaled by the median of the temporal standard deviation distribution, b) scaled as described in Eq. 4.17.....	205
Figure 4.19.	a,c,e,g,i) Raw CM4 data temporal variance and b,d,f,h,j) scaled CM4 temporal variance of temperature, salinity, pH, chlorophyll, and oxygen respectively. Variance was calculated at each of the 4 depth levels and sorted from smallest to largest in dataset.	206

Figure 4.20. Zonal average of total variance for all variables and depths 207

LIST OF TABLES

Table 1.1.	RAFOS-enabled Argo profiling floats tracked in the Weddell Sea deployed from February 26, 2008 to February 4, 2013. Argo data graphics are available at http://www.ifremer.fr/co-argoFloats/	44
Table 2.1.	WMO ID Numbers of 22 Previously Untracked Weddell Sea Floats	92
Table 2.2.	Sequential Calculations of Kalman Smoother Algorithm	94
Table 2.3.	Uncertainties Considered for Sensitivity Experiments	96
Table 3.1.	Spatial and temporal resolution of transition matrices calculated.	136
Table 3.2.	Planned GO-SHIP Cruises	136

ACKNOWLEDGEMENTS

This dissertation is possible because of the teachers in my life who took a risk and believed in me.

First, I would like to thank my advisor, Dr. Lynne Talley. Lynne is a supportive and patient (8 years patient) mentor who simultaneously brings years of tempered experience and a honed curiosity to any problem she works on. Lynne is brilliant and it has been a pleasure to work with her.

Thank you to my committee members: Sarah Gille, Cathy Constable, Bruce Cornuelle, Armin Scharzman, and Matthew Mazloff. I am truly lucky to have the support of such talented people; thank you for helping me be a better scientist.

I would also like to thank Captain Mark Pickett (Retired) - an old bull who taught a young bull how to drive ships, how to study the ocean, and a lot about life.

Thank you to Randy LeVeque and my undergraduate mentors: Monty Mola, Wes Bliven, and Jeff Haag. You lit a fire and gave me the tools to be successful in my adventures.

Finally, thank you to my parents and wife. You are my greatest teachers and make me a better person everyday.

Chapter 1, in full, is a reprint of the material as it appears in *Journal of Geophysical Research: Oceans* 2018. Chamberlain, P. M., Talley, L. D., Mazloff, M. R., Riser, S. C., Speer, K., Gray, A. R., & Schwartzman, A., Wiley Press 2018. The dissertation author was the primary investigator and author of this paper.

Chapter 2, in full, has been submitted for publication of the material as it may appear in *Journal of Atmospheric and Oceanic Technology*, 2022, Chamberlain, P. M., Cornuelle, B., Talley, L. D., Mazloff, M. R., Speer, K., Hancock, C., & Riser, S. C., American Meteorological Society 2022. The dissertation author was the primary investigator and author of this paper.

Chapter 3, in full, has been submitted for publication of the material as it may appear in *Journal of Atmospheric and Oceanic Technology*, 2022, Chamberlain, P. M., , Talley, L. D.,

Mazloff, M. R., van Seville, E., Gille, S. T., Tucker T., Scanderbeg, M., & Robbins, P., American Meteorological Society 2022. The dissertation author was the primary investigator and author of this paper.

Chapter 4, in full, has been submitted for publication of the material as it may appear in Journal of Atmospheric and Oceanic Technology, 2022, Chamberlain, P. M., Talley, L. D., Cornuelle, B., Mazloff, M. R., & Gille, S. T., American Meteorological Society 2022. The dissertation author was the primary investigator and author of this paper.

VITA

- 2006 Bachelor of Science, Humboldt State University
- 2006–2014 National Oceanic and Atmospheric Administration Commissioned Officer Corps
- 2012 Masters of Science, University of Washington
- 2014–2022 Research Assistant, University of California San Diego
- 2022 Doctor of Philosophy, University of California San Diego

PUBLICATIONS

Chamberlain, Paul M., et al. "Observing the ice-covered Weddell Gyre with profiling floats: Position uncertainties and correlation statistics." *Journal of Geophysical Research: Oceans* 123.11 (2018): 8383-8410.

Houghton, I. A., et al. "Performance statistics of a real-time Pacific Ocean weather sensor network." *Journal of Atmospheric and Oceanic Technology* 38.5 (2021): 1047-1058.

Chamberlain, Paul M., et al. "Application of a Kalman Smoother to underice float tracking." *Journal of Atmospheric and Oceanic Technology*: Accepted

Chamberlain, Paul M., et al. "Using existing Argo trajectories to statistically predict future float positions with a Transition Matrix." *Journal of Atmospheric and Oceanic Technology*: Submitted

Chamberlain, Paul M., et al. "The Performance of Present, Future, and Optimal Argo Infrastructure." *Journal of Atmospheric and Oceanic Technology*: Submitted

ABSTRACT OF THE DISSERTATION

Semi-Lagrangian Float Motion and Observing System Design

by

Paul McNab Chamberlain

Doctor of Philosophy in Oceanography

University of California San Diego, 2022

Lynne Talley, Chair

We show the implementation of techniques to improve the estimation of where floats are, where they will be, and how to make the best use of their observations. This work expands in spatial scale from regional estimates while floats are under ice to uncertainty estimation and optimization of the global observing system design. Chapter 1 considers floats that venture under sea-ice in the Weddell Sea. While under ice, floats cannot communicate with satellites (the usual positioning method), and collected profiles are saved for later transmission. Common practice estimates under-ice positions by linearly interpolating between known satellite locations. We estimate the position uncertainty of this linear interpolation and the representation error this interpolation causes in temperature and salinity profiles. Satellite positioning is not the only

positioning scheme available for profiling floats: floats can be acoustically positioned and the Weddell Sea has been insonified. Weddell Sea sound conduction is not as efficient as the open ocean because of a relatively shallow and narrow Sound Fixing and Ranging (SOFAR) channel. When sound is conducted close to the surface, unknown interactions and reflections with sea ice occur that attenuate the range of sound transmission. Chapter 2 explains the development of a Kalman smoother algorithm for tracking under-ice floats and is an improvement to the current state of acoustic tracking. Increasing to larger scale, Chapter 3 describes the construction and use of an Argo-specific transition matrix: a transition matrix is a statistical construction that uses Argo float trajectories to assess the probability of a float transitioning from one location to another. We assimilate 20 years of Argo trajectories to statistically predict Argo location without external models. Finally, chapter 4 combines the transition matrix of chapter 3 with output from the CM4 model to estimate how well current and future biogeochemical (BGC) Argo arrays will observe the anomaly of BGC fields. We also estimate the variance constrained by a uniformly distributed global BGC array at different densities as well as suggest an array distribution that is optimized for constraining the BGC anomalies.

Introduction

The Argo float array is one of the great oceanographic accomplishments of the 21st century. Since its humble beginnings (Davis, 1991), the Argo array has grown to now include more than 3900 floats and has collected over 2 million temperature and salinity profiles spanning 20 years of data (Wong, Annie PS and Wijffels, Susan E and Riser, Stephen C and Pouliquen, Sylvie and Hosoda, Shigeki and Roemmich, Dean and Gilson, John and Johnson, Gregory C and Martini, Kim and Murphy, David J and others, 2020) (Fig. 1). Argo floats typically drift at 1000 meters for 10 days, descend to 2000 meters, rise to the surface, and transmit collected data back to researchers via satellite. The Argo platform is a pressure case, batteries, and a buoyancy engine that can be augmented with different sensors: core Argo floats are equipped with temperature and salinity sensors; while biogeochemical (BGC) Argo floats are equipped with temperature, salinity, oxygen, nitrate, pH, fluorescence (converted to chlorophyll concentration), backscatter, and downwelling irradiance. Variants of the Argo platform have been proposed to measure temperature and salinity at much deeper depths, as well as ocean mixing and hyperspectral ocean color (Roemmich, Dean and Alford, Matthew H and Claustre, Hervé and Johnson, Kenneth and King, Brian and Moum, James and Oke, Peter and Owens, W Brechner and Pouliquen, Sylvie and Purkey, Sarah and others, 2019; Barnard et al., 2018). The 3 most prominent Argo configurations: core Argo, BGC Argo, and deep Argo. The array formed by these 3 variants is now called One Argo (Roemmich, D and Boebel, O and Freeland, H and King, B and LeTraon, PY and Molinari, R and Brechner Owens, W and Riser, S and Send, U and Takeuchi, K and others, 1998).

In particular, the endurance and autonomy of Argo floats makes them particularly ef-

fective in remote and treacherous regions of the world's oceans (Fig. 1). The Southern Ocean significantly controls and regulates global nutrients, carbon, and heat (Sarmiento et al., 2004; Purkey and Johnson, 2010; Landschützer, Peter and Gruber, Nicolas and Haumann, F Alexander and Rödenbeck, Christian and Bakker, Dorothee CE and Van Heuven, Steven and Hoppema, Mario and Metzl, Nicolas and Sweeney, Colm and Takahashi, Taro and others, 2015) but is the least observed. The Southern Ocean Carbon and Climate Observation and Modeling (SOCCOM) project combines BGC Argo float observations with models to understand the complicated physical pathways and BGC processes in the Southern Ocean.

In the Southern Ocean, sea ice formation and melt are important components of water mass transformation (Abernathey et al., 2016). These transformed water masses are essential drivers of the global overturning circulation and world ocean ventilation. Changes in these transformation regions and budgets impact global ocean heat budgets and nutrient availability (Purkey and Johnson, 2012; Sarmiento et al., 2004). Sea ice is intimately connected to light availability and spring phytoplankton blooms. These blooms greatly affect the structure and budget of Southern Ocean carbon uptake; however, sea ice is a challenging operational environment for oceanographic research vessels (the traditional platform for hydrographic observations), and a paucity of high-quality scientific data exists in the Southern Ocean seasonal sea-ice regions.

Partly due to the success of the SOCCOM project, a new U.S. project called GO-BGC has begun to deploy 500 BGC floats globally. The added sensor package of the BGC float makes them more expensive than a core Argo float, and researchers must be strategic about the location of their deployments so as to best observe the ocean. Choosing this best location is challenging because Argo floats drift in unexpected ways, and the spatial and temporal scales of variability of BGC variables in the ocean can be very different. Additionally, BGC variables can co-vary, meaning that observations about one variable can provide information about another variable. For example, through solubility effects, information about temperature can provide insight into the behavior of oxygen.

This dissertation aims to develop and implement techniques to improve the estimation of

where floats are, where they will be, and how to best use their observations. This work is formed into 4 chapters, expanding in spatial scale from a regional estimation of uncertainty to global observing system design.

Chapter 1 considers floats that venture under sea-ice in the Weddell Sea. Sea-ice can crush or damage floats at or near the surface, so control software called the “ice avoidance algorithm” has been successfully installed to abort profiling float breach at 50 meters. Water greatly attenuates satellite communication at 50 meters and the satellite derived positions (the only positioning available to most floats) are unknown for under ice profiles. Collected profiles are saved onboard for later transmission and once the sea ice recedes are transmitted without position information. Common practice is to assign under-ice positions by linearly interpolating between the last satellite position before the float went under the ice and the first satellite position when the float comes out of the ice. We estimate the position uncertainty of this linear interpolation; additionally, we estimate the representation error induced in the temperature and salinity profiles collected under ice due to this linear interpolation position reassignment.

Satellite positioning is not the only positioning scheme available for profiling floats: a rich tradition of acoustic positioning exists for Lagrangian floats (Swallow, 1955; Rossby et al., 1986). Floats are acoustically positioned by an array of sound sources that broadcast sound pulses at specified daily intervals. An array of sound sources has been deployed in the Weddell Sea continuously since 1999. In the Weddell Sea, sound conduction is not as efficient because of a relatively shallow and narrow Sound Fixing and Ranging (SOFAR) channel. When sound is conducted close to the surface, unknown interactions and reflections with sea ice occur. This causes sound transmission ranges in the Weddell Gyre to vary from 700 km to as little as about 300 km (Klatt et al., 2007). In addition to this issue, both measurements and sound speed have uncertainties, most notably the slow drift of sound source clocks and float clocks. Chapter 2 explains the development and sensitivity testing of a Kalman smoother algorithm (Rauch et al., 1965) for tracking under-ice floats acoustically. The Kalman smoother produces an estimate that considers all GPS locations and acoustic ranging data. We show this estimate to

be an improvement to the current state of tracking. We apply the Kalman Smoother to a set of acoustically tracked floats deployed during the DIMES experiment (Gille et al., 2007; Balwada et al., 2016) and in the Weddell Sea.

Chapter 3 describes the construction and use of an Argo specific transition matrix: a transition matrix is a statistical construction that uses Argo float trajectories to assess the probability of a float transitioning from one location to another (Markov, 1906). Transition matrices have been applied in the ocean to surface drifter datasets (Van Sebille et al., 2012) and to an idealized Argo dataset that sought to eliminate upper ocean shear (Sevellec et al., 2017), but never used operationally. We analyze 20 years of core Argo trajectories to construct a tool that makes statistical inferences about Argo float motion with no external models.

Finally, chapter 4 combines the transition matrix of chapter 3 with output from the CM4 coupled ocean-atmosphere model (Held, IM and Guo, H and Adcroft, A and Dunne, JP and Horowitz, LW and Krasting, J and Shevliakova, E and Winton, M and Zhao, M and Bushuk, M and others, 2019; Adcroft, Alistair and Anderson, Whit and Balaji, V and Blanton, Chris and Bushuk, Mitchell and Dufour, Carolina O and Dunne, John P and Griffies, Stephen M and Hallberg, Robert and Harrison, Matthew J and others, 2019) to estimate how well current and future BGC Argo arrays will observe the anomaly from the mean of temperature, salinity, pH, chlorophyll and oxygen. We quantify the amount of variance an observing system constrains with the objective mapping techniques of Bretherton et al. (1976). We create these estimates for the upper 2000 m of the ocean (BGC Argo depth) and consider the cross-covariance of BGC variables. We also estimate the variance constrained by a uniformly distributed global BGC array at different array densities as well as suggesting an array distribution that is optimized for constraining the BGC anomaly from the mean.

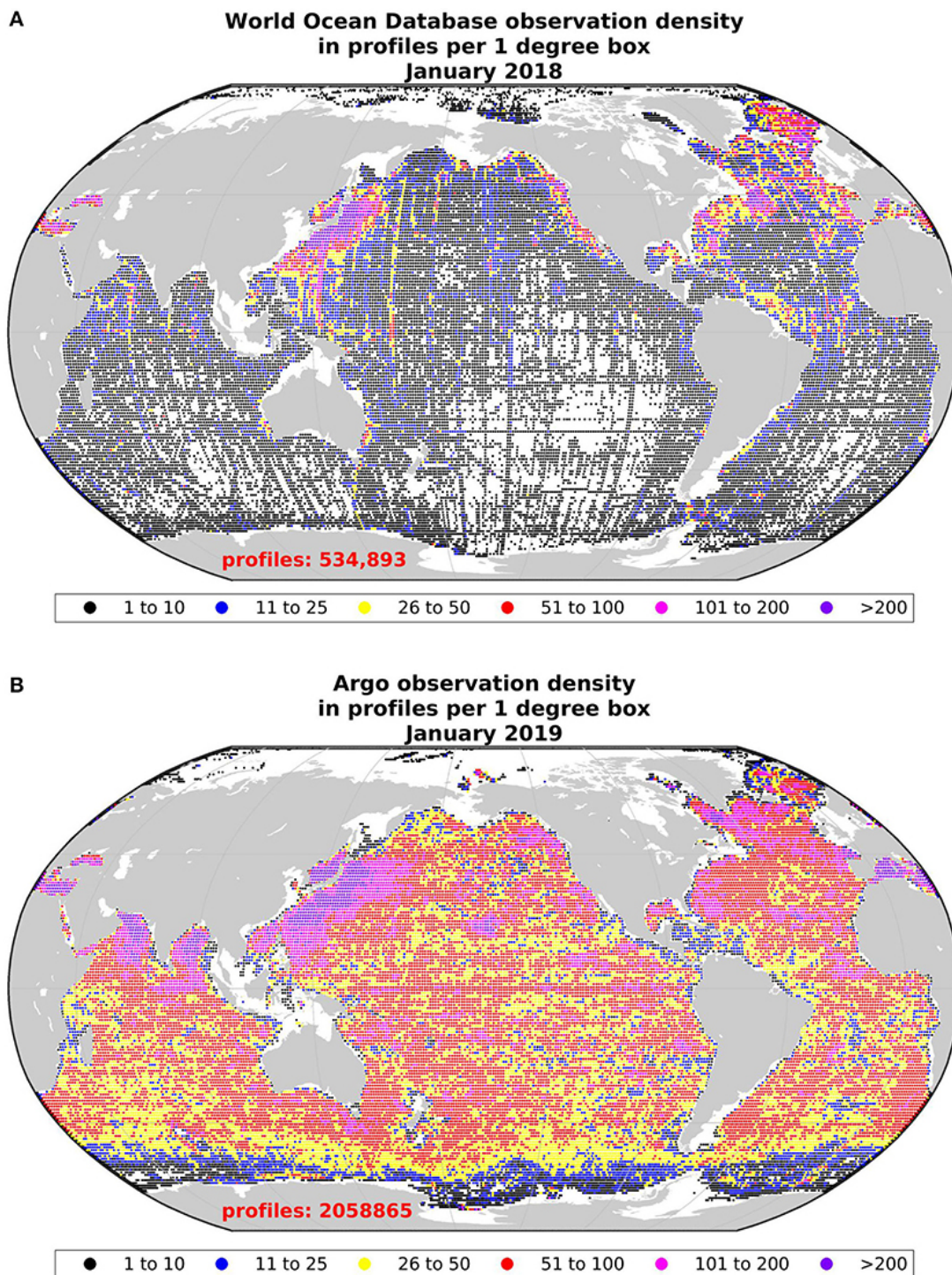


Figure 1. Figure from Wong et al., 2019: Total number of profiles with temperature and salinity that extend to at least 1,000 dbar for every 1° square of latitude and longitude. (A) World Ocean Database 2013 with updates from January 2018. These represent profiles collected by research or other vessels over the past 150 years. (B) Profiles collected by Argo up to January 2019.

Chapter 1

Observing the ice-covered Weddell Gyre with profiling floats: position uncertainties and correlation statistics

1.1 Abstract

Argo-type profiling floats do not receive satellite positioning while under sea ice. Common practice is to approximate unknown positions by linearly interpolating latitude-longitude between known positions before and after ice cover, although it has been suggested that some improvement may be obtained by interpolating along contours of planetary-geostrophic potential vorticity. Profiles with linearly interpolated positions represent 16% of the Southern Ocean Argo dataset; consequences arising from this approximation have not been quantified. Using three distinct datasets from the Weddell Gyre - 10 day satellite-tracked Argo floats, daily-tracked RAFOS-enabled floats, and a particle release simulation in the Southern Ocean State Estimate (SOSE) - we perform a data withholding experiment to assess position uncertainty in latitude-longitude and potential vorticity coordinates as a function of time since last fix. A spatial correlation analysis using the float data provides temperature and salinity uncertainty estimates as a function of distance error. Combining the spatial correlation scales and the position uncertainty, we estimate uncertainty in temperature and salinity as a function of duration of position loss. Maximum position uncertainty for interpolation during 8 months without position data is $116 \pm$

148 km for latitude-longitude and 92 ± 121 km for potential vorticity coordinates. The estimated maximum uncertainty in local temperature and salinity over the entire 2,000 m profiles during 8 months without position data is 0.66 °C and 0.15 psu in the upper 300 m and 0.16 °C and 0.01 psu below 300 m.

1.2 Introduction

Antarctic winter sea ice covers an enormous region (18.5×10^6 km² average maximum winter extent); 85% of this sea ice is seasonal (Fetterer et al., 2016). The ocean interior circulates heat and freshwater, and supports a vigorous seasonal cycle in carbon, oxygen, and nutrients. These processes, and the ocean-ice-atmosphere exchanges that occur within the ice-covered region, impact the climate both regionally and globally. Formation of Antarctic Bottom Water (AABW), one of the densest water masses of the world ocean, occurs in polynyas along the coast of Antarctica in winter; changes in its production, temperature and salinity over the past 60 years have contributed significantly to changes in the global ocean heat budget and regional freshwater budget (Purkey and Johnson, 2010, 2012; Desbruyères et al., 2016; Rhein, Met al and Rintoul, SR and Aoki, S and Campos, E and Chambers, D and Feely, RA and Gulev, S and Johnson, GC and Josey, SA and Kostianoy, A and others, 2013). Upwelling of deep water to the surface of the Southern Ocean supplies the source water for formation of both AABW and thermocline/Subantarctic Mode Water (SAMW).

Changes in salinity of these source and sink waters have been linked to changes in sea ice formation as well as to ice shelf melt (Haumann et al., 2016; Jones et al., 2015) and are likely associated with changes in the basic freshwater fractionation mechanism associated with sea ice formation near Antarctica and export of that sea ice northward to where it melts, which salinifies the coastal waters and freshens the surface waters of the Antarctic Circumpolar Current (Abernathey et al., 2016). This freshening affects the properties of SAMW when these surface waters are driven northward across the Subantarctic Front by wind (Cerovečki and Mazloff,

2016). Sarmiento et al. (2004) showed that nutrients in the upwelled deep waters that enter the SAMW have significant global impacts on nutrient availability in the upper ocean.

The seasonally ice-covered region of the Southern Ocean is relatively inaccessible to ships during winter. Through growing deployments of autonomous Argo-type profiling floats, many of which now carry biogeochemical sensors (Johnson and Claustre, 2016b), these observational gaps are being filled. However, almost all Argo-type floats are tracked only through satellite positioning at the sea surface. Argo-type floats have a serious vulnerability when operating in the polar oceans: sea ice is very destructive to instruments at and near the surface. To protect floats from sea ice, a temperature-controlled ice avoidance algorithm has been implemented in Argo float buoyancy control software since 2001 (Klatt et al., 2007). This algorithm instructs the float to initiate a descent if the upper ocean temperature is below a threshold that implies the strong probability of sea ice. Float profiles collected under ice are saved in memory for later ice-free transmission without the satellite-derived position fixes of open water Argo profiles. In the Southern Ocean (south of 55° S), there are 11,856 temperature-salinity profiles with position flags indicating interpolation due to lack of position information, from 231 Argo floats since July 21, 2006 (Figs. 1.1, 1.2). Most interpolated locations are due to sea ice cover. These data represent 16% of the Southern Ocean Argo dataset.

The question we address in this paper is the extent to which analysis and use of these under-ice profiles are compromised because their positions are interpolated. The most common approach to dealing with missing Argo position information is to linearly interpolate latitude-longitude between known positions (Wong and Riser, 2011), although interpolation along contours of planetary-geostrophic potential vorticity has been proposed as an improvement (Reeve et al., 2015). Linear interpolation is apparent in Fig. 1.1 where the normally curved float trajectories are instead a series of straight lines within the sea ice zone. Clearly, floats do not follow these straight paths, which means, among other things, that their total track length and speed are underestimated (Wong and Riser, 2011). The error and impact of assigning under-ice locations to float profiles that can be tens to hundreds of kilometers from their true position

is studied here for the first time; the resulting position errors introduce uncertainties in the attribution of temperature and salinity profile measurements to a given position. We refer to these temperature and salinity profile uncertainties as “representation errors”, which are necessary to characterize float data mapped onto Eulerian coordinates - for instance when assimilated into state estimates (e.g. Mazloff et al., 2010; Nguyen et al., 2017) or used for gridded estimates of transport (e.g. Gray and Riser, 2014). In addition, the lack of position information is not only a concern when using float data in the Eulerian reference frame. In the Lagrangian perspective, interpretations of changes in properties of water parcels often utilize surface observations or products such as air-sea fluxes, surface temperature, ice cover, surface height, and ocean color (D’Ortenzio et al., 2014; Wong and Riser, 2011). The uncertainty in the surface boundary conditions that is introduced by uncertainty in under-ice Argo float position is quantified here.

Some Argo floats are tracked acoustically in the sea-ice zone, between their 10-day satellite position fixes when they profile; such acoustic (or “RAFOS”) tracking (Rossby et al., 1986) has had widespread success in ice-free areas. Moored acoustic sources have been deployed by the Alfred Wegener Institut (Klatt et al., 2007; Fahrback et al., 2011) in the Weddell Sea. RAFOS-enabled floats work with a network of sound sources that broadcast sound pulses at specified intervals, permitting tracking if enough sources are within range. Full insonification and acoustic tracking of all autonomous under-ice instruments in the Southern Ocean would be ideal; expense and logistics have made this goal presently impractical. A complication here is that the Sound Fixing and Ranging (SOFAR) channel is less efficient at conducting sound travel in the Weddell Sea compared with mid-latitudes: this reduces the range of acoustic transmission of polar compared to mid-latitude sound sources and therefore requires a higher density of sources (Klatt et al., 2007). Acoustic float tracks are helpful for determining the uncertainty of linearly-interpolated track approximations, and the uncertainty in linear approximations is essential in evaluating the scientific effectiveness of acoustic tracking versus interpolation.

We present a method to estimate representation error associated with position interpolation of any Lagrangian measurement over any time interval and in any geographic region. We

split the problem of finding representation error as a function of duration of position loss (Section 4.2.1) into the problem of finding position uncertainty as a function of duration of position loss (Section 1.4) and spatial correlations of observed fields (Section 1.5), focusing on temperature and salinity, and peripherally on uncertainty in air-sea fluxes ascribed to the uncertain profile locations.

In section 1.4, we estimate the position uncertainty of latitude-longitude and potential vorticity coordinate interpolation as a function of duration of position loss by performing a series of data withholding experiments on 3 distinct data sets: daily RAFOS-enabled float track data, 10-day satellite-tracked float data (non-ice periods only), and model output generated from a particle release simulation (Wang et al., 2014) with a 0.16° Southern Ocean State Estimate (SOSE; Mazloff et al., 2010). We interpolate in both latitude-longitude and potential vorticity geometries. The results of the data withholding experiment are used to estimate position uncertainty as a function of time since the most recent position observation for periods of up to 8 months.

In Section 1.5.1.1, we estimate representation error as a function of distance uncertainty by using Ninove et al.'s (2016) approach to compute temperature and salinity correlation within a binned spatial grid in both latitude-longitude and potential vorticity coordinates- this gives us correlation as a function of distance. We then use distance as a linear predictor of uncertainty, and compute uncertainty in temperature and salinity as a function of distance uncertainty. In section 1.5.1.2 we reverse this viewpoint and consider the uncertainty in surface fluxes associated with positions of a float lost beneath the ice. We calculate correlation length scales of SOSE heat flux, salinity flux, and buoyancy flux, and use these correlations to predict uncertainty in these fluxes as a function of distance. Finally, in section 1.5.2.3, we combine these statistics and estimate temperature, salinity, and air-sea flux uncertainty at the interpolated position as a function of position loss time.

To recapitulate, position uncertainty is calculated as a function of position loss time, representation error (mapping uncertainty) is calculated as a function of position uncertainty, and total uncertainty is calculated by combining the two.

1.3 Float Data and Model Output

The Weddell Sea supports a wind-driven cyclonic gyre; the northern side of the gyre is the southern boundary of the Antarctic Circumpolar Current. For this study, we define the Weddell Gyre as the ocean south of 60°S and between 60°W and 20°E (black dashed area in Fig. 1.1). The southwest quadrant of the Weddell Gyre is shallower and generally ice covered year round. Sea ice covers the entire Weddell Gyre during austral winter (Fig. 1.1).

The Weddell Sea was chosen for this study because it has a high density of standard satellite-tracked Argo floats compared with other Southern Ocean regions, and because of its unique record of under-ice, continuously-tracked, RAFOS-enabled Argo floats deployed through U.S. Argo and AWI (Klatt et al., 2007). The Weddell Sea also has the longest under-ice float records (51 floats since July 21, 2006) of any Southern Ocean region irrespective of insonification.

Depending on their location in the Weddell Gyre, all of which experiences seasonal ice cover, some floats may be forced to operate below ice - without surfacing - for 10 months or more. Figure 1.2 shows the distribution of periods of position loss for floats circulating in the Weddell Gyre. We observe two major modes of the under ice distribution - transient position loss events lasting 50 days or less, and seasonal position loss events lasting between 200 and 300 days. The former represent floats that experience sea ice and then are advected either to an ice free region or, more likely, out of the gyre entirely. The latter are floats that are caught in the cyclonic Weddell Gyre circulation and experience entire seasons of sea ice cover: these are the floats of primary interest in the uncertainty analysis of this paper.

1.3.1 Satellite-tracked Argo floats

Argo floats typically profile from a maximum depth of 2,000 m to the surface every 10 days, although operational or experimental considerations can change this schedule. While at the surface, satellite positioning information is recorded when possible. All Argo data prior to July 17, 2018, in our specified region, were downloaded from the USGODAE Argo GDAC Data

Browser (SEANOE, 2000) (regional map of satellite-tracked floats Fig. 1.3a). An example of these data, from Argo float 5901717, has been plotted in Fig. 1.4, with the under-ice profiles lightened. In general, there are far fewer observations in the southwestern Weddell Gyre, most likely due to a deliberate deployment choice to avoid ‘losing’ floats under multi-year ice (Fig. 1.3).

The Argo user’s manual (Carval, Thierry and Keeley, Robert and Takatsuki, Yasushi and Yoshida, Takashi and Schmid, Claudia and Goldsmith, Roger and Wong, Annie and Thresher, Ann and Tran, Anh and Loch, Stephen and others, 2015) lists 9 different possible metadata flags for position quality control, although only 3 are commonly used: flag “1” for good positions, flag “4” for bad positions, and flag “8” for interpolated positions. Argo metadata and flags do not currently include the position interpolation method. Linear interpolation in spatial coordinates is the only method currently used, although adding variants of position reconstruction is under discussion [M. Scanderbeg, personal communication, 2017].

Only Argo locations with position flag “1” or “8” and Argo temperature and salinity profiles with position flag of “1” were retained for the calculations presented. Of the float data considered, 91 floats were tracked from June 10, 2002, to the present with ARGOS satellites, and 73 floats were tracked with GPS satellites from Nov 12, 2007, to present. The GPS constellation tracking is more accurate than ARGOS tracking, with stated location uncertainties of better than 7.8 meters. The ARGOS constellation uses the Doppler shift of received transmissions to estimate position and is sensitive to the number of received transmissions, and the configuration of the constellation at the time the messages were received. ARGOS positioning has four levels of accuracy ranging from “better than 250 m radius”, to “over 1500 m radius”. For ARGOS satellite derived positions, 19.4 % of positions were deemed “better than 1500 m radius”, 43.2% were deemed “better than 500 m radius”, and 37.4 % were deemed “better than 250 m radius”. Only 3 positions were deemed “greater than 1500 m radius” and were rejected from the dataset.

Argo floats that use the ARGOS constellation for positioning and data transmission may spend up to 12 hours at the ocean surface, whereas GPS tracked floats, which use Iridium satellites

for data transmission, typically spend less than an hour. During this period of transmission, Argo floats are essentially undrogued drifters, affected by surface winds and currents. After transmission, floats conduct their profiling mission and are advected by the shear in the ocean velocity field both on descent and ascent. Although techniques have been developed to correct for these dynamical errors (Gille and Romero, 2003), we have not applied them here.

1.3.2 RAFOS-enabled Argo floats

Quantifying position error for under-ice Argo floats, which have linearly interpolated positions between satellite fixes, is greatly facilitated in the Weddell Gyre because of the installed long-term acoustic float tracking system and deployment of RAFOS-enabled (Rossby et al., 1986) Argo floats between Feb. 26, 2008, and Feb. 4, 2013. A subset of 22 of these floats was processed and tracked for this study (Table 1.1) (Boebel, 2009; Fahrbach and de Baar, 2010). These data spanned 1,806 days and 29,183 position measurements (Fig. 1.3b) and were restricted to the Weddell Gyre.

The 22 RAFOS-enabled Argo floats used here are identical to standard (only satellite tracked) Argo floats, in that every 7-10 days they collect temperature and salinity profiles and then attempt to surface, transmit their data, and receive a satellite fix. The only difference is that they additionally listen for RAFOS signals while drifting at depth. All Argo float profiles, including RAFOS-enabled float profiles, have been entered into the Argo database as part of the normal Argo data stream. According to Argo database standard practice, under ice profile locations are assigned positions using linear interpolation. (Note that although these 22 floats had RAFOS receivers, their Argo database locations are based on satellite positioning and linear interpolation since RAFOS positions were not available; Argo data management does not include RAFOS-tracked positions at this time.)

A network of moored sound sources (Boebel, 2009; Fahrbach and de Baar, 2010) in the Weddell Gyre has been maintained since 1999 by the Alfred Wegener Institute (Klatt et al., 2007) (gold stars in Figs. 1.1, 1.3, 1.4, 1.13). Sound sources broadcast at carefully coordinated daily

intervals to avoid interfering with one another. RAFOS-enabled Argo floats listen for acoustic pings and record the time of arrival (TOA) of the sound pulses. By subtracting the known sound source clock time from the TOA, we calculate the time of sound travel. Dividing time of sound travel by the sound speed then gives a range from the float to the sound source. The sound speed is determined from Argo temperature and salinity measurements, which provide an approximate ocean density structure between the float and sound source (McDougall and Barker, 2011). The average sound speed in the upper 1,000 m of the Weddell Gyre was calculated using all Argo temperature and salinity profiles, yielding $1,441.9 \text{ m s}^{-1}$. We used this average sound speed for our positioning calculations to account for the complex paths that sound pulses take in the ice-covered Weddell Sea. Float and sound source clock times are subject to errors and offsets, and because of the rapid propagation of sound in the ocean, small timing errors can cause large changes in float track solutions.

The location of a float, which includes positioning error, can be determined if three or more distinct ranges are known. The ARTOA II software package (Wooding et al., 2005) is the most commonly used approach for constructing float track solutions from acoustic data. Typically, the ARTOA II software uses a least squares approach to solve for float position although other schemes are available. Like standard Argo floats, the RAFOS-enabled Argo floats attempt to surface every 10 days and recorded satellite derived positions when conditions allow. ARTOA II does not use satellite positioning to constrain float tracks, instead it informs the user of potential tracking biases by overlaying satellite positioning information onto acoustically derived float tracks and TOA scatter plots.

Unfortunately, tracking floats in the polar oceans is not as simple as in mid-latitudes. In mid-latitudes, large sound source transmission range ($>1000 \text{ km}$) is achieved through the efficient sound conduction of a broad and deep Sound Fixing and Ranging (SOFAR) channel; in the Weddell Gyre, the SOFAR channel is relatively shallow and narrow. When sound is conducted close to the surface, unknown interactions and reflections with sea ice occur. This causes transmission ranges in the Weddell Gyre to vary from 700 km to as little as about 300

km (Klatt et al., 2007). The acoustic tracking data for the 22 floats that we processed from this region frequently had less than 3 ranges. In addition to this issue, both measurements and sound speed have uncertainties, most notably the slow drift of sound source clocks and float clocks. As will be described in a subsequent publication, the least squares solution commonly used by ARTOA II is susceptible to becoming unstable if float and sound source clock drift have not been precisely accounted for in preprocessing or if only sparse range data is available.

Broader processing challenges can occur when dealing with the specifics of this formulation of acoustic tracking: what quantitatively defensible adjustments to the clock offsets should be made when acoustic ranging differs significantly from satellite positioning? If two acoustic ranges differ significantly, which one should be trusted? Can information learned about the clock drift of one source be propagated to the rest of the float tracking network? Can we estimate float location if we have just one or two acoustic range estimates instead of the three required in a least-squares solution?

Motivated by these questions and to overcome the greater challenges of intermittent and noisy range data in the ice-covered regions, we developed a Kalman smoother approach (Rauch et al., 1965) to process these Weddell Gyre RAFOS-enabled floats, which combines intermittent satellite positioning, noisy acoustic TOA, and dynamical information to reconstruct float tracks. The Kalman filter is a minimum mean square error estimator that is commonly used to combine intermittent and disparate sensor observations. In the computationally efficient formulation of the Kalman smoother that we have developed, the state variables and covariances are saved on the forward pass and applied during the backward pass to compute improved state estimates.

Our Kalman smoother method has been designed to solve the entire float system simultaneously - it treats all float positions, float velocities, sound source clock offsets, and sound source clock offset drifts as state variables. The Kalman smoother takes as input all GPS locations and acoustic ranging data. A priori estimates of state variables are based on crude predictive models

$$x_{t+1} = x_t + v_t \Delta t, \quad offset_{t+1} = offset_t + drift_t \Delta t \quad (1.1)$$

where x is the float position, v is the float velocity, *offset* is the sound source clock offset, and *drift* is the sound source clock offset drift. In this formulation, every time a float receives a satellite position on the same day as it acquires acoustic ranging data, the smoother calibrates the sound source clock offset and recalculates the offset drift. Our Kalman smoother approach has been validated using many ARTOA II processed acoustically-tracked float trajectories from the DIMES experiment, which benefited from both lack of sea ice and sufficient sound sources to allow accurate tracking (LaCasce et al., 2014). For our calculations, we used a 0.05 (units of degrees²) uncertainty in satellite derived positions, 10 (units of seconds²) uncertainty in acoustic ranging, 3×10^{-3} for process noise in position (units of degrees²), velocity (units of degrees² day⁻²), and sound source clock offset (units of seconds²), and 1×10^{-4} seconds² day⁻² in process noise of sound source clock offset drift. The 22 Weddell Gyre RAFOS-enabled floats had satellite positions for 1,155 days on a 10 day sampling interval, acoustically-derived positions on 12,281 days on a daily sampling interval, and had no positioning on 10,356 days. The Kalman smoother provides an estimate of float position for every day regardless of how many acoustic ranges are available.

1.3.3 SOSE Particle Release Simulations

To complement the RAFOS-enabled and satellite-tracked datasets for estimating uncertainties due to position loss while profiling floats are under ice, we conducted particle release experiments in the Southern Ocean State Estimate (SOSE) (Mazloff et al., 2010). SOSE is an eddy-permitting 0.16° Massachusetts Institute of Technology General Circulation Model, which is fit by constrained least squares to altimetry and water property data sets; depths are discretized into 42 levels of decreasing resolution with a domain spanning from 24.7°S to 78°S. The current SOSE version (iteration 100) spans six years (2005-2010). While SOSE has been extensively validated (Cerovečki et al., 2013; Abernathey et al., 2016), SOSE has known errors and biases, but is a powerful tool that can be used to diagnose Southern Ocean variability. SOSE currently assimilates all satellite-tracked and linearly interpolated Argo profiles. A module has

been developed to simulate and track the release of Lagrangian particles (Wang et al., 2014) at specified depths in the water column. 1000 simulated particles were released at locations distributed throughout our geographic region in water depths greater than 1000 m. The particles were tracked for 1500 days starting Jan. 1, 2005, saving the resulting positions every 2 days. All particles were assigned to depth level 23, corresponding to a depth of 950 m. Only particle trajectories within the original region are analyzed here. The final model output contained 611,022 position measurements (a subsample of particle tracks is shown in Fig. 1.3c).

1.3.4 SOSE Air-Sea Fluxes

One goal of this manuscript is to assess the uncertainty in interpreting under-ice processes that arises from projecting external Eulerian surface boundary conditions onto Lagrangian observations at interpolated positions. Direct flux observations lack the temporal and spatial resolution in this region to perform this calculation, so we analyzed daily-averaged surface heat flux, salinity flux, and buoyancy flux output from SOSE (Cerovečki et al., 2011). As a validation of the SOSE air-sea fluxes, Cerovečki et al. (2011) show that the air-sea fluxes that are adjusted by SOSE from initial National Center for Environmental Prediction (NCEP) or European Reanalysis (ERA) Interim flux fields are more representative of directly observed air-sea fluxes than the initial NCEP or ERA-Interim reanalysis fields.

Following Cerovečki et al. (2011), buoyancy flux is expressed in units of heat-equivalent buoyancy flux, and is the sum of air-sea heat flux and freshwater heat-equivalent flux

$$Q_{BF} = Q_{HF} - Q_{FW} = \frac{\rho_0 c_p}{g\alpha} B \quad (1.2)$$

where the buoyancy flux B is given by

$$B = B_{HF} + B_{FW} = \frac{g}{\rho_0} \left[\frac{\alpha Q_{HF}}{c_p} - \rho_0 \beta S(E - P) \right] \quad (1.3)$$

and g is the gravitational constant, ρ_0 is a reference density, c_p is the specific heat of seawater, S is the surface salinity, E is evaporation, P is precipitation, and α and β are the thermal expansion and saline contraction coefficients, respectively. In the Southern Ocean, the freshwater contribution to buoyancy flux is significantly greater than the air-sea heat flux and dominates Eqn. 1.2 (Cerovečki et al., 2011). For our analysis, we restricted our model output to the Weddell Gyre and to locations where the modeled ice concentration value was greater than 20%. This SOSE output comprised 28,470 daily averaged model values for each flux type.

1.3.5 Float Velocity Comparisons

Our results rely heavily on the assumption that the position statistics of the RAFOS, satellite-tracked, and SOSE datasets are similar. To validate this hypothesis, we compared the derived speeds of all three datasets. Float speeds are calculated by finding the difference between successive positions and dividing by the positioning time interval. A probability density function of the RAFOS-enabled float (daily sampling), satellite-tracked float (10 day sampling), and SOSE particle (2 day sampling) speeds is shown in Fig. 1.5. As can be seen by the progressive leftward shift in the peak of the normalized histogram, the mean speed of the more frequently tracked RAFOS-enabled float dataset is 2.75 km day^{-1} , the mean speed of the satellite-tracked float dataset is 2.16 km day^{-1} , and the mean speed of the SOSE particle experiment is 1.90 km day^{-1} .

There is no difference between the pressure case of RAFOS-enabled and satellite tracked Argo floats, so we expect their motion through the water to be the same. To further investigate the 0.6 km day^{-1} difference between the RAFOS and satellite-tracked mean speeds, we subsampled the RAFOS-enabled float positions at a 10 day interval - the same used by satellite-tracked floats; the position subsampled RAFOS-enabled dataset had a mean speed of 2.32 km day^{-1} . In addition to the tracking method, the main differences between the subsampled RAFOS-enabled dataset and the satellite-tracked dataset are that the former contains far fewer floats, and also samples in the southern (and ice-covered) regime of the Weddell Gyre. The subsampled RAFOS-

enabled dataset consisted of 2,239 calculated speed instances compared to 3,640 speed instances in the satellite-tracked dataset. We suspect that the difference of 0.16 km day^{-1} is likely due to statistical uncertainty due to sample size, and comparison of the derived speeds (and positions) of these datasets is appropriate, although it is possible that either there exists a Weddell Gyre circulation regime sampling bias in these datasets, or a tendency of the Kalman smoother to overestimate velocities.

As shown in the previous calculation, when float tracks are linearly interpolated, calculated speed is biased low because the distance between linearly interpolated positions is shorter than the true float path. To further compare the 10-day sampling interval of satellite-tracked floats and the daily sampling interval of RAFOS float tracking, we calculated the difference in mean speed between acoustically positioned float tracks and the interpolated float tracks of the RAFOS-enabled float dataset during all periods of position loss (Fig. 1.5 b). These data are color coded by duration of position loss. In general, we see greater speed differences during periods of longer position loss, as expected.

There are two limits for the speed difference between the acoustically positioned float tracks and linearly interpolated float tracks: the turbulent limit where the float speed difference is equal to the acoustically tracked speed, and the mean limit where the float speed difference is equal to zero. We observe a significant number of float paths approaching both of these limits. Average speed differences between RAFOS-enabled float velocities and interpolated Argo float velocities were 1.59 cm s^{-1} for periods of position loss greater than 180 days and 0.39 cm s^{-1} for periods of position loss less than 180 days. This discrepancy in speed underscores the need for an assessment of the uncertainty of the linear interpolation approximation. Wong and Riser (2011), analyzing seasonal ice zone Argo floats in the East Antarctic sector, similarly noted that the 10-day satellite derived tracks of ice-free Argo floats are almost 3 times longer than when those are linearly interpolated through the sea ice season.

1.4 Position Uncertainty Estimate

Autonomous floats are increasingly being used for under ice observations, e.g. 30 SOCCOM floats are under ice in austral winter 2018. Linear interpolation of latitude-longitude is the commonly used (and accepted) approximation for position while under ice, but uncertainties arising from this approximation have never been quantified. A related question is whether linear interpolation in latitude-longitude is the most reasonable choice, or might another interpolation scheme be better? Bathymetry has been demonstrated to affect float trajectories in the Southern Ocean, e.g. floats in equivalent barotropic flows tend to follow potential vorticity (PV) contours (LaCasce and Speer, 1999; Reeve et al., 2015), and isolated bathymetric features form Taylor columns that steer float trajectories (Meredith et al., 2015); these examples suggest that a PV-contour following approach might better approximate the trajectories and improve the uncertainties.

We use float and model position datasets, including highly resolved RAFOS-tracked positions as well as 10-day GPS-tracked profiling float positions, to estimate position uncertainty as a function of time of position loss. We estimate position uncertainty by withholding known position information and linearly interpolating in both latitude-longitude and PV coordinates. These linearly interpolated tracks are then compared to known position information, and statistics are averaged.

1.4.1 Methods

We assess the uncertainty in position loss due to lack of tracking with trajectories for our three independent data sets during periods of complete tracking without sea ice cover (satellite-tracked, RAFOS-enabled, and SOSE particle release) and compare the actual positions with interpolated positions during simulated sea ice cover. Ice cover is simulated by the application of a data withholding experiment; as the name implies, the experiment withholds information from a test case and compares the conclusions drawn from the limited information test to those of the

full information case. In this application, we compare a specified duration of float or particle track locations (which we call a “record”) to the positions generated by a linear interpolation of the endpoints of this record (see Fig. 1.7a). The time of each position as well as the great circle distance between the actual and linearly-interpolated positions are saved.

All interpolation in this chapter is linear, and is carried out in either latitude/longitude coordinates, which is the method applied in the Argo float data set, or PV coordinates. The location of any linearly interpolated profile is calculated in each axis by multiplying the axis distance between record end points by the ratio of time of the interpolated profile to total time of the record. Interpolation in latitude and longitude coordinates is straightforward. It is important to note that linear interpolation in latitude-longitude does not necessarily follow a great circle path.

Linear interpolation in potential vorticity (PV) coordinates requires more work. PV conservation in barotropic planetary-geostrophic flows is expressed as:

$$\frac{D(PV)}{Dt} = 0, \quad PV = \frac{f + \zeta}{h} \approx \frac{f}{h}, \quad (1.4)$$

where PV is potential vorticity, f is the Coriolis parameter, h is the water depth, and ζ is the relative vorticity. Under these conditions, potential vorticity is a material invariant and barotropic flows align with $f h^{-1}$ contours. At high latitudes, such as in the Weddell Sea, where the water column is much less stratified than at lower latitudes, flow is close to equivalent barotropic (unidirectional from top to bottom, although vertically sheared), and thus likely to follow $f h^{-1}$ contours. Consequently, in PV coordinates, our two axes of consideration are along $f h^{-1}$ contours and across $f h^{-1}$ contours. PV at the beginning and end point of a record is not usually the same (hence floats are not perfectly conserving PV). We linearly interpolate along the two axes: along-PV and across-PV.

PV ($f h^{-1}$) is computed using the Gaussian smoothed 0.16° bathymetry from SOSE, which is based on the Earth Topography Five-Minute Grid (etopo5) and Smith and Sandwell;

these data sets are binned to a 0.25° resolution and then interpolate to the SOSE grid. A steepest descent (or ascent depending on the change in PV) algorithm is applied to the location at the end of the record to find the across-PV axis, and an along gradient algorithm is used from the start of the record to find the along-PV axis (examples in Fig. 1.6 a,b,c). The intersection of the along gradient and steepest descent algorithms define the lengths of the PV axis. The two axes are then linearly interpolated to find the track in PV coordinates. Bathymetry is, in general, non-linear; the track generated by reversing the start and end point may not be the same as the original. We calculate both the forward and backward PV interpolation and save the record with the minimum mean error. Records with no intersection between the along and across PV contours were rejected from our analysis.

The character of position uncertainty as a function of time depends on the total time of position loss (record length, i.e. the total amount of time under ice), and the length of time since the position was measured for that given record length. We define these two separate quantities as ‘total interpolated position time’ (TIPT) and ‘interpolated position time’ (IPT). TIPT is identical to record length. We have used TIPTs of 1 month to 8 months (30 days to 240 days), in increments of 1 month. IPT ranges from zero to TIPT, in increments of 1 day. To estimate position uncertainty as a function of TIPT and IPT, we use float position records that are complete (no missing positions), and perform data withholding experiments. We randomly sampled 1000 records for each specified period of TIPT and calculated the ensemble standard deviation relative to linear interpolation for IPT intervals of 1 day within the TIPT. This procedure was then repeated for a range of TIPTs, from 1 to 8 months in monthly intervals. To estimate a robust standard deviation of the position uncertainty for a given IPT (within a given TIPT), we repeated this data withholding experiment many times using many different observed records.

To ensure the position data were appropriate for estimating the impact of linear interpolation in the Weddell Gyre, we imposed several criteria: records with data gaps 3 times longer than the sampling interval (6 days of position loss for SOSE, 30 days of position loss for satellite tracking, and 3 days of position loss for RAFOS-enabled tracking) were rejected. Similarly,

records with positions outside of the Weddell Gyre were rejected. Lastly, in order to enforce a degree of independence, we allowed no greater than a 50% time overlap in records.

The entire Weddell Gyre is ice-covered during austral winter. Consequently, the number of satellite-positioned float tracks that satisfied our linear interpolation criteria decays significantly in winter (data density in Fig. 1.6 d). Because of this, we were only able to compute statistically significant satellite-tracked position uncertainty for 4 months. This was not an issue for the acoustically-tracked floats and SOSE simulated floats, for which under-ice positions are known. Also, because of the relatively long sampling interval (10 days) of the Argo float tracks, we binned and averaged the mean satellite-tracked dataset position uncertainty estimates in 10 day segments. This was not necessary for the acoustically-tracked floats and the SOSE output due to the much higher frequency of positioning.

In the Southern Ocean (Fig. 1.1), the sea ice edge moves from north to south from winter to summer. In the Weddell Gyre, the longest interpolation-free records are located in the northeast. The northeastern region is dynamically different from the west, as seen in the kinetic energy field (regional map Fig. 1.3 b). This may cause a sampling bias in the satellite-tracked uncertainty estimate, which is based on records with no missing positions, as these ice-free records are biased towards the northeastern Weddell Gyre. Our estimate in latitude-longitude assumes position uncertainty to be isotropic within this region, whereas the estimate in PV coordinates accounts for bathymetrically controlled fronts and current meanders. Both estimates assume the position uncertainty statistics are unvarying in time; in the following section we show a seasonal analysis that supports this assumption.

1.4.2 Results

The standard deviation of the position uncertainty relative to linear interpolation as a function of IPT, for all TIPTs, data type, and interpolation scheme, is shown in Fig. 1.7. The interpolated latitude-longitude position uncertainty estimates derived from the satellite and the RAFOS tracked datasets show excellent agreement for all TIPTs for which we had sufficient

data to make these estimates. The SOSE position uncertainties are consistently lower than those from both float analyses. Comparisons of PV interpolation to linear interpolation were spatially structured and generally confirmed the hypothesis that floats follow PV contours: PV interpolation was better than linear interpolation for all datasets.

The averaged position uncertainty curves (Fig. 1.7a,b, c) have a quadratic shape as a function of IPT, for all three datasets, with highest position uncertainty at the middle of the time interval, and with that maximum uncertainty increasing with total period of position loss. This maximum amplitude of position uncertainty increases linearly with period of position loss (Fig. 1.7d). The quadratic shape is clearly defined for the SOSE model (2 day timing), and similarly for the relatively continuously tracked RAFOS data (1 day tracking). The satellite-tracked results (10 day interval) are much more variable especially for the longer position loss periods (3 and 4 months), likely due to the smaller number of long records available for analysis since they must be collected during ice-free periods (Fig. 1.7 a).

The position uncertainty curves are summarized by selecting the maximum position uncertainty for each monthly time period (TIPT), plotted in Fig. 1.7 d. The maximum value for a TIPT of 8 months of position loss, from the interpolated latitude-longitude RAFOS-tracked dataset (the value we report in our summary and abstract), is 116 ± 148 km, and increased essentially linearly from 0 TIPT at a rate of 0.48 km day^{-1} . PV interpolation for the same TIPT and dataset was 92 ± 121 km and increased 0.38 km day^{-1} . The satellite-tracked dataset linear interpolation position uncertainty increased 0.54 km day^{-1} . PV interpolation position uncertainty for the same dataset increased at 0.47 km day^{-1} . The high 4 month PV interpolation position uncertainty estimate is an unexpected result and could be an outlier because it does not match the linear trend of the rest of the graph and because of the small number of 4 month satellite-tracked records that met our PV interpolation criteria. The SOSE particle release simulations have a categorically smaller maximum position uncertainty. Latitude-longitude and PV interpolation yield a position uncertainty of 98 ± 130 km and 72 ± 97 km for 8 months of position loss, respectively. Position uncertainty of the SOSE dataset increased at a rate of 0.41 km day^{-1}

for linear interpolation and 0.30 km day^{-1} for PV interpolation. The ranges of these position uncertainty estimates (Fig. 1.7d) suggest that SOSE underestimates the position uncertainty compared with both the satellite and RAFOS-tracked datasets by a factor of 80%. Note that the position uncertainty estimates of each of the 3 datasets are within a standard deviation of the other two, which means that the differences might not be significant.

Fig. 1.7d also shows the seasonal differences in maximum position uncertainty. Summer RAFOS derived position uncertainty is generally higher than winter position uncertainty, conversely, winter SOSE derived position uncertainty is categorically higher than summer position uncertainty. Satellite derived position uncertainty (a more variable signal) is higher in summer or winter depending on the prescribed TIPT. Maximum difference between the winter and summer estimated positions uncertainties is for the 120 day satellite estimated position uncertainty, which seems to be an outlier. All other winter-summer position uncertainty differences were within 15%. From this we conclude that there is an insignificant seasonal difference in the position uncertainty statistics, which suggests similarities in the under-ice and open ocean eddy fields .

The spatial structure of linear interpolation minus PV interpolation for the SOSE dataset is shown in Fig. 1.8 and adds some qualification to the hypothesis of Reeve et al. (2015) that floats follow PV contours in the Weddell Gyre. PV interpolation is generally more accurate at the edge of the gyre in regions of consistent and steep bathymetry and fails in relatively flat areas or regions of complicated bathymetry. This analysis, although intuitive, may be biased by SOSE's underestimation of position uncertainty.

The quadratic shape of the position uncertainty curves is discussed from basic principles in the next subsection. The equivalence between the satellite-tracked and RAFOS-tracked results, and difference from the SOSE results, are also discussed, with suggestions for estimating position uncertainty in other ice-covered regions that do not have acoustic tracking.

1.4.3 Discussion

1.4.3.1 Quadratic form of position uncertainty

The mean position uncertainty curves for each TIPT shown in Fig. 1.7 a, b, c have distinctive quadratic shapes, especially when many records are available. Float position decorrelates in time (Balwada et al., 2016). When a float is under ice, we have in hindsight the most accurate position information about the float both immediately after the float submerges under the ice and immediately before the float emerges from the ice. Averaged over many realizations, we observe that float position uncertainty is maximum when IPT is half of TIPT. This is clearly because this time is most removed from the start and end times, when the position is known. Less obvious is why the functional relationship of position uncertainty to time is quadratic.

A well developed body of literature surrounding the so-called "Brownian Bridge" explains continuous-time stochastic processes with fixed probabilities at both the start and end points. As we will show below, this mathematical construction describes the quadratic shape of the uncertainty curves shown in the previous section and provides some insight into the oceanic mechanisms at play. We will first show that our interpolation process matches the definitions of a Brownian Bridge in one dimension, then expand to show the Brownian Bridge criteria are satisfied in two dimensions, and finally introduce advection.

As the simplest example of a Wiener process, let $x(t) \in \mathbb{R}$ be Brownian motion observed on $0 < t < T$: that is to say that the motion of the float path is random. By definition for Brownian motion, the expected value $E[x(t)] = 0$, or the motion is unbiased, and the covariance is $Cov[x(t_1), x(t_2)] = \sigma^2 t_1$, where $t_1 < t_2$ for some $\sigma > 0$. In the context of the ocean's velocity field, σ^2 has units of diffusivity and is the instantaneous variance at any time t of float velocity perturbations, which are assumed to be uncorrelated over time. This variance results from any random process that affects float position - this could be shear in the upper ocean, advection from wind before or after positioning, perturbation from the eddy field, etc. It is important to note that σ^2 is not diffusivity as typically defined (LaCasce et al., 2014) because it is calculated using the

absolute distance away from an interpolated position track instead of the actual mean flow.

Suppose the process is not observed over an interval $0 < t < T$. Its interpolated positions, as described in section 1.4.1, are:

$$x_L(t) = x(0) + \frac{t}{T}[x(T) - x(0)]. \quad (1.5)$$

Conditioned on the values $x(0)$ and $x(T)$, the anchored process $x(t) \mid x(0), x(T)$ is a Brownian bridge (Revuz and Yor, 2013). Then the following are well known:

$$E[x(t) \mid x(0), x(T)] = x_L(t), \quad \text{Cov}[x(t_1), x(t_2) \mid x(0), x(T)] = \sigma^2 \frac{t_2(T - t_1)}{T}.$$

In particular, the mean squared error is

$$E[x(t) - x_L(t) \mid x(0), x(T)]^2 = \text{Var}[x(t) \mid x(0), x(T)] = \sigma^2 \frac{t(T - t)}{T}.$$

Note that this expression does not depend on $x(0)$ and $x(T)$, so it also holds *unconditionally* at $x(0)$ and $x(T)$:

$$\begin{aligned} E[x(t) - x_L(t)]^2 &= \sigma^2 \frac{t(T - t)}{T}. \\ \sqrt{E[x(t) - x_L(t)]^2} &= \sqrt{\sigma^2 \frac{t(T - t)}{T}}. \end{aligned} \quad (1.6)$$

This is similar to the quadratic structure that we see in our results.

To show that this is a robust result in two dimensions, let $(x(t), y(t)) \in \mathbb{R}^2$ be composed of two independent Brownian motion processes $x(t)$ and $y(t)$ with the same variance. Let d denote Euclidean distance. Based on the results of the previous section:

$$E \{ d^2 [(x(t), y(t)), (x_L(t), y_L(t))] \} = E[x(t) - x_L(t)]^2 + E[y(t) - y_L(t)]^2 = 2\sigma^2 \frac{t(T - t)}{T}. \quad (1.7)$$

which is of the same functional form as the one dimensional case and matches the quadratic structure seen in our results (Fig. 1.7).

Finally, consider the addition of advection to our two-dimensional diffusive process: A simple advective-diffusion process with a constant velocity field (u, v) can be described as $(x(t) + ut, y(t) + vt)$, where $x(t)$ and $y(t)$ are independent Brownian motion processes as before. Conditioned on two known locations $(x(0), y(0))$ and $(x(T) + uT, y(T) + vT)$ at times $t = 0$ and $t = T$, the process in between is a Brownian bridge with mean

$$(x_L(t) + ut, y_L(t) + vt).$$

This is also the same as linear interpolation between the two points. Subtracting the mean gives the Brownian bridge process $(x(t), y(t))$ in \mathbb{R}^2 , which is the same as in the previous subsection. Therefore, the position uncertainty that we have estimated from observations should be approximated by (1.7). This implicitly assumes that over many realizations of the data, tracks generated from linear interpolation approximate the mean circulation and any deviations from the latitude-longitude or PV interpolation are due to float velocity perturbations caused by the mesoscale eddy field: random processes explain the growth of position uncertainty after a float is lost under the ice and the decline of position uncertainty before a float emerges from the ice. Over many realizations, the float velocity perturbation variance (σ^2), which affects the growth and decline of position uncertainty, should be the same. The Gaussian statistics that this method assumes might break down in fronts or regions of strong velocity gradients. In those regions, other methods of position uncertainty analysis should be considered.

The float velocity perturbation variance σ^2 estimated by fitting the position uncertainty curves in Figs. 1.7a,b,c ranges from $159 \text{ m}^2 \text{ s}^{-1}$ to $2614 \text{ m}^2 \text{ s}^{-1}$. It is smallest for shortest TIPT and increases with TIPT. If σ^2 represented the actual lateral diffusivity, it would be independent of TIPT. Its dependence on TIPT results from calculating σ^2 relative to the linearly interpolated tracks rather than the actual (unknown) mean flow. That is, unsurprisingly, the longer the period

of linear interpolation, the less representative the linearly-interpolated track is of the actual mean flow.

1.4.3.2 Application to ice-covered regions other than the Weddell Gyre

Can we usefully apply this method of deriving position uncertainty statistics in other ice-covered regions where RAFOS-tracked floats are not available? The agreement between the linearly interpolated satellite-tracked and RAFOS-tracked results (Fig. 1.7) suggests that we can, recognizing the sampling interval (10 days) for the satellite-tracked floats is longer than for RAFOS tracking (1 day) and there are shorter and fewer continuously tracked records (during ice free periods) for satellite-tracked floats. The detailed position uncertainty curves for these patchier satellite-tracked records have a more variable mean and standard deviation because of the lack of samples, but the maximum uncertainties appear robust in this Weddell Gyre example. This may seem surprising given that Fig. 1.5a shows that the frequency of position sampling matters in the composition of the velocity spectrum. A wide range of physical phenomena affect float position on different space and time scales, from mesoscale variations and basin circulations to eddy instabilities and inertial motion. 10-day sampling may under-resolve this mesoscale variability and because of this, the satellite tracking may be expected to underestimate some of the true position uncertainty.

As seen in Fig. 1.7 d, these potential sources of difference between the satellite-tracked and RAFOS-enabled datasets do not seem to matter. We conclude that even though the RAFOS-tracked floats have a higher mean daily velocity and greater probability of higher speeds (Section 1.3.5; Fig. 1.5 a), the higher frequency components of the velocity spectrum cancel out on time scales of months, so that over many realizations the position uncertainty estimates are the same. Therefore we suggest that position uncertainties using satellite-tracked floats alone could be informative, given that RAFOS tracking is not available in any other Southern Ocean ice-covered regions.

The difference between the float and the 0.16° SOSE results suggests caution in using

SOSE particle tracking to estimate position loss uncertainty, although the quadratic functional form is correct. SOSE is an eddy-permitting simulation; hence the model resolution of 0.16° does not capture the first baroclinic Rossby radius at these higher latitudes, which may underestimate the uncertainty due to an unresolved mesoscale field. Additionally, ice cover may mask the dynamic sea surface height derived from satellite products and used by SOSE. With few advective measurements in the Weddell Gyre, SOSE may underestimate the true mesoscale variability. We see this in the results as SOSE position uncertainty estimates are universally lower than either the satellite positioning or RAFOS-enabled track estimates (Fig. 1.7d). While SOSE is quantitatively different from in-situ measurements, the linear increase of the SOSE uncertainty estimate is qualitatively the same. This suggests that a higher resolution SOSE model with a more energetic mesoscale eddy field might more accurately reproduce position uncertainty statistics with fidelity.

With planned missions to deploy floats in the inflow of the southwestern sector of the Weddell Gyre, we anticipate that floats under ice for two ice seasons will become more common. It is tempting to extrapolate the straight lines of Fig. 1.7d to estimate position uncertainty of floats with position loss greater than 8 months. It is not clear, though, that the uncertainty will remain linear for periods longer than this.

1.5 Temperature, Salinity, and Air-Sea Flux Spatial Correlation and Uncertainty

Temperature and salinity are spatially and temporally correlated. Many types of surface processes - solar forcing, buoyancy or heat fluxes from storms, sea ice melt - span large spatial areas. Our overall goal is to estimate the representation error that the linear interpolation of position introduces in temperature and salinity products. Representation error is independent of float sensor error. Applications like state estimation or objective mapping incorporate observations and require a robust and accurate accounting of all uncertainties in the observations, which

include both representation and sensor error.

In the previous section, we estimated how far floats might deviate from interpolated latitude-longitude or PV coordinates; this is the distance for which we will calculate the strength of the oceanic connection. In this section we calculate the correlation length scales of temperature, salinity, and associated fluxes; this is the strength of the oceanic connection at all distances. We then combine correlation length scales and position uncertainty to estimate the representation error.

1.5.1 Methods

The method for calculating temperature and salinity spatial correlations from discrete, randomly spaced Argo floats that do not measure the entire field continuously is described in section 1.5.1.1, and is based on Ninove et al. (2016). For analysis of Lagrangian data following a float, gridded Eulerian fields are often employed. Float position uncertainty introduces representation errors when using Eulerian fields; the representation errors are estimated from spatial correlations. In section 1.5.1.2 we estimate spatial correlation scales of temperature and salinity surface flux from gridded SOSE output. Finally, in section 1.5.1.3 we use distance as a linear predictor to estimate the representation error field of using one temperature and salinity profile to approximate another at a specified distance.

1.5.1.1 Temperature and Salinity Correlation Length Scales

Resolving the statistics of a field with irregular space and time sampling is a common problem for oceanographers. We use a modified version of the approach in Ninove et al. (2016), who assembled float data collected in the same timeframe, detrended the data, and binned the data by distance to create a discrete and time dependent dataset from which they estimated a continuous time independent correlation field as a function of distance. In particular, they calculated the seasonally corrected anomaly field by first subtracting the 2009 World Ocean Atlas (WOA) 1° objectively mapped annual mean climatology (Locarnini, RA and Mishonov,

AV and Antonov, JI and Boyer, TP and Garcia, HE and Baranova, OK and Zweng, MM and Johnson, DR, 2010; Antonov et al., 2010) and then removing a localized seasonal climatology calculated from in-situ observations.

Our goal is to assess the induced representation error of projecting a true profile location onto a linearly interpolated position. Observations made in the same season experience similar forcing with relatively little spatial variability over the scale of the Weddell Gyre, which increases their correlation (reduces representation error). Leaving the seasonal signal of the temperature and salinity profiles intact reflects knowledge that the true observation and the linearly interpolated observation are recorded at the same time. Consequently, we move the profile only in space and not time, so we depart from Ninove et al. (2016) and remove only the SOSE temperature and salinity mean at the location of the profile.

Most Argo floats profile at 10-day intervals, so, to prevent successive measurements from the same float being compared against themselves, we bin the data set by weekly intervals. Next, we calculate the distance between every float pair in a given week. Paired measurements for all depths and densities are binned in increments of 35 km. Ninove et al. (2016) chose to bin results by their zonal and meridional distance. It is hypothesized that water properties should have higher correlation along streamlines. LaCasce and Speer (1999) found that modeled particles were 6 times more dispersive along PV coordinates than across. Reeve et al. (2015) objectively mapped the subsurface temperature maximum using similar reasoning but with length scales determined by the realities of data density. Building on this, it is more useful to bin temperature and salinity data by absolute distance in latitude-longitude and PV coordinates than by the axis of each metric. A description of our method to calculate PV coordinates can be found in section 1.4.1

We calculate the correlations between measurements in these distance and depth bins using a Pearson r test masked at a 90% confidence level using a temporal decorrelation of 35 days, determined by Gille and Kelly (1996) using altimetry data averaged over the whole Southern Ocean.

Correlation is expressed as:

$$\rho = \text{corr}(X, Y) = \frac{\text{cov}(X, Y)}{\sigma_X \sigma_Y} = \frac{E[(X - \mu_X)(Y - \mu_Y)]}{\sigma_X \sigma_Y}. \quad (1.8)$$

In words, this is an expression for how X and Y change together scaled by the standard deviation of both X and Y, where X and Y represent the binned pairs of temperature or salinity, σ is the standard deviation, and μ is the mean.

The vertical sampling intervals reported for individual float profiles are not uniform. We linearly interpolate all profiles to WOA 2013 version 2 depths (Zweng et al., 2013; Locarnini et al., 2013), to the maximum depth of 2,000 m for Argo floats. This is sufficient to resolve significant features such as the mixed layer and pycnocline. Additionally, we interpolate these data to prescribed levels of potential density referenced to surface pressure using the Gibbs Sea Water package (McDougall and Barker, 2011) in 0.05 kg m^{-3} increments. Observed densities varied from 1026.2 to 1028.2 kg m^{-3} , although there were only enough data to calculate correlations in the range 1027.1 - 1027.7 kg m^{-3} .

1.5.1.2 Temperature and Salinity Flux Correlation Length Scales

As a separate question of spatial uncertainty, it is often useful to interpret the measured Lagrangian profiles in the context of surface fluxes from an external gridded data set. If a float is assigned an interpolated position, what is the uncertainty in these boundary values? Although any gridded surface data could be used, we have chosen the adjusted air-sea fluxes of heat, freshwater, and buoyancy from SOSE (section 1.3.4).

We estimate the correlation length scales for SOSE heat, buoyancy, and salinity fluxes by creating a grid of points within the domain at 3° intervals of latitude and longitude. Using the heat, buoyancy, and salinity flux time series at all of these grid points, we calculated several spatially lagged correlations with the time series record of all points within a higher resolution grid of the Weddell Gyre separated by 0.5° intervals of latitude and longitude. The calculations

had three time domains: the entire time series, austral summer (November 15-March 15), and austral winter (May 15-September 15). We assumed heat, salinity, and buoyancy fluxes have a similar decorrelation time scale as temperature and salinity (35 days); because of this, we were generous in our seasonal definitions (4 months for summer and winter) to include as many degrees of freedom as possible.

After the correlation calculations, we binned the results by distance in 5 km segments and calculated the average salinity, heat, and buoyancy flux correlation in each bin. Results are given in section 4.2.2.

1.5.1.3 Uncertainty Field and Representation Error Calculation

Finally, we used the calculated correlations to estimate the uncertainty (error) of a field. Our analysis is motivated by the intuition that if 2 locations are perfectly correlated, knowing a value at one location should allow you to know the value at the other. Similarly, if 2 locations are perfectly uncorrelated, knowing the value at one location yields no information about the value at the other location.

Expanding on this, let $T(x) \in \mathbb{R}$ be a random temperature or salinity field, as a function of location. Let $X \in \mathbb{R}^2$ be a random assumed location of the float and let $X_{true} \in \mathbb{R}^2$ be the true location. Assuming that the field $T(x)$ changes slowly in x , we make a linear approximation at X_{true} , by defining the linear predictor:

$$L[T(X)|T(X_{true})] = E[T(X)] + \frac{cov[T(X), T(X_{true})]}{var(T(X_{true}))} [T(X_{true}) - E(T(X_{true}))]$$

where $L[T(X)|T(X_{true})]$ is the linear predictor, $cov[T(X), T(X_{true})]$ is the covariance of the value of the field at the random location and the value of the field at the true location, $E(X)$ and $E(X_{true})$ are the expected values of the field at X and X_{true} respectively, and $var(T)$ is the variance of the

field. We can write the mean square error of this linear predictor:

$$\begin{aligned}
\sigma_{rep}^2 &= E[(T(X) - L)^2] = var(T) - \frac{cov[T(X), T(X_{true})]^2}{var(T)} \\
&= var(T) \left[1 - \frac{cov[T(X), T(X_{true})]^2}{var(T)^2} \right] \\
&= var(T) [1 - cor[T(X), T(X_{true})]^2].
\end{aligned} \tag{1.9}$$

σ_{rep} is the representation error. $cor[T(X), T(X_{true})]$ is the correlation of T between positions X and X_{true} . X can be distance in any metric - herein, we consider both latitude-longitude and PV coordinates. Notice that if $cor[T(X), T(X_{true})] = 1$, meaning the interpolated position is perfectly correlated with the true position, the measured value projects exactly onto the interpolated data and the total error will be only the measurement error. Conversely, if $cor[T(X), T(X_{true})] = 0$, the interpolated position is exactly uncorrelated with the interpolated position and the measured value provides us no information about the value at the interpolated location. The error is then maximum and equal to the entire variance of the data set. This is the quantified uncertainty that matches our original intuition.

The total error, due to both representation error σ_{rep} and sensor error σ_{sensor} , arising from accuracy of the instrumental observation, is:

$$\sigma_{total} = \sqrt{\sigma_{sensor}^2 + \sigma_{rep}^2}. \tag{1.10}$$

where σ_{sensor} is reported from the manufacturer as 0.002 PSU for salinity and 0.002°C for temperature. Total error results are presented in the following sections.

1.5.2 Results

1.5.2.1 Temperature and salinity correlation scales and total error

Temperature and salinity correlations are illustrated in Figs. 1.9 - 1.12, along with the total error, which is the sum of representation error and sensor error (Eqn. 1.10). (The error

field is discussed further in section 1.5.2.3, where it is shown that representation error dominates the total error, with sensor error much smaller.) Correlations in temperature and salinity as a function of depth and distance were calculated in 65 depth layers from the surface to 2,000 m and distances from 35 - 1000 km in 35 km increments (Figs. 1.9, 1.10). Correlations and total error as a function of potential density and distance were calculated in 4 layers at 0.1 kg m^{-3} increments from 27.3 to 27.7 kg m^{-3} with the same distance binning as for depth (Figs. 1.11, 1.12).

The plotted correlations and errors are divided into two regimes: upper (0-300m) and deeper (300-2000m) ocean. The upper layer encompasses the fresh, very cold surface layer affected directly by sea ice, down through the halocline to the temperature maximum/salinity maximum core of the upwelled North Atlantic Deep Waters. The deeper layer includes the rest of these northern waters and the top of the Weddell Sea Deep Water (Orsi et al., 1993).

All correlation calculations (Figs. 1.9-1.12) show, unsurprisingly, that temperature and salinity correlation decays with increasing distance. Correlation length scales were longer in isopycnal layers (Figs. 1.11, 1.12) than in depth layers (Figs. 1.9, 1.10). This is likely a result of transient eddies and waves causing isopycnal heave, or the sloping density structure of the gyre in the Weddell Gyre, which introduces noise and reduces correlation along depth surfaces. Correlation length scales were marginally longer in PV than Euclidean coordinates and with largely the same structure.

Total error within each layer increases with increasing distance, due to its dependence on correlation (Eqn. 1.9). Correlation scales were longest in the upper ocean with significant correlation extending to 550 km and 350 km in temperature and salinity respectively (Figs. 1.9a and 1.10a). The higher upper ocean correlation compared with the deeper ocean is interpreted as resulting from the large spatial scale of air-sea buoyancy flux due to the annual cycle and longer timescale atmospheric variability.

Low correlations between 100-200 m are apparent in the full depth-resolution figures (Figs. 1.9a, c 1.10a, c). This is the depth range of the surface mixed layer and halocline (Fig.

1.4), and as explained above, correlations are low because of transient, localized heave of the highly stratified halocline.

Notably, the larger correlation scales in the upper ocean correspond to larger total error (Figs. 1.9e, f and 1.10e, f): the upper layer error is higher because the surface layer variance is high while the deeper layer has more uniform temperature and salinity. We hypothesize that this is due to the wide range of overall variability in surface temperature and salinity and their fluxes during ice-free periods. The float time series example in Fig. 1.4 shows the strong seasonal dependence of the temperature, salinity, and mixed layer depth in the upper 200 m. This is a response to local surface forcing. An example of the along track fluxes (from SOSE output) experienced by WMO ID # Argo Float 5901717 (Fig. 1.13) shows large variations in heat and salinity flux during the ice-free seasons, with large spikes in fluxes during both ice-formation and ice-melt. The deeper layer does not have such large external forcing. Temperature and salinity variance in the lower layer is smaller and hence the total error is smaller.

1.5.2.2 Air-sea fluxes and spatial correlation scales

SOSE surface fluxes into the ocean, along interpolated Argo tracks and RAFOS-enabled float tracks, are illustrated for float 5901717 (Fig. 1.13). (Differences between the satellite-tracked and RAFOS-enabled float track fluxes during ice-free periods are solely due to the difference in sampling interval between 10 day satellite fixes and the daily acoustic positions; the fluxes match on the days of satellite fixes.) Fluxes were diagnosed from SOSE output.

SOSE's under-ice heat flux into the ocean for float 5901717 is relatively constant with a mean of -6.77 W m^{-2} (where positive flux heats the ocean). This trend of stable under ice heat fluxes is seen over all floats. The average under-ice heat flux over the entire dataset was -8.06 W m^{-2} . At the end of periods of position loss, we observe a flux of fresh water into the ocean, closely followed by positive heat flux into the ocean which peaks close to 200 W m^{-2} . The time lag between the significant spikes in heat and salinity flux can be explained by the seasonal cycle of sea ice formation and melt. At the end of the sea ice season, the energy that would be entering

the ocean due to increased solar forcing is instead stored in latent heat and used to melt sea ice. Once a significant fraction of the ice has melted, then heat enters the ocean as seen by the large spike in positive heat flux and the observed time lag.

Conversely, at the beginning of the ice season, there is a significant flux of heat out of the ocean (on the order of -200 W m^{-2}) closely followed by a salinity flux into the ocean. This is an example of seasonal forcing causing sea ice formation followed by brine rejection. The sea ice, once formed, acts as a blanket on the ocean and prevents significant air-sea flux.

We have plotted the correlations and related uncertainties of mean under-ice surface fluxes into and out of the ocean for heat, salinity, freshwater, and buoyancy as a function of distance (Fig. 1.14). Similar to float salinity and temperature measurements, surface fluxes at close separations are more correlated than locations that are far apart. We observe that overall buoyancy flux is dominated by the salinity flux signal for these Weddell Gyre floats. For 8 months of position loss, we calculate maximum heat flux, buoyancy flux, and salinity flux errors to be 28.5 W m^{-2} , 212.4 W m^{-2} , $1.8 \times 10^{-3} \text{ kg m}^{-2} \text{ s}^{-1}$, respectively. Heat flux correlations are independent of season. In contrast, salinity correlations are about 0.2 higher in summer than in winter; buoyancy correlations follow salinity. This seasonal change in correlation results in a seasonal variation in the flux uncertainty of buoyancy and heat of 34.2% and 27.2% respectively. As seen in Fig. 1.13, flux regimes depend strongly on season and ice conditions. The difference between summer and winter salinity correlations is due to greater modeled regional structure during ice formation (and hence brine rejection) than to melting.

The SOSE flux results can also be used to examine our assumption of temporal invariability of correlation scales of upper-ocean properties - we hypothesize that correlation length scales of the upper ocean heat and salinity should correspond with associated heat and salinity flux correlations. In Fig. 1.14 we compare the qualitative and quantitative structure of these calculated values by overlaying the ocean temperature and salinity correlation averaged over the upper 50 meters (described in section 1.5.2) on the heat and salinity flux plots respectively. We observe that temperature correlation is about 0.1 greater than heat flux correlation and salinity

correlation matches well with wintertime salinity flux correlation. One component of upper ocean temperature or salinity is the time integral of surface heat or salinity flux, so we hypothesize that the upper ocean smooths high-frequency flux components of the heat and salinity flux signal. This could result in longer correlation scales for upper ocean temperature and salinity than for heat and salinity flux. It is problematic then that upper-ocean salinity correlation closely matches wintertime salinity flux correlation because we would expect it to be higher, and because much of the satellite tracked float data was collected in the summertime. This suggests that the modeled correlation scales of heat and salinity flux in the Weddell Sea region of SOSE may be inaccurate and should be treated with some skepticism.

1.5.2.3 Salinity and Temperature Error as a Function of Position Loss Time

We have estimated position uncertainty in latitude-longitude as a function of time (Section 1.4) and temperature and salinity uncertainty as a function of latitude-longitude distance (Section 1.5). In this section, we combine these two calculations to estimate representation error as a function of position loss. These uncertainty estimates are useful for synthesizing Lagrangian data of unknown position into gridded Eulerian products, and are calculated for the first time.

Maximum total error in temperature and salinity, as a function of depth for a location to which an under-ice float profile has been assigned through interpolation, is estimated as follows: given a specified TIPT, maximum position uncertainty is estimated using Fig. 1.7 (Section 1.4). The temperature and salinity error profiles are then taken from the temperature and salinity error maps (Figs. 1.9d and 1.10d). For example, the column between 70 and 105 km would be used for a position uncertainty of 90 km.

The maximum total temperature and salinity error due to linear interpolation of positions for 120, 180, and 240 days of position loss as well as the standard deviation of the Weddell Gyre Argo float temperature and salinity data are shown in Fig. 1.15. For the upper ocean (shallower than 300 m), maximum error can equal 0.66°C or 94.5% of the total variance in the temperature field and 0.15 psu or 91.4% of the variance in salinity. Gridded products that do not

account for this linear interpolation error in position measurement will project this uncertainty onto model error. The prescribed model error for SOSE (Mazloff et al., 2010) averaged over our study area is also shown in Fig. 1.15. In the Weddell Gyre, SOSE uses a maximum model error of 0.24°C in temperature and 0.067 PSU in salinity. Comparing prescribed model error with maximum linear interpolation uncertainties, we find that linear interpolation uncertainty is 276% of SOSE model error in temperature and 229% in salinity. These representation errors are not only significant in the upper ocean. For the deeper parts of Argo float profiles (300-2,000 m), we find that uncertainty due to linear interpolation can be as high as 0.16°C, or 55.9% of the total variance in the temperature field, and 0.01 psu, or 91.1% of the signal in salinity.

In the broader sense, this highlights the importance of this type of accounting for use in all applications. If higher uncertainty due to interpolated positions is not combined with measurement uncertainty, any product generated is likely to overfit the data. The Southern Ocean contributes to the long-term oceanic heat gain. Desbruyères et al. (2016) found a warming trend in the deep ocean below 2,000 m of $2.17 \pm 0.70 \times 10^{-3} \text{ }^\circ\text{C yr}^{-1}$ averaged from 1991 to 2010. At 2,000 m, we estimate a temperature uncertainty of $8.49 \times 10^{-2} \text{ }^\circ\text{C}$, which represents 39.1 years of warming at the Desbruyères et al. rate. This comparison might be misleading because of the different depth ranges, given that the warming trend has been minimal in the Southern Ocean's Deep Water layer between the thermocline and abyssal water (Purkey and Johnson, 2010). Nevertheless, the reader is cautioned that as autonomous technologies advance and the Argo array heads into the abyss with the deployment of Deep Argo, linear interpolation uncertainty, if inappropriately accounted for, could mask subtle residual signals.

A noteworthy point is that theinsonification of the Weddell Gyre and use of RAFOS-enabled profiling floats eliminates linear interpolation error for the temperature and salinity profiles when RAFOS tracking is possible. In our study, RAFOS-enabled floats received satellite positioning on 4% of days, and were acoustically tracked on 56% of days. As noted in Klatt et al., sound transmission in the Weddell Sea is more efficient during ice free conditions and consequently floats were acoustically tracked on 52% of days while under the ice and 61%

of days while out of ice. A denser network of sound sources, or improvements in under ice sound transmission or detection could improve this tracking rate. Any long term study of under ice processes should consider acoustic tracking to reduce representation error due to linear interpolation.

1.6 Conclusions

Position uncertainty and spatial correlation scales for temperature and salinity were combined to produce error estimates as a function of time-of-position-loss for a set of Argo floats deployed in the Weddell Gyre. Position uncertainty was calculated by linearly interpolating float track data, in latitude-longitude and PV coordinates, at intervals from 1 to 8 months. Float positions were derived from satellite-tracked Argo floats, RAFOS-enabled Argo floats (when available), and a SOSE particle release simulation. The position uncertainty estimated from the RAFOS-enabled float tracks for 8 months of ice cover was 116 ± 148 km. The estimates derived from satellite-tracked and RAFOS-enabled datasets were in good agreement, although there were only enough satellite-tracked data during ice-free periods to make estimates for 4 months of position loss. PV interpolation reduced position uncertainty for all datasets. We interpreted the quadratic structure of the position loss as a function of time using a Brownian Bridge, which assumes that the deviation from the linearly interpolated track is due to random motion resulting from the mesoscale eddy field. Maximum position uncertainty was similar during summer and winter which suggests that the parametrized diffusivity (σ^2) is temporally invariant.

The agreement between position uncertainties estimated from satellite-tracked floats (during ice free periods of continuous 10-day sampling) and RAFOS-tracked floats, as well as the similarities of winter and summer position uncertainty statistics, suggests that satellite-tracked profiling floats can be used to estimate position uncertainties in other parts of the seasonally ice-covered Southern Ocean that have no RAFOS tracking. In contrast, particle tracking in the 0.16° SOSE iteration yielded position uncertainties that were approximately 75% of the

observation-based method, possibly because SOSE at this spatial resolution underestimates eddy energy. Therefore we cannot recommend using the 0.16° SOSE to estimate these statistics throughout the Southern Ocean.

Within the range of 1 to 8 month position uncertainty, maximum error in salinity and temperature above 300 m was 0.15 psu and 0.66°C, respectively; maximum uncertainty in temperature and salinity between 300 and 2,000 m was 0.01 psu and 0.16°C, respectively. Spatial correlation was longer along isopycnal surfaces and in the mixed layer. Error due to linear interpolation of float positions increased as a function of time of position loss, and was up to 81.9% of the variance in Weddell Gyre float temperature measurements and 96.5% of the variance in Weddell Gyre float salinity measurements for 8 months of position loss. Temperature and salinity uncertainties are important inputs to state estimates, which are constrained by observations. We recommend that temperature and salinity uncertainties in state estimates be increased above measurement error for Argo floats that are under the ice.

We also found maximum heat flux, salinity flux, and buoyancy flux errors to be 28.5 W m⁻², 1.8 × 10⁻³ kg m⁻² s⁻¹, and 212.4 W m⁻², respectively. Heat flux errors had little seasonal variability. Salinity, freshwater, and buoyancy flux correlation values were approximately 0.2 greater during austral summer than in austral winter. Spatial correlation scales in temperature and salinity were calculated along both depth and density surfaces and presented as a function of total distance.

If an observing system aims to resolve spatial variations in upper ocean temperature and salinity, acoustic tracking is recommended. The RAFOS float tracking used for the Weddell Gyre floats here was carried out with a new approach that we developed in the course of this study, using a Kalman smoother, to be described in a subsequent publication. This approach reduces the tracking error. These errors are not treated here; rather, the tracking is treated as if it is exact.

As the volume of biogeochemical data increases, our uncertainty analysis can be repeated for variables other than temperature and salinity. For a biogeochemical tracer such as alkalinity, which is likely to have distributions that are similar to salinity (Lee et al., 2006), we would expect

alkalinity correlation scales to be similar to those for salinity. Biogeochemical tracers that are closely linked to surface ventilation and seasonal blooms will likely have correlation scales and uncertainties that differ from temperature and salinity, and will need to be calculated from in situ data sets, which are as yet inadequate.

1.7 Acknowledgements

Acoustic TOA processing for the RAFOS floats was carried out by Dr. Cathrine Hancock. Dr. Bruce Cornuelle suggested and assisted with development of the Kalman smoother algorithm for RAFOS-tracking. Drs. Sarah Gille and Ivana Cerovecki provided insightful comments. The authors also thank two anonymous reviewers for their thoughtful and detailed edits. This work was supported by the SOCCOM project under NSF Award PLR-1425989. K. Speer acknowledges support from NSF OCE 1231803. S. Riser acknowledges support from NOAA grants NA17RJ1232 and NA15OAR4320063 and NSF grant OPP1429342. Argo data sources are listed in the references. Our quality control of the float locations revealed issues that have been reported to Argo and subsequently corrected. The RAFOS float trajectory data are preliminary and available on request from the authors. SOSE output is publicly available for download at <http://sose.ucsd.edu/>. Chapter 1, in full, is a reprint of the material as it appears in *Journal of Geophysical Research: Oceans* 2018. Chamberlain, P. M., Talley, L. D., Mazloff, M. R., Riser, S. C., Speer, K., Gray, A. R., & Schwartzman, A., Wiley Press 2018. The dissertation author was the primary investigator and author of this paper.

WMO Identifiers for RAFOS-Enabled Argo Floats						
5901716	5901717	5901718	5901720	5901721	5901723	5901724
5901728	5901730	5901731	5901733	5901734	5901735	5901736
5901737	5901738	5901739	5901740	5901741	5901742	5901743
5901744						

Table 1.1. RAFOS-enabled Argo profiling floats tracked in the Weddell Sea deployed from February 26, 2008 to February 4, 2013. Argo data graphics are available at <http://www.ifremer.fr/co-argoFloats/>.

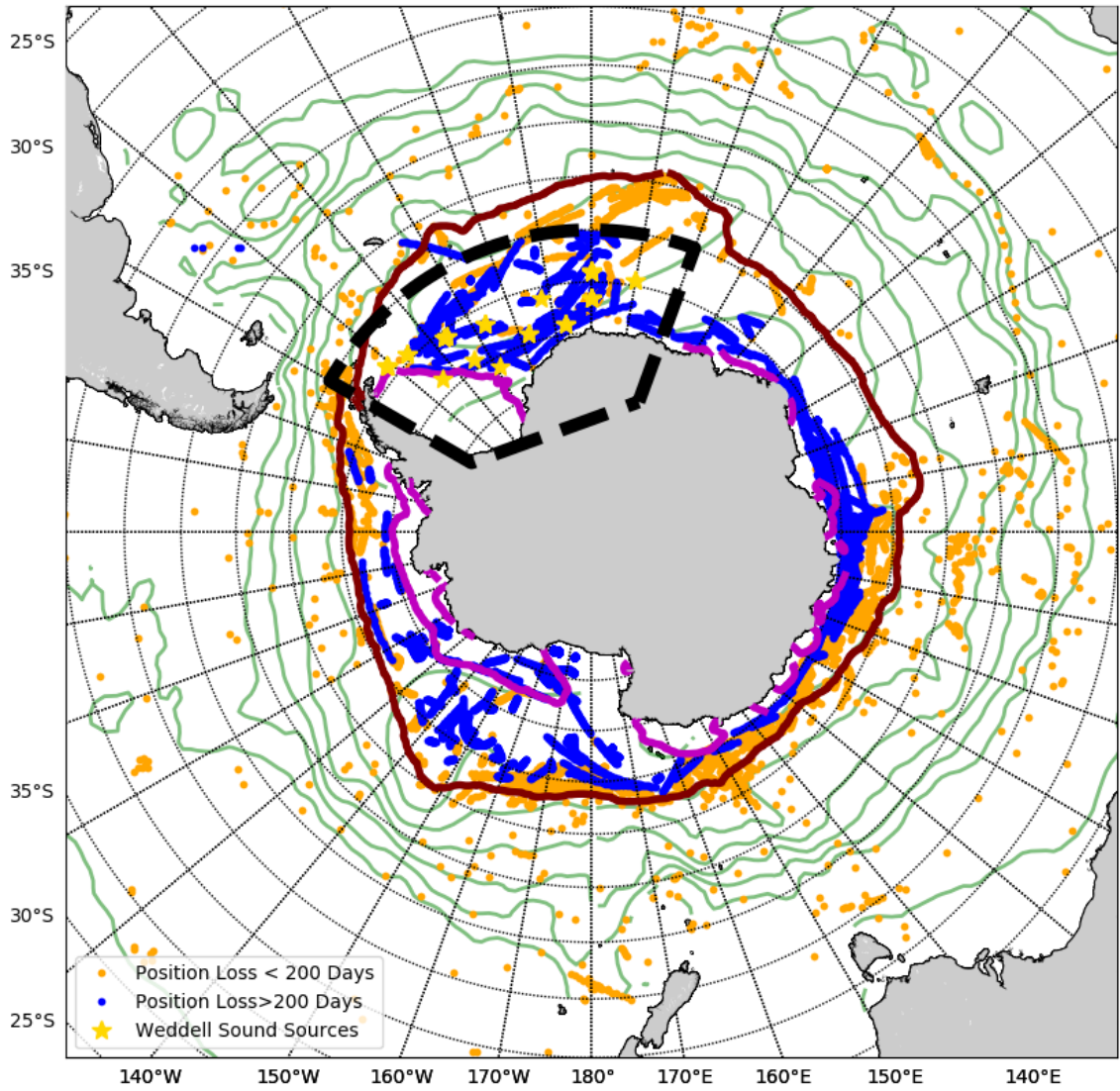


Figure 1.1. All interpolated Argo float positions in the Southern Ocean. Yellow and blue dots: interpolated Argo positions with position loss < 200 days (Y) and > 200 days (B). Gold stars: Weddell Sea sound sources (Klatt et al., 2007). Green curves: average 1000 m streamlines from Argo data (Gray and Riser, 2014). Dashed black lines enclose our Weddell Sea study area. Mean September ice edge (red) and mean February ice edge (magenta) from NSIDC (Fetterer et al., 2016), averaged from 1978 to present.

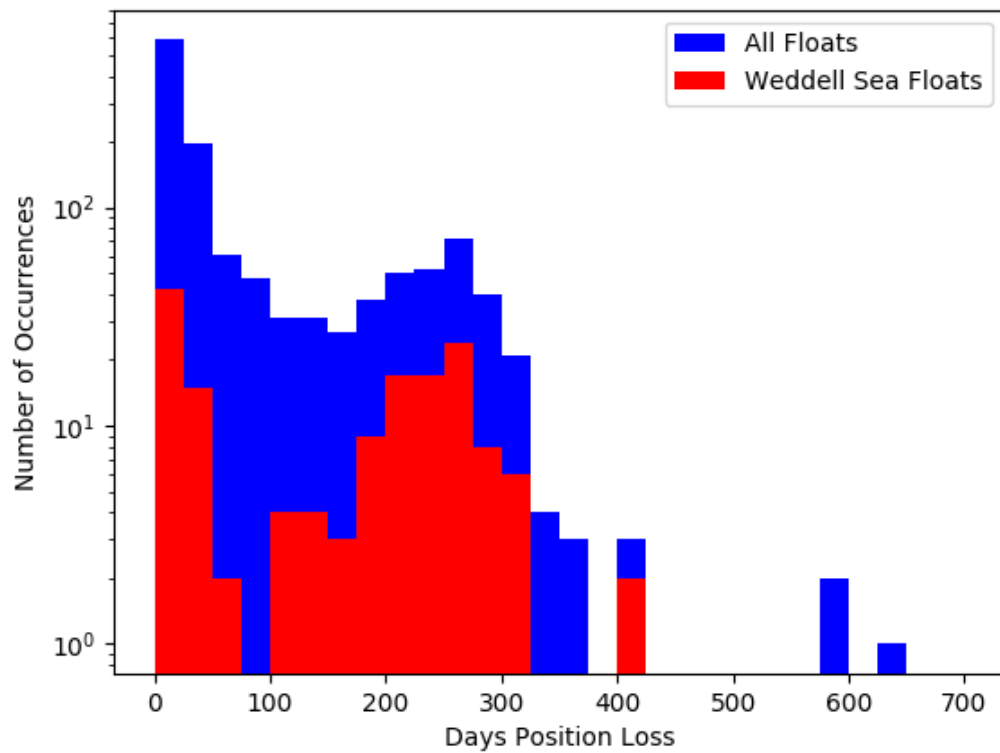


Figure 1.2. Histogram of Total Interpolated Position Time (TIPT) for all Antarctic Argo floats (blue bars, based on all yellow and blue dots in Fig. 1) and all Weddell Sea Argo floats (red bars, based on study area in Fig. 1).

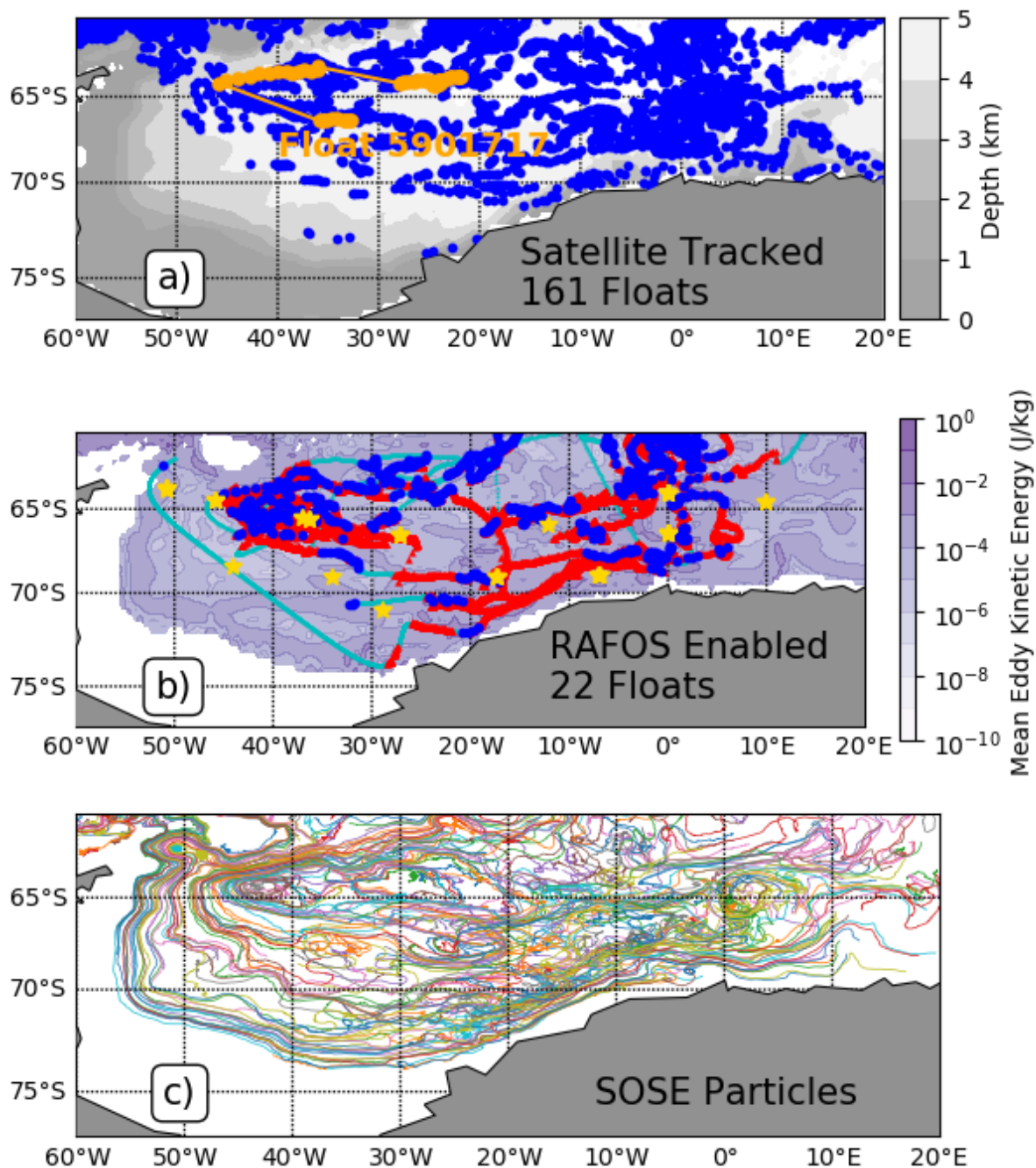


Figure 1.3. (a) Satellite-tracked Argo float positions (blue dots) in the Weddell Sea with bathymetry (gray shading). Float 5901717 used in Figs. 1.4 and 1.13 is highlighted in orange. (b) AWI sound sources (gold stars), acoustically tracked positions of RAFOS enabled Argo floats (red dots), satellite-tracked positions of RAFOS enabled floats (blue dots), Kalman smoother interpolation (cyan dots), and 950 m mean eddy kinetic energy from SOSE (shading). See Table 1.1 for list of RAFOS-enabled Argo floats. (c) 240 SOSE particle tracks of particle release experiment (1000 particles total) in the Weddell Sea.

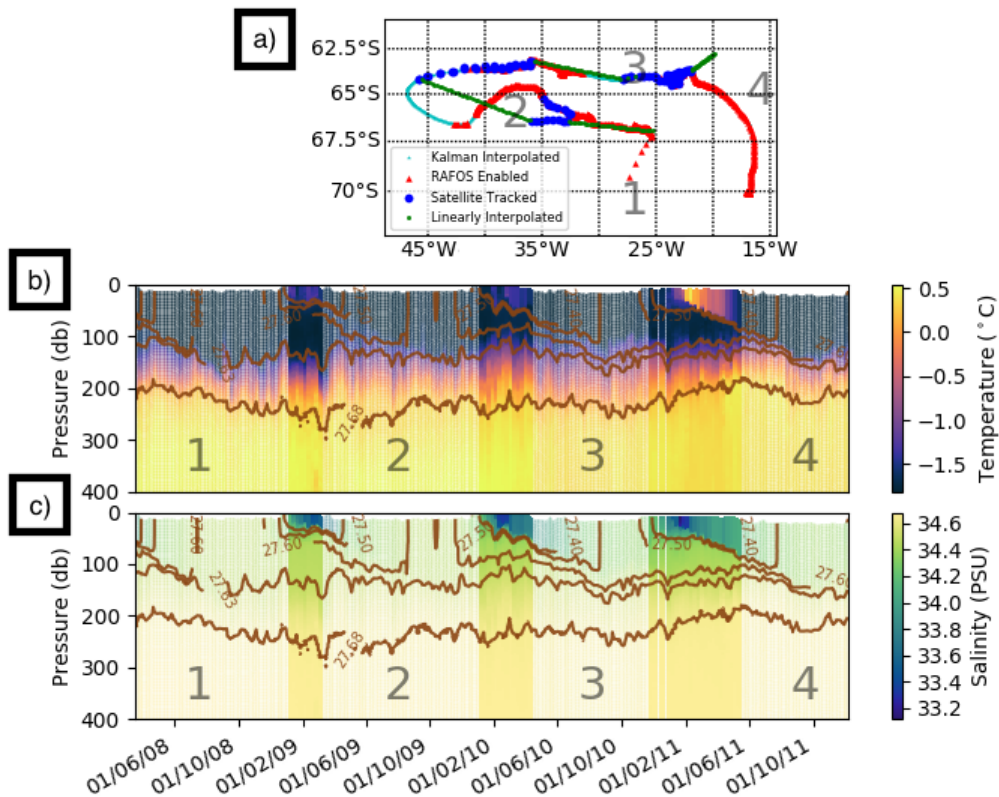


Figure 1.4. (a) WMO ID Float 5901717 float track (blue dots showing 10-day satellite-tracked positions) in the Weddell Sea. Straight segments (green) are periods of Argo linear interpolation due to position loss in the presence of sea ice. Acoustic tracking has been produced for this float (red) (Fig. 3b). (b) Potential temperature for WMO ID float 5901717 with superimposed potential density σ_θ (brown curves). (c) Salinity for WMO ID float 5901717 with superimposed potential density σ_θ (brown curves). Numbers and lightened regions in (b) and (c) are periods of position loss due to the presence of sea ice.

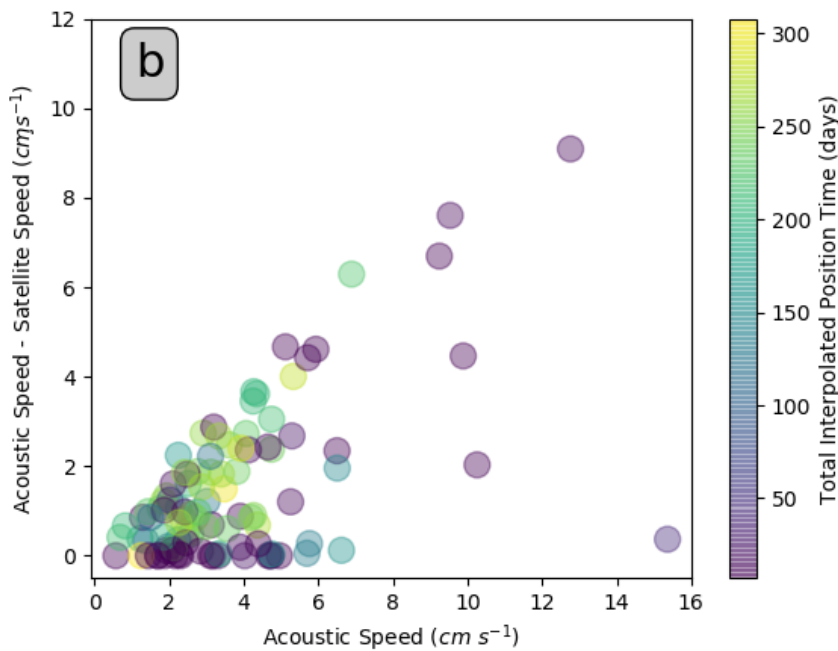
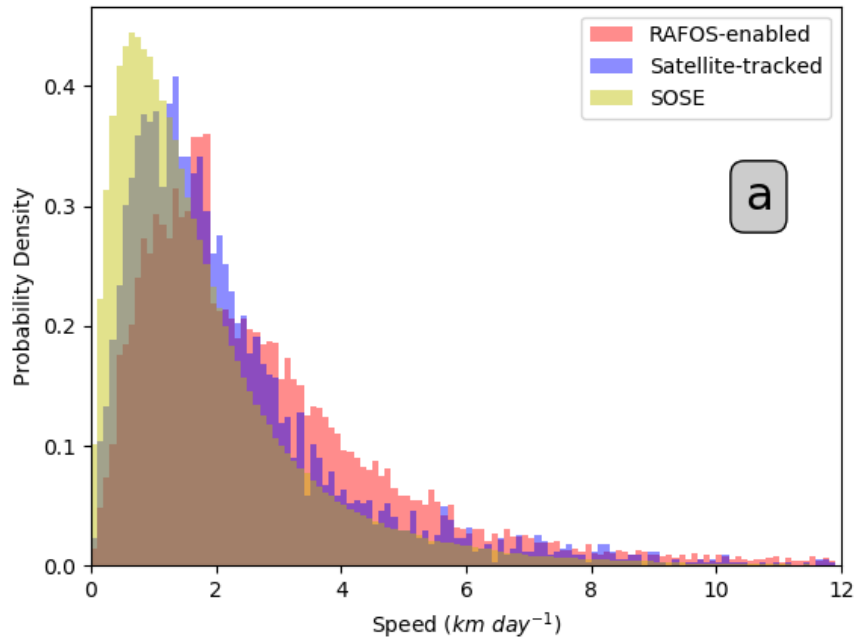


Figure 1.5. (a) Normalized probability density function of RAFOS-enabled float speeds (red), satellite-tracked float speeds (blue), and SOSE particle speeds (yellow) in the Weddell Sea; (b) Mean acoustically derived speed minus mean interpolated speed for all periods of Total Interpolated Position time in the RAFOS-enabled float dataset. Color of points indicates duration of position loss.

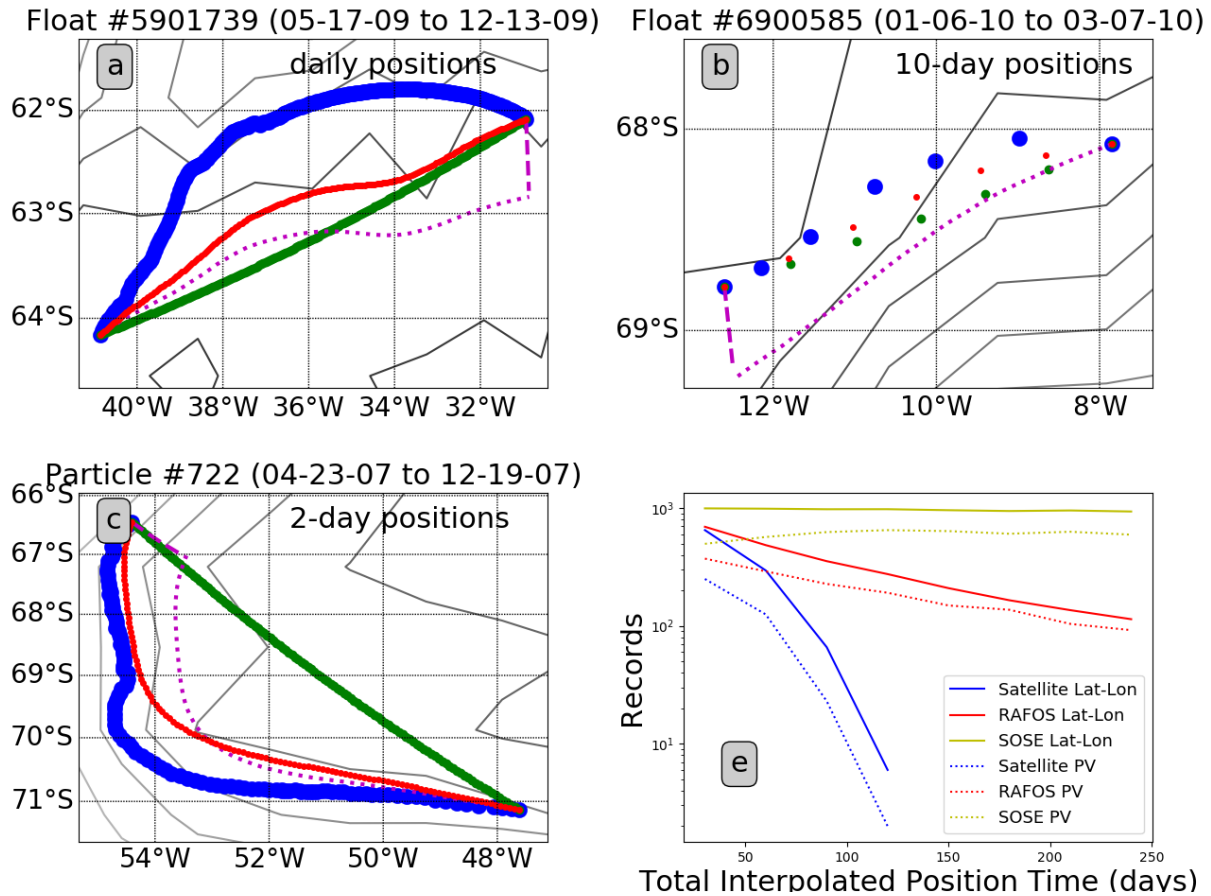


Figure 1.6. Selected float track data for RAFOS, Satellite, and SOSE particle datasets. Actual trajectories (blue dots) are compared with PV interpolation (red dots) and linear interpolation (green dots). Along PV axis (pink dots), across PV axis (pink dashes), and bathymetry (black lines) are provided for context. (a) RAFOS tracking of WMO float ID # 5901739 for 210 days from May 17, 2009 to December 13, 2009; (b) Satellite tracking of WMO float ID # 6900585 for 60 days from Jan 6, 2010 to March 7, 2010; (c) SOSE particle 722 subsampled for 240 days from April 23, 2007 to December 19, 2007; (d) Size of all datasets: Satellite (yellow), RAFOS (red), and SOSE (blue) for linear (solid) and PV (dotted) interpolation by time interval.

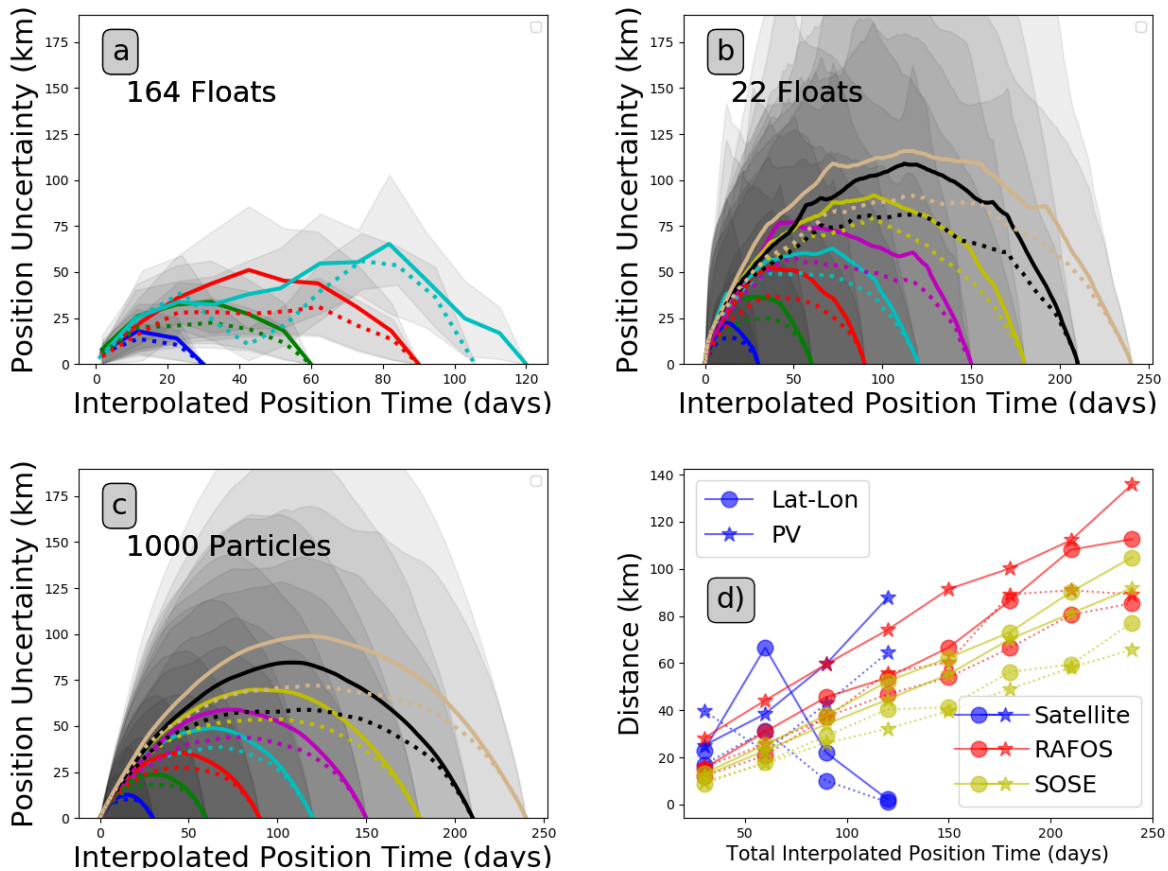


Figure 1.7. Position uncertainty as a function of interpolated position time (IPT), based on the difference between the actual track and the linear and potential vorticity interpolations of the track: (a) satellite positioning derived standard deviation of position uncertainty from 164 floats; (b) RAFOS positioning derived standard deviation of position uncertainty from 22 floats; (c) SOSE derived standard deviation of position uncertainty from 1000 particles. For all uncertainty estimates (a, b, c), colored curves are mean position uncertainty of linear (solid) and PV (dots) interpolation in monthly time intervals (TIPT). Shaded gray areas are standard deviation in the uncertainty estimate. (d) Maximum seasonal position uncertainty estimates for all three datasets for summer (stars) and winter (circles) with linear (solid) and PV (dotted) interpolation.

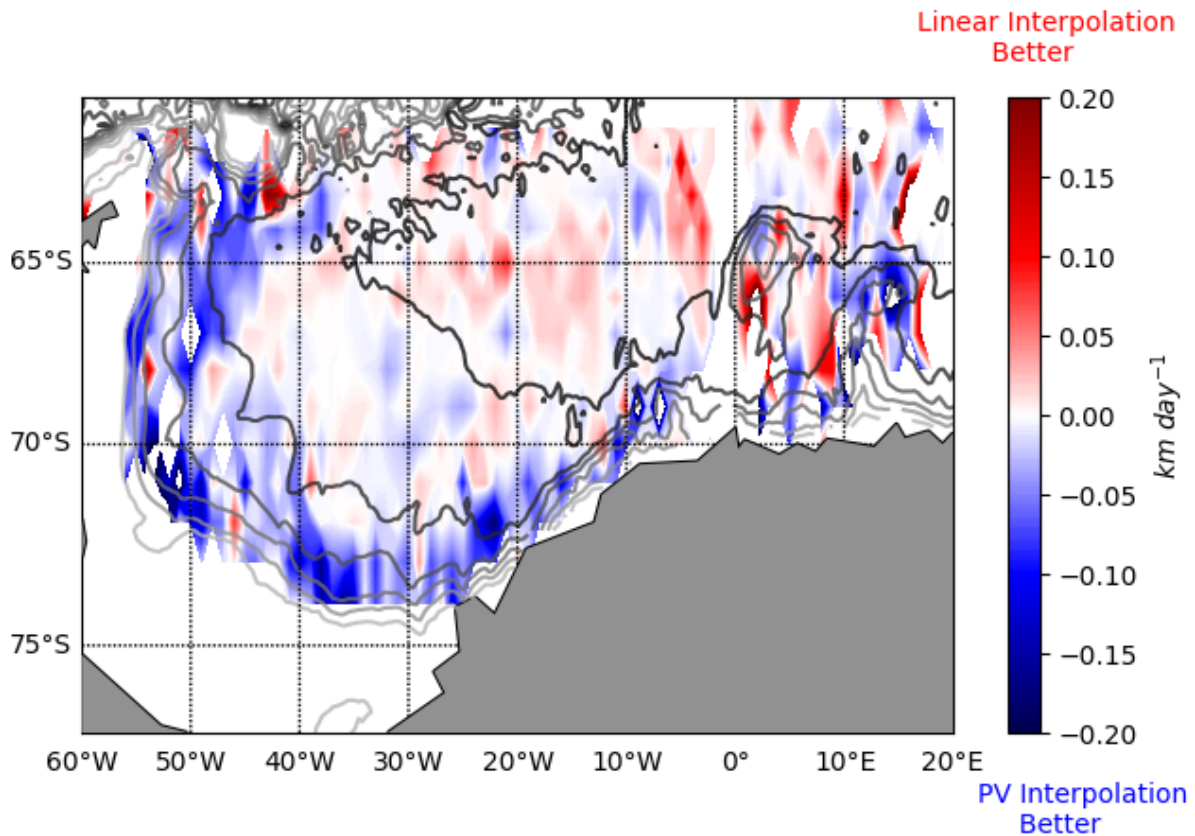


Figure 1.8. Spatial distribution of linear interpolation uncertainty minus PV interpolation uncertainty (km/day) of SOSE data withholding experiment. Red and blue coloring represents the spatially binned and averaged maximum position uncertainty for linear and PV interpolation normalized by period of position loss. Grey lines represent isobaths in 1 km intervals.

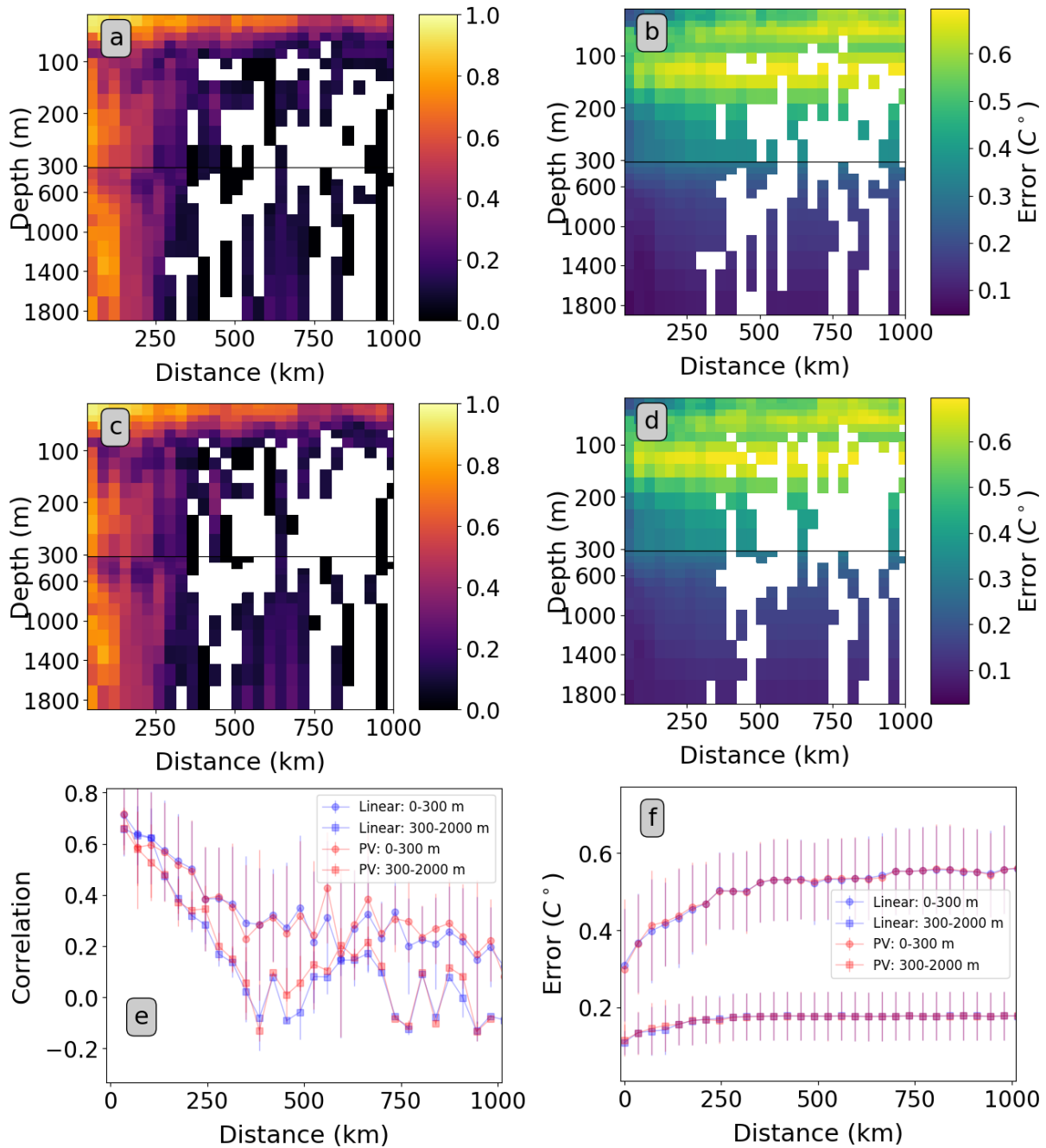


Figure 1.9. (a) Temperature correlation as a function of distance and depth at 90% confidence. (b) Total temperature error as a function of distance and depth at 90% confidence in regimes above and below 300m. (c) Temperature correlation as a function of distance in PV coordinates and depth at 90% confidence. (d) Total temperature error as a function of distance in PV coordinates and depth at 90% confidence in regimes above and below 300m. (e) Temperature correlation as a function of distance averaged over 0-300m and over 300-2,000 m depth at 90% confidence; error bars represent standard deviation in correlation over these depth ranges. (f) Total temperature error as a function of distance at 90% confidence averaged over 0-300m and 300-2,000 m depth; error bars represent standard deviation in error over regime depths.

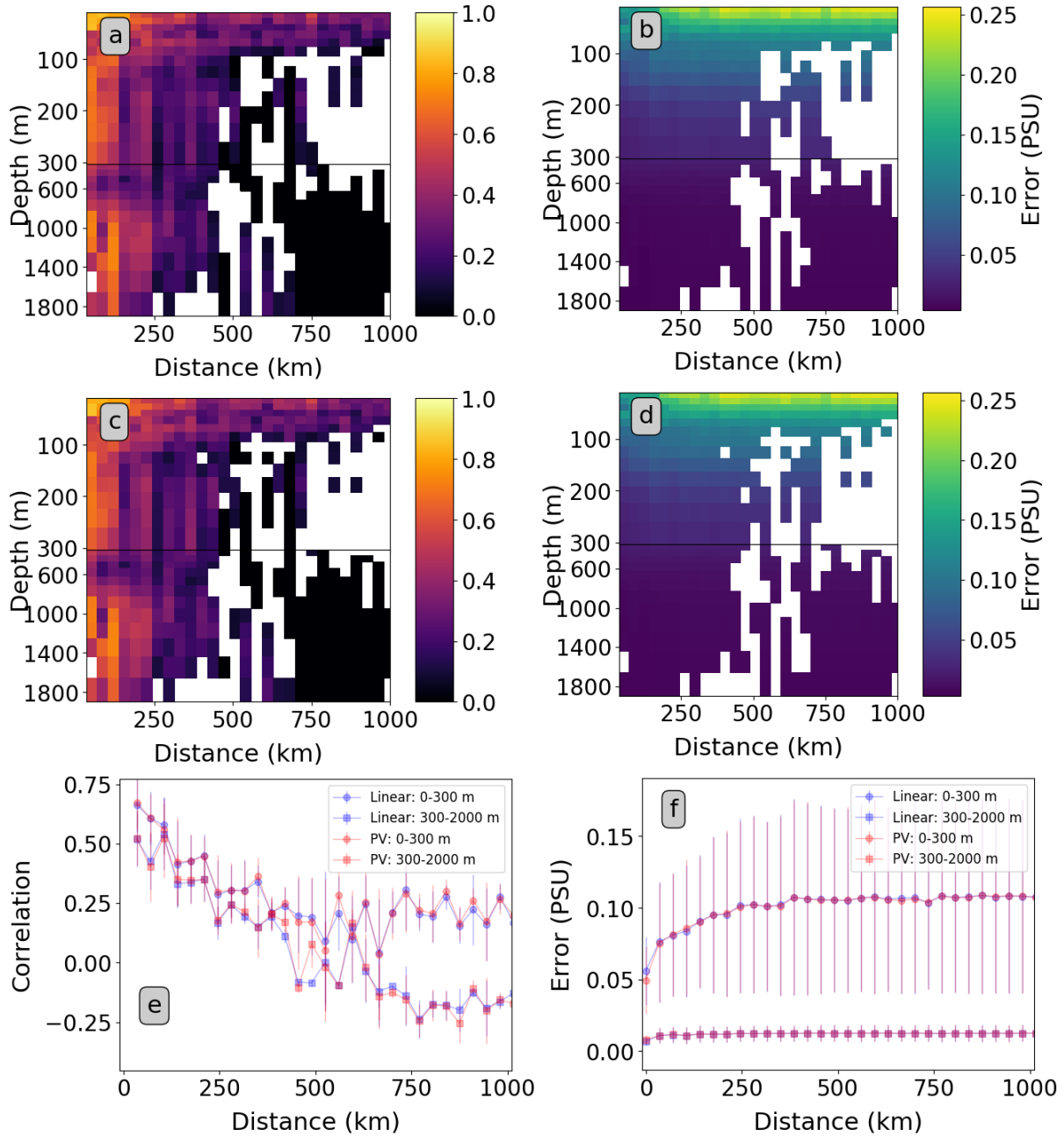


Figure 1.10. (a) Salinity correlation as a function of distance and depth at 90% confidence. (b) Total salinity error as a function of distance and depth at 90% confidence in regimes above and below 300m. (c) Salinity correlation as a function of distance and depth at 90% confidence. (d) Total salinity error as a function of distance and depth at 90% confidence in regimes above and below 300m. (e) Salinity correlation as a function of distance averaged over 0-300m and 300-2,000 m depth at 90% confidence; error bars represent standard deviation in correlation over these depth ranges. (f) Total salinity error as a function of distance at 90% confidence averaged over 0-300m and 300-2,000 m depth; error bars represent standard deviation in error over regime depths.

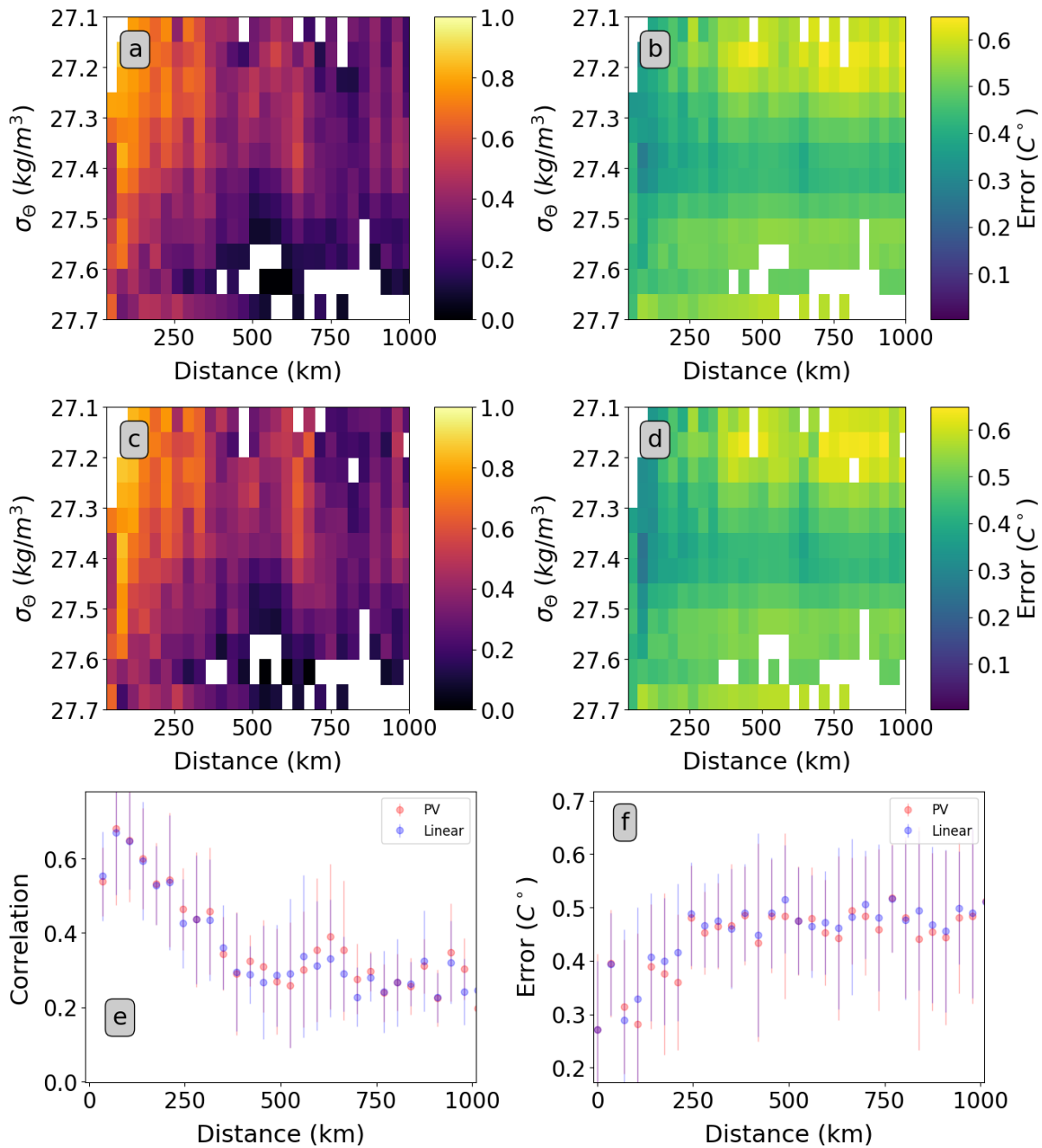


Figure 1.11. (a) Temperature correlation as a function of density and distance at 90% confidence. (b) Total temperature error as a function of distance and density at 90% confidence. (c) Temperature correlation as a function of density and distance in PV coordinates at 90% confidence. (d) Total temperature error as a function of distance in PV coordinates and density at 90% confidence. (e) Temperature correlation as a function of distance averaged over all density surfaces at 90% confidence; error bars represent standard deviation in correlation over all densities. (f) Total temperature error as a function of distance at 90% confidence averaged over all density surfaces; error bars represent standard deviation in error over all densities.

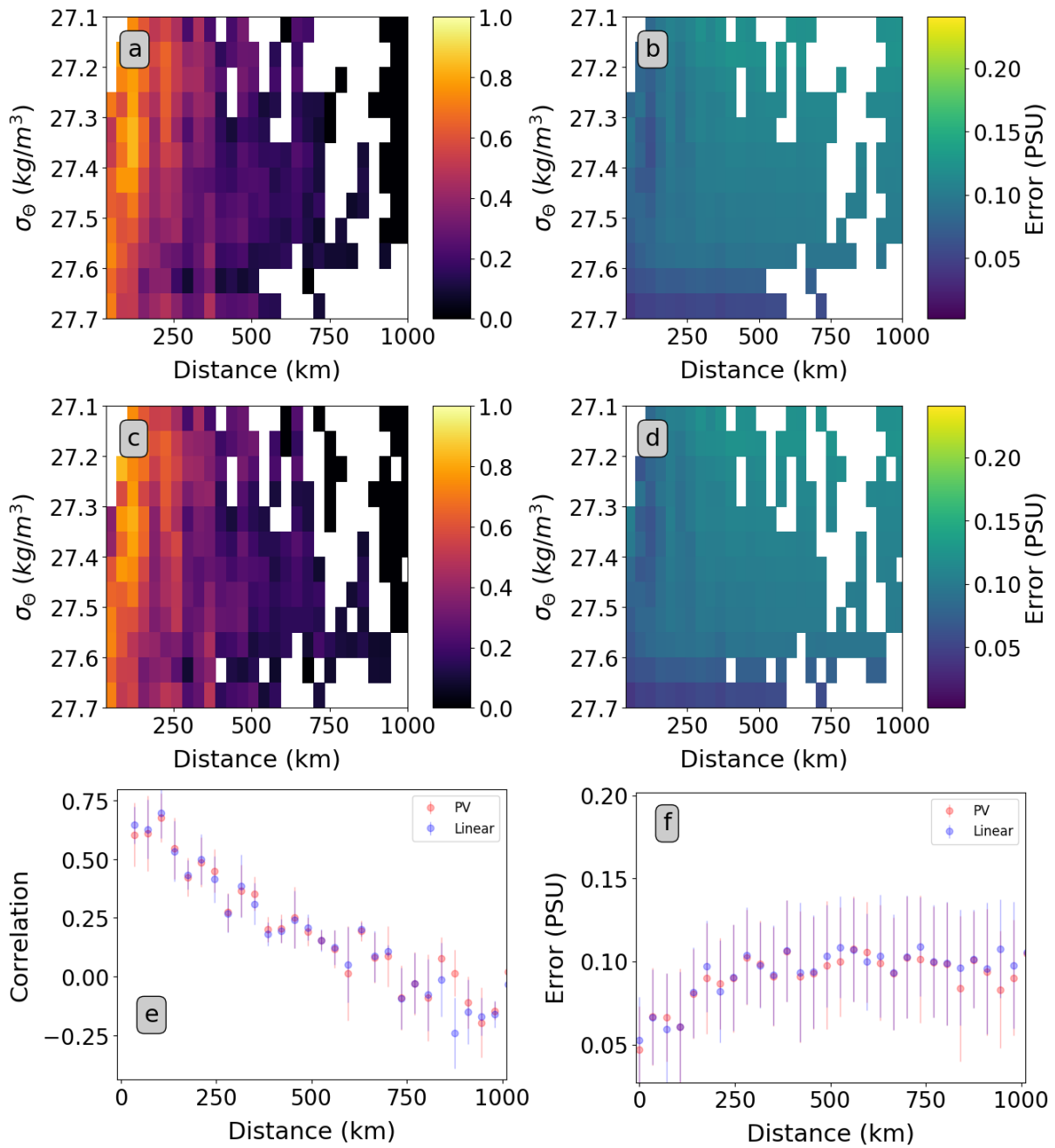


Figure 1.12. (a) Salinity correlation as a function of density and distance at 90% confidence. (b) Total salinity error as a function of distance and density at 90% confidence. (c) Salinity correlation as a function of density and distance in PV coordinates at 90% confidence. (d) Total salinity error as a function of distance in PV coordinates and density at 90% confidence. (e) Salinity correlation as a function of distance averaged over all density surfaces at 90% confidence; error bars represent standard deviation in correlation over all densities. (f) Total salinity error as a function of distance at 90% confidence averaged over all density surfaces; error bars represent standard deviation in error over all densities.

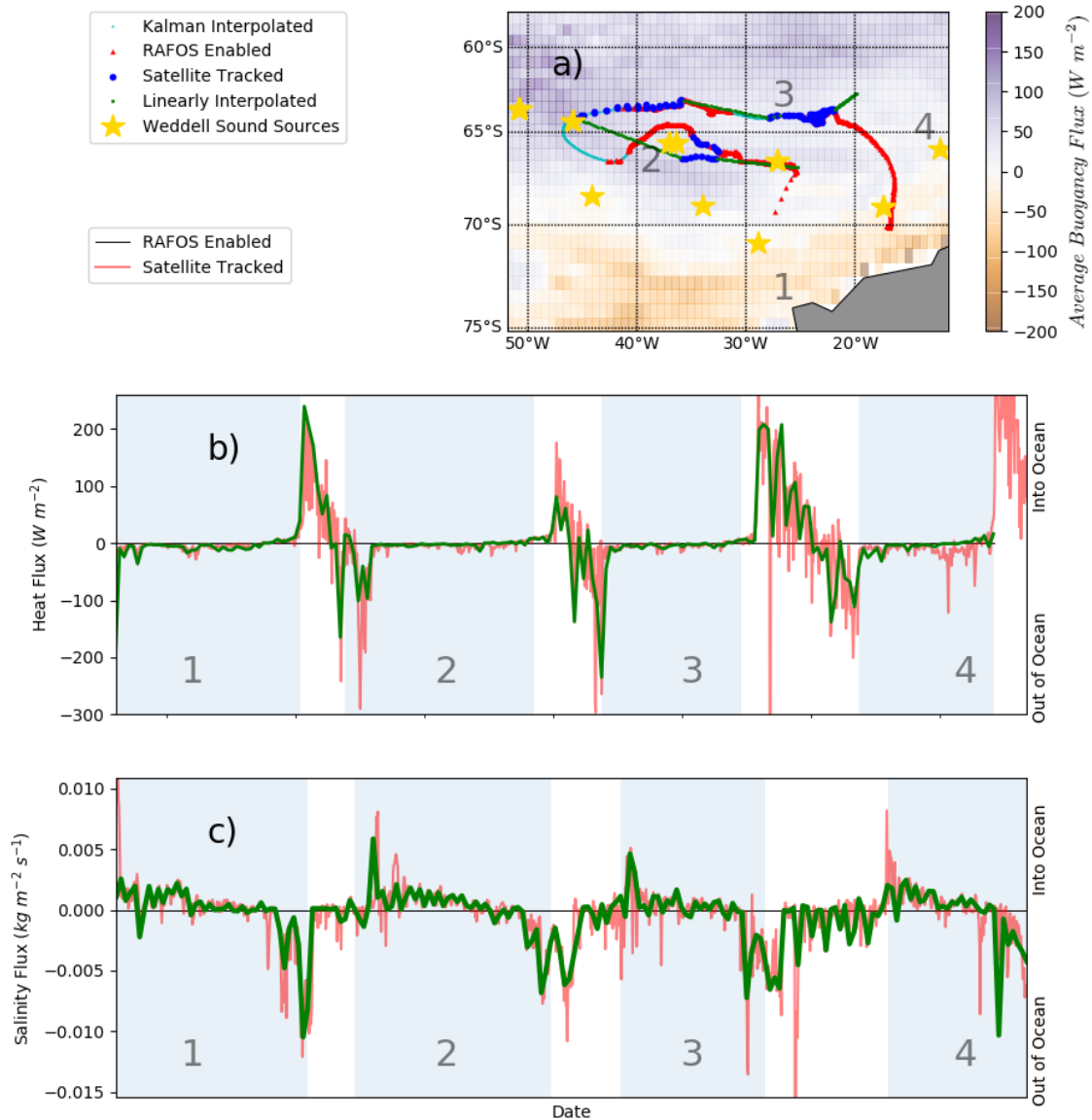


Figure 1.13. Comparison of RAFOS-enabled float and interpolated Argo float for float WMO5901717. (a) Map of tracks. Acoustically tracked float locations (red dots), satellite-tracked float locations (blue dots), linearly interpolated location (green dots), and acoustic sound sources (stars). Shading is buoyancy flux, temporally averaged over the entire SOSE record, reported in units of equivalent heat flux ($W m^{-2}$). (b) Surface heat flux along the RAFOS-enabled (red) and interpolated (green) Argo float tracks. (c) Surface salinity flux along the RAFOS-enabled (red) and interpolated (green) Argo float tracks. Gray shading indicates periods of position loss due to sea ice, also labeled on the map.

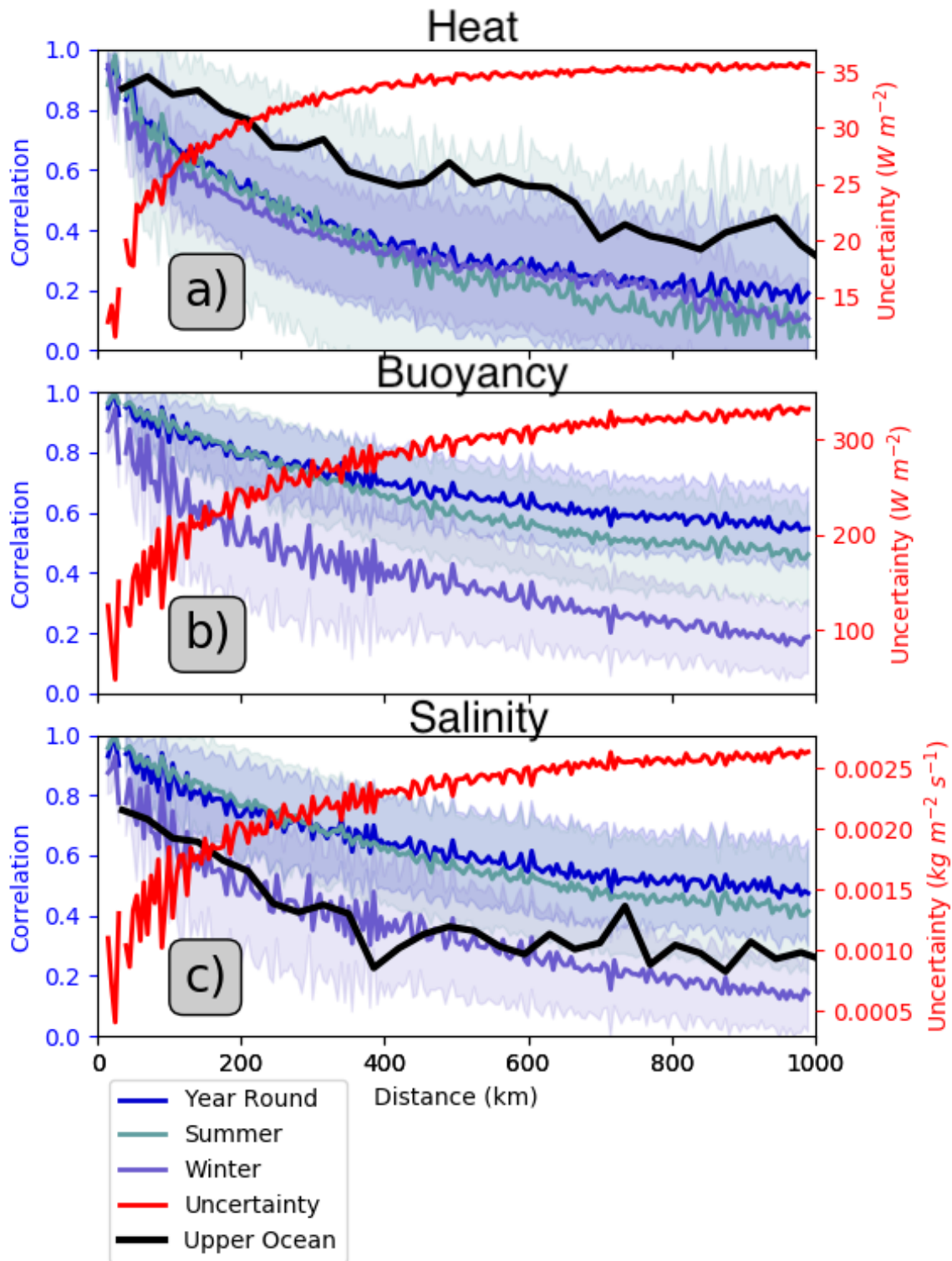


Figure 1.14. Spatial correlation of surface fluxes from SOSE for (a) heat (b) buoyancy, and (c) salinity, for winter (May 15 - September 15), summer (November 15 - March 15), and year round. Colored swath around lines represent standard deviation of data in each bin. Red line is uncertainty calculated from year round correlation curve. Black line is upper ocean temperature and salinity correlation averaged over top 50 meters (from Figs. 1.9 and 1.10).

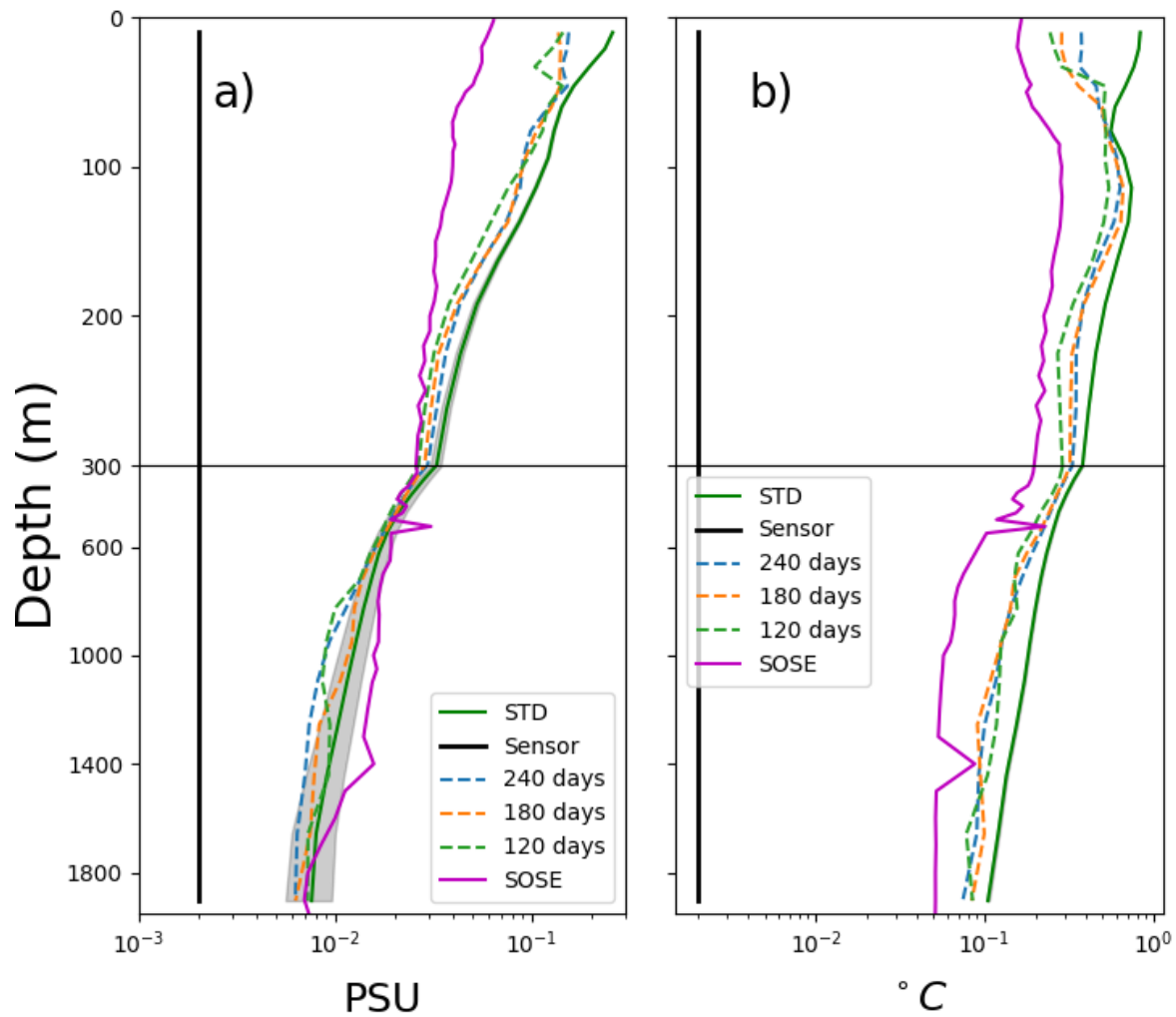


Figure 1.15. (a) Salinity and (b) temperature error in the Weddell Sea as a function of depth and time of position loss. Solid green curve represents standard deviation of temperature and salinity of all satellite-tracked float profiles. Shaded region on either side of the green curve is the sensor error. Dashed lines are measurement uncertainty for various durations of position loss. Cyan curve is average of SOSE model uncertainty in the study area. Black lines represent sensor uncertainty: 0.002 psu and 0.002°C respectively.

Chapter 2

Acoustic Float Tracking with the Kalman Smoother

2.1 Abstract

Acoustically-tracked subsurface floats provide insights into ocean complexity and were first deployed over 60 years ago. A standard tracking method uses a Least-Squares algorithm to estimate float trajectories based on acoustic ranging from moored sound sources. However, infrequent or imperfect data challenge such estimates, and Least-Squares algorithms are vulnerable to non-Gaussian errors. Acoustic tracking is currently the only feasible strategy for recovering float positions in the sea ice region, a focus of this study. Acoustic records recovered from under-ice floats frequently lack continuous sound source coverage. This is because environmental factors such as surface sound channels and rough sea ice attenuate acoustic signals, while operational considerations make polar sound sources expensive and difficult to deploy. Here we present a Kalman Smoother approach that, by including some estimates of float behavior, extends tracking to situations with more challenging data sets. The Kalman Smoother constructs dynamically constrained, error-minimized float tracks and variance ellipses using all possible position data. This algorithm outperforms the Least-Squares approach and a Kalman Filter in numerical experiments. The Kalman Smoother is applied to previously-tracked floats from the southeast Pacific (DIMES experiment), and the results are compared with existing trajectories constructed using the Least-Squares algorithm. The Kalman Smoother is also used to reconstruct the trajectories of

a set of previously untracked, acoustically-enabled Argo floats in the Weddell Sea.

2.2 Introduction

From their introduction, autonomous, acoustically tracked instruments have explored poorly sampled ocean areas and provided fundamental insight into ocean dynamics (Gould, 2005). First deployed in 1955 (Swallow, 1955), autonomous float endurance has improved from days to years and now represents a mature technology (Rossby et al., 1986; Roemmich, Dean and Alford, Matthew H and Claustre, Hervé and Johnson, Kenneth and King, Brian and Moum, James and Oke, Peter and Owens, W Brechner and Pouliquen, Sylvie and Purkey, Sarah and others, 2019). Thousands of acoustically tracked floats have been deployed in most of the world's oceans at depths ranging from just below the surface to 4,000 meters (Ramsey et al., 2018). Acoustically tracked floats are typically localized at 6-hour to daily intervals and have relatively high temporal resolution compared to mesoscale circulation. Lagrangian observations have been used to study mesoscale eddies, infer large-scale circulation (Boebel et al., 1997), and investigate stirring (Gille et al., 2007) and abyssal circulation (Hogg and Owens, 1999).

Modern acoustic float instrumentation and methodology, developed by Rossby et al. (1986), is called RAFOS and consists of an acoustic receiver on each float. An array of moored sound sources (see Figs. 2.1, 2.2, and 2.3) transmits sound at staggered intervals. Sound pulses received and recorded by a float are used to calculate a range from the float to the sound source. The float can be localized if multiple sound pulses are heard (ideally three or more) (Figs. 2.2 and 2.3). Unstable or unusable trajectories can result if sufficiently precise ranging observations are not available. The publicly available ARTOA software package has automated this localization process with a Least-Squares algorithm (Wooding et al., 2005; ARTOA, 2017). All sound sources broadcast at the same frequency, and this ambiguity can confound float tracking, as noted by Hogg and Owens (1999). The ARTOA algorithm makes no predictive estimate of float location; hence it can be difficult to distinguish likely sound sources.

Autonomous floats can be particularly useful in sea ice-covered polar regions with substantial seasonal cycles (Gray et al., 2018). Polar regions are important for water mass transformation, subduction of heat and carbon, and ventilation of nutrients (Sarmiento et al., 2004). Polar regions are difficult to navigate; consequently, shipboard data coverage is poor and seasonally biased towards the warmer summer months (Riser, Stephen C and Freeland, Howard J and Roemmich, Dean and Wijffels, Susan and Troisi, Ariel and Belbéoch, Mathieu and Gilbert, Denis and Xu, Jianping and Pouliquen, Sylvie and Thresher, Ann and others, 2016). Argo floats are a tool for studying ocean structure and processes on many spatial and temporal scales (Riser, Stephen C and Freeland, Howard J and Roemmich, Dean and Wijffels, Susan and Troisi, Ariel and Belbéoch, Mathieu and Gilbert, Denis and Xu, Jianping and Pouliquen, Sylvie and Thresher, Ann and others, 2016; Johnson et al., 2022). With the advent of increasingly miniaturized sensors, Argo floats are now collecting data relevant to biogeochemistry and mixing (Johnson and Claustre, 2016b; Roemmich, Dean and Alford, Matthew H and Claustre, Hervé and Johnson, Kenneth and King, Brian and Moum, James and Oke, Peter and Owens, W Brechner and Pouliquen, Sylvie and Purkey, Sarah and others, 2019). The Weddell Sea has been observed with numerous autonomous drifting Argo floats that profile to the sea surface every 10 days, operating with sea ice avoidance software (Klatt et al., 2007; Reeve et al., 2016; Campbell et al., 2019). However, such polar observations are still challenging due to environmental factors (Abrahamsen, 2014). Argo floats that happen to journey underneath the ice may spend more than a year unable to acquire position data. The geographical context of geophysical observations is important for understanding their true significance, but position uncertainty grows with the duration of position loss (Chamberlain et al., 2018; Yamazaki et al., 2020; Wallace et al., 2020; Nguyen et al., 2020). Float trajectories can also infer important ocean dynamics. These dynamics are resolved at a scale of motion related to both the density of float trajectories and the fidelity to which the true float trajectories are resolved from observations.

Acoustic tracking is, currently, the only technology for estimating float position under sea ice. In addition to non-profiling RAFOS-type floats, some Argo floats in the Weddell

Sea have been outfitted with acoustic RAFOS receivers to allow under-ice tracking (Klatt et al., 2007). However, the polar latitudes are environmentally challenging for straightforward acoustic tracking. Temperature decreases towards the surface in ice-covered seas; thus, sound is refracted to the surface - a region where surface scattering from waves and jagged ice-bottom formations dramatically attenuate acoustic signals (Klatt et al., 2007). Additionally, logistical and operational realities make acoustic sound sources difficult and expensive to deploy. Consequently, the acoustic data records recovered in these regions may be noisy or incomplete; this makes tracking difficult.

In addition to acoustic ranging, satellite positioning, dynamical knowledge of the circulation, and past float velocities can also be used to constrain float trajectories. As a step beyond the established Least-Squares acoustic tracking method, ARTOA (Wooding et al., 2005; ARTOA, 2017), we present a Kalman smoothing algorithm for float tracking that can work with more fragmented acoustic data by incorporating additional information and constraints. The Kalman Smoother presented here is an innovation over ARTOA in that it uses simple kinematics to make predictions of the future system state and error covariances. ARTOA assumes persistence of the system state and does not predict error covariances. The Kalman Smoother performs this calculation in both forward and reverse time, which applies an additional constraint on the trajectories over ARTOA calculations which are done in forward time only. Using variants of Kalman filters for vehicle or contact tracking is not new and is common for Autonomous Underwater Vehicle localization (Kimball and Rock, 2011; Webster et al., 2015), but to our knowledge, has never been applied to acoustically-tracked oceanographic floats.

The Kalman Filter generates sequential predictions of a float trajectory using kinematics (also known as the Forecast). The prediction made in the Forecast is shown as the orange X in Figure 2.2. The Kalman Filter then updates this prediction with positioning data when available; this update step is also known as the Analysis and is shown as the green X in Figure 2.2. During this Analysis, new data can be checked against the predicted position (Figure 2.2). Data that are highly improbable based on physical constraints and estimated uncertainties can be flagged or

discarded, reducing the ambiguity of acoustic sources that broadcast with the same frequency. In the construction of the Kalman Filter, we perform what is called a regularization on the trajectory solution by imposing several dynamical constraints to varying degrees. These include: restricting the maximum float displacement, float velocity, and float velocity uncertainty. Float displacement was also minimized by imposing a tendency for the float trajectory to relax to a linearly interpolated position between satellite positions, as shown in Wong and Riser (2011). We implement dynamical regularization by including a tendency term for float trajectories to follow barotropic planetary geostrophic streamlines (LaCasce, 2000; Reeve et al., 2016; Chamberlain et al., 2018; Yamazaki et al., 2020) and geostrophic streamlines calculated from objectively mapped Argo-based dynamic height and velocity (Gray and Riser, 2014).

When a float emerges from under sea ice, it communicates its acoustic ranging data so that the floats under-ice trajectory can be estimated. The last satellite-derived position before the float went under the ice and the first satellite position when the float emerges from the ice are both strong constraints on its trajectory. Using the last satellite position before the float went under ice, and working in forward time, we can estimate the float's trajectory with available acoustic ranging. The forward prediction is shown as the orange X along the light blue track in Figure 2.2. Similarly, a different estimate of the float's trajectory is produced using the first satellite position after the float emerged from the ice and working backward in time. The reverse time estimate is shown as the orange X along the dark blue track in Figure 2.2. A Kalman Smoother combines these forward and reverse time trajectory estimates to create an error-minimized estimate of position (green X in Fig. 2.2).

Here we present a new method based on Kalman smoothing that extends the useful data, allowing consistent acoustic float tracking when acoustic signals are of lower quality, and incorporating surface GPS-positioning when available. This method can also incorporate additional external constraints, such as satellite-altimetry and the influence of bathymetry, on the currents that advect the floats. In section 2.3, we describe the acoustically-tracked float data sets, the basics of acoustic tracking, and the data sets used as external constraints. In section 2.4, we

describe the synthetic data set used to test the Kalman Smoother approach. In section 2.5, we present the new Kalman Smoother approach for locating acoustically-enabled floats. We then quantify the Kalman Smoother performance using the particle simulation experiments (section 2.6.1) and compare the Kalman Smoother float track solutions to a previously tracked (using ARTOA) set of floats deployed in the Drake Passage during the DIMES experiment (Gille et al., 2007; Balwada et al., 2016) (section 2.6.2). Finally, with insight gained from this, solutions are presented for a previously untracked set of acoustically-enabled Argo floats deployed in the Weddell Sea (section 2.6.3). Throughout this text, we use the convention of capitalizing hyper-parameters or other terms that are germane to the Kalman Smoother method presented.

2.3 Data

For the application and testing of our Kalman Smoother method for tracking acoustic floats, we use two separate acoustic float data sets from the Southern Ocean and a numerical simulation of acoustically-tracked floats (next section). One of the acoustic data sets is derived from acoustically-enabled Argo floats, so we first describe Argo profiling floats and then the acoustic tracking. Finally, we describe the DIMES and Weddell Sea experiment floats and ancillary data sets.

2.3.1 Core Argo

Argo profiling floats now comprise a global sustained observing system of about 4000 floats (Roemmich, Dean and Alford, Matthew H and Claustre, Hervé and Johnson, Kenneth and King, Brian and Moum, James and Oke, Peter and Owens, W Brechner and Pouliquen, Sylvie and Purkey, Sarah and others, 2019), and are the most widely-used deep-ocean floats. Argo floats drift at about 1000 m and then profile from 2000 m to the sea surface. Satellites are used to track Argo floats when they surface (only a few experiments have used acoustically-enabled Argo floats). Argo floats attempt to surface when they profile nominally every 10 days. However, Argo floats in sea ice regions, such as the Weddell Sea floats presented here, may not be able

to surface when they profile, and the observations they collect while under-ice will not have a satellite-derived position. These under-ice profiles are commonly assigned a position based on a linear interpolation between the satellite-derived positions at the beginning and end of the sea ice season; the resulting position errors under the ice can reach 100 to 200 km (Chamberlain et al., 2018; Yamazaki et al., 2020). While Argo float observations are motivated mainly by temperature, salinity, and other properties measured during the vertical profiling (Roemmich, Dean and Alford, Matthew H and Claustre, Hervé and Johnson, Kenneth and King, Brian and Moum, James and Oke, Peter and Owens, W Brechner and Pouliquen, Sylvie and Purkey, Sarah and others, 2019), the 10-day positions are of great value for deep ocean circulation studies (Katsumata and Yoshinari, 2010; Gray and Riser, 2014; Ollitrault and Colin de Verdière, 2014).

2.3.2 Acoustically-tracked floats

Floats with the modern RAFOS-type receiver (Rossby et al., 1986) are localized much more frequently than the 10-day intervals of Argo profiling floats. Standard RAFOS floats are ballasted to remain at a single drift pressure after deployment. These floats surface only at the end of their mission to report a final position and relay the acoustic-ranging data they have collected throughout their mission. Daily or more frequent positions provide information about the velocity field not represented in the 10-day positions of Argo floats. Argo profiling floats can also be equipped with RAFOS receivers (RAFOS-enabled Argo floats). Like Argo profiling floats, RAFOS-enabled Argo floats provide full 2000-m temperature and salinity profile every 10 days. However, they have the advantage of being much more frequently tracked while they drift (nominally) at 1000 m than the standard Argo float.

Acoustically-tracked floats require an array of sound sources, optimally at least three sources, within range of each tracked float; however, 2 acoustic ranges combined with a prior position can typically position a float. Figure 2.3 shows an example of typical acoustic ranging. Each acoustic source in the regional arrays described here is programmed to broadcast at staggered times every day. As all sources broadcast the same tone, the identity of each received

transmission is deduced by recognizing the operational limit of the broadcast range (\approx 300-700 km within sea ice (Klatt et al., 2007) and 1000 km or greater in the open ocean (Hogg and Owens, 1999)) and finding local sources in this broadcast window that could be responsible. Skilled operators do sound source identification, but sound sources can be ambiguous and misidentifications are a fundamental nonlinearity in this workflow. Once the source is identified, the Time of Arrival (TOA) is calculated by subtracting the time the source transmitted sound from the time the float receives the signal.

Both float and source clocks are imperfect and drift over time. Due to the high speed of sound in seawater compared to the drift speed of instruments, these biases and uncertainties can result in substantial positioning errors if left uncorrected. Float clocks may be calibrated against satellite clocks while at the surface. During extended periods under the ice, floats cannot recalibrate clocks, and errors can become substantial. Upon deployment and recovery, acoustic source clock times are checked against ship-based clocks, and their offsets are measured. If sources cannot be recovered, their final clock offsets are unknown.

In our analysis, all measured source clock offsets were linearly interpolated from the time of source deployment to recovery; linearly interpolated sound source clock drift is then used to correct the TOA record of any floats positioned from a given sound source. Sound source clock linear interpolation introduces uncertainty, which is included in the parameterized TOA noise discussed in Section 2.5. TOA can be transformed to distance if the sound speed of the medium is known. We assume sound signals travel along geodesics; however, refracted sound paths in the ocean have (one or more) arc lengths that are farther than the geodesic distance - especially in the ice-covered ocean (Spiesecke, 2018). Errors in timing translate to errors in acoustic ranging distance; the error in the positioning fix based on the errors in ranging distance depends on the sound sources' geometry. A straightforward strategy for reducing error due to increased path length is to lower the speed of sound to account for the slower distance over ground that bending sound paths take. Our analysis did not account for the potential of multi-path sound detections (the process through which one sound transmission can take two or more paths to get

to a receiver and be recorded). This is a fundamental gap in our analysis.

2.3.3 DIMES floats

The first of two acoustically-tracked data sets we examine is from the DIMES experiment (Gille et al., 2007), in which 138 neutrally buoyant RAFOS floats were deployed west of Drake Passage. The first floats were deployed in January, 2009; the last float surfaced in March, 2012. 12 different sound sources tracked the floats deployed west of and within Drake Passage (Fig. 2.1). In total 142015 TOA observations were made by the DIMES floats throughout the experiment. DIMES trajectories were estimated from these TOAs (Balwada et al., 2016) using the Least-Squares ARTOA tracking method (Wooding et al., 2005; ARTOA, 2017), and have been used in studies of mixing and dynamics of this region (LaCasce et al., 2014; Balwada et al., 2016, 2021). These ARTOA-based trajectories are deemed robust because the number and location of sound sources were sufficient.

2.3.4 Weddell Sea floats

Our second (and primary) data set, which prompted the development of the Kalman Smoother approach for estimating trajectories (Chamberlain et al., 2018), is a set of 22 acoustically-enabled Argo floats deployed in the Weddell Sea from February 2008 to February 2013 (Fig. 1; Table 2.1). During this period, an array of 14 sound sources maintained by the Alfred Wegener Institute was available for multi-year float tracking (Fahrbach et al., 2011). Argo floats profile every 10 days and, unless prevented by sea ice, surface and broadcast their data. Argo floats also record a satellite-derived position when at the surface. The 10-day temperature and salinity profiles were disseminated as part of the operational global Argo data set, with satellite positions when the floats surfaced and linearly-interpolated positions when the floats were under sea ice.

These 22 Weddell Sea floats were acoustically enabled to allowing tracking through the winter. However, sea ice and local stratification degrade the acoustic range in the Weddell Sea

(Klatt et al., 2007); this degradation resulted in difficulties with the standard ARTOA method for tracking the floats despite the large number of sound sources. To improve the tracking, the Kalman Smoother was applied, and the resulting float trajectories were used in Chamberlain et al. (2018) to estimate position uncertainty arising from the lack of satellite fixes for the 10-day Argo profiles during the sea ice season. The Weddell Sea acoustically-enabled Argo float dataset includes 13966 TOA measurements and 1263 GPS satellite positions. GPS position data were downloaded from the USGODAE Argo GPS GDAC Data Browser (Argo, 2019).

2.3.5 Ancillary Data

For our Kalman Smoother solution (Section 2.5), we used two dynamical constraints: a tendency to follow (i) barotropic planetary geostrophic streamlines (LaCasce, 2000; Reeve et al., 2016; Chamberlain et al., 2018; Yamazaki et al., 2020), and (ii) geostrophic streamlines calculated from objectively-mapped Argo-based dynamic height and velocity (Gray and Riser, 2014). The mathematical shorthand of $f H^{-1}$ will refer to barotropic planetary geostrophic streamlines, where f is the Coriolis parameter, and H is the water depth; Geostrophic Streamlines will refer to the Gray and Riser (2014) product. We used the ‘ETOPO1’ 1 Arc-Minute Global Relief Model (Amante and Eakins, 2009) for H in the $f H^{-1}$ contours. A Gaussian filter with a standard deviation of 4 arc-minutes was applied to the bathymetry dataset to reduce high wavenumber variability through convolution with a Gaussian function. This relatively aggressive smoothing was necessary to make it possible to calculate a meaningful gradient.

2.4 Numerical Particle Tracking Experiment

In addition to comparing the DIMES float trajectories calculated using the Kalman Smoother with those from the ARTOA method, we compare these tracking schemes using a series of numerical particle tracking experiments. In the ocean, the true trajectory of a float are unknown, but we designed artificial experiments where true particle position and velocity statistics is known. The artificial experiments quantified the relative performance of the Least

Squares, Kalman, and Kalman Smoother filters in various observational uncertainty and float motion scenarios.

Our numerical experiments simulated float motion in the Weddell Sea by seeding numerical particles into the ocean and tracking them with each of the filters presented. Particles experienced horizontal advection at a depth of 1000 m and did not profile up and down; these numerical particles were intended to simulate float behavior. The numerical experiments used 30,000 particles to generate performance metrics over a wide range of positioning and instrument noise scenarios. Each particle had a unique trajectory and an observational dataset with distinct observation noise and observational density. The particles all had a starting location of 64°S, 23.5°W and were advected forward for 100 days in a semi-random horizontal flow. A hybrid Brownian motion model was used to simulate particle advection; a simple stochastic differential equation estimated daily particle velocity

$$V(t) = V(t)_{mean} + sW(t), \quad (2.1)$$

where $V(t)_{mean}$ is a mean velocity that we chose to have the same amplitude as the standard deviation of the Weddell Sea Argo velocity data (7.4 km day⁻¹ zonal velocity, and 5.3 km day⁻¹ meridional velocity). $W(t)$ is a normally-distributed random increment with an amplitude equal to the standard deviation of the Weddell Sea Argo array velocities. Here s is a scalar that is varied to test the effects of signal (mean flow) to noise (random increment) ratio in this simple example of particle flow. We report experiments with s values of 0.1, 0.3, and 0.7, and equally divide the particles between these advection states. Larger values of s were experimentally calculated, but the performance of each seemed to saturate above s values of 0.7. The simulated sound source array consisted of 6 sources uniformly distributed within a 600 km radius of the starting position.

One of the goals of the numerical float experiment is to assess the variables that control the position estimate errors. A distinct TOA noise amplitude, number of sound sources heard, and chance of satellite positioning was randomly assigned to each of the 30,000 particles upon

initialization. TOA noise amplitude was uniformly distributed between 1 and 50 seconds; the number of sound sources heard was uniformly distributed between 1 and 6; and the chance of satellite positioning was uniformly distributed between 0 and 100 %.

At every timestep in each particle's trajectory, a number of TOA observations equal to the sound source number was generated for the particle; each TOA observation was randomly assigned to be transmitted from a source within the array with uniform distribution. The true distance from each sound source to the particle was known, and the acoustic travel time was calculated using this distance and a speed of sound of 1.5 km s^{-1} . This true TOA was then degraded by adding a normally distributed term with an amplitude equal to the TOA noise amplitude. At every timestep, these "noisy" TOA were then used to test each filter's performance in reconstructing the true trajectory. In addition to acoustic tracking, RAFOS-enabled Argo floats also receive satellite positioning; to assess the impact of intermittent satellite observations, we included satellite positioning with uniform probability equal to the chance of satellite positioning at each daily time step.

2.5 Methods

The Kalman filter literature is ample and mature (Wunsch, 2006; Rauch et al., 1965) so the following is a brief recapitulation in the notation of Ide et al. (1997) and is described sequentially in Table 2.2: specifically, the subscript "*i*" denotes the timestep, bold lower case variables denote vectors, bold upper case letters denote matrices, and unbolded upper case letters denote nonlinear processes. We also adopt the convention of capitalizing the hyperparameters necessary for the trajectory calculation.

For the reader's convenience, this section (and the associated table) is broken into the following subsections: Kalman Forward Filter, Kalman Smoother, Regularizations, and Processing techniques. A flow chart (Fig. 2.4) also provides an overview of these calculations.

2.5.1 Kalman Forward Filter

Kalman filtering is a sequential Least-Squares linear estimator that assumes all observations have zero mean with normal distribution. In words: the Kalman Filter starts with an estimate of the state of the system which we call the Analysis (yellow box in Fig. 2.4), and uses a model to create a predicted state which we call the Forecast (orange box in Fig. 2.4), then compares the predicted state to observations to create a new Analysis (green box in Fig. 2.4), and finally uses the Analysis as the initial state to create the Forecast in the next timestep. This process of sequentially propagating the Analysis forward to create a Forecast and then updating the Forecast with new observations can continue as long as there are new observations to assimilate. The superscripts a and f denote the Analysis and Forecast, respectively. The superscript t denotes true state vectors, and the superscript T denotes transposes.

We begin with the position and velocity of the previous timestep ($i - 1$) which we call the true state vector $\mathbf{x}^t(t_{i-1})$. The true state vector is propagated to the next timestep with a simple kinematic transition matrix with a frictional term such that

$$\mathbf{x}^t(t_i) = M_{i-1}\mathbf{x}^t(t_{i-1}) + \boldsymbol{\eta}_{i-1}, \quad (2.2)$$

where $\boldsymbol{\eta}$ is the model noise process, which is the error of the model M_{i-1} , which we assume to have a zero-mean normal distribution that is stationary over time. The covariance \mathbf{Q} of the model noise process is written:

$$\mathbf{Q} = E[\boldsymbol{\eta}_{i-1}\boldsymbol{\eta}_{i-1}^T], \quad (2.3)$$

where E is the expectation operator. Process Noise (\mathbf{Q}) will generally be used to describe both Process Position Noise and Process Velocity Noise. Process Noise is the effect of unmodeled velocities and accelerations caused by forcing (such as ocean variability) not accounted for in the simple kinematics. The deterministic component of Equation 2.2, M_{i-1} , is written using \mathbf{z} for

the horizontal location of the float:

$$\left\{ \begin{array}{l} \mathbf{x}(t_i) = \begin{bmatrix} \mathbf{z}(t_i) \\ \dot{\mathbf{z}}(t_i) \end{bmatrix} \quad (a) \\ \mathbf{z}(t_i) = \mathbf{z}(t_{i-1}) + \Delta t \dot{\mathbf{z}}(t_{i-1}) \quad (b) \\ \dot{\mathbf{z}}(t_i) = \alpha \dot{\mathbf{z}}(t_{i-1}) \quad (c) \end{array} \right. \quad (2.4)$$

where α is a frictional factor that we set to 0.95, Δt is the timestep, \mathbf{z} is the position component of \mathbf{x}^f , and $\dot{\mathbf{z}}$ is the velocity component of \mathbf{x}^f . The implementation of the Kalman Filter presented here only includes float position and velocity. Acceleration is modeled as a white noise process (Eq. 2.2).

We begin tracking with an estimate of the position and velocity from a prior timestep (the Analysis or $\mathbf{x}^a(t_{i-1})$) and an estimate of the Analysis Error Covariance from the previous timestep. The Analysis Error Covariance is written as follows:

$$\mathbf{P}^a(t_{i-1}) = E[(\mathbf{x}^f(t_{i-1}) - \mathbf{x}^a(t_{i-1}))(\mathbf{x}^f(t_{i-1}) - \mathbf{x}^a(t_{i-1}))^T]. \quad (2.5)$$

The Analysis and the Analysis Error Covariance are then predicted forward to the next timestep by the kinematic model, including Process Noise:

$$\mathbf{x}^f(t_i) = M_{i-1} \mathbf{x}^a(t_{i-1}), \quad (2.6)$$

$$\mathbf{P}^f(t_i) = M_{i-1} \mathbf{P}^a(t_{i-1}) M_{i-1}^T + \mathbf{Q}(t_{i-1}). \quad (2.7)$$

This is the Forecast in Figure 2.4 and is represented by the orange X in Figure 2.2.

The next step is to use new observations to update the Forecast using observations. Satellite-derived positions are linear, but other observations contain non-linear terms in the calculation used to constrain position (for example magnitude of distance expressed as $\sqrt{\mathbf{r}_i \cdot \mathbf{r}_i^T}$ where \mathbf{r}_i is the vector from source to float position). As such, we use the Extended Kalman Filter

formulation of the equations. The Extended Kalman Filter approximates the non-linear terms with a first-order Taylor expansion, which may lead to unstable performance if the observation and state variables differ substantially. The linearized observation matrix transforms the state vector into observation space and in the nonlinear formulation is expressed as the Jacobian $H'_i = \mathbf{H}_i = \left. \frac{d\mathbf{g}}{d\mathbf{x}} \right|_{\mathbf{x}^f}$, where \mathbf{g} is the nonlinear functional form of the observation expressed in terms of elements of the state vector. Specifically, the Jacobian elements for travel time are equal to

$$\mathbf{H}_i = \frac{r_i}{\sqrt{\mathbf{r}_i \cdot \mathbf{r}_i^T} * c} \quad (2.8)$$

where c is the sound speed, and the Jacobian elements for $f H^{-1}$ Contours and Geostrophic Streamlines are numerically derived. Observations are represented in the usual way as

$$\mathbf{y}_i^o = \mathbf{H}_i \cdot \mathbf{x}^f(t_i) + \boldsymbol{\varepsilon}_i, \quad (2.9)$$

where \mathbf{y}_i^o is the observation, $\mathbf{H}_i \cdot \mathbf{x}^f(t_i)$ is the true location transformed into observation space, and $\boldsymbol{\varepsilon}$ is the observational noise process. Unlike the model noise process, we expect the observational noise process to change in time as we record a varying number of observations. The observation noise process is assumed to have a normal distribution and zero mean. We can write the covariance of the noise process as the following:

$$\mathbf{R}_i = E[\boldsymbol{\varepsilon}_i \boldsymbol{\varepsilon}_i^T] \quad (2.10)$$

where \mathbf{R}_i is the Observation Noise at timestep i . The difference between this prediction from the actual observations is called the Innovation and is written as

$$\mathbf{d}_i = \mathbf{y}_i^o - \mathbf{H}_i \cdot \mathbf{x}^f(t_i). \quad (2.11)$$

The new observations are used to update the Forecast state (orange stars in Figure 2.2)

to the new Analysis state by adding the Innovation multiplied by a term known as the Kalman Gain, \mathbf{K} :

$$\mathbf{x}^a(t_i) = \mathbf{x}^f(t_i) + \mathbf{K}(t_i)\mathbf{d}_i(t_i) \quad (2.12)$$

$$\mathbf{K}(t_i) = \mathbf{P}^f(t_i)\mathbf{H}_i^T(\mathbf{H}_i\mathbf{P}^f(t_i)\mathbf{H}_i^T + \mathbf{R}_i)^{-1}, \quad (2.13)$$

where \mathbf{x}^a is the Analysis state and is shown as the orange X in Figure 2.2.

The Kalman Gain is dependent on the relative magnitudes of the Observation Noise and the Process Noise. Suppose the Observation Noise is much smaller than the Process Noise (we trust the observations more than the kinematic forecast). In that case, the Innovation (difference of observations from the Forecast transformed into observation space) strongly influences the new Analysis state. Alternatively, suppose the Observation Noise is much greater than the Process Noise (we trust the kinematic forecast more than the observations). In that case, the Kalman Gain is close to zero, and the Innovation does not influence the new Analysis state. The Analysis Error Covariance (\mathbf{P}^a) is proportional to the Forecast Error Covariance (\mathbf{P}^f) multiplied by a correction term proportional to the identity matrix, \mathbf{I} , minus the Kalman Gain

$$\mathbf{P}^a(t_i) = (\mathbf{I} - \mathbf{K}(t_i)\mathbf{H}_i)\mathbf{P}^f(t_i). \quad (2.14)$$

Consider the two limits to relative Observation Noise Covariance (\mathbf{R}) versus Process Noise (\mathbf{Q}) in Equation 2.14: suppose we trust the observations more than the kinematic forecast, then the Kalman Gain (\mathbf{K}) is relatively large and the Analysis Error Covariance (\mathbf{P}^a) is less than the kinematic model Forecast Error Covariance (\mathbf{P}^f) (we gained new information from the observations and reduced position and velocity uncertainty); now suppose we trust the forecast more than the observations, then the Kalman Gain (\mathbf{K}) is close to zero and the Analysis Error Covariance (\mathbf{P}^a) will be of similar magnitude to the Forecast Error Covariance (\mathbf{P}^f) (we gained little from the new observations and the position and velocity uncertainties remain the

same). In the special case when there are no observations, the Forecast Error Covariance (\mathbf{P}^f) will be increased by the prescribed Process Noise (\mathbf{Q}) every timestep, and the Analysis Error Covariance (\mathbf{P}^a) will equal the Forecast Error Covariance (\mathbf{P}^f). Because Process Noise (\mathbf{Q}) is the unexpected acceleration due to unaccounted forcing, we can think of the increasing Forecast Error Covariance (\mathbf{P}^f) as the growing summation of all of the unknown changes in the trajectory a float can take in the absence of ranging data. Equations 2.12 and 2.14 comprise the Analysis step (Fig. 2.4). The Analysis is then propagated forward in time via the Forecast and updated with available observations in the Analysis steps until new observations are exhausted (Forward Filter Output in Fig. 2.4).

2.5.2 Kalman Smoother

The Kalman Filter is purely a forward calculation, meaning that time moves in only one direction and sequential information improves the state estimate. The forward Kalman Filter is useful in applications where operational necessity prohibits collecting all observations before estimating the state, e.g. landing an airplane or tracking a missile. Floats cannot communicate with satellites while under ice, meaning that all acoustic ranging and depth data are communicated only after a float reaches open water or sea ice melts. As we will show, having all the observations available allows an additional constraint on the solution that reduces position error. The impact of these complete data is maximized here by using a variant of the Kalman Filter called the Kalman Smoother. Our application of the Kalman Smoother estimates float tracks by creating trajectory estimates in both forward and reverse time, then combining the two in such a way as to minimize uncertainty (Fig. 2.2). Beginning with the analysis at the final timestep of the forward Kalman Filter, we have

$$\begin{aligned}\mathbf{x}^s(t_N) &= \mathbf{x}^a(t_N) \\ \mathbf{P}^s(t_N) &= \mathbf{P}^a(t_N)\end{aligned}\tag{2.15}$$

where $\mathbf{x}^s(t_N)$ and $\mathbf{P}^s(t_N)$ are the smoothed estimates of the state vector and covariance matrix, respectively. Reproducing the error minimizing sequential calculation as the previous section, but in reverse time, leads to the following equations:

$$\begin{aligned}\mathbf{K}^s(t_i) &= \mathbf{P}^a(t_i) \mathbf{M}_i^T (\mathbf{P}^f(t_{i+1}))^{-1} \\ \mathbf{P}^s(t_i) &= \mathbf{P}^a(t_i) - \mathbf{K}^s(t_i) (\mathbf{P}^s(t_{i+1}) - \mathbf{P}^f(t_{i+1})) \mathbf{K}^s(t_i)^T \\ \mathbf{x}^s(t_i) &= \mathbf{x}^a(t_i) + \mathbf{K}^s(t_i) (\mathbf{x}^s(t_{i+1}) - \mathbf{x}^f(t_{i+1}))\end{aligned}\tag{2.16}$$

where \mathbf{K}^s is the smoothed Kalman Gain. $\mathbf{x}^a(t_i)$ and $\mathbf{x}^f(t_{i+1})$ are orange Xs along the dark and light blue tracks in Figure 2.2, respectively. Equation 2.16 is the Smoothed Analysis (Fig. 2.4) and shown as the green X in Figure 2.2.

2.5.3 Regularizations

To improve the stability and realism of our solution, we imposed several regularizations on the filter. Velocity uncertainty is restricted to be no greater than 60 km day^{-1} , maximum velocity is restricted to be no greater than 35 km day^{-1} , and the maximum daily change in position can be no more than 50 km. These velocity and position constraints are larger than the fastest velocity and position displacement recorded in the ARTOA-tracked DIMES solutions.

To improve the dynamics of the model and reduce ambiguities in the filter when there is an absence of ranging data, we imposed constraints that nudge the float to follow selected interpolation schemes. Linear interpolation between known satellite positions is referred to as Satellite Linear Interpolation and is the simplest and first interpolation scheme suggested for under-ice data (Wong and Riser, 2011). The uncertainty of this estimate has been studied (Chamberlain et al., 2018; Yamazaki et al., 2020), yielding mean uncertainty estimates of approximately 100 km for 6 months of position loss. The second scheme was a tendency for the float to follow $f H^{-1}$ contours by nudging the current Analysis such that the value of $f H^{-1}$

was equal to that of the previous timestep. A third scheme similarly nudged floats to follow Geostrophic Streamlines by updating the Analysis such that the current Geostrophic Streamline value was equal to that of the previous timestep. At each timestep, these nudging terms were added via Equation 2.11.

The code includes an optional check that helps flag spurious sound source identifications. This check compares the observed TOA anomaly (Innovation) to the Forecast Error Covariance and discards observations outside the 95% confidence interval of our forecast position. Removing these unlikely TOA observations helped mitigate sound source ambiguity (and the resultant nonlinearity of misidentification). ARTOA does not (and cannot) perform these checks.

2.5.4 Preprocessing

Pre-processing the acoustic data to remove sound source clock bias and drift was found to be important in reconstructing meaningful tracks. The DIMES float tracks are included in this analysis as a reference standard, and, as such, are assumed to be correct. Any TOA difference between the calculated TOA (using the sound source to DIMES trajectory distance) and TOA in the acoustic record is considered TOA misfit. Misfit is defined as

$$\boldsymbol{\varepsilon}_i^s = \mathbf{y}_i^o - \mathbf{H}_i \cdot \mathbf{x}^s(t_i). \quad (2.17)$$

The Kalman Smoother assumes that observational data are unbiased with a normal distribution of uncertainty; consequently, the mean TOA misfit and clock drift for each float was removed before running the Kalman Smoother. TOA misfits greater than 35 seconds compared with the ARTOA DIMES trajectories were also deemed spurious and were excluded from our reconstructed float trajectories. Typically, ARTOA trajectories use a subset of available sound sources to produce float trajectories. For our calculations, all available sound source data were used. For the Weddell Sea floats, some satellite observations are available; we calculated a set of TOA based on the distance from the satellite-derived float position to the sources. We assume the

difference between measured TOA and calculated TOA is caused by two sources of uncertainty: drift in the sound source clock and the regionally variable speed of sound. To correct these errors, a multiple linear regression was used to solve for optimal sound source clock drift and optimal sound speed. The multiple linear regression simultaneously calculated a sound source clock drift to minimize TOA misfit as a function of time since sound source deployment and a sound speed to minimize TOA misfit as a function of distance from float to sound source. The optimal correction to sound speed and clock drift was then used for all trajectory solutions.

2.5.5 Tuning Experiment

One subtlety of our estimates is that they use the prescribed noise of various synthetic ($f H^{-1}$ Contours, Geostrophic Streamlines, Satellite Linear Interpolation) and real (Acoustic Ranging, Satellite Positioning) observations as well as Process Noise to generate the final trajectory. The Process Noise and Observation Noise are variables \mathbf{Q} and \mathbf{R} in Equations 2.6 and 2.12 respectively. When the observations do not fully constrain the trajectory solution, the final trajectories can be sensitive to these choices.

To explore sensitivities to these prescribed uncertainties, we conducted an experiment that varied these parameters in what we considered to be extra small, small, medium, and large ranges. We explored the sensitivity of Process Position Noise and Process Velocity Noise in the \mathbf{Q} matrix (Eq. 2.6) and sensitivity to Geostrophic Streamline noise, $f H^{-1}$ noise, and Satellite Linear Interpolation noise (when GPS positions were available) in the Observation Noise (\mathbf{R} of Eq. 2.12). Consequently, the total number of calculated runs scales as the fifth and sixth power (for DIMES and the Weddell Sea, respectively) of the number of values considered for each filter parameter. This is a computational burden.

Medium values were chosen to be either the variance of the observational dataset, or a dynamically reasonable value: specifically, 3 km for Process Position Noise, 3 km day⁻¹ for Process Velocity Noise, 2.1×10^{-7} rad m⁻¹s⁻¹ for $f H^{-1}$ Contour noise, and 20.0 m² s⁻¹ for Geostrophic Streamline noise. The DIMES and Weddell Sea experiments (for which no

trajectory solution has been published) used the same medium values. The Weddell Sea dataset also includes infrequent satellite positions, which vary by season and location within the gyre (Chamberlain et al., 2018). The medium noise value for Satellite Linear Interpolation was 120 km. Extra small and small values were 25% and 50% of the medium value, respectively. Large values were 150% of the medium value.

Acoustic data misfit will be sensitive to the prescribed TOA noise. Because of this dependence, trajectory solutions were calculated for seven TOA noise conditions ranging from 2 s to 24 s. The Medium TOA noise value is defined as 8 s. Table 2.3 records all noise values used in these tuning experiments.

The data misfit (Eq. 2.17) is sensitive to the values of Process Noise (\mathbf{Q} in Eq. 2.6) and Observation Noise (\mathbf{R} in Eq. 2.12). The ideal filter tuning will have prescribed noise equal to the true uncertainty of the available positioning data and kinematic model skill. Adjusting the relative confidence in the Forecast or the data may achieve lower TOA misfit (going to the limit of Least Squares when there is no confidence in either). However, it may not reproduce the true trajectories with fidelity. Reducing the prescribed TOA noise will cause the filter to more closely match TOA observations but may produce an overfit solution that adjusts too rapidly to noisy data. Conversely, too little confidence in the TOA data will result in an underfit solution that does not appropriately respond to real changes in the true float trajectory. To address these competing concerns, we introduce the following cost function (Ide et al., 1997; Parker, 1994)

$$J = \sum_{i=0}^n (\boldsymbol{\varepsilon}_i^s)^T \mathbf{R}_0^{-1} \boldsymbol{\varepsilon}_i^s + \sum_{i=0}^n [\mathbf{x}^s(t_i) - \mathbf{x}^f(t_i)]^T \mathbf{P}_0^{-1} [\mathbf{x}^s(t_i) - \mathbf{x}^f(t_i)], \quad (2.18)$$

where \mathbf{P}_0 is an approximate background Process Noise covariance based on the medium values of Position Process Noise and Velocity Process Noise, and \mathbf{R}_0 is the Observation Noise covariance constructed from the medium TOA noise. The first term in Equation 2.18 is a penalty on misfit between the data and the trajectory estimate and is called the Data Misfit. This term penalizes solutions that do not adequately adapt to data. The second term represents a penalty

for Smoothed solutions that update the Forecast by a large amount relative to the prescribed Process Noise and is called the Model Norm. This term penalizes overfit solutions that may overcompensate the final trajectory based on noisy data. We wish to minimize Model Norm and Data Misfit simultaneously. Only idealized multi-parameter optimization problems have a single cost minimum, and the choice of metric that relates the Model Norm to the Data Misfit is a fundamental assumption. Thus we explore J by calculating many different solutions over the range of parameter values shown in Table 2.3. The curve defined by the lower bound of the calculated J in Model Norm - Data Misfit space is known as the Pareto frontier (Jahan et al., 2016). We choose to weight Model Norm and Data Misfit equally, and, consequently, the minimum of the second derivative of the Pareto frontier defines the location of the optimal solution.

In our calculations, we assume that satellite positioning uncertainty is well studied and comparably very accurate to all other forms of positioning discussed. These calculations used a satellite position uncertainty of 0.1 km, and considered no other values for satellite position uncertainty. We did not explore the parameter space of the numerical particle experiment because the true particle velocities and the uncertainty of the observations were previously known.

2.6 Results

We tested our method in three different scenarios:

1. We performed a numerical experiment with many examples of satellite positioning frequency and acoustic ranging data density and quality. These data tested the ability of the Least Squares (a method used by ARTOA), Kalman Filter, and Kalman Smoother algorithms to reconstruct the true trajectories.
2. We compared the Kalman Smoother's performance against an ARTOA-tracked float dataset used in the DIMES experiment.

3. The Kalman Smoother generated 22 trajectories for previously untracked floats in the Weddell Sea.

2.6.1 Particle Release Experiment

To generate additional confidence in the Kalman Smoother and Kalman Filter, and to compare their performance to other methods, we simulated the tracking of many numerically generated particles seeded in the Weddell Sea. All three filters considered in this analysis tracked particles. Simulated observations explored the observational parameter space by varying the number of satellite-derived positions available, the amount of acoustic tracking error, and the number of sound sources heard. The motion of the numerically generated particles was calculated with a simple stochastic differential equation (Eq. 2.1) which decomposed the motion into a mean velocity component and a scaled normally distributed random component with amplitude proportional to the mean velocity. The skill of both the Kalman Filter and the Kalman Smoother is related to the predictive skill of the kinematics used to create the forecast (M in Eq. 2.6). The Least Squares filter as formulated uses persistence as the kinematic model (i.e. $\mathbf{z}(t_i) = \mathbf{z}(t_{i-1})$ and $\dot{\mathbf{z}}(t_i) = \dot{\mathbf{z}}(t_{i-1})$) for the forecast. Although this is mathematically a least-squares solution, it only approximates the routine used by ARTOA (Wooding et al., 2005). ARTOA includes a variety of other corrections that were not included in this calculation; however, we assume that this approximation is similar enough to be considered the null hypothesis for our tracking filter intercomparison.

One of the hypotheses of this particle release experiment was that the performance of the Kalman Filter and Kalman Smoother would degrade relative to the Least Squares Filter as the motion of the particles became more random. This is because increasingly random particles reduce the kinematic model's predictive skill (M in Eq. 2.6) compared to persistence. Eventually, as the kinetic model loses all skill, the performance of the Kalman Filter and Kalman Smoother should converge to the Least Squares solution. Additionally, because our formulation of the Least Squares solution makes no Forecast, we expect the Least Squares trajectory error to be

insensitive to the character of the float motion. To assess this, we varied the scaling of the random component of motion (s in Eq. 2.1), which is the ratio of mean to random advection in low, medium, and high signal-to-noise scenarios. For our simulations, the total amplitude of the low, medium, and high cases was 5.1 km day^{-1} , 2.2 km day^{-1} , 0.7 km day^{-1} , respectively.

Process Noise (\mathbf{Q} in Eq. 2.6) is kinematic model uncertainty or unexpected acceleration. For these experiments, \mathbf{Q} is defined by the random component of motion (s in Eq. 2.1) and was set accordingly. These experiments test the relative response of the tracking filters to the random component of motion; the schemes nudging tracked floats to follow Satellite Linear Interpolation, $f H^{-1}$ Contours, and Geostrophic Streamlines distort these results and are turned off for all particle runs.

The first observational variable considered is the availability of satellite positioning. Satellite positioning was varied from 0% to 100% of the days each particle was tracked (Fig. 2.6) for the 3 signal-to-noise cases considered. As expected, mean trajectory error decreases with increased satellite positioning frequency for all filters. The mean error of the Kalman Smoother outperformed the mean error of the Kalman Filter and the Least Squares filter for all satellite positioning and signal-to-noise cases considered. We also find that the relative performance of the Kalman Smoother decreased as particle advection signal-to-noise decreased. These results agree with our hypothesis that the decreased signal-to-noise of the float advection will decrease the skill of the kinematics used in the Forecast step of the Kalman Smoother and Kalman Filter. Consequently, their relative performance will approach that of the Least Squares filter.

Particle tracks were estimated with a range of acoustic noise to test the sensitivity of the filters to TOA uncertainty. TOA uncertainty is included in our calculation as Observation Noise (\mathbf{R} in the Kalman Gain of the Forecast Update step of Equation 2.12). TOA uncertainty was varied between 0 and 50 seconds for all three signal-to-noise cases considered. Mean trajectory error increased with increased simulated TOA uncertainty. The mean error produced by the Kalman Smoother outperforms the mean error produced by the Kalman Filter and Least-Squares for all values of TOA uncertainty and random float advection considered (Fig. 2.7). Linear fits of

aggregated position errors show that the Kalman Smoother not only outperforms the other filters at all three signal-to-noise levels but that the Kalman Smoother's performance increases with increasingly noisy TOA observations. However, the Least Squares solution was insensitive to the signal-to-noise ratios. As the signal-to-noise decreased, this outperformance of the Kalman Smoother relative to the Least Squares filter also decreased.

Finally, we considered the number of acoustic sources heard (Fig. 2.8). Increasing the number of sound sources heard increases the length of \mathbf{y}_i^o in Equation 2.11, and, if unbiased, should improve tracking. Mean trajectory error decreased with increasing numbers of acoustic sources, and the mean trajectory error of the Kalman Smoother was lower than both the Kalman Filter and the Least Squares Filter. The relative mean trajectory error of the Kalman Smoother compared to the Kalman Filter also decreased with increasing sound sources heard. This means that the relative performance increase of the Kalman Smoother is most pronounced when the most positioning information is available. Mean trajectory error was inversely proportional to the number of sound sources heard for the Kalman Filter and Kalman Smoother, but initially increased for the Least Squares filter. This may be due to the fundamental ambiguity of tracking with less than three sources, or because the Least Squares filter has no Forecast, its solutions can easily fall victim to noisy TOA data.

2.6.2 DIMES Intercomparison

After our synthetic experiment, we apply the Kalman Smoother to real float data, calibrate our filter to optimal cost, and compare our trajectories to ARTOA-derived tracks. DIMES float trajectories were reconstructed with the Kalman Smoother and compared with the previously-calculated ARTOA trajectories (Balwada et al., 2016) following the pre-processing conventions described in section 2.5.4. As in the DIMES ARTOA tracking, a sound speed of 1.5 km s^{-1} was used in all calculations.

The output of the Kalman Smoother depends on prescribed errors and uncertainties; to assess these sensitivities we conducted a tuning experiment to find the ideal combination of Data

Misfit and Model Size (Eq. 2.18). The optimal parameters for the DIMES experiment as defined in section 2.5.5 are 4.5 km for Process Position Noise (large case), 0.75 km day⁻¹ for Process Velocity Noise (extra small case), 1.4×10^{-7} rad m⁻¹s⁻¹ for $f H^{-1}$ Contour noise (large case), 5.0 m² s⁻¹ Geostrophic Streamline noise (extra small case), and 2 s TOA noise (extra small case) (Fig. 2.9). This parameter configuration places relative importance on following Geostrophic Streamlines, TOA observations, and the velocity Forecast, and relatively less importance on $f H^{-1}$ Contours and the position Forecast.

We observe that the mean misfits are relatively insensitive to Process Velocity Noise and Stream Noise and that the misfit distributions are non-Gaussian, underscoring the importance of properly tuning the filter to the data. Mean misfit appears primarily sensitive to $f H^{-1}$ Contour noise. The Hero and Shackleton Fracture Zones run roughly perpendicular to the Antarctic Circumpolar Current in this region, and this may reduce the skill of $f H^{-1}$ Contour-following algorithms.

A fundamental difficulty of reproducing the DIMES trajectories with any filter is that the problem is under-constrained. Over three-quarters of the available ranging data have fewer than the 3 sound sources necessary for an unambiguous fix. This means that two or more solutions can be equally consistent with the available ranging data and yet have substantial differences in trajectories. Figure 2.10 shows several example trajectories highlighting the similarities and differences between the Kalman Smoother and ARTOA trajectories. We observe small differences in well-tracked floats (Fig. 2.10 a), but the general structure is consistent, and the positioning error is relatively low. Under-constrained trajectories (Fig. 2.10 b, c, and d) may have brief periods of close agreement but then diverge for long periods. This divergence can also be seen in the increase of TOA misfit as a function of days since the last acoustic source was heard (Fig. 2.11). The aggregate of the acoustic record also shows a decrease in mean misfit as a function of the total percent of the trajectory where the float was acoustically positioned (Fig. 2.12). The ARTOA to Kalman Smoother trajectory difference increased an average of 3.8 km day⁻¹ for periods without acoustic ranging.

The ARTOA float tracks achieved lower TOA misfit than the Kalman Smoother tracks (Fig. 2.13a). Unsurprisingly, the ARTOA Least-Squares algorithm produces a solution that is more consistent with available ranging data; our algorithm imposes additional dynamics on the acoustic ranging. Therefore the Kalman Smoother trajectories will, in general, have greater misfit. However, because of potential errors in the acoustic ranging, the hypothesis is that those dynamics may help the Kalman Smoother have overall better performance at reproducing the true trajectory (as shown in section 2.6.1). Because our algorithm imposes limits on velocity and position change, it may take many additional time steps for the algorithm's solution to converge to an error tolerance within the mean and standard deviation of the experiment. The Least Squares solutions can re-position its trajectory without bound to achieve maximum consistency with available data. The mean TOA misfit for the ARTOA solution was -0.3 ± 13.1 s, whereas the mean TOA misfit for the Kalman Smoother trajectories was -4.1 ± 35.9 s.

The TOA error as a function of sound sources heard is also considered (Fig. 2.14): a hypothesis for explaining the difference between the ARTOA tracks and our algorithm's tracks has been that the solution becomes unconstrained without regular positioning, and, one might assume, that an increased number of sound sources would decrease TOA misfit. These results are more subtle than that line of thinking. We observe the distribution of the TOA misfit between the twentieth and eightieth percentiles to be between 1.0 s and 7.1s for one sound source, increasing to between 2.5 s and 7.6 s for two sound sources, then increasing to a maximum between 4.4 s and 12.2 s for three or more sources. A float trajectory can be consistent with one or two lines of position regardless of the uncertainty in the ranging data. However, it can only be consistent with three or more lines of position if the ranging data has no bias or uncertainty. Perfect data, unfortunately, does not occur in the ocean, and all the sources of timing error (sound source clocks, float clocks, speed of sound estimates) may be responsible for this increase in TOA error. The ARTOA to Kalman Smoother trajectory difference decreased an average of 13.4 *km* for each additional sound source heard.

Despite these challenges, ARTOA and Kalman Smoother trajectories showed many

similarities (Figure 2.13). The histogram of the trajectory difference between the Kalman Smoother trajectories and the ARTOA trajectories peaks at 15.4 km with a mean of 157.9 km and a median value of 44.4 km. A comparison of the Kalman Smoother and ARTOA speeds shows a similar distribution, with a higher Kalman Smoother velocity peak and a fat tail in the faster end of the distribution (Fig. 2.13 c). The ARTOA float speed pdf peaks at 1.4 km day^{-1} with a mean and median of 6.9 and 4.9 km day^{-1} respectively. The Kalman Smoother pdf speed also peaks at 1.4 km day^{-1} with a mean and median of 7.5 and 4.3 km day^{-1} .

2.6.3 Weddell Sea Floats

Having validated our method with both the numerical experiment and the DIMES float trajectories, we focus on the set of previously untracked floats in the Weddell Sea.

Similar to the DIMES inter-comparison, the sensitivities of the trajectory solutions were assessed to prescribed parameter uncertainties. Intermittent satellite positioning is available in the Weddell Sea dataset, so we also considered Satellite Linear Interpolation's prescribed uncertainty. The optimal parameter configuration for the Weddell Sea experiment (Fig. 2.16) as explained in section 2.5.5 are: 4 s TOA uncertainty (small case), 4.5 km for Process Position Noise (large case), 0.75 km day^{-1} for Process Velocity Noise (extra small case), $0.6 \times 10^{-7} \text{ rad m}^{-1} \text{ s}^{-1}$ for $f H^{-1}$ Contour noise (extra small case), $30.0 \text{ m}^2 \text{ s}^{-1}$ stream function noise (large case). TOA misfit was found to be insensitive to Satellite Linear Interpolation noise at any reasonable values and was set to 120 km. This parameter configuration puts relative importance on the velocity Forecast, TOA Observations, and the tendency to follow $f H^{-1}$ Contours. We observe that data misfit is primarily sensitive to Process Position Noise.

Weddell Sea float trajectories and associated position uncertainties are estimated for the first time (Fig. 2.15). TOA misfits for the Weddell Sea dataset are generally higher than those for the DIMES dataset (Figs. 2.11, 2.12, and 2.14). However, the mean Weddell Sea TOA Error is much less after long periods without positioning. This could imply that the data quality of the Weddell Sea experiment is worse than that of DIMES but that the skill of the nudging schemes

(particularly $f H^{-1}$ contours) is greater. This implication is reasonable because the Weddell Sea is relatively quiescent compared to Drake Passage and likely has dynamics that are easier to model. Contrary to the DIMES floats, the mean Weddell Sea TOA Error continually increases while the standard deviation of TOA Error continually decreases (Fig. 2.14): we observe the distribution of TOA misfit between the twentieth and eightieth percentiles to be between 2.9 s and 43.8s for one sound source, changing to between 3.8 s and 35.0 s for two sound sources, finally increasing to between 15.1 s and 39.6 s for three or more sources.

Overall, TOA Misfit was higher, and speed was slower than those calculated for DIMES. Similar to the DIMES data (Fig. 2.17), the residuals are non-Gaussian. Weddell Sea TOA misfit had more bias but less standard deviation compared to the DIMES Kalman Smoother trajectories. The mean TOA misfit for the ensemble of reconstructed trajectories was -9.0 ± 14.4 s. While dynamical differences such as the magnitude of mean currents and eddy activity exist between the DIMES experiment and the Weddell Sea, the primary difference between the Weddell Sea and DIMES datasets is that Weddell Sea floats received intermittent satellite positioning, while the DIMES floats did not. The intermittent satellite positioning not only provides a powerful constraint on the trajectory solutions but also helps to calibrate sound source clock drift and moderate the potential nonlinearities associated with sound source misidentification. It is difficult to quantify these effects, but they may be less than the displacement due to the vertically integrated ocean shear that neutrally buoyant floats that drift at depth for long periods have sought to avoid. The speed histogram (Fig. 2.17 b) shows a mean float speed of 5.4 km day^{-1} , and a median float speed of 2.1 km day^{-1} .

2.7 Discussion

Our implementation of the Kalman Smoother offers theoretical and operational benefits over the standard Least-Squares solutions. This formulation of Kalman smoothing is designed to be added to updates of float tracking software packages. Checking sound source identification

was also an important step in successfully localizing floats in the under-ice Weddell Sea.

The Kalman Smoother is not without weaknesses. Long periods of position loss can cause the filter to produce unphysical estimates that cross onto land or travel against known circulation features. The acceptable time of position loss will depend on many factors, including the uncertainty of positioning, sound source configuration, the complexity of the float motion, available satellite positioning, and the tendency of the float to follow Geostrophic Streamlines. In our analysis, we have found the purely acoustic position estimates of the Kalman Smoother after 60 days of position loss to be dubious.

The optimal DIMES and Weddell Sea trajectory solutions have parameter configurations of Position Noise, Velocity Noise, and dynamical constraints that imply the Kalman Smoother has skill. The ARTOA Least Squares solution can be approximated by prescribing enormous Process Noise and nudging scheme noise such that the filter only regards acoustic ranging; this was not the result of the sensitivity experiments. The calculated optimal noise for each dataset emphasizes inputs from specific nudging schemes and the Forecast. The low Geostrophic Streamline noise of the DIMES tuning experiment and the $f H^{-1}$ Contour noise of the Weddell Sea tuning experiment highlight the need to include multiple nudging inputs. We have found adding these physical constraints to be important in producing trajectories in the direction of known circulation features with reasonable velocities. It is encouraging that the ideal Weddell Sea float trajectory solution was more strongly affected by the depth-following constraint. At the same time, the Geostrophic Streamlines were less helpful, as Gray and Riser (2014) note the high uncertainty in their Weddell Sea streamlines due to the very sparse Argo data at the time of their analysis. Satellite Linear Interpolation was also important in producing reasonable trajectories, although the data misfit was observed to be insensitive to the scaling of 120 km presented in Chamberlain et al. (2018).

2.8 Conclusion

We have demonstrated a method that combines acoustic ranging, satellite observations, and geostrophic dynamics to constrain float tracks. Our Kalman Smoother method includes constraints to follow $f H^{-1}$ Contours, Geostrophic Streamlines, or Satellite Linear Interpolation (when available), and it limits maximum uncertainty in velocity and maximum allowed position change. We have shown that this method is a possible improvement over Least-Squares in an ensemble of numerical simulations and real-world float tracking experiments with degraded acoustic signals.

We validated the Kalman Smoother using previous DIMES experiment acoustic ranging data and ARTOA float tracks. We found the trajectories produced by the Kalman Smoother to be consistent with available ranging data. We also validated the Kalman Smoother using a numerical experiment in which we released and tracked 30,000 artificial particles using simulated acoustic ranging and satellite positioning. Our numerical experiment found that the Kalman Smoother was more consistent with the true particle trajectories than the Kalman Filter or the Least-Squares solution.

Finally, we applied the Kalman Smoother to a previously untracked set of floats in the Weddell Sea. Weddell Sea float tracks and acoustic ranging errors are within standard ranging uncertainties and have been made available publicly through the NOAA Subsurface Float Data Assembly Center. Our dynamical model, which assumes floats follow a combination of $f H^{-1}$ Contours, Geostrophic Streamlines, and Satellite Linear Interpolation, is still somewhat simple. Subsequent software versions that consider known circulation features or sea surface height observations may lead to improvements.

A version of Kalman Filtering could be incorporated in future software to identify sound sources; for example, while identifying sources, forecast predictions could be generated from previous sound source selections that inform the user of statistically improbable source choices. In general, clock drift introduced substantial challenges in trajectory reconstruction

because of the ocean's relatively high speed of sound. Additionally, although sound sources are identified manually by careful and skilled practitioners, and the Kalman Smoother can quantify the statistical probability of a sound source, mistakes in identification are possible - particularly after a long period of ranging loss. Sound source misidentification is a fundamental nonlinearity in this calculation that we do not address. Other methods (Li et al., 2015) or insonification strategies that uniquely identify sound sources have been advanced and could be considered in future deployments (Duda et al., 2006).

This study has focused on the Southern Ocean, but under-ice Argo tracking is also of interest in the Arctic Ocean. Further tests are needed to determine the applicability of the Kalman Smoother with our chosen regularizations in the Arctic Ocean.

2.9 Acknowledgements

This work was supported by the SOCCOM project under NSF Award PLR-1425989 and by GO-BGC under NSF OCE-1946578. BC was supported by NOAA Grant NA18OAR4310403. We thank 4 anonymous reviewers for their helpful suggestions and remarks, Dr. Olaf Boebel for his dedication to and advancement of acoustic tracking, and Dr. Mathias Morzfeld for insightful conversations and recommendations. KS and CH received support from NSF OCE-1658479. Chapter 2, in full, has been submitted for publication of the material as it may appear in *Journal of Atmospheric and Oceanic Technology*, 2022, Chamberlain, P. M., Cornuelle, B., Talley, L. D., Mazloff, M. R., Speer, K., Hancock, C., & Riser, S. C., American Meteorological Society 2022. The dissertation author was the primary investigator and author of this paper.

Table 2.1. WMO ID Numbers of 22 Previously Untracked Weddell Sea Floats

RAFOS Enabled Argo Floats			
5901716	5901717	5901718	5901720
5901721	5901723	5901724	5901727
5901728	5901730	5901731	5901733
5901734	5901735	5901737	5901738
5901739	5901740	5901741	5901742
5901743	5901744		

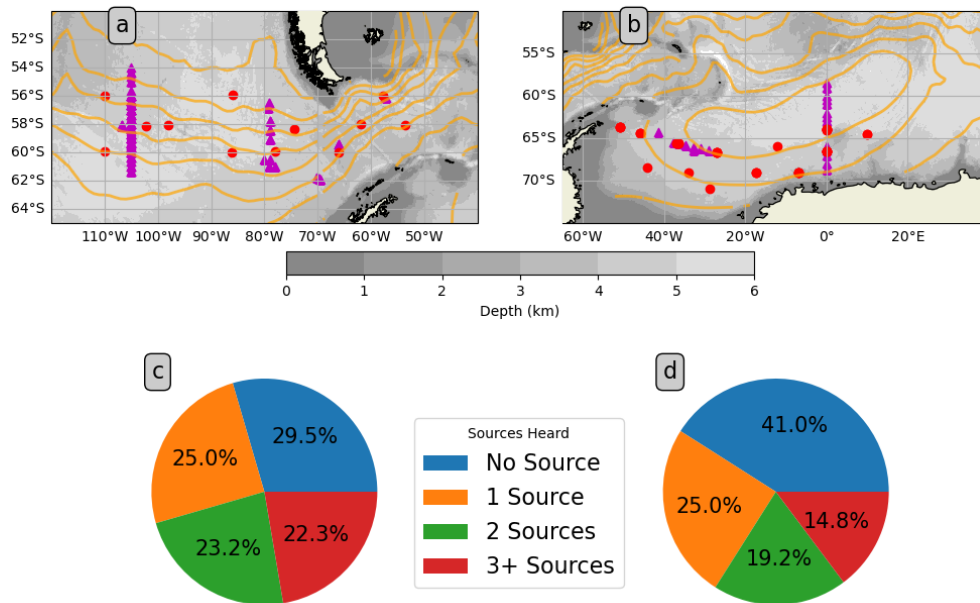


Figure 2.1. Bathymetry (gray shading) and sound source locations (red dots) for the a) Drake Passage and b) Weddell Sea. Magenta triangles indicate float deployment locations and orange lines indicate Geostrophic Streamlines at 1000 m depth contoured at $15 \text{ m}^2 \text{ s}^{-2}$ intervals (Gray and Riser, 2014). Distribution of the number of sources heard in the acoustic record for the c) DIMES experiment and the d) Weddell Sea, respectively.

Table 2.2. Sequential Calculations of Kalman Smoother Algorithm

Forward Filter	
Initialization	$x^a(t_0) = \mu_0$ with error covariance $P^a(t_0)$
Model Forecast Step/Predictor (Eq. 2.6)	$x^f(t_i) = M_{i-1}x^a(t_{i-1})$ $P^f(t_i) = M_{i-1}P^a(t_{i-1})M_{i-1}^T + Q(t_{i-1})$ $d_i = y_i^o - \mathbf{H}_i \cdot x^f(t_i)$
Data Assimilation Step/Corrector (Eq.2.11, 2.12 and 2.14)	$\mathbf{K}(t_i) = P^f(t_i)\mathbf{H}_i^T(\mathbf{H}_iP^f(t_i)\mathbf{H}_i^T + R_i)^{-1}$ $P^a(t_i) = (I - \mathbf{K}(t_i)\mathbf{H}_i)P^f(t_i)$ $x^a(t_i) = x^f(t_i) + \mathbf{K}(t_i)d_i(t_i)$
Smoother	
Initialization	$x^s(t_N) = x^a(t_N)$ $P^s(t_N) = P^a(t_N)$
Update	$\mathbf{K}^s(t_i) = P^a(t_i)M_i^T(P^f(t_{i+1})^{-1})$ $P^s(t_i) = P^a(t_i) - \mathbf{K}^s(t_i)(P^s(t_{i+1}) - P^f(t_{i+1}))(\mathbf{K}^s(t_i))^T$ $x^s(t_i) = x^a(t_i) + \mathbf{K}^s(t_i)(x^s(t_{i+1}) - x^f(t_{i+1}))$
Regularizations	
Max Velocity Uncertainty	60 km day ⁻¹
Max Velocity	35 km day ⁻¹
Max Displacement	50 km

Table 2.3. Uncertainties Considered for Sensitivity Experiments

Parameter	$XS (\frac{M}{4})$	$S (\frac{M}{2})$	M	L ($1.5 \times M$)	XL ($2 \times M$)	XXL ($2.5 \times M$)	XXXL ($3 \times M$)
TOA (s)	2	4	8	12	16	20	24
Process Position (km)	0.75	1.5	3	4.5			
Process Velocity ($km \text{ day}^{-1}$)	0.75	1.5	3	4.5			
Satellite Linear Interpolation (km)			120				
Geostrophic Streamline ($m^2 s^{-1}$)	0.6×10^{-7}	1.1×10^{-7}	2.1×10^{-7}	3.2×10^{-7}			
$f H^{-1}$ Contour ($rad \text{ m}^{-1} s^{-1}$)	5	10	20	30			

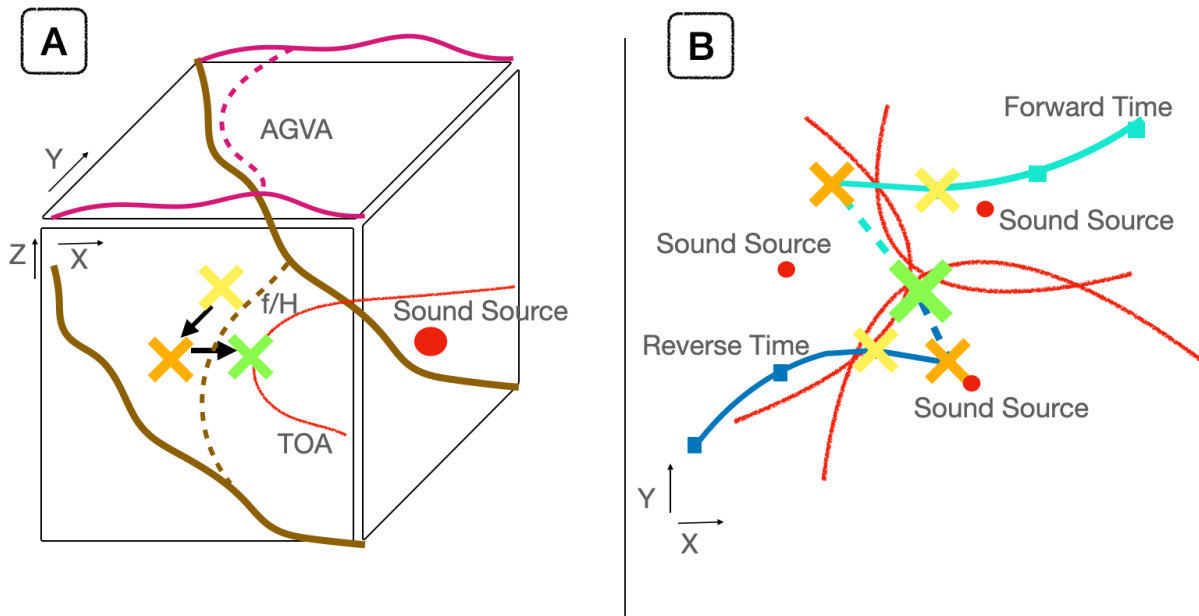


Figure 2.2. Cartoon of Kalman Smoother acoustic tracking scheme. Red dots represent sound source locations. Red arcs represent lines of position from ranging data observed on the float. a) Dashed brown contour represents f/H field, dashed magenta contour represents Geostrophic Streamlines 'AGVA' (Gray and Riser, 2014). Yellow X represents previous position. Orange X represents the Forecast. Green X represents the Analysis all in forward time. b) Light blue and dark blue squares represent Kalman Filter derived positions in forward and reverse time respectively. Yellow Xs represents previous position in both forward and reverse time. Orange Xs represent the Kalman Filter Analysis in both forward and reverse time. Dashed light blue and dark blue lines represent position updates due to smoothing routine. Green X represents Kalman Smoother position estimate.

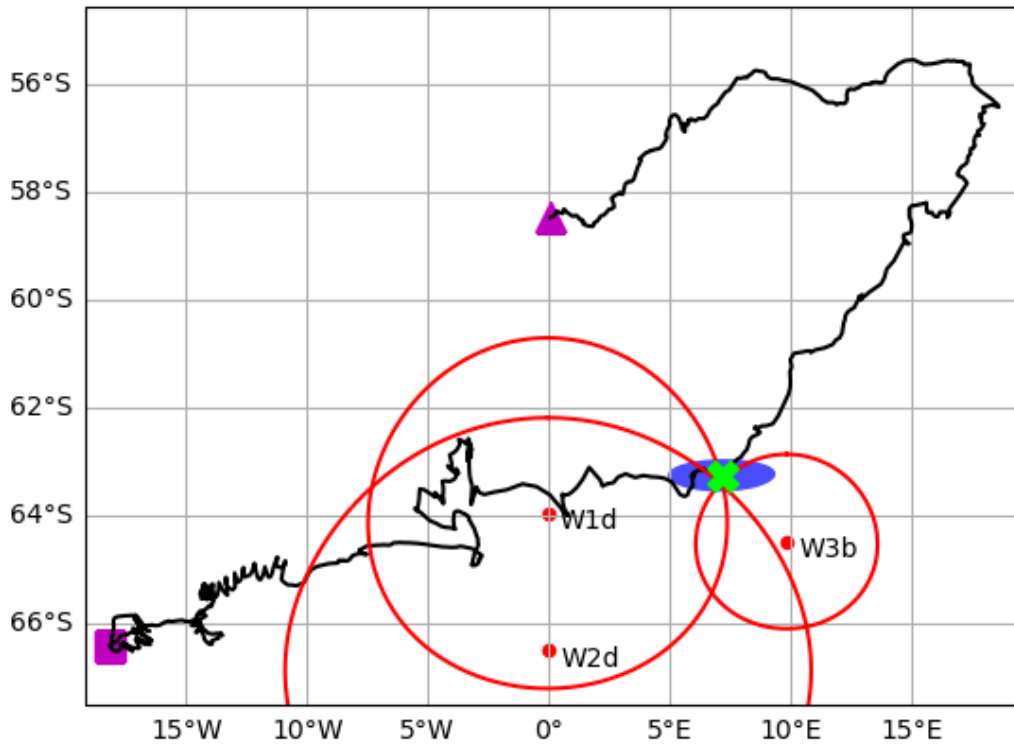


Figure 2.3. Example of acoustic tracking from Float 5901718 in the Weddell Sea. Green cross represents the most likely float position. Magenta triangle and square represent float start and end points respectively. Black line represents the reconstructed float trajectory. Teal ellipse represents the position uncertainty ellipse at the 95 % confidence interval (1.96 standard deviations). Red dots and lines represent locations and estimated time fronts for sound sources W1d, W2d, and W3b.

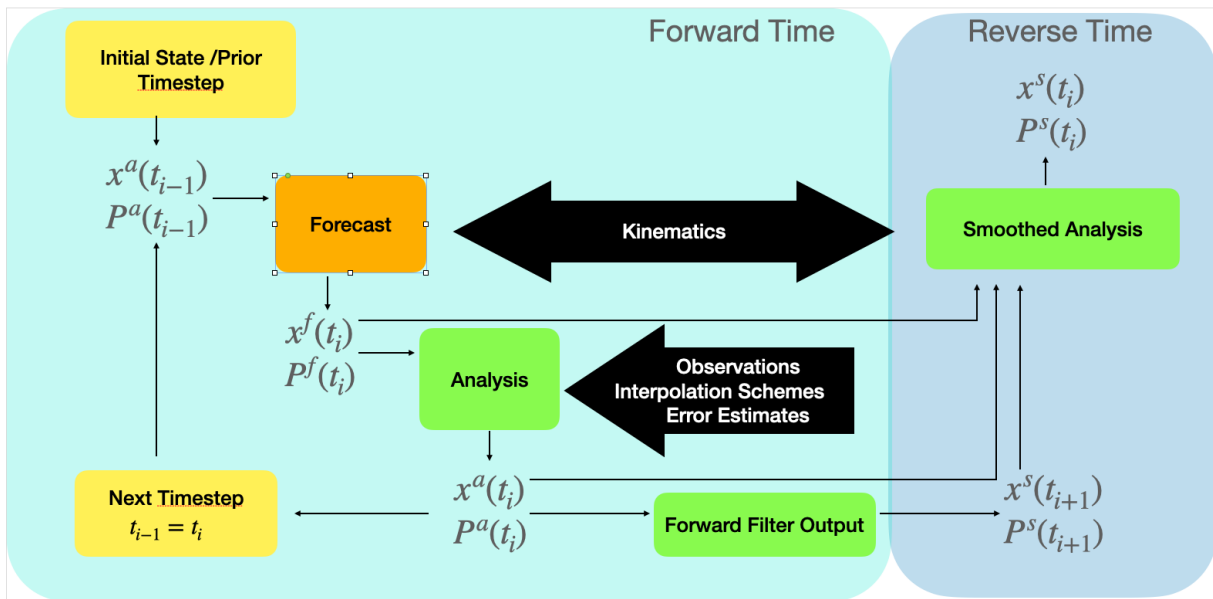


Figure 2.4. Flow chart describing the Kalman Smoother calculation. Light blue shading represents calculations in forward time, dark blue shading represents calculations in reverse time. Yellow boxes represent initial timesteps, orange boxes represent the Forecast, and green boxes represent the Analysis.

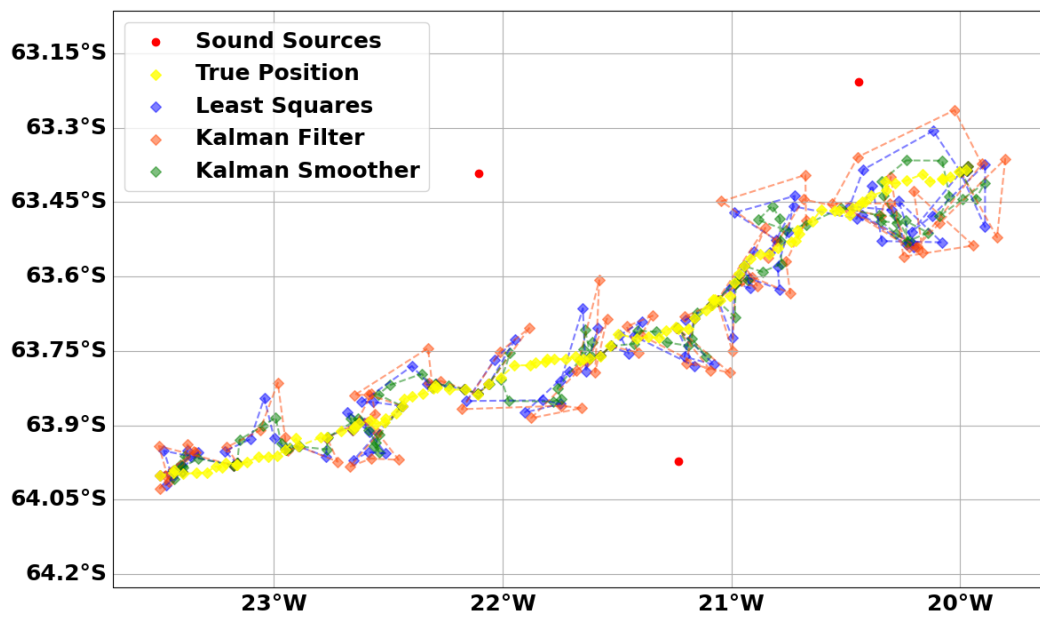


Figure 2.5. Example trajectory reconstruction of particle release experiment. The true particle trajectory is represented by yellow diamonds with trajectories estimated from Least Squares (blue diamonds), Kalman Filter (light red diamonds), and Kalman Smoother (green diamonds). Red circles represent sound source locations.

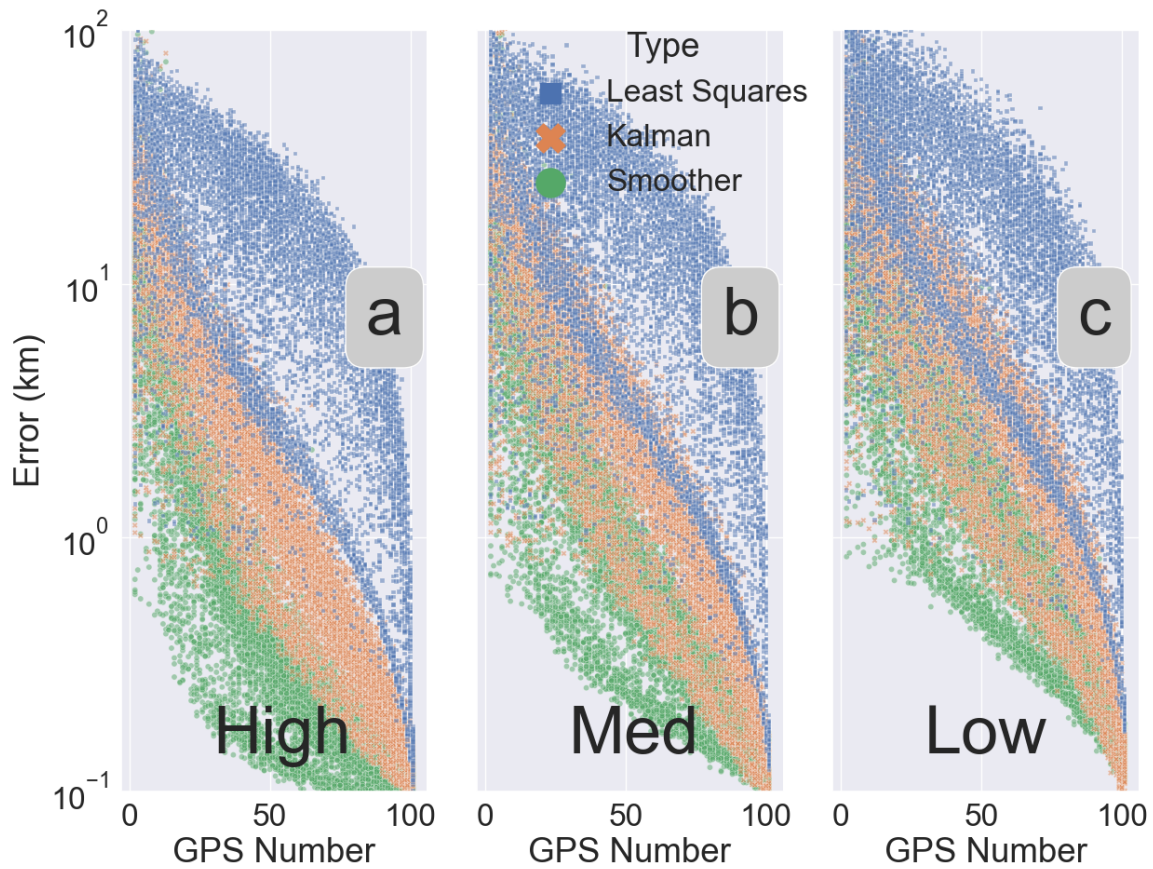


Figure 2.6. Trajectory error for numerical simulation for Kalman Smoother (green circle), Kalman filter (orange X), and Least-Squares (blue squares) algorithm for varying percent of GPS positioning. s value (Eq. 2.1) equal to a) 10% - high signal-to-noise case, b) 30% - medium signal-to-noise case, and c) 70% of mean flow - low signal-to-noise case.

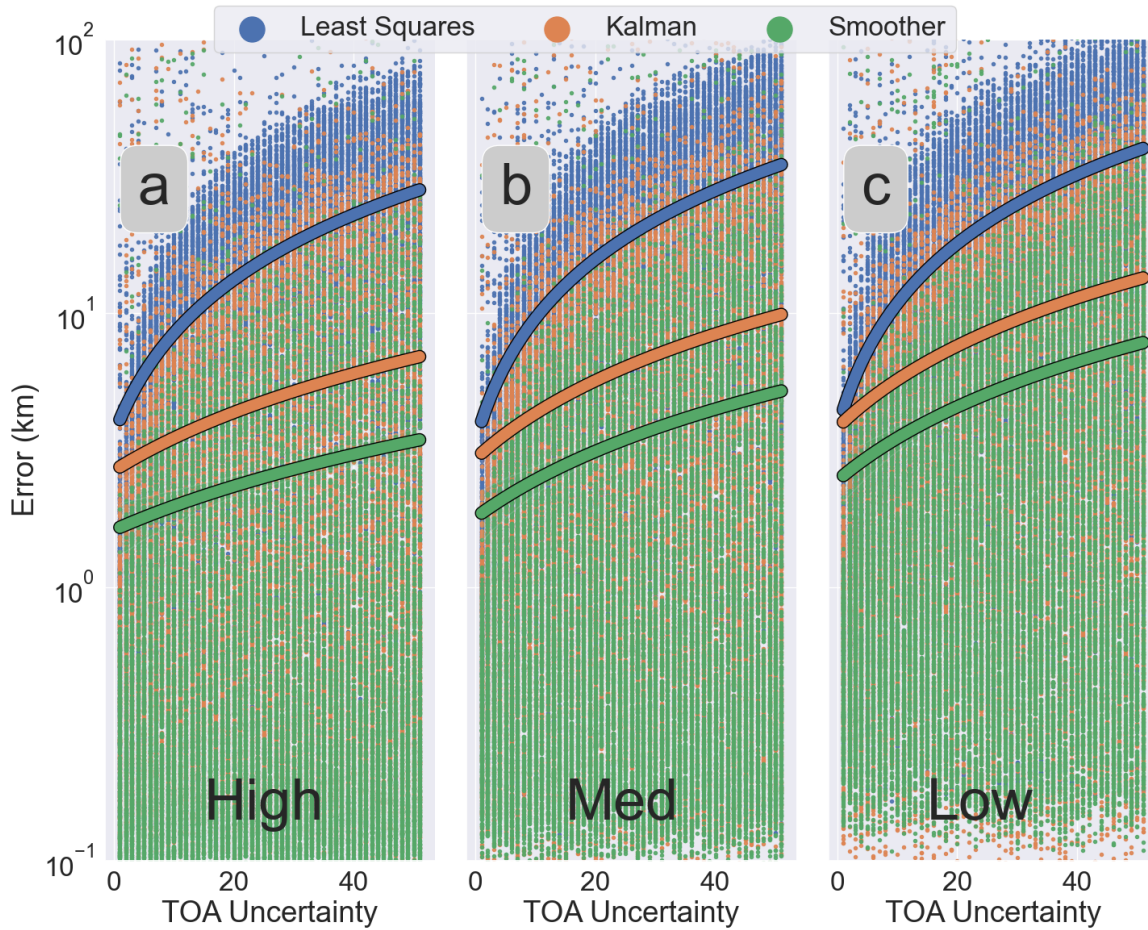


Figure 2.7. Trajectory error for numerical simulation for Kalman Smoother (green circle), Kalman filter (orange circle), and Least-Squares (blue circle) algorithm for varying quality of acoustic positioning. Solid lines represent linear fit of available data, s value (Eq. 2.1) equal to a) 10% - high signal-to-noise case, b) 30% - medium signal-to-noise case, and c) 70% of mean flow - low signal-to-noise case.

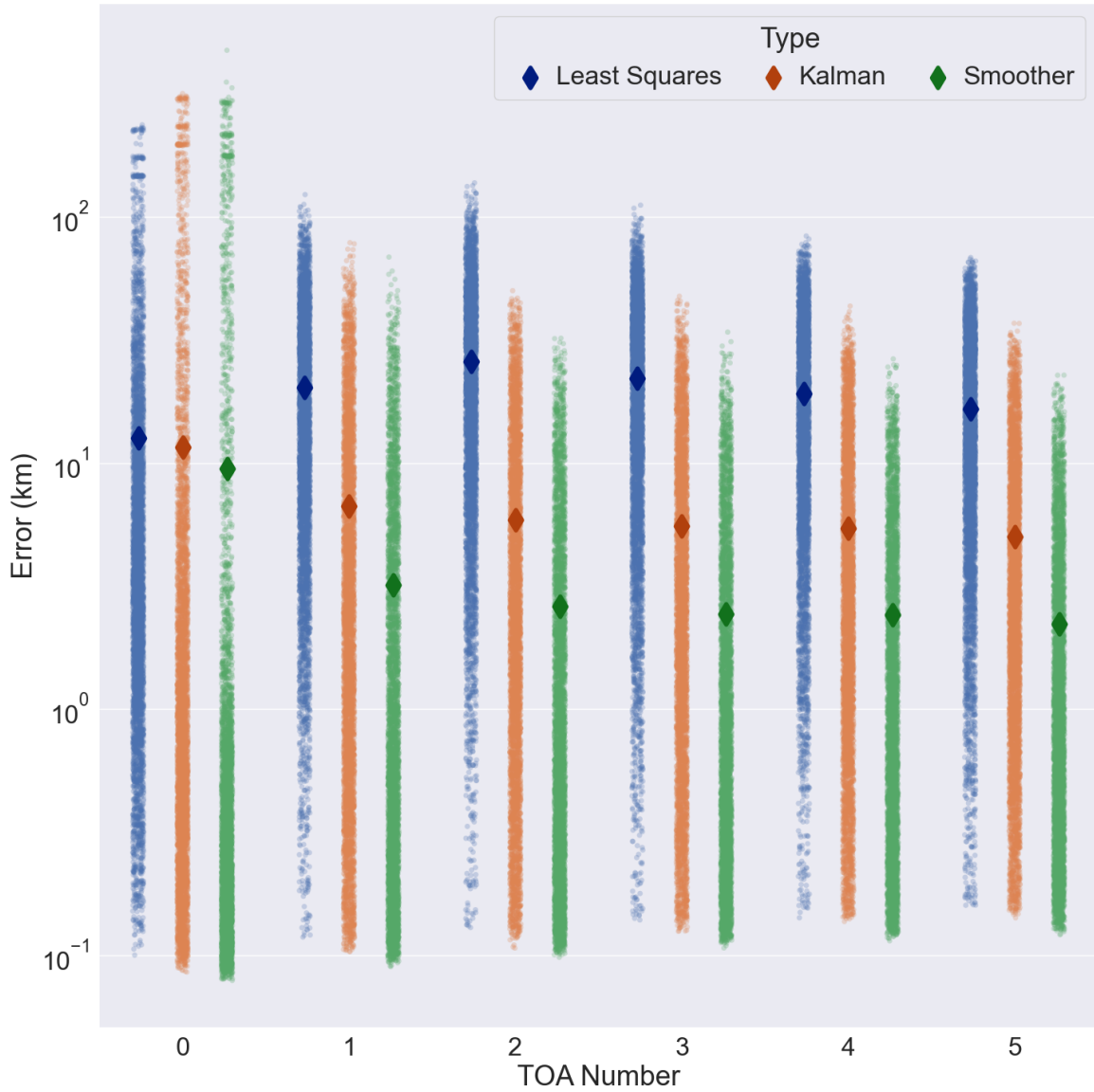


Figure 2.8. Trajectory error for numerical simulation for Kalman Smoother (green diamond), Kalman Filter (orange diamond), and Least-Squares (blue diamond) algorithm for varying quantity of acoustic positioning. Large solid diamonds represent the mean value of each distribution.

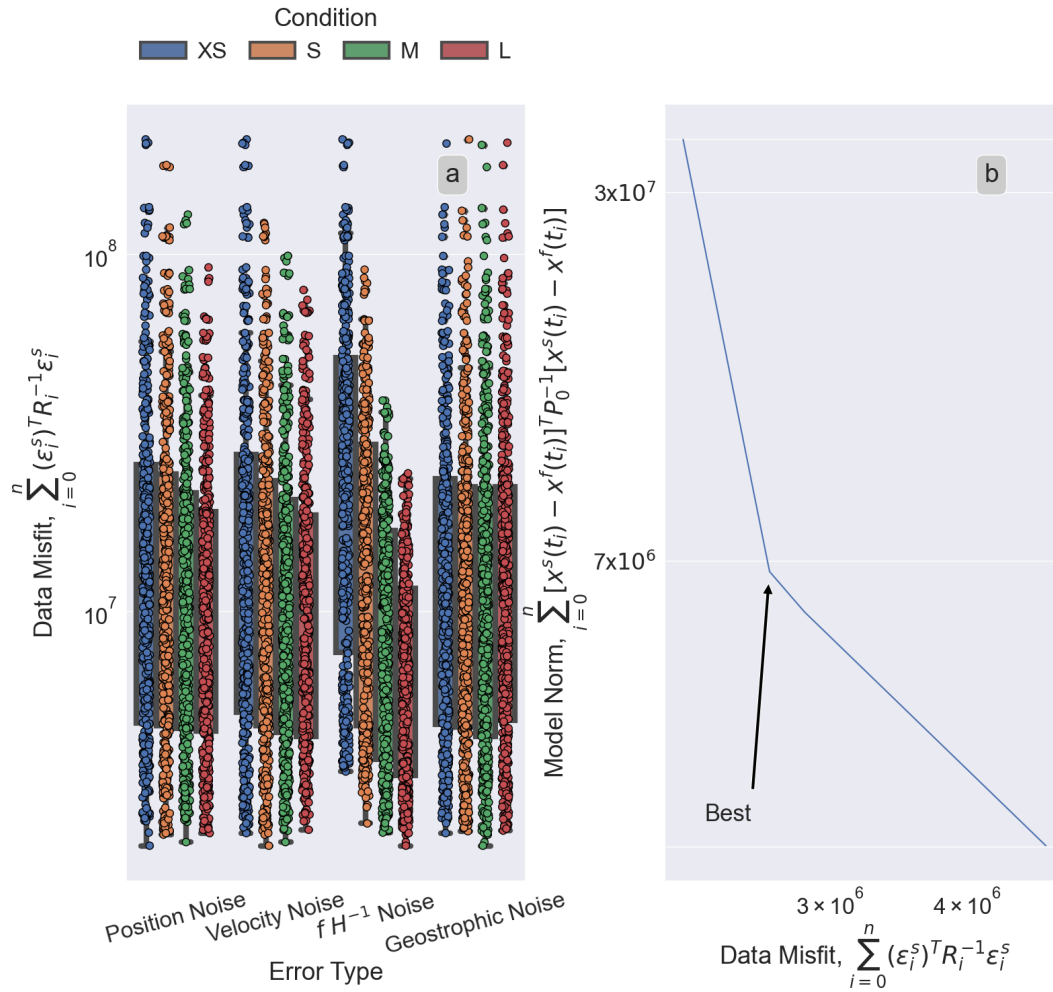


Figure 2.9. a) Sensitivity of DIMES experiment Data Misfit (Eq. 2.18) to changes in Position Process Noise, Velocity Process Noise, fH^{-1} Contour Noise, and Geostrophic Streamline Noise at extra small (blue), small (orange), medium (green), and large (red) values. b) Minimum cost overall Weddell Sea tuning runs (J in Eq. 2.18) while varying λ from 0 to 100. Curvature minimum of J is identified as the optimal parameter configuration.

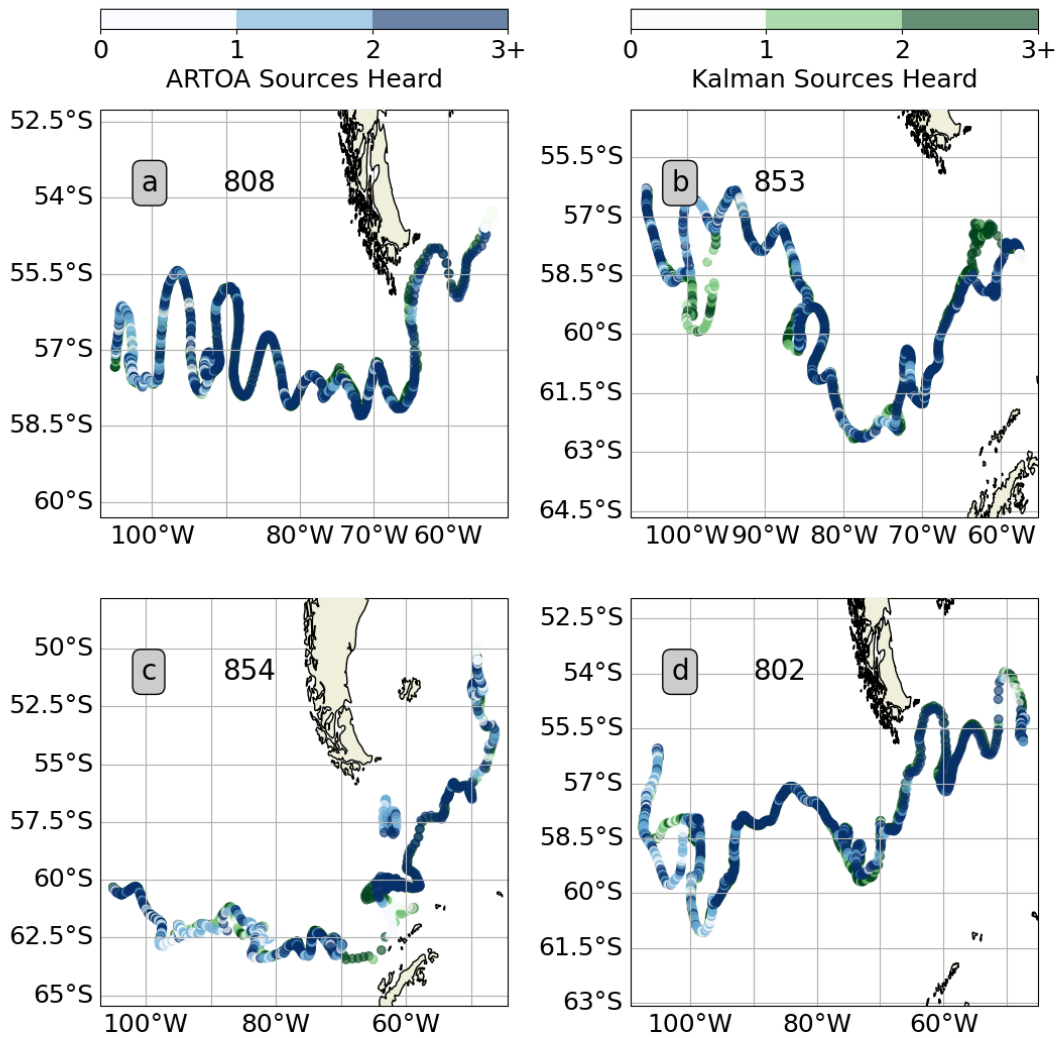


Figure 2.10. Comparison of Kalman Smoother (green) and ARTOA (blue) trajectories for DIMES floats a) 808, b) 853, c) 854, d) 802. Float 808 represents a well-tracked float with relatively little difference between Kalman Smoother and ARTOA trajectories. Floats 853, 854, and 802 highlights some of the divergences that happen when the solution is not fully constrained.

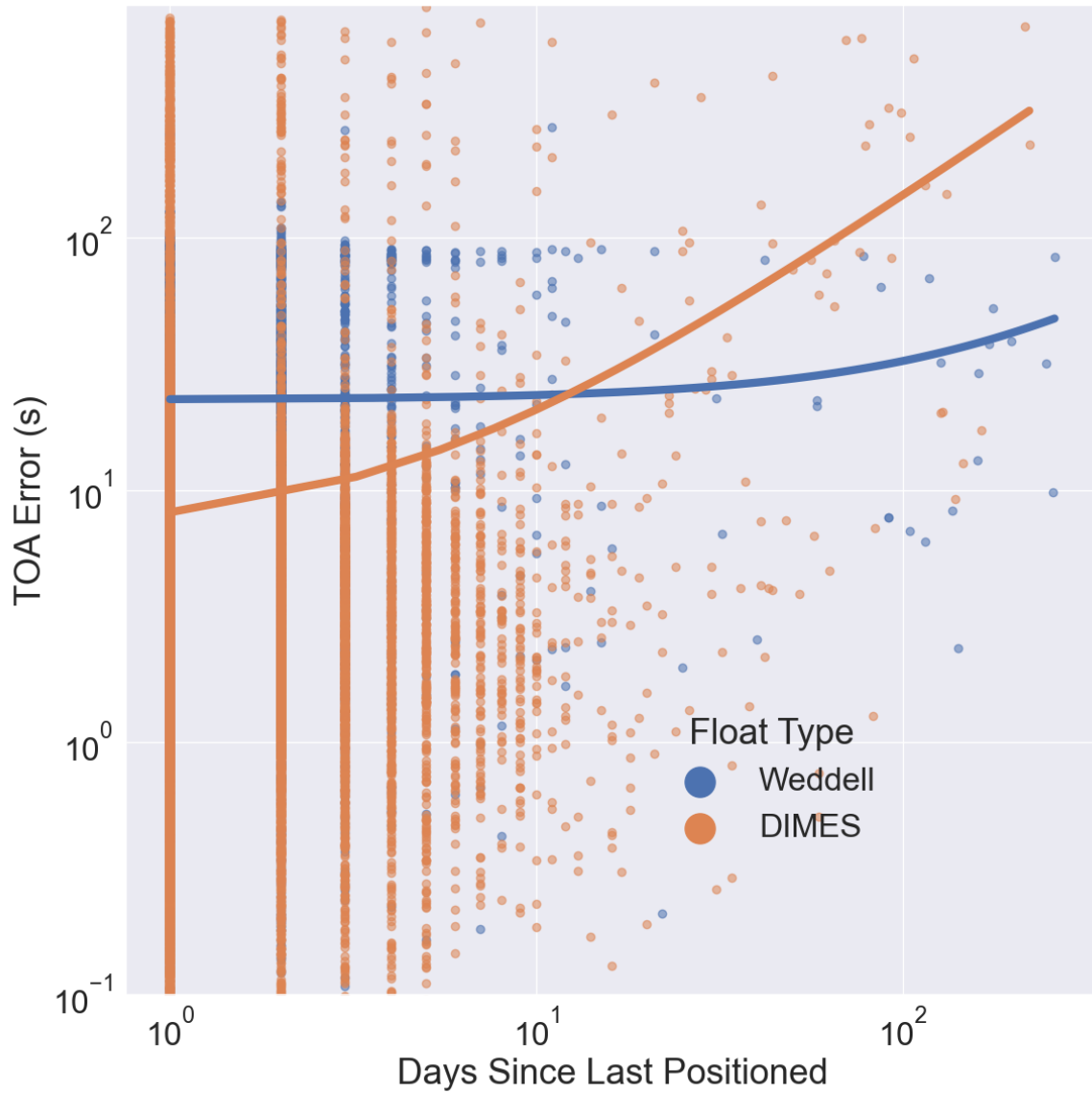


Figure 2.11. TOA error for Kalman Smoother tracking of the DIMES experiment (orange circle), Weddell Sea dataset (blue circle) by days since last positioned. Solid lines represent the mean of each distribution.

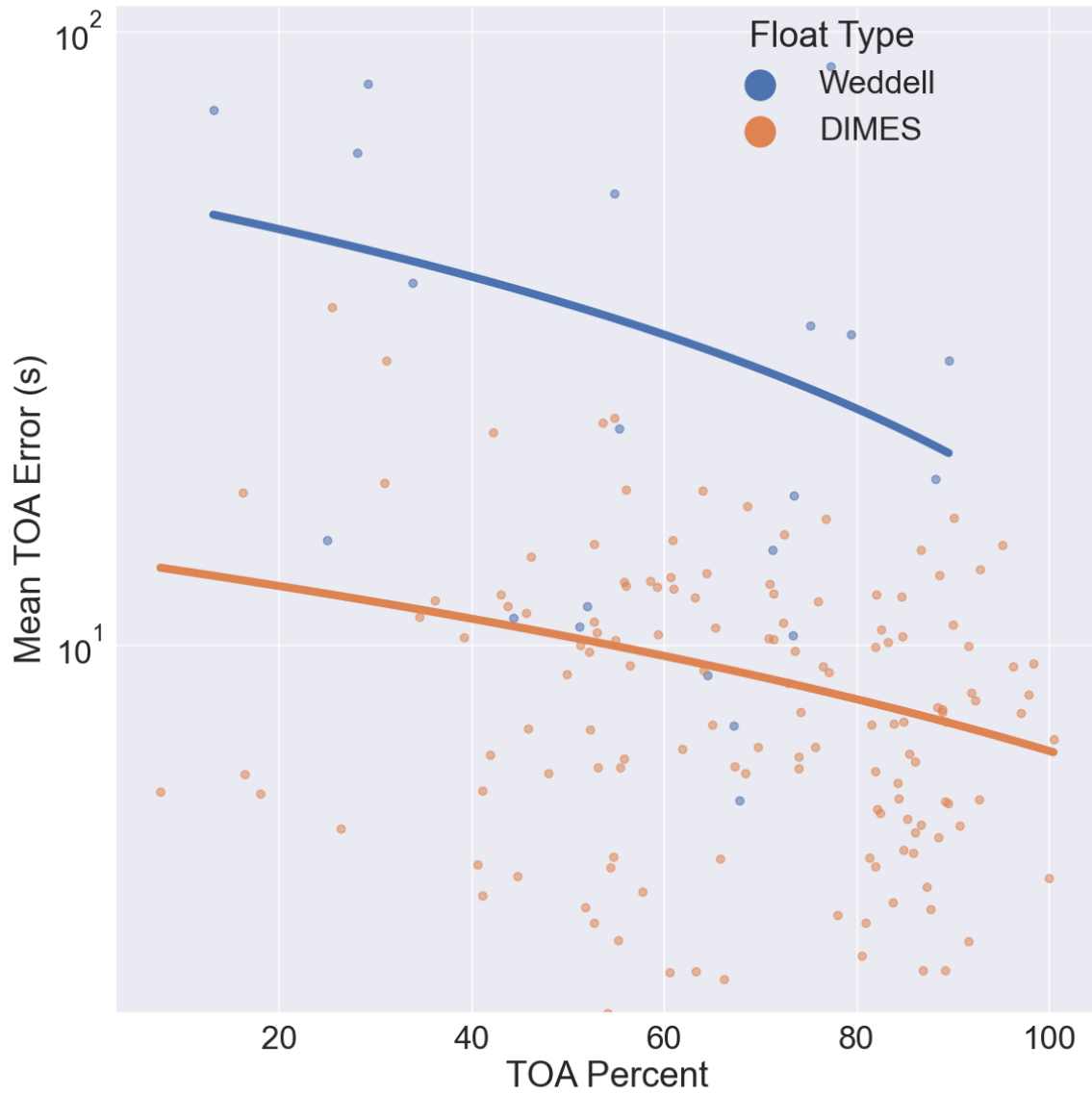


Figure 2.12. Mean TOA error for Kalman Smoother tracking of the DIMES experiment (orange circle), and Weddell Sea dataset (blue circle) by percent of trajectory which was acoustically tracked. Solid lines represent the mean of each distribution.

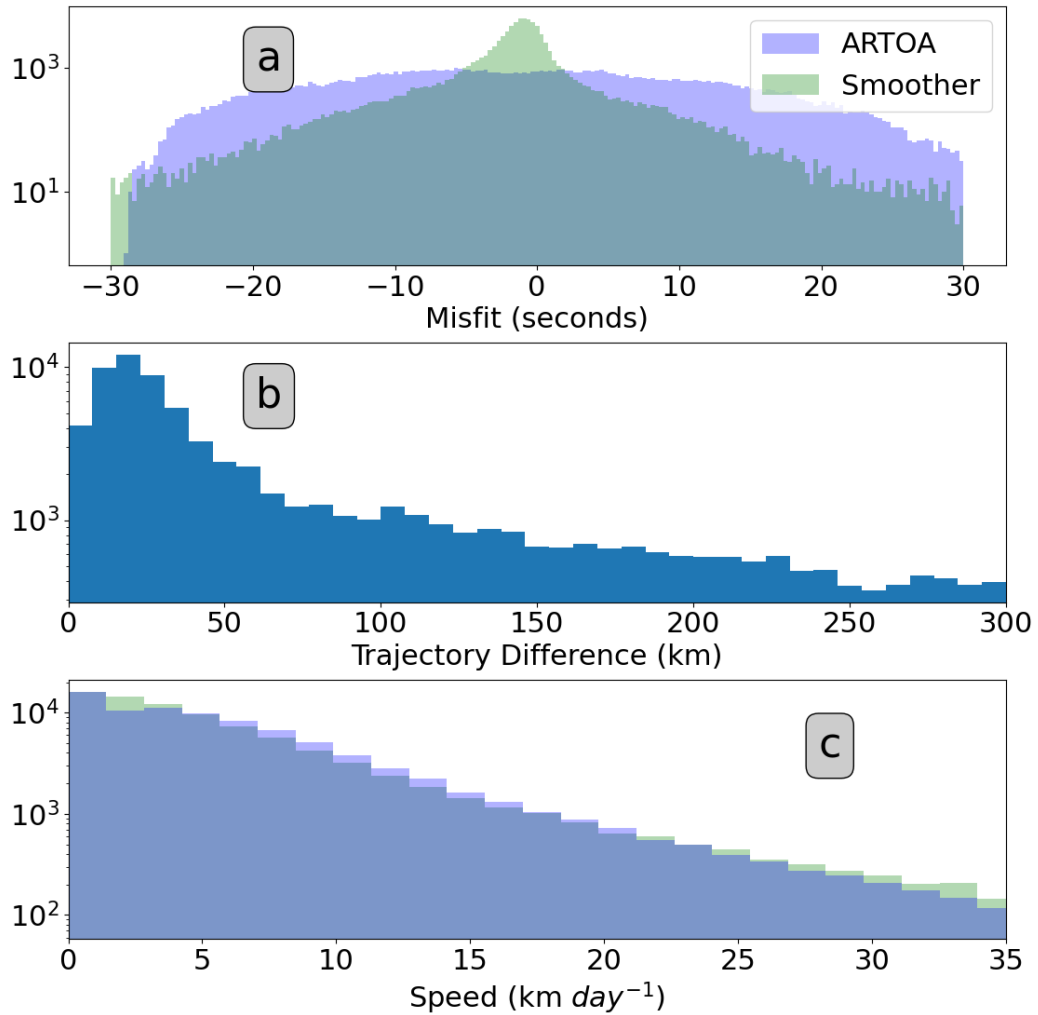


Figure 2.13. a) Histogram of misfit of trajectory with available acoustic ranging for ARTOA (blue) and Kalman Smoother (green). b) Histogram of trajectory difference between Kalman Smoother and ARTOA trajectories. c) Speed histogram for ARTOA trajectories (blue) and Kalman Smoother trajectories (green).

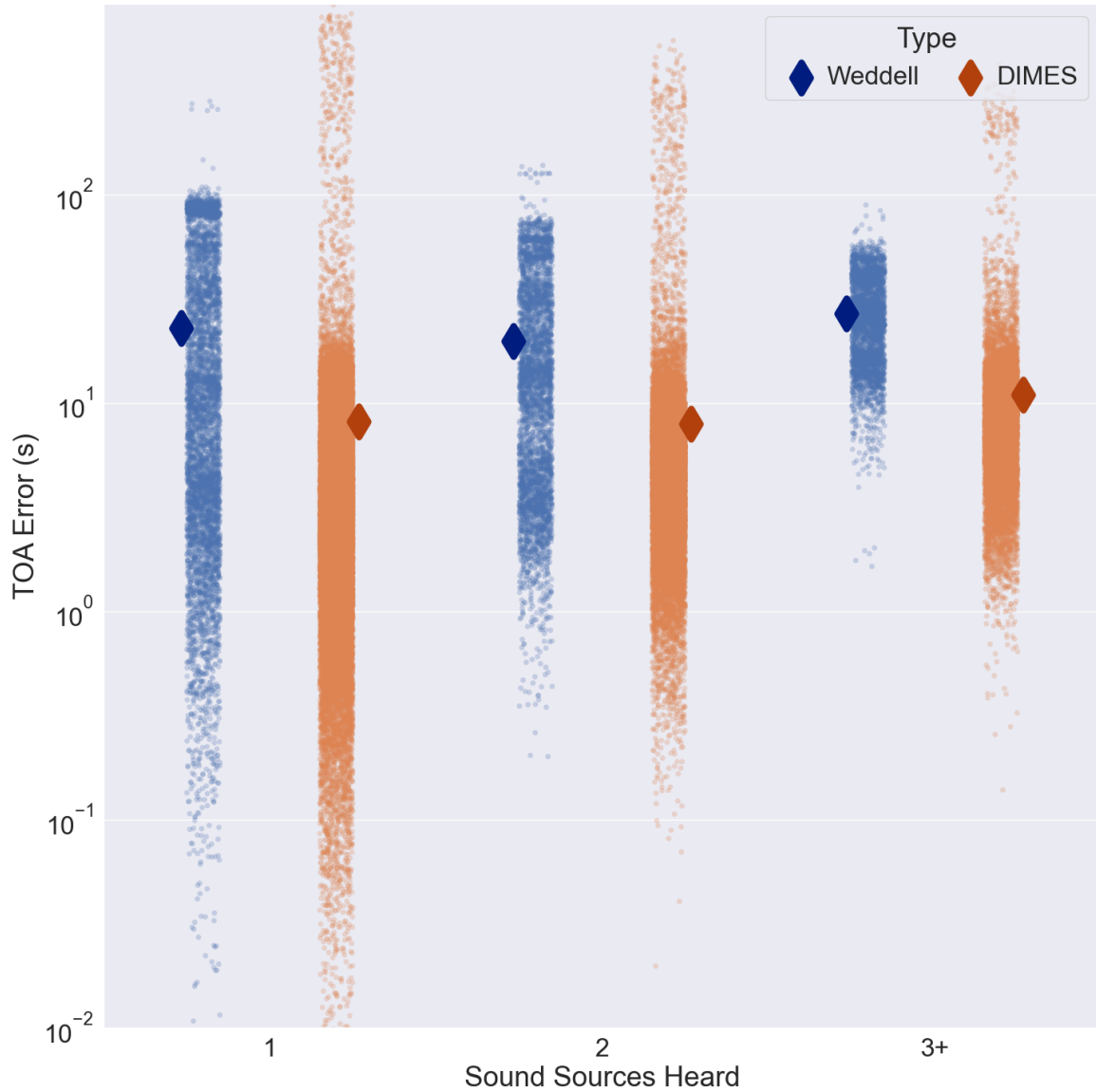


Figure 2.14. TOA error for Kalman Smoother tracking of the DIMES experiment (orange diamond), Weddell Sea dataset (blue diamond) for the number of discrete sound sources heard. Large solid diamonds represent the mean value of each distribution.

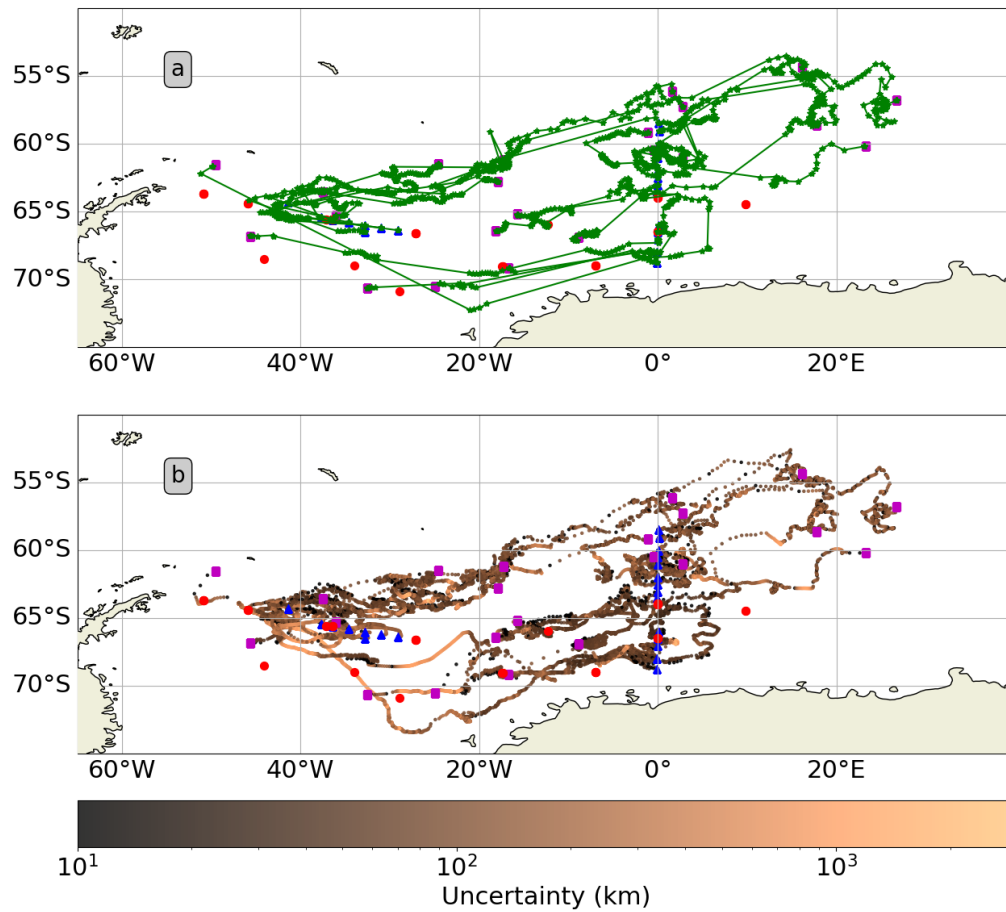


Figure 2.15. Trajectories of 22 previously untracked Weddell Sea RAFOS-enabled Argo floats. Red dots represent an array of 13 sound sources. Blue triangles and magenta squares represent the first and last known positions, respectively. a) Green stars and lines represent GPS positions and Satellite Linear Interpolations as provided by the Argo Global Data Assembly Center, which does not include acoustic tracking. b) Kalman Smoother estimate of true trajectories. Trackline colors represent position uncertainty.

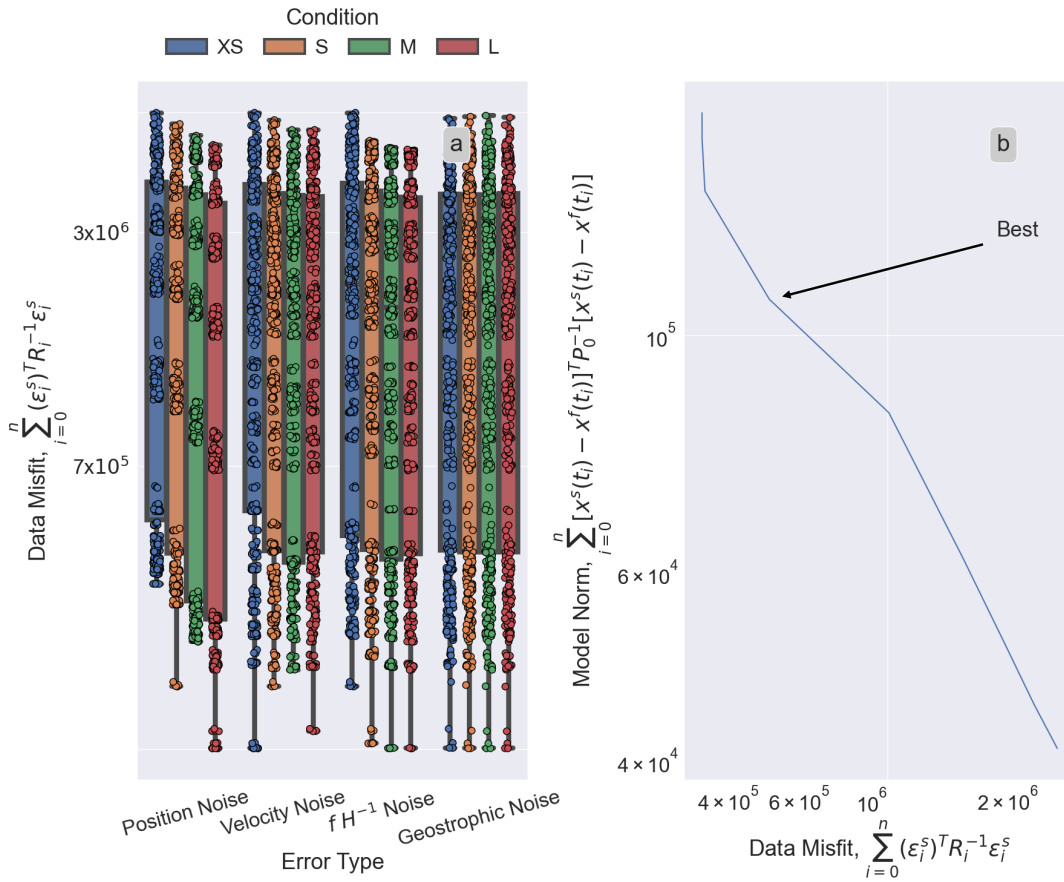


Figure 2.16. a) Sensitivity of Weddell Sea experiment Data Misfit (Eq. 2.18) to changes in Position Process Noise, Velocity Process Noise, $f H^{-1}$ Contour Noise, and Geostrophic Streamline Noise at extra small (blue), small (orange), medium (green), and large (red) values. b) Minimum cost overall Weddell Sea tuning runs (J in Eq. 2.18) while varying λ from 0 to 100. Curvature minimum of J is identified as the optimal parameter configuration.

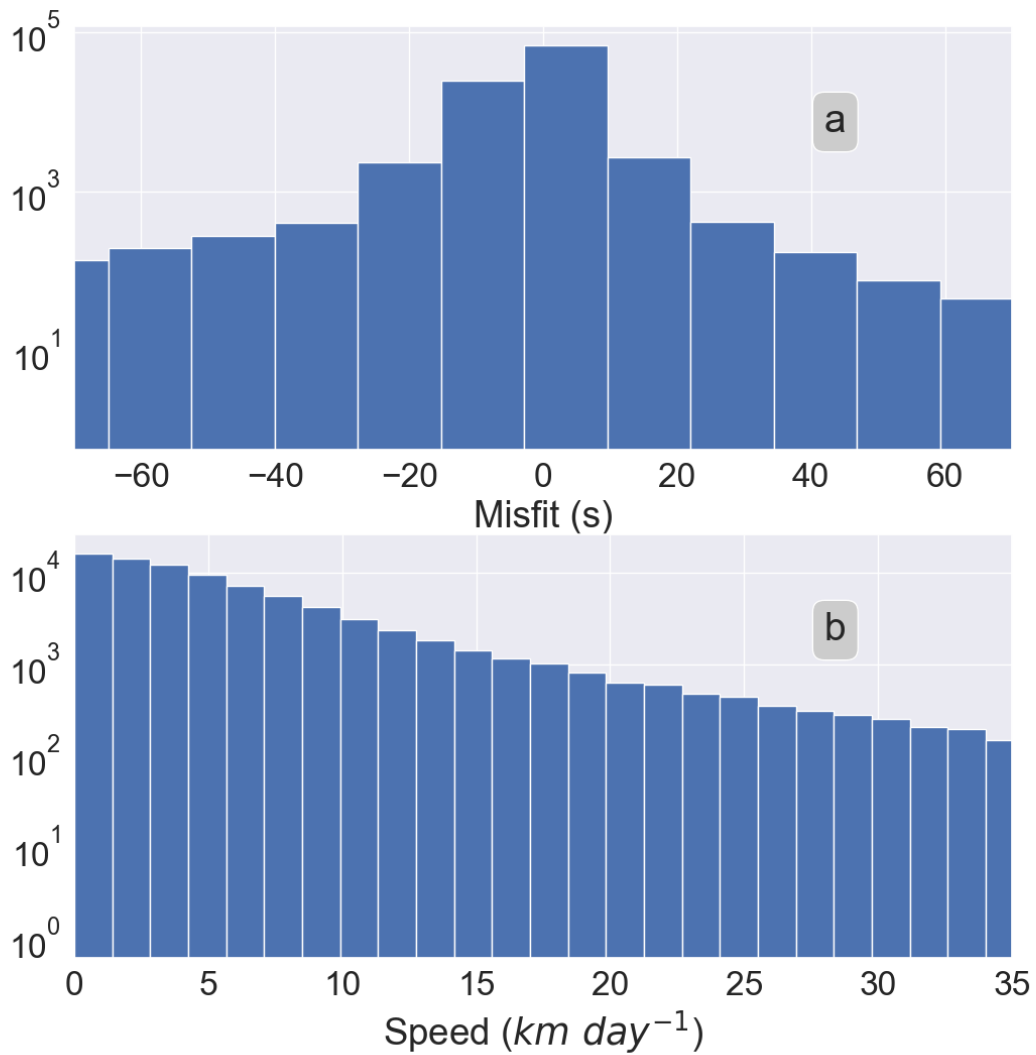


Figure 2.17. a) Histogram of TOA misfit of reconstructed Weddell Sea trajectories with available acoustic ranging. b) Histogram of calculated Weddell Sea trajectory speeds.

Chapter 3

Using existing Argo trajectories to statistically predict future float positions with a Transition Matrix

3.1 Abstract

The Argo array provides nearly 4000 temperature and salinity profiles of the top 2000 meters of the ocean every 10 days. Still, Argo floats will never be able to measure the ocean at all times everywhere. Optimized Argo float distributions should match the spatial and temporal variability of the many societally important things they observe, and this is challenging because float advection is difficult to predict. Using no external models, transition matrices based on existing Argo trajectories provide statistical inferences about Argo float motion. We use the 23 years of Argo locations to construct an optimal Transition Matrix that minimizes estimation bias and uncertainty. This Transition Matrix is then used to predict the probability of future float locations of the Core Argo array, the Global Biogeochemical Array, and the Southern Ocean Carbon and Climate Observations and Modeling (SOCCOM) array. A comparison of transition matrices derived from floats using Argos System and Iridium communication methods shows the impact of surface displacements, which is most apparent near the equator. Additionally, we demonstrate the utility of transition matrices for validating models by comparing the matrix derived from Argo floats with that derived from a particle release experiment in the Southern

Ocean State Estimate (SOSE).

3.2 Introduction

The endurance and economy of Argo profiling floats revolutionized how oceanographers practice their craft by providing unprecedented spatially distributed and frequent observations. Since the development of the first Argo prototypes almost 30 years ago (Davis et al., 1992), the global Argo array has grown to include more than 3800 active floats and has collected over 20 years of data (Roemmich, Dean and Alford, Matthew H and Claustre, Hervé and Johnson, Kenneth and King, Brian and Moum, James and Oke, Peter and Owens, W Brechner and Pouliquen, Sylvie and Purkey, Sarah and others, 2019). Core Argo floats observe temperature and salinity from 2000 m to the surface every 10 days. The recent integration of miniaturized nitrate, oxygen, pH, and optical sensors has enabled the development of the biogeochemical (BGC) Argo float (Johnson, Kenneth S and Plant, Joshua N and Coletti, Luke J and Jannasch, Hans W and Sakamoto, Carole M and Riser, Stephen C and Swift, Dana D and Williams, Nancy L and Boss, Emmanuel and Haëntjens, Nils and others, 2017). An array of these BGC Argo floats has been successfully deployed as part of the Southern Ocean Carbon and Climate Observations and Modeling (SOCCOM) project (Johnson and Claustre, 2016a; Talley, LD and Rosso, I and Kamenkovich, Igor and Mazloff, MR and Wang, J and Boss, E and Gray, AR and Johnson, KS and Key, RM and Riser, SC and others, 2019). Recently funded projects in multiple countries will deploy them globally through the BGC Argo Mission.

The substantially higher costs of BGC Argo floats relative to core Argo floats accelerates the need for informed strategic decisions about the optimal deployment positions for the BGC array. Any observing array should be optimized to sample the temporal and spatial scales of the phenomena of interest. Each variable measured by BGC floats has distinct scales of spatial and temporal variability. In the past, core Argo array deployment locations were selected to optimize a uniform distribution with a spacing of about $3^{\circ} \times 3^{\circ}$ separation in latitude and longitude (Davis,

1991; Roemmich, D and Boebel, O and Freeland, H and King, B and LeTraon, PY and Molinari, R and Brechner Owens, W and Riser, S and Send, U and Takeuchi, K and others, 1998). With increased prior knowledge of the ocean state, recent core Argo array proposals have suggested increasing array density where variability is higher, along the equator and in western boundary regions (Roemmich, Dean and Alford, Matthew H and Claustre, Hervé and Johnson, Kenneth and King, Brian and Moum, James and Oke, Peter and Owens, W Brechner and Pouliquen, Sylvie and Purkey, Sarah and others, 2019). The Biogeochemical Argo Implementation Plan (Johnson and Claustre, 2016a) explored spatial variability of measured BGC variables, concluding that initial deployments should try to achieve a uniform distribution, but finally suggesting that uniform deployments “be tested as more experience is obtained” (Johnson and Claustre, 2016a).

This raises the question: should we update recommended deployment strategies now that more BGC Argo floats have been deployed? Past studies have quantified the improvement that BGC float observations make to either modeled and calculated fields of an individual BGC variable for both random data distributions (Johnson and Claustre, 2016a; Majkut et al., 2014) and snapshots of past Argo array distributions (Ford, 2020; Kamenkovich et al., 2017). But optimal design strategies for the BGC Argo array deserve dedicated studies.

The work presented here addresses the largely operational concern of optimal ship-based float deployment strategy for the integrated core and BGC Argo arrays. We propose an array design strategy that consists of three innovations: first, the system will statistically predict the future location of currently deployed instruments to recognize the gaps in coverage at the time of deployment; second, the array strategy will account for the global inhomogeneities of BGC variables in spatial covariance and temporal variance by putting greater float density in regions of high temporal variability and low spatial covariance; finally, the optimal array strategy will account for the cross-covariance of the full BGC Argo float sensor suite by considering the additional constraint imposed by the prior knowledge of covarying properties. In this chapter, we approach the first question of float location prediction and leave the latter two questions for the subsequent chapter.

Several successful pilot projects have created regional BGC float arrays in regions that play an outsized role in global biogeochemistry (Morrison et al., 2015). The largest regional array, the SOCCOM program, deploys floats in unique provinces of the Southern Ocean by analyzing observed float trajectories and numerical particle release experiments (Talley, LD and Rosso, I and Kamenkovich, Igor and Mazloff, MR and Wang, J and Boss, E and Gray, AR and Johnson, KS and Key, RM and Riser, SC and others, 2019). This approach has potential shortcomings: visual analysis of previous Argo trajectories is subjective, and particle release experiments do not consistently reproduce actual Argo trajectories (Talley, LD and Rosso, I and Kamenkovich, Igor and Mazloff, MR and Wang, J and Boss, E and Gray, AR and Johnson, KS and Key, RM and Riser, SC and others, 2019).

Indeed, the ocean is a complex system, and Lagrangian trajectories can be challenging to predict deterministically. Figure 3.1 shows an example of historic float trajectories passing through a region off Cape Agulhas; there exists a potential time-varying bifurcation of float trajectories in this complex current system as shown by Boebel et al. (2003) and by Van Sebille et al. (2010). Argo float trajectories are dependent on the mesoscale eddy field, which models may not resolve. Eddies result from the intrinsic instabilities of the ocean, and, even in eddy-permitting models (Mazloff et al., 2010), the positions and timing of observed eddies can differ from modeled eddies. The rectified effect of these unresolved or omitted processes is typically stochastically parameterized in Lagrangian models (Van Sebille, Erik and Griffies, Stephen M and Abernathey, Ryan and Adams, Thomas P and Berloff, Pavel and Biastoch, Arne and Blanke, Bruno and Chassignet, Eric P and Cheng, Yu and Cotter, Colin J and others, 2018). Argo floats also experience ocean shear during their ascent and descent and are advected by winds and waves at the surface. Some Argo derived velocity products do not include these processes (Gray and Riser, 2014), or actively remove them (Sevellec et al., 2017; Ollitrault and Rannou, 2013; Gille and Romero, 2003).

Since Argo floats are not propelled, Argo managers should carefully choose deployment locations to optimize Argo array distribution throughout the lifetime of the float. To address

these challenges, we generate a statistical model, known as a Transition Matrix, from existing Argo array trajectories to predict the probability density function (PDF) of future float locations. This is done by using the large number of Argo float trajectories to diagnose the probability that a float transitions from one location to the other in a given time step (Fig. 3.2). Transition Matrices represent a potential complement to dynamical models because they contain a probabilistic representation of the complexities of the eddy field, ocean shear, and surface processes that models may miss. Transition Matrices are also a way of quantifying the information gained from visually inspecting previous float trajectories.

Transition Matrices are an established method (Markov, 1906; Van Sebille et al., 2012; Maximenko et al., 2012; Sevellec et al., 2017) to model semi-Lagrangian ocean drifters, and have been primarily applied to surface ocean drifters (Maximenko et al., 2012; Van Sebille et al., 2012) and surface drifter array design (Lumpkin et al., 2016). Sevellec et al. (2017) generated a Transition Matrix based on processed Argo trajectories obtained from the ANDRO dataset (Ollitrault and Rannou, 2013) to study the evolution of deep water masses. The ANDRO dataset estimates the displacements of Argo floats at their drift depth and removes displacements due to ocean shear and surface currents. However, these displacements are important for operational float prediction and should not be removed, so a new Transition Matrix was required.

In this paper, we first broadly explain the relatively simple theory of the construction and use of Transition Matrices in Section 3.4. The biases and uncertainties of the estimates Transition Matrices produce are sensitive to spatial and temporal spacing and are quantified in Section 3.5.1. In this section, we also define the criteria to define the optimal Transition Matrix that minimizes these biases and uncertainties based on the available datasets.

Transitioning to application, in Section 3.5.2, we use our optimal Transition Matrix to estimate the future density of the existing Core Argo array and the future array health of the Core Argo and SOCCOM Arrays. In Section 3.5.3, we consider the long-term fates of floats deployed from GO-SHIP cruise tracks and the ocean regions that upcoming cruises will populate with floats. Then, in Section 3.5.4, we quantify the different drift patterns of Argos System and

Iridium-equipped floats using Transition Matrices derived from these different float trajectories.

BGC Argo floats do not all carry the same sensor suite, and some BGC sensors are more ubiquitous in the ocean than others. Estimating where individual BGC sensors will observe the ocean is important for BGC Argo managers to determine where to deploy BGC floats and where the gaps will be in our BGC observing systems. In Section 3.5.5, we quantify the probability of sampling by BGC sensor type.

Finally, in Section 3.5.6, the Argo float Transition Matrix is compared against a Transition Matrix derived from the modeled particle trajectories derived from the Southern Ocean State Estimate (SOSE) (Mazloff et al., 2010). Modeled particles were programmed to profile to the surface every 10 days, similar to real Argo floats, and were advected by SOSE currents.

3.3 Data

These results use Argo float trajectories from the May 2021 Argo Snapshot (Argo, 2021). The data processing for Argo files excluded trajectories with the following conditions: poor quality flags for position, time, and pressure, along with floats with problematic file formats and floats that were not functioning in a manner consistent with their configured mission; drift depths shallower than 500 db and deeper than 1,500 db; floats that had unrealistic velocities or traveled over 500 nm in successive positions. After these quality control procedures, the total dataset comprised 2,167,492 positions collected by 14,331 unique floats. These trajectories were measured from May 13, 1998, to May 10, 2021, and spanned the globe from 77.7°S to 89.7°N.

Floats have used two different means for satellite communications: 8,506 floats used the Argos constellation, and 5,825 floats used Iridium (Fig. 3.3). The Iridium and Argos constellations of satellites are both low-Earth orbiting. Floats transmit their data more efficiently to Iridium satellites than to Argos; therefore, Iridium-enabled floats typically spend less than 1 hour at the surface compared to the 8 hours Argos-enabled floats usually spend at the surface.

To validate the results base on Argo float data, we also built an independent Transition Ma-

trix from a Lagrangian particle release experiment in the Southern Ocean State Estimate (SOSE) (Mazloff et al., 2010). SOSE is an eddy-permitting 0.16° configuration of the Massachusetts Institute of Technology General Circulation Model (MITGCM), which is fit by constrained least-squares to available Southern Ocean satellite and hydrographic observations. The current SOSE version (iteration 100) spans six years (2005-2010) and is calculated from 24.7°S to 78°S . For the particle experiment using Octopus (<http://github.com/jinbow/Octopus>), we randomly released 10,000 particles over the spatial domain and tracked their motion over the full six years of model output. The particles in this release experiment were programmed to drift at 1,000 meters, dive to 2,000 meters then surface once every ten days with an ascent mission and surface time similar to real Argo floats to simulate the effect of upper ocean shear on particle trajectories.

3.4 Methods

A Transition Matrix is a square matrix used to define the transitions of a discrete-time Markov Chain of a state vector in the state space. For our application, the state space is a discrete spatial grid S . In the real ocean, Argo float position is continuous; an approximation of this method is that it restricts the locations where Argo floats can be in the ocean to the positional grid cells of S . The state vector is the distribution of the Argo floats that we wish to study. The Markov Chain is the future probability of these originally deployed Argo floats at subsequent locations. The distribution of Argo floats (the state vector) could be a single float or the entire array. This is expressed mathematically as

$$\boldsymbol{\rho}(t+k) = \mathbf{H}\boldsymbol{\rho}(t), \quad \mathbf{H} = \mathbf{Q}^k \quad (3.1)$$

where \mathbf{Q} is a square $S \times S$ matrix, $\boldsymbol{\rho}(t)$ is a column vector in the state space of dimension $S \times 1$ at a given timestep t , and \mathbf{H} is the product of \mathbf{Q} multiplied by itself k times and defines the probability of transition to the k^{th} timestep. The Transition Matrix can then give the probability of an initial array of Argo floats, $\boldsymbol{\rho}(t)$, propagating to a future state at the k^{th} timestep, $\boldsymbol{\rho}(t+k)$.

The process for creating a Transition Matrix from Lagrangian data is well described (Sevellec et al., 2017), so we provide only a brief explanation here.

First, we spatially and temporally quantize the trajectory data set by a defined timestep and spatial grid (Fig. 3.2). These choices define the dimension of the state space S and the nature of the discrete-time Markov Chain. For our application, these choices determine the spatial grid of latitude and longitude that Argo floats transition between and the timestep in days of these transitions.

A consideration of space-time resolution is the representativeness of positioning: the approximation of projecting continuous Argo trajectories onto a discrete spatial grid increases when the grid cells are larger. This approximation can lead to biases and uncertainties in estimating future float distribution produced by a Transition Matrix. For example, if the spatial grid size is too large, some floats may enter along the edge of grid cells and quickly leave; this will cause a bias in transition statistics compared with floats that transit across the entirety of the grid cell.

Decreasing grid cell size reduces position discrepancies between grid centers and edges but can also lead to fewer transition data per grid cell as smaller grid cells will typically have fewer floats pass through them. Transition Matrices are naive to all dynamics and need many data to resolve skillful transition statistics. Section 3.5.1 explores the trade-offs between grid cell size, timestep, and data density. The distribution of floats relative to the nature of the velocity field is another potential bias; an unequally spaced float array placed in fields of inhomogeneous diffusivity may infer biased velocity statistics that do not resolve the mean (Freeland, 1975; Davis, 1991). For example, many floats placed in the middle of a random velocity field with no mean flow may appear divergent due to simple Brownian motion. For these calculations, we assumed the float density to be homogeneous.

Float trajectories assimilated into the Transition Matrix must be temporally statistically independent. Successful floats carry out long missions (five years or more), much longer than any Transition Matrix considered in this analysis. Therefore, these longer float trajectories are broken

down into shorter trajectories equal to the timestep of the Transition Matrix. Figure 3.2 shows the segments corresponding to these shorter trajectories as black circles. Our algorithm tolerated small overlaps between the shorter trajectories to increase data density. The time separation between the start of the smaller trajectories was the greater of either 30 days (Gille and Romero, 2003) or one third of the Transition Matrix time step; e.g., the time separation for the start of trajectories must be 30 days for a 60 day timestep and 60 days for a 180 day timestep.

We now describe how we quantify the transition probability for an arbitrary spatial grid cell (which we call Cell_{blue} in Figure 3.2) and must be repeated for all spatial Grid Cells in the domain. The number of spatial grid cells is equal to S , the dimension of the state space. First, all the independent Argo profiles that start in Cell_{blue} are identified (colored circles in Figure 3.2) and the total number of starting positions is defined as N_{blue}^{total} (blue circles in Figure 3.2). Figure 3.2 shows the float trajectory segments that start in Cell_{blue} as blue lines. We next count the total number of floats that start in Cell_{blue} and have ended up in the surrounding grid cells. In Figure 3.2, the grid cells connected to Cell_{blue} via trajectories are Cell_{green} , Cell_{red} , and Cell_{yellow} with number of transitions into each grid cell of N_{blue}^{green} , N_{blue}^{red} , and N_{blue}^{yellow} respectively. The colored circles surrounding the “+1” text in Figure 3.2 denote a trajectory segment that has ended in a grid cell and are included in the total count of transition statistics. It is possible (and, depending on the location of the ocean and the grid cell size, probable) for floats to stay in the grid cell they started in. The blue circle surrounding the “+1” text in Figure 3.2 represents a trajectory segment that started and stayed in Cell_{blue} . Therefore, in this example, $N_{blue}^{blue} = 1$.

The probability of a float transitioning from Cell_{blue} (arbitrarily of index k) to Cell_{red} (arbitrarily of index q) is equal to $N_{blue}^{red} / N_{blue}^{total}$ and is the value of the Transition Matrix in the index k^{th} column and q^{th} row. The probability of a float staying in the grid cell it started in (the probability of a float transitioning from the Cell_{blue} to Cell_{blue}) is found on the diagonal of the Transition Matrix and calculated as $N_{blue}^{blue} / N_{blue}^{total}$. Our model does not consider the possibility of float failure: floats can neither be created nor destroyed. Consequently, we impose a conservative tracer constraint such that all columns of the Transition Matrix sum to one, and the entire column

vector is scaled accordingly. For dynamical reasons, the Transition Matrix is very sparse: floats in the middle of the Atlantic have no chance of transitioning to the Pacific in weeks or months. The total number of nonzero rows in each column will equal the number of grid cells into which floats transition during the timestep. After performing this calculation for all spatial grid cells, the resultant matrix is $S \times S$.

To quantify the biases and uncertainties of the Transition Matrix, we considered the performance of transition matrices at several different spatial and temporal resolutions. Timesteps ranged from 30 to 180 days, and grid cells ranged in size from $1^\circ \times 1^\circ$ to $4^\circ \times 6^\circ$. Table 3.1 lists these timesteps and gridsizes.

Low trajectory density or errors in the trajectory dataset can create isolated grid cells disconnected from the rest of the Transition Matrix. These points have no predictive value and are removed. Intuition regarding the connected float distribution modes can be gained through eigenvector decomposition and analysis (Miron et al., 2019; Froyland et al., 2014); regions defined by eigenvectors with eigenvalues close to one tend to have closed circulations and are difficult for floats to leave. To eliminate isolated grid cells, we required all 50 gravest eigenvectors to have at least 3 grid cells and a total number of at least 3 transitions in each grid cells of the Transition Matrix. The limiting values for minimum grid cells and transitions were chosen empirically based on the data density.

Ocean dynamics are seasonal; therefore, the statistics of where floats are advected to must also have seasonal variability. The Argo trajectory dataset is not sufficiently large to resolve seasonal dynamics, and, by necessity, we assumed these statistics are stationary in time. This assumption is a fundamental gap in our analysis, adding uncertainty to our estimates.

Expanding this statistical prediction for two special cases relevant to the Argo array, the probability of a float sampling a given region within a range of timesteps is expressed as

$$\mathbf{P}^{total} = \sum_{k=1}^n \mathcal{Q}^k \boldsymbol{\rho} \quad (3.2)$$

where \mathbf{P}^{total} is the chance of sampling and n is the number of timesteps considered. And, the probability of a float sampling a given region within all timesteps is expressed as

$$\mathbf{P}_j^{range} = \Pi\{(\mathbf{Q}^k \boldsymbol{\rho})_j : k = 1, \dots, n\} \quad (3.3)$$

where the product is taken elementwise over the product $\mathbf{Q}^k \boldsymbol{\rho}$. The first statistical moment of a generic spatial grid k can be expressed as

$$R_j = \sum_{i=1}^M q_i r_i, \quad (3.4)$$

where r_i is the relative displacement vector from spatial grid j to spatial grid i , and q_i is the probability of transition from spatial grid j to spatial grid i . The second statistical moment of the generic grid k can be expressed as the following:

$$\mu_j = \sqrt{\sum_{i=1}^M q_i (R_j - r_i)^2}. \quad (3.5)$$

These calculations are the first and second moments of a probability distribution. They can be interpreted as the expected value and variance (the tendency for Lagrangian particles to disperse) for a linear probability distribution. These metrics may not be appropriate in regions where a strong bifurcation in the advection statistics predicts two (or more) distinct and narrowly defined probability distributions. Fortunately for our analysis, most of the ocean does not behave this way.

Standard Error relates the second moment of the probability distribution to the number of realizations. It quantifies the quality of our Transition Matrix as an estimator of the most probable trajectory. Standard Error is written as the following

$$\mu_{\bar{j}} = \frac{\mu_j}{\sqrt{N_j^{total}}}, \quad (3.6)$$

where μ_j is the second moment from Equation 3.5, and N_j^{total} is the Transition Density (N_{blue}^{total} in Fig. 3.2).

Standard Error also determines the statistical significance of differences between distributions in a Z test. The Z test is defined as

$$Z_j = \frac{\bar{X}_j - R_j}{\mu_j}, \quad (3.7)$$

where \bar{X} is the sample mean of the j^{th} grid cell, R_j is the first moment of the j^{th} grid cell.

3.5 Results and Discussion

Previous BGC Argo array design studies have considered both the actual Argo array at snapshots in time and randomly distributed float arrays (Johnson and Claustre, 2016a; Majkut et al., 2014; Ford, 2020; Kamenkovich et al., 2017). The omission of float displacement has been a major limitation. Accounting for this float motion is critical for planning arrays over timespans long enough for instruments to drift significantly, as is the case with Argo. Ocean currents, and the trajectories of floats carried by these currents, follow predictable patterns. Inspired by this, we consider the construction and assessment of a Transition Matrix approach for float prediction in several applications: section 3.5.1 quantifies the biases and uncertainties of transition matrices of various spatial and temporal resolutions and present our justification criteria for the optimal Transition Matrix; section 3.5.2 predicts the future distribution of the existing Argo array; section 3.5.3 predicts the future distribution of Argo floats deployed from planned GO-SHIP cruises within the next 5 years; section 3.5.4 estimates the regions of convergence and divergence for Argos System and Iridium floats; section 3.5.5 predicts the future sampling of existing BGC Argo floats broken down by sensor class; section 3.5.6 estimates the effective diffusivity of the SOSE model with derived Transition Matrices.

3.5.1 Bias and Uncertainty Quantification

Although computationally straightforward, a limiting assumption of the Transition Matrix is that it is a linear approximation to a nonlinear process (Lagrangian Argo trajectories in the ocean) (McAdam and van Sebille, 2018). Given a dataset of finite size, the choice of resolution and timestep is fundamentally a trade-off of model bias versus model uncertainty. Using short space and long time scales reduces the impact of errors from the linearity assumption (less bias). But, these dimensional choices also reduce the amount of data available to construct the Transition Matrix (more uncertainty). As such, the timestep and grid spacing, which define the Transition Matrix, are factors that determine the accuracy of Transition Matrix prediction.

A representation of the difference in estimates derived from approximating a longer time step Transition Matrix by multiplying many short timestep transition matrices together is shown for an example grid cell in the Antarctic Circumpolar Current (ACC) in Figure 3.4 a and b. While this is only one example, it illustrates the uncertainty in the linear approximation made in this method: approximating long-term float behavior with short-term float statistics will result in a smoothed PDF distribution. Indeed, this approximation-induced smoothing can change the first moment (Eq. 3.4) of the future float PDF. Over long durations, these differences compound (Figure 3.4c and d); in the aggregated statistics of this figure, misfit in mean transition and standard deviation generally decrease with increasing timestep. The slope of the misfit decrease is similar among two groups of resolutions: resolutions of $1^\circ \times 1^\circ$, $1^\circ \times 2^\circ$, $2^\circ \times 2^\circ$, and $2^\circ \times 3^\circ$ of latitude and longitude; and resolutions of $3^\circ \times 3^\circ$, $4^\circ \times 4^\circ$, and $4^\circ \times 6^\circ$ of latitude and longitude. The former had a lower misfit at the shortest timestep, and a shallower slope of misfit decrease with increasing timestep. In comparison, the latter had a higher misfit at the shortest timestep and showed a steeper misfit decrease with increasing timestep. The misfit of the higher resolution group also plateaued at the 90-day timestep.

An example of the differences introduced by choices in spatial resolution is shown for the same example grid cell in the ACC (Fig. 3.5a and b). These differences have also been

quantified for transition matrices of different grid resolutions and time steps (Fig. 3.5c). Mean misfit is proportional to timestep and inversely proportional to resolution, and the misfit slope is generally lowest between the 60 and 90 day timestep.

Figure 3.6 shows standard error (Eq. 3.6) for 2 matrices of differing resolution. Spatial area decreases geometrically with increasing resolution, and, broadly speaking, because the Core Argo distribution is homogeneous, the number of Argo trajectories through a grid cell will be proportional to the grid cell size. Unsurprisingly, we see from this example that the lower resolution Transition Matrix has a lower mean standard error and will produce estimates of the expected value and variance (Equations 3.4 and 3.5) with less uncertainty.

For all transition matrices considered, the mean standard error is proportional to resolution and timestep except for the $1^\circ \times 1^\circ$ 30 day Transition Matrix, which has a lower mean standard error than its $1^\circ \times 2^\circ$ 30-day counterpart (Fig. 3.5 d). This is due to the specific criteria for Transition Matrix construction that exclude certain high variance regions from the $1^\circ \times 1^\circ$ Transition Matrix (namely the southern ACC where trajectory variance is high and data density is low).

Comparing specific matrices and timesteps, we notice Figure 3.4c shows substantial misfit improvement between the $1^\circ \times 2^\circ$ and the $2^\circ \times 2^\circ$ resolutions, but little improvement between the $2^\circ \times 2^\circ$ and the $2^\circ \times 3^\circ$ resolutions, as well as a curvature minimum at the 90 day timestep $2^\circ \times 2^\circ$ Transition Matrix. Figure 3.4d shows a misfit minimum for the $2^\circ \times 2^\circ$ resolution Transition Matrix. Figure 3.5c shows a misfit plateau between the 60 and 90 timestep in the $2^\circ \times 2^\circ$ resolution. For these reasons, the $2^\circ \times 2^\circ$ spatial resolution and 90 day timestep is considered the Optimal Transition Matrix configuration and was used in several subsequent calculations.

The transition density of each grid cell (N_{blue}^{total} in Figure 3.2) of the Optimal Transition Matrix dataset (Fig. 3.7) shows near-global coverage with 8037 grid cells. Transition density suffers primarily in ice-covered regions, where data are sparse, and selection criteria often reject data. The mean number of transitions per grid cell is 76.3 ± 43.9 . The mean transition and

variance ellipse of the derived Transition Matrix (plotted in Fig. 3.8) resolve the major features of ocean circulation. Regions of large mean transition are also regions of large observed kinetic energy. The 3-year mean Lagrangian pathways of each grid cell are computed from the Transition Matrix (Fig. 3.9) and show the first statistical moment (Eq. 3.4) at 12 timesteps of the Markov Chain. The overall pattern of this figure generally resembles the known circulation features in the ocean and closely resembles the 1000 db absolute geostrophic streamfunction maps from Gray and Riser (2014).

3.5.2 Argo Array Prediction

Starting from the actual Argo float distribution of May 10, 2021, with 3262 floats, the Transition Matrix projected the float array density forward for one and two years. We show the current and projected float spacing of the array in Figure 3.10 and resulting projected density maps for the Pacific, Atlantic, and Southern Ocean in Figures 3.11, 3.12, and 3.13 respectively. Argo floats older than 4 years were removed from the array estimate due to the high likelihood of poor sensor performance or float failure, as is a common practice by Argo managers. From these projections: large and growing holes in array distribution exist in the north-central and eastern-equatorial Pacific; sparse distributions exist in the Benguela Current and the middle of the North Atlantic subtropical gyre; and the Pacific sector of the Southern Ocean will become sparsely observed. We recommend ships transiting or conducting operations in these areas in 2022 or 2023 prioritize Argo deployments.

As another example of the utility of transition matrices, we demonstrate an improvement of the Density/Age map - currently calculated and used by Argo managers (<https://www.ocean-ops.org/board>) as a metric of core Argo array health. Repopulating old or sparse regions of the network is a goal of Argo managers; the Density/Age map displays the density of Argo floats within a grid cell divided by the average age of those Argo floats. Array health maps use a present snapshot of float distribution and do not make future estimates of what the Density/Age map will be in the future. Procurement and cruise organization occur many months before putting a

float in the water, and estimates of how Argo array health will change in the future may improve planning. The Optimal Transition Matrix can propagate the Density/Age map forward in time to assess the future distribution of the array at the time of deployment, which has been done for the Core Argo and SOCCOM arrays (Fig. 3.14). This analysis shows that core Argo array health deficits exist in the Southern Ocean and off the east coast of Africa.

Argo float location prediction is an observing system priority. Because of this, we have added our transition matrices to the Argovis web app and database (<https://argovis.colorado.edu/ng/covar>) (Tucker et al., 2020) to allow access and to predict Argo float locations. The website displays the statistical prediction of Argo float up to 5 years in the future (the designed float lifetime). Figure 3.1 shows an example of the website.

3.5.3 Estimating Future Array Density from Float Deployments Along Set Ship Tracks

Argo floats are often deployed from research ships of opportunity, with the ship tracks set by other projects. BGC Argo deployments are preferably from projects such as GO-SHIP that provide high quality biogeochemical data that can be used as a reference to validate BGC sensor calibrations. To determine what fraction of the ocean future GO-SHIP cruises may populate with floats, grid cells containing GO-SHIP cruise tracklines were initialized with floats at the time these GO-SHIP cruises are scheduled to sail (Table 3.2 and red lines in Figure 3.15). The optimal Transition Matrix was used to estimate ocean sampling in the next 5 years based on these deployments. Typically, only a handful of BGC floats are deployed on any cruise. By initializing all grid cells along the trackline, we are showing the greatest possible extent.

The resultant sampling densities and mean Lagrangian pathways (Fig. 3.15) show that in many of the regions floats are deployed, floats do not travel very far during their lifetimes. Based on this projections, GO-SHIP alone cannot populate the world with floats. Holes will exist in the eastern and western equatorial Pacific, The Gulf of Mexico, the Gulf Stream, and the western tropical Indian Ocean. To achieve uniform distributions of the Core Argo and BGC Argo arrays,

ships of opportunity will be needed in these areas for deployments .

3.5.4 Iridium vs. Argos System Communications

Long-term differences in Argos and Iridium equipped float trajectories are well known to Argos data managers (Robbins, 2021). The Transition Matrix methodology allows us to quantify, for the first time, the implications of the increased surface time of Argos enabled floats distributed over many profiles. Argos floats transmit data through 2 distinct satellite constellations: Iridium and the Argos system. Floats have the hardware to transmit on one or the other, but not both. Data transmission is much faster via the Iridium constellation. Consequently, Iridium-enabled floats spend about 15 minutes at the surface compared to their Argos counterparts which can take up to 12 hours. Surface velocities are also different from velocities at 1000m depth (the typical Argos drift depth), and Argos floats are undrogued and advected by winds and waves while transmitting.

Dividing the full trajectory dataset into only Argos or Iridium enabled trajectories results in significantly less data density for both; we accommodate this by reducing spatial resolution. Transition matrices were constructed using $2^{\circ} \times 3^{\circ}$ grid cells of latitude and longitude and a 180 day timestep. The statistical difference between the Argos and Iridium enabled transition matrices is subtle and could not be distinguished from the null hypothesis by a Z test (Eq. 3.7).

Transition Matrices were multiplied by themselves 15 times to estimate the transition statistics after 8 years - the upper range of current Argos float lifetimes - to highlight the differences in transition statistics. We then uniformly seeded the world ocean with theoretical Argos floats and considered the differences in resultant future float densities predicted with the Transition Matrix (Fig. 3.16). In the long-term estimates, the relative density of Iridium-enabled floats stays relatively uniform, and the regional differences in float density do not have a spatial structure consistent with known circulation. In contrast, the Argos System-derived prediction shows strong aggregation in the middle of the subtropical gyres and relative divergence of floats along the equator. This corresponds to divergence in surface currents similar to transition matrices derived

from surface drifters (Van Sebille et al., 2012).

This analysis has several implications. Firstly, Argos-enabled floats do not stay on the equator because they are more susceptible to the divergent Ekman transport caused by easterly trade winds. In the Roemmich, Dean and Alford, Matthew H and Claustre, Hervé and Johnson, Kenneth and King, Brian and Moum, James and Oke, Peter and Owens, W Brechner and Pouliquen, Sylvie and Purkey, Sarah and others (2019) vision of the future Argo array, the equator is a prioritized region for increased float density. This analysis supports the decision made by Argo managers that floats deployed near the equator be equipped with Iridium communications to prevent them from being advected off the equator during their time at the surface. Secondly, Argos- and Iridium-enabled floats move differently, especially on long timescales: the performance of hybrid transition matrices derived from both types of floats may be degraded, primarily in equatorial regions.

For this reason, Argos System and Iridium transition matrices are provided separately in our data products. However, hybrid transition matrices' improved resolution and data density may offer enhanced performance for shorter duration predictions. Because the current Argo fleet is composed of Iridium- and Argos-enabled floats, the hybrid matrix has general utility for predicting Argo fleet dynamics. Further, the innovation of new sensors has increased the quantity of data that BGC floats transmit; the increased data requires an average time of an hour at the surface (Riser, 2022), and, depending on the sensor suite, traditional core Argo Iridium-enabled float statistics may underrepresent surface advection.

3.5.5 BGC Argo Sampling Predictions

Temperature and salinity sensors are ubiquitous within the Argo fleet, but recently developed and more expensive BGC sensors are not. BGC float managers need to know where specific BGC sensors will be in the future when planning deployment cruises.

Motivated by the spatial inhomogeneities of BGC sensors, we estimate the future probability of sampling by sensor class. For these calculations, we used a Transition Matrix with

$3^\circ \times 3^\circ$ grid cells of latitude and longitude and a 90 day timestep to match the designed separation of the Core Argo array (Roemmich, D and Boebel, O and Freeland, H and King, B and LeTraon, PY and Molinari, R and Brechner Owens, W and Riser, S and Send, U and Takeuchi, K and others, 1998). This is a departure from the Optimal Transition Matrix of Section 3.5.1 and is used to match maps like Figure 3.10 commonly used by Argo managers.

Using equation 3.2, the probability of current Argo sensors sampling in the next year is inhomogeneously distributed by various sensor classes (Figs. 3.17–3.18). Temperature and salinity sensors achieve global sampling over the course of a year (Fig 3.17). Oxygen sensors are the second most widely deployed, with a mean chance of any annual sampling of 35.5% over the spatial domain and no ocean regions omitted (Fig. 3.18 a). Chlorophyll is the third most widely deployed sensor, with a mean chance of any annual sampling of 21.8% over the spatial domain and a potential hole in the northeast Atlantic Ocean (Fig. 3.18 b). Finally, pH is the most sparsely deployed sensor, with a mean chance of sampling any annual sampling of 15.8% over the spatial domain and holes in the Indian and northwest Pacific Oceans (Fig. 3.18 c).

Another important metric to consider is the regions of the ocean that will be sampled year-round. Historically, BGC variables have only been sampled during hydrographic cruises with follow-up cruises years or decades later. Indeed, BGC float observations in the Southern Ocean have led to discoveries about the seasonal variability of BGC variables following fully resolved seasonal observations (Gray et al., 2018). Equation 3.3 was used to calculate the chance of year-round observation for temperature and salinity observations (Fig 3.17). Temperature and salinity have the highest probability of year-round sampling, with a mean chance of 44.9% of the domain covered. The BGC array is not yet a fully developed network, and year-round sampling has thus far rarely been achieved. The year-round oxygen sampling has a chance of 1.2% of the domain covered. Chlorophyll and pH have a substantially smaller than 1% chance of year-round sampling in the domain.

Strong currents, such as the ACC, require a uniform density of float coverage to achieve year-round sampling (Davis, 1991), and creative methods such as creating regional composites

of observations to resolve seasonal signals (Gray et al., 2018) may be necessary for some time.

3.5.6 SOSE Comparison

Models, including the Southern Ocean State Estimate (SOSE), have been used to predict Lagrangian trajectories for both operational (Talley, LD and Rosso, I and Kamenkovich, Igor and Mazloff, MR and Wang, J and Boss, E and Gray, AR and Johnson, KS and Key, RM and Riser, SC and others, 2019) and scientific (Tamsitt, Veronica and Drake, Henri F and Morrison, Adele K and Talley, Lynne D and Dufour, Carolina O and Gray, Alison R and Griffies, Stephen M and Mazloff, Matthew R and Sarmiento, Jorge L and Wang, Jinbo and others, 2017) applications. However, models generally do not reproduce Argo float dispersion well, even when the Lagrangian particles simulate the full Argo 10-day cycle (Talley, LD and Rosso, I and Kamenkovich, Igor and Mazloff, MR and Wang, J and Boss, E and Gray, AR and Johnson, KS and Key, RM and Riser, SC and others, 2019). As a validation for both the SOSE model and the transition matrices, we compared Transition Matrices derived from SOSE model-based trajectories with the Argo-derived Transition Matrices.

Transition matrices composed of $1^\circ \times 2^\circ$ and $4^\circ \times 6^\circ$ grid cells of latitude and longitude with a 180 day timestep were used to recreate the upper and lower limits of available grid resolution for this region. Across both resolution levels, the zonal mean transitions in the ACC were greater in the SOSE-derived matrices. The $1^\circ \times 2^\circ$ matrix comparison had a 1 cm s^{-1} increase in the ACC while the 4×6 comparison had a 0.5 cm s^{-1} increase. The second moment was also compared (Eq. 3.5, Fig. 3.19) and shows that SOSE consistently under-represents ACC Lagrangian diffusion in the high-resolution case with a mean difference of $-6.8 \times 10^{-1} \pm 6.2 \times 10^{-1} \text{ cm}^2 \text{ s}^{-2}$, and well resolves ACC diffusion in the low-resolution case with a mean difference of $0.00 \pm 5.8 \times 10^{-1} \text{ cm}^2 \text{ s}^{-2}$.

SOSE is an eddy-permitting model but does not have sufficient resolution to fully resolve high-latitude eddies. This analysis suggests that SOSE ACC kinetic energy, at high resolution, is concentrated in the mean flow and does not sufficiently cascade into smaller-scale features; this

manifests in lower diffusivity. The low-resolution case seems to have the effect of smoothing these differences. From this analysis, scientific conclusions derived from SOSE Lagrangian particle statistics should only be considered accurate for coarse resolution studies. Changes in parameterized diffusivities in the offline Lagrangian model Octopus could potentially address these problems, but these changes have not been studied.

3.6 Conclusion

In this paper, we have explained, justified, and tested the construction of a Transition Matrix for Argo float location prediction, following the surface drifter work by Van Sebille et al. (2012). Our work was done in the broader context of BGC Argo global array design, and a companion paper will describe an optimal float deployment algorithm.

After quantifying a wide range of temporal and spatial biases and uncertainties, we have concluded that using the available Argo trajectory data, the Transition Matrix constructed from a $2^\circ \times 2^\circ$ spatial resolution at a 90 day timestep is optimal. This Transition Matrix is used for: core Argo predictions, GO-SHIP deployment predictions, an interactive website (<https://argovis.colorado.edu/ng/covar>), and array health products. We will update the Transition Matrix as more trajectory data are made available and is available as supplemental material for this paper. This Transition Matrix is a hybrid of Argos- and Iridium-enabled float trajectories.

We have shown a significant difference in transition matrices derived from floats equipped with different communication systems. We recommend that floats deployed in equatorial waters use Iridium communications. We additionally provide supplementary material for the Argos and Iridium transition matrices for investigators who wish to make specific predictions based on communication type.

Finally, we compared the Argo transition matrices to transition matrices derived from a particle release experiment in the SOSE model. We found that the overall mean particle transition in the ACC was greater in the SOSE Transition Matrix, and particle diffusion was

too low in the SOSE Transition Matrix at high resolution but consistent with the Argo-derived Transition Matrix at low resolution. We hypothesize this is because SOSE does not fully resolve the mesoscale eddy field.

The ever-growing Argo float dataset will continue to improve both the statistical accuracy and resolution of transition matrices. However, we find that the array is already of sufficient size for Transition Matrix construction, enabling significant insights into difficult questions that BGC Argo managers face now. BGC Argo floats offer new technology to answer questions of critical societal importance. We hope the Transition Matrix tools presented here will contribute to the ongoing community conversation regarding optimal array design.

3.7 Acknowledgements

This work was supported by the SOCCOM project under NSF Award PLR-1425989 and Global Ocean Biogeochemical Array (GO-BGC) under NSF Award OCE-1946578. Co-authors acknowledge NSF EarthCube Award 1928305. EvS was supported by the Netherlands Organization for Scientific Research (NWO), Earth and Life Sciences, through project OCENW.KLEIN.085. We thank Dr. Isa Rosso for providing SOSE Lagrangian particle trajectories. Chapter 3, in full, has been submitted for publication of the material as it may appear in *Journal of Atmospheric and Oceanic Technology*, 2022, Chamberlain, P. M., Talley, L. D., Mazloff, M. R., van Sebille, E., Gille, S. T., Tucker T., Scanderbeg, M., & Robbins, P., American Meteorological Society 2022. The dissertation author was the primary investigator and author of this paper.

Table 3.1. Spatial and temporal resolution of transition matrices calculated.

Timestep (days)	Grid size (lat × lon)
30	1° × 1°
60	1° × 2°
90	2° × 2°
120	2° × 3°
160	3° × 3°
180	4° × 4°
	4° × 6°

Table 3.2. Planned GO-SHIP Cruises

Cruise Section	Year Planned
I5	2022
A12	2022
SR4	2022
A13.5	2022
P2	2022
P4	2022
I9	2023
I8	2023
A16	2023
P16	2024
P15	2024
S4P	2025
ARC1	2025
P6	2026

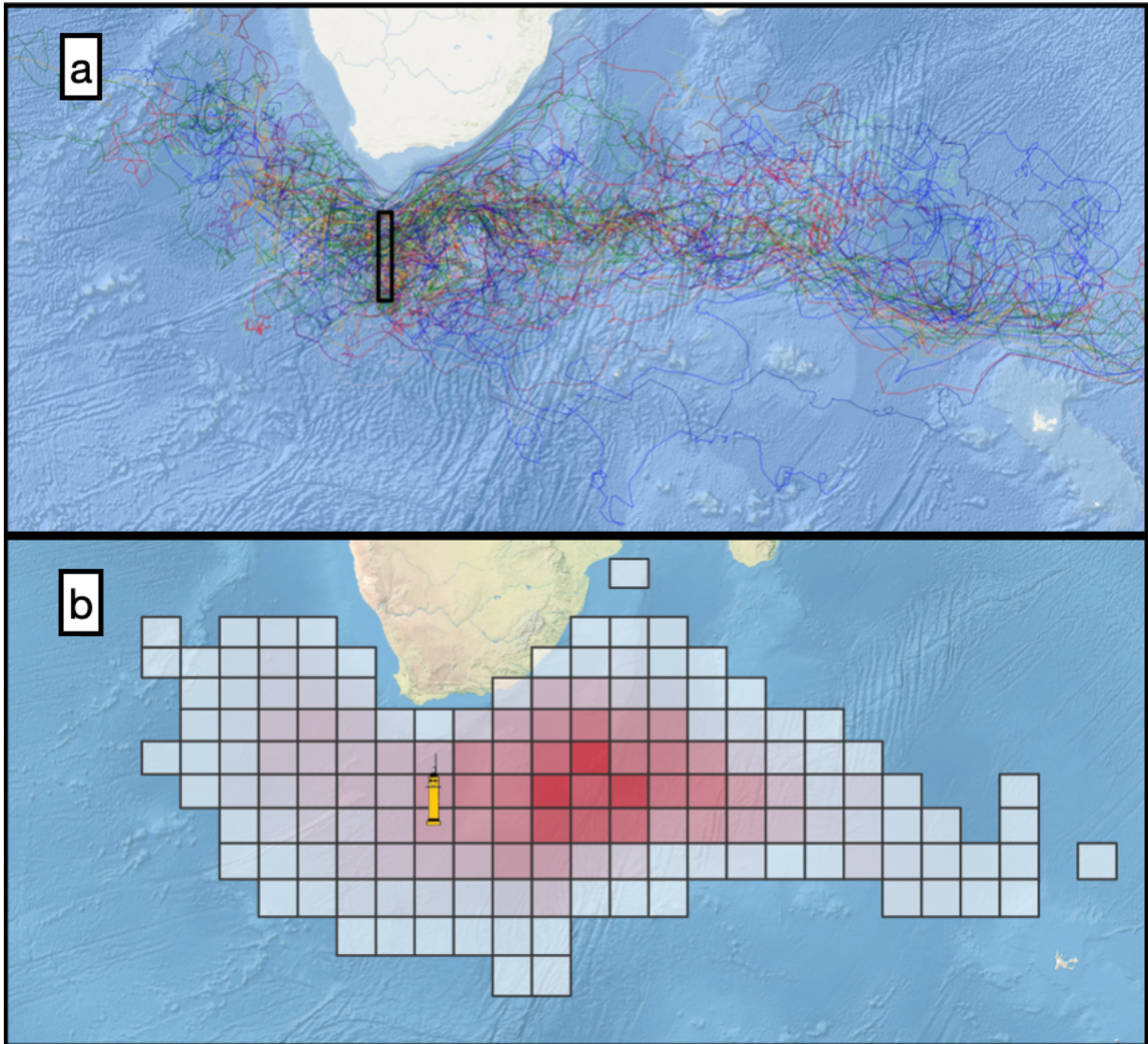


Figure 3.1. a) Historical Argo trajectories off Cape Agulhas passing through black box. White shading indicates land, colored lines indicate individual float tracks. b) Example of float prediction website (<https://argovis.colorado.edu/ng/covar>) for float in same region. Base of small Argo symbol represents deployment location, colored grid cells represents Argo float probability density function after 240 days with initial deployment at float icon.

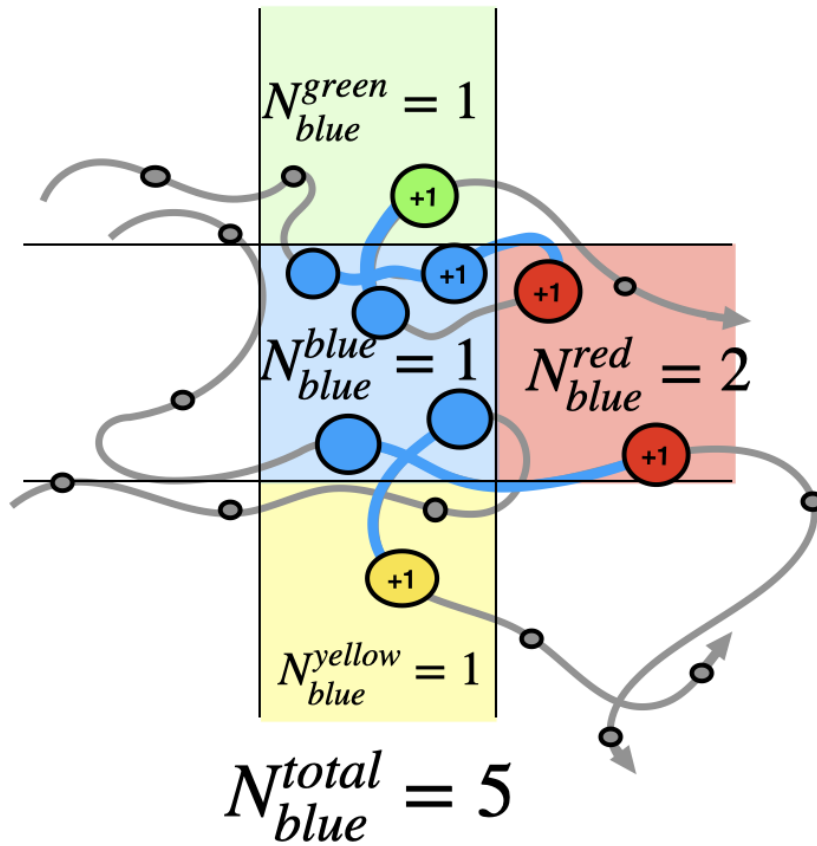


Figure 3.2. Cartoon of Transition Matrix calculation for an arbitrary $Cell_{blue}$. Gray lines represent hypothetical paths of 3 distinct floats, and circles represent independent float profile locations given Transition Matrix timestep. The timesteps are long enough (e.g. greater than 30 days) that each segment can be considered independent even if they come from the same float. Black squares represent grid cells. Blue lines represent trajectory segments originating from $Cell_{blue}$. Colored circles and “+ 1” text represents trajectory segments that ended in correspondingly colored grid cells. Small gray circles represent float positions that are not included in the transition statistics for $Cell_{blue}$. Total probability for each element of the Transition Matrix will equal the total number of transitions within a grid cell divided by the total number of transitions in the dataset (N_{blue}^{total}).

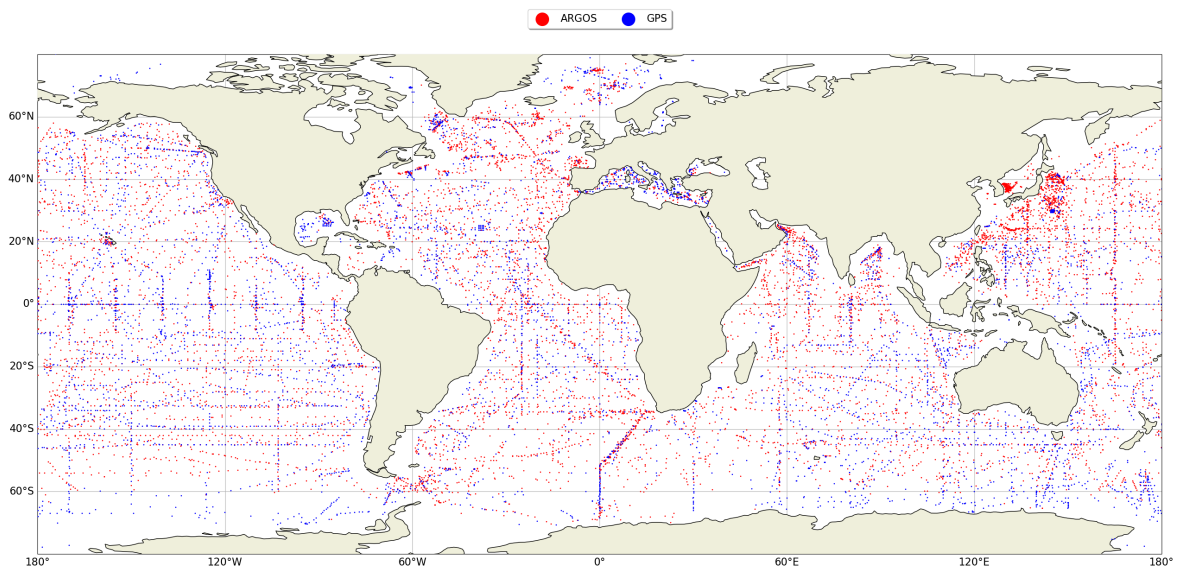


Figure 3.3. Initial deployment locations for all Argo floats in the dataset, using both Argos System (red) and Iridium (blue) communications.

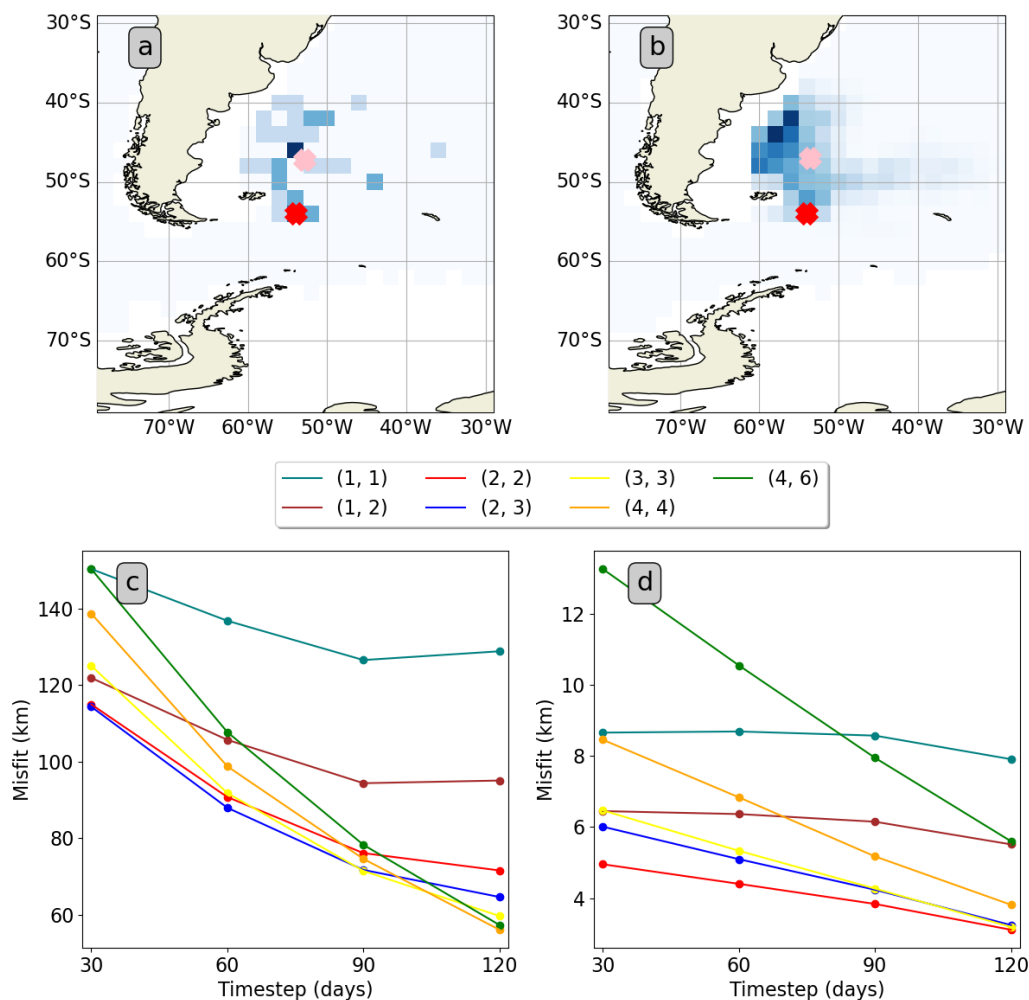


Figure 3.4. Examples of $2^\circ \times 2^\circ$ 180 day transition probabilities starting from red X for (a) a native 180 day Transition Matrix, and (b) a 30 day Transition Matrix multiplied by itself 5 times. Blue shading represents transition probability and pink X represents spatial mean of all transition probabilities. Beige shading represents land. (c) Difference in the first statistical moment (Eq. 3.4) of Transition Matrices of various timesteps and Transition Matrix with 180 day timestep of same resolution. (d) Difference in the second statistical moment (Eq. 3.5) of Transition Matrices of various timesteps and Transition Matrix with 180 day timestep of same resolution. Colored lines represent different resolutions.

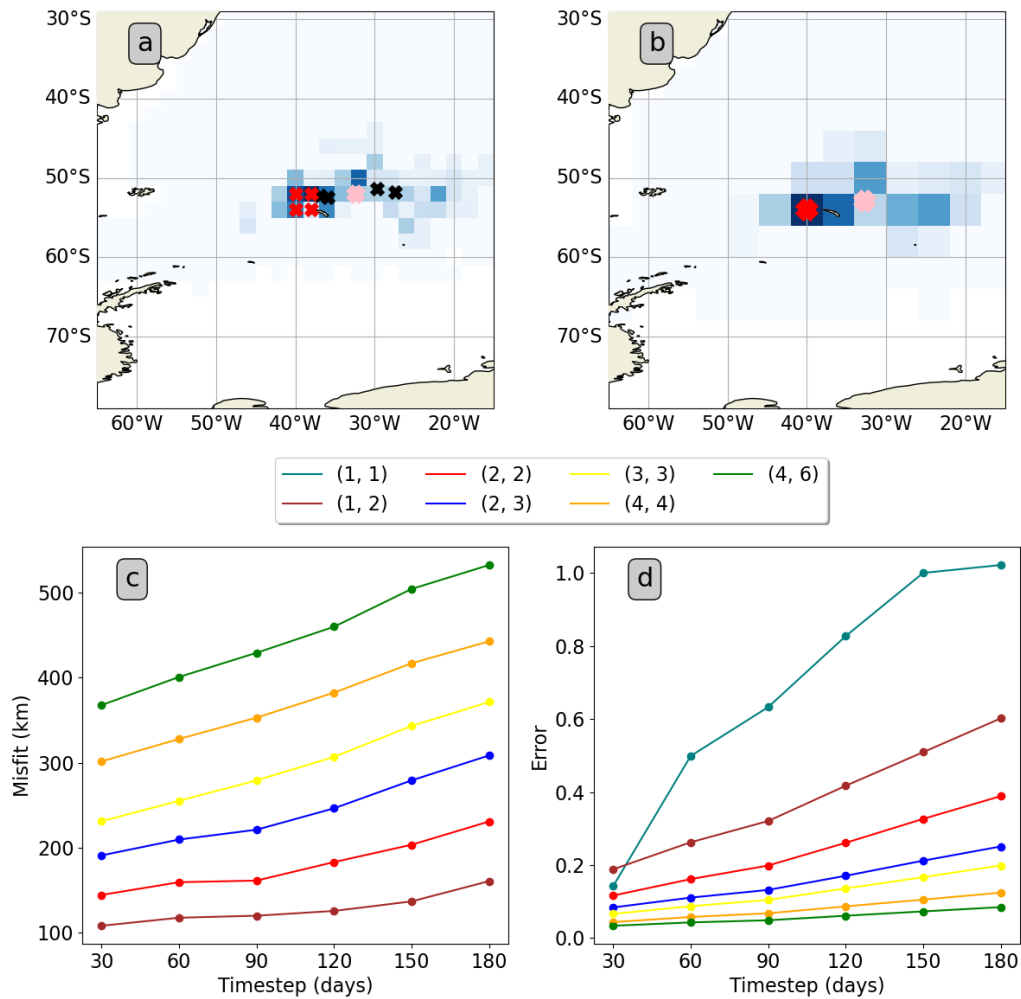


Figure 3.5. Examples of 180 day transition probabilities starting from red Xs for (a) $2^\circ \times 2^\circ$ Transition Matrix and (b) $4^\circ \times 4^\circ$ degree Transition Matrix. Shading represents transition probability, black Xs represent mean transition from individual grid cells and pink X represents spatial mean of all transition probabilities. (c) Difference in derived mean transition between $1^\circ \times 1^\circ$ derived mean transition and reduced resolution transition matrices derived from $1^\circ \times 1^\circ$ transition statistics. (d) Standard error of transition matrices. Colored lines represent different resolutions.

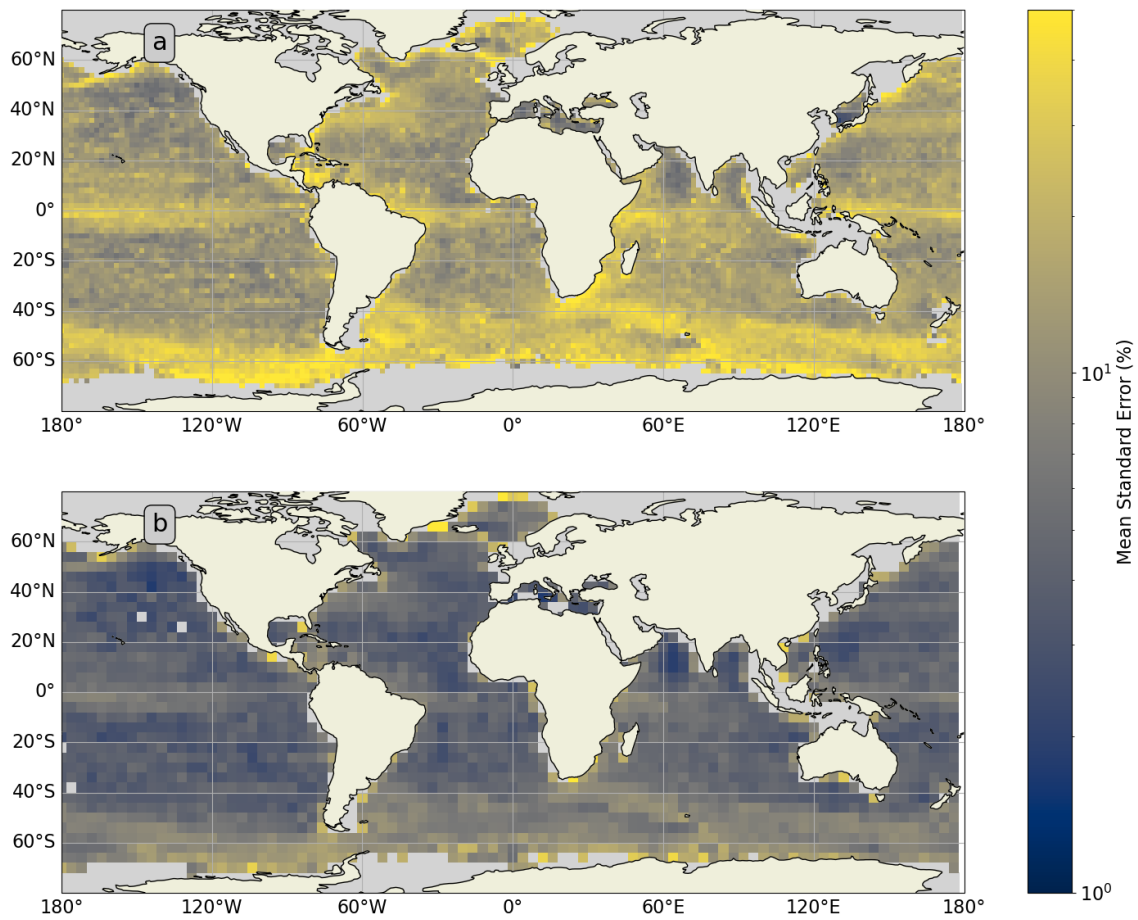


Figure 3.6. Standard error for (a) $2^\circ \times 2^\circ$ degree Transition Matrix and (b) $4^\circ \times 4^\circ$ degree Transition Matrix at 90 day timestep. Colormap represents standard error; gray shading represents areas outside domain of the Transition Matrix; beige shading represents land.

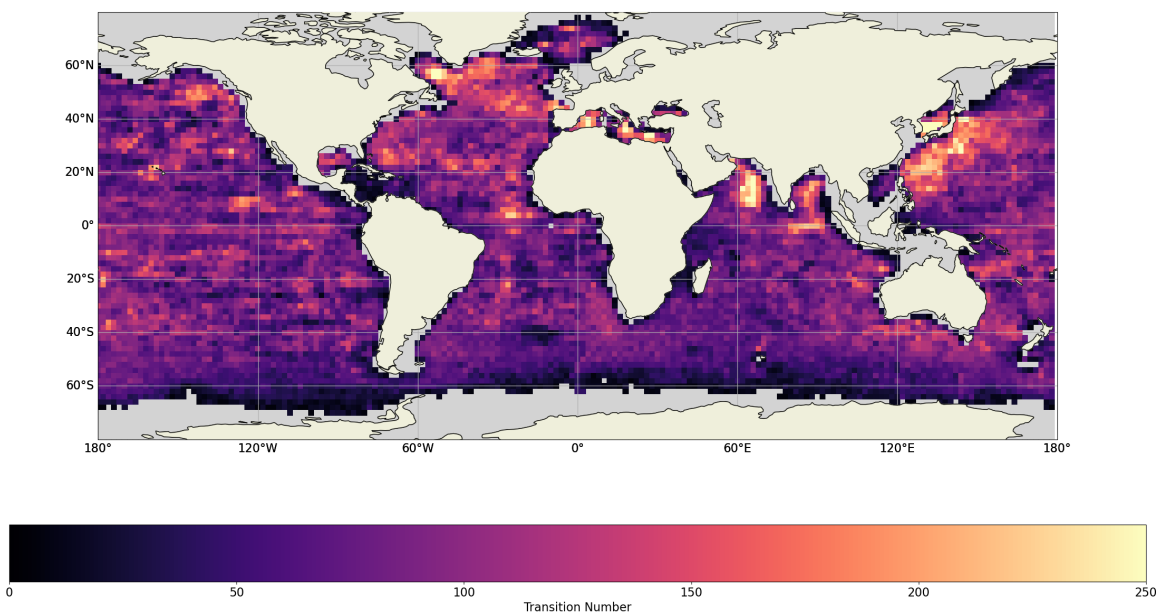


Figure 3.7. Transition density based on global Argo trajectories binned in $2^\circ \times 2^\circ$ degree grid cells with a 90 day timestep. Colormap represents transition density of each grid cell; gray shading represents areas outside domain of the Transition Matrix; beige shading represents land.

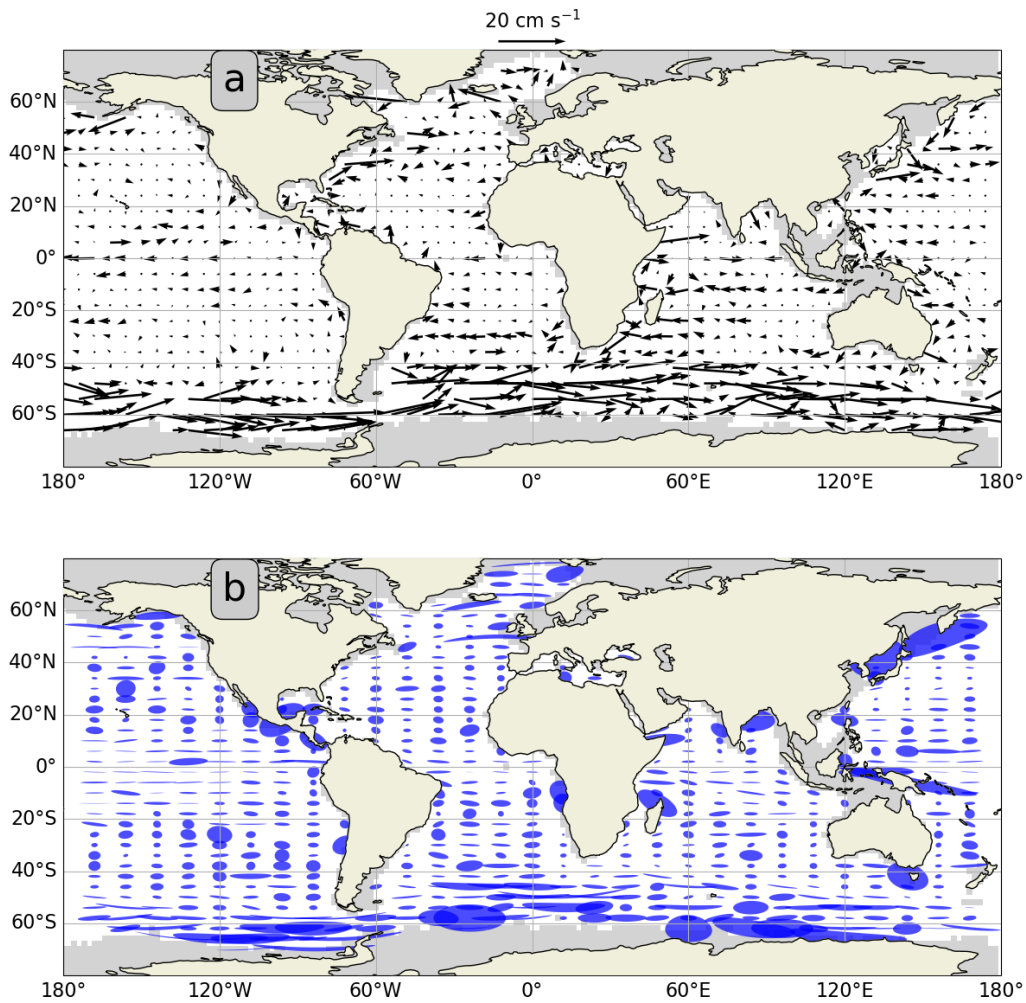


Figure 3.8. (a) Mean transition and (b) variance ellipse based on $2^\circ \times 2^\circ$ binned 90 day timestep Transition Matrix. Arrows represent the mean transition vectors. Blue shapes represent variance ellipses. Gray shading represents areas outside domain of the Transition Matrix; beige shading represents land.

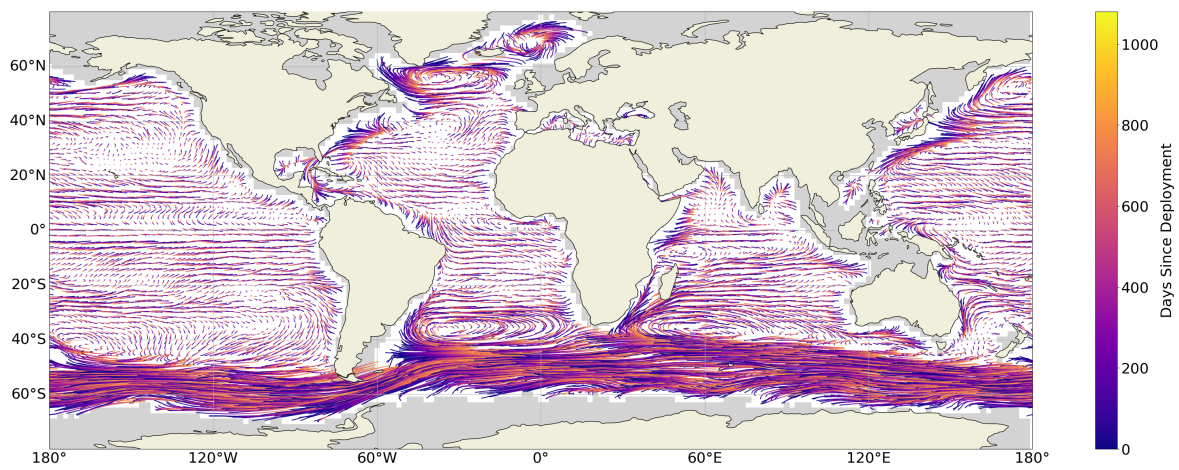


Figure 3.9. Mean Lagrangian pathways for Argo floats at each step in 12 step Markov Chain derived from $2^\circ \times 2^\circ$ grid cell 90 day timestep Transition Matrix (Eq.3.4). Colored lines represent time of mean transition. Gray shading represents areas outside domain of the Transition Matrix; beige shading represents land.

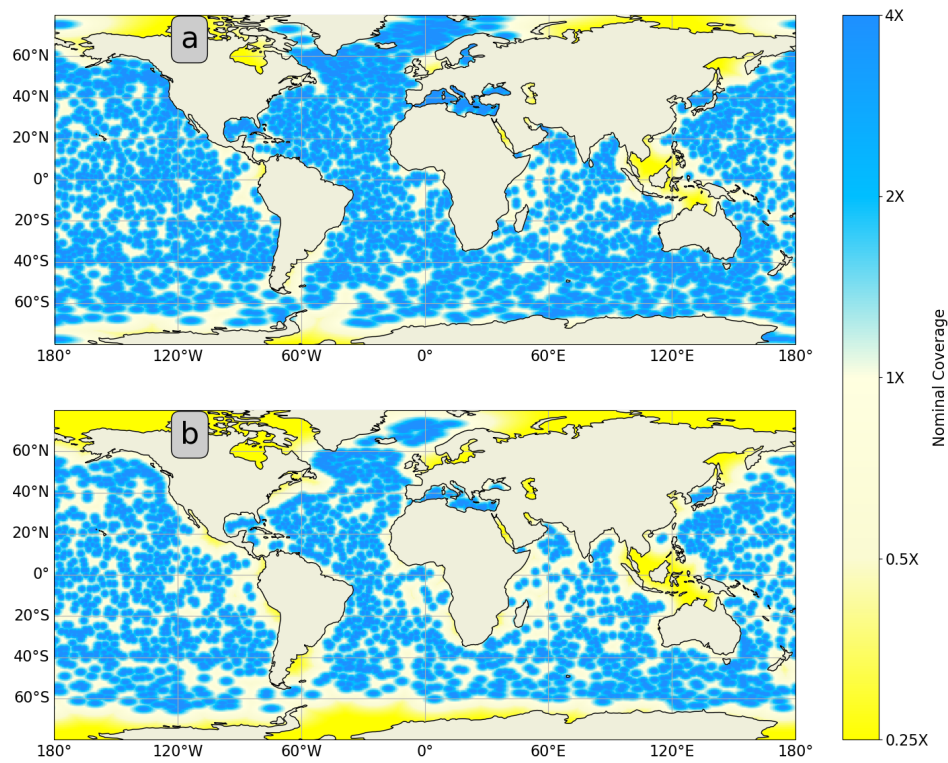


Figure 3.10. (a) Current and (b) one year prediction of density of Core Argo array. Prediction based on mean transition streamlines of Figure 3.9 and a float lifetime of 4 years. Colormap represents array density. 334 km spacing is "1X" nominal coverage. Beige shading represents land.

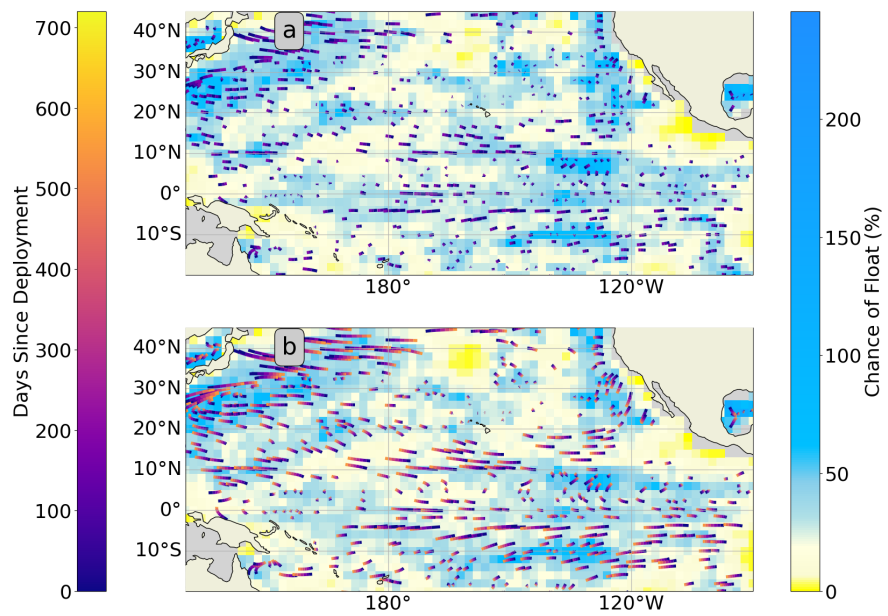


Figure 3.11. (a) One year and (b) two year predictions of density of Core Argo array in the Pacific Ocean. Colored lines represent time of mean transition. Grid cell shading represents estimated array density. Gray shading represents areas outside domain of the Transition Matrix; beige shading represents land.

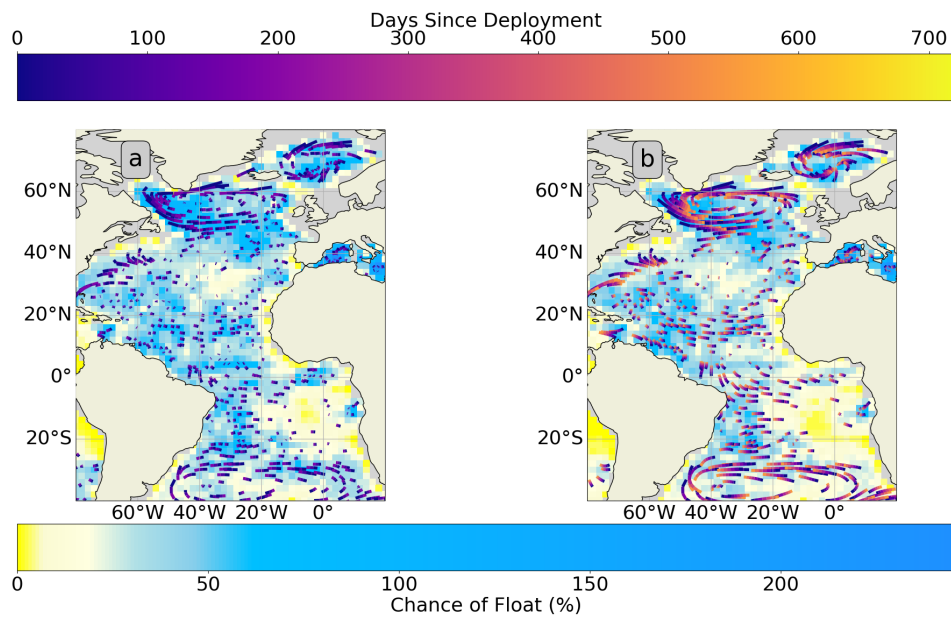


Figure 3.12. (a) One year and (b) two year predictions of array density of Core Argo array in the Atlantic Ocean. Colored lines represent time of mean transition. Grid cell shading represents estimated array density. Gray shading represents areas outside domain of the Transition Matrix; beige shading represents land.

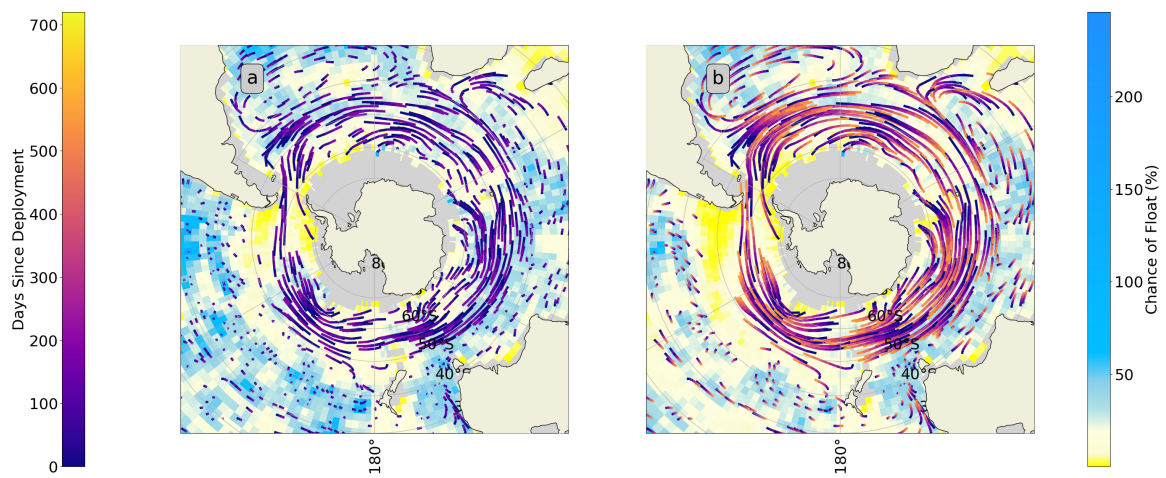


Figure 3.13. (a) One year and (b) two year predictions of array density of Core Argo array in the Southern Ocean. Colored lines represent time of mean transition. Grid cell shading represents estimated array density. Gray shading represents areas outside domain of the Transition Matrix; beige shading represents land.

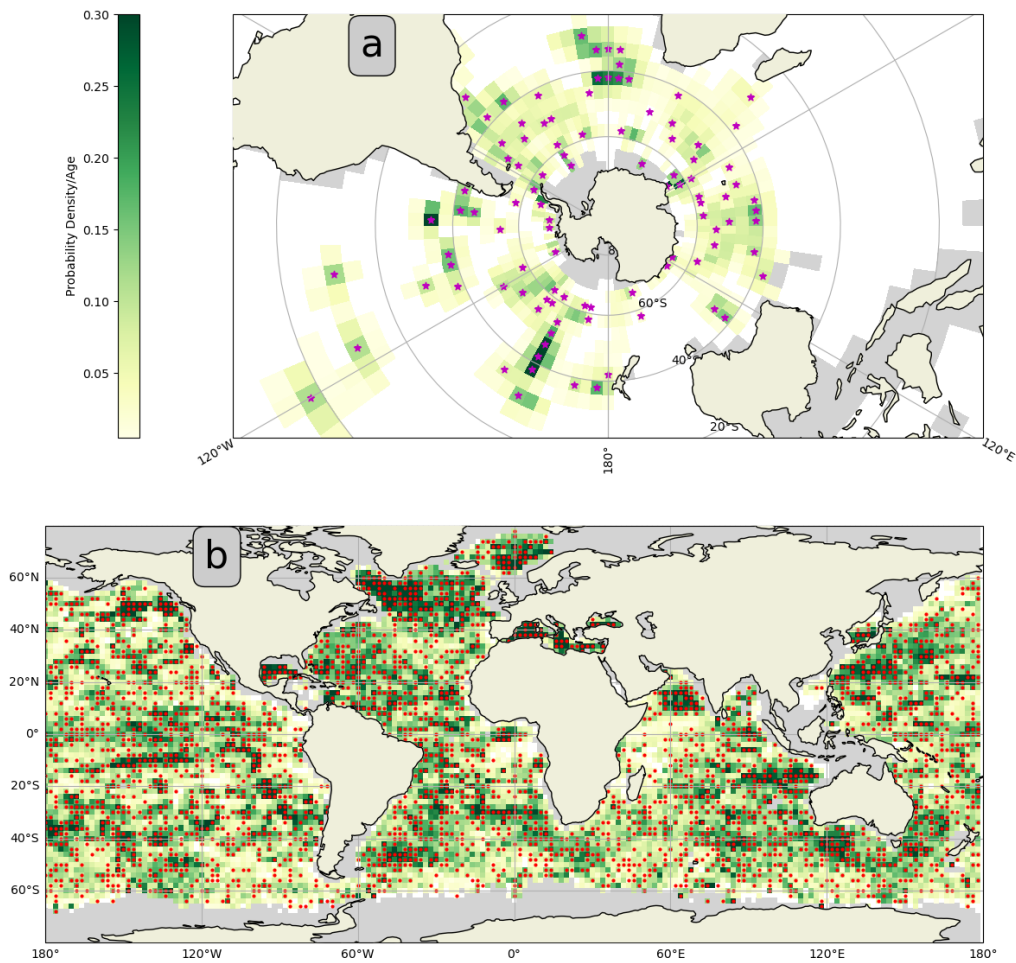


Figure 3.14. 180 day projection of (a) SOCCOM and (b) Argo arrays measure of survivability. Colormap represents probability density divided by age. High probability density divided by low age indicates locations where having a surviving float is likely. Magenta stars indicate active SOCCOM floats, red dots indicate active Core Argo floats. Gray shading represents areas outside domain of the Transition Matrix; beige shading represents land.

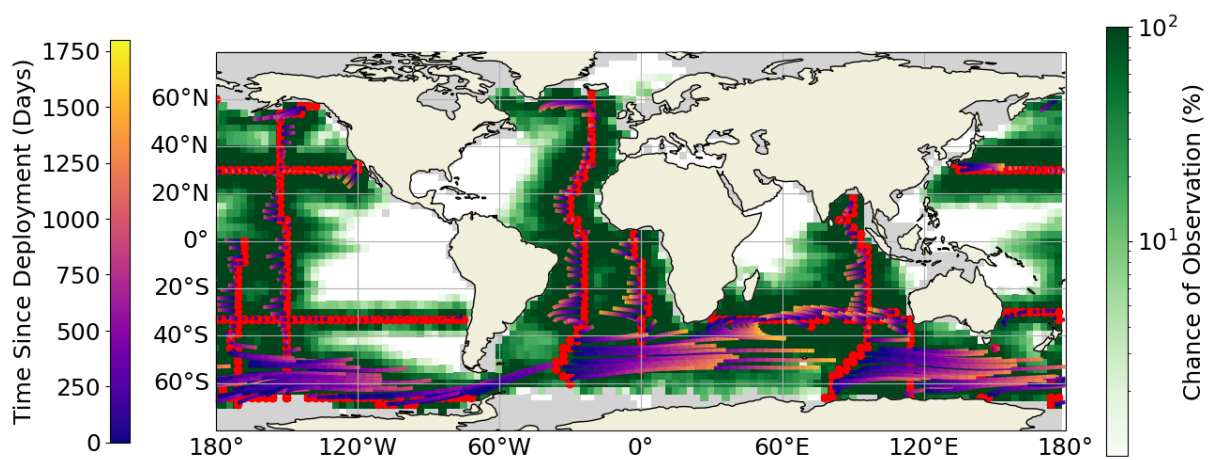


Figure 3.15. Chance of observation for floats deployed in each gridcell along ship tracks of GO-SHIP cruises organized for the next 5 years. Colormap represents chance of observation; white shading indicates less than 1 % chance of observation; Colored lines represent time of mean transition. lines represent gray shading represents areas outside domain of the Transition Matrix; beige shading represents land.

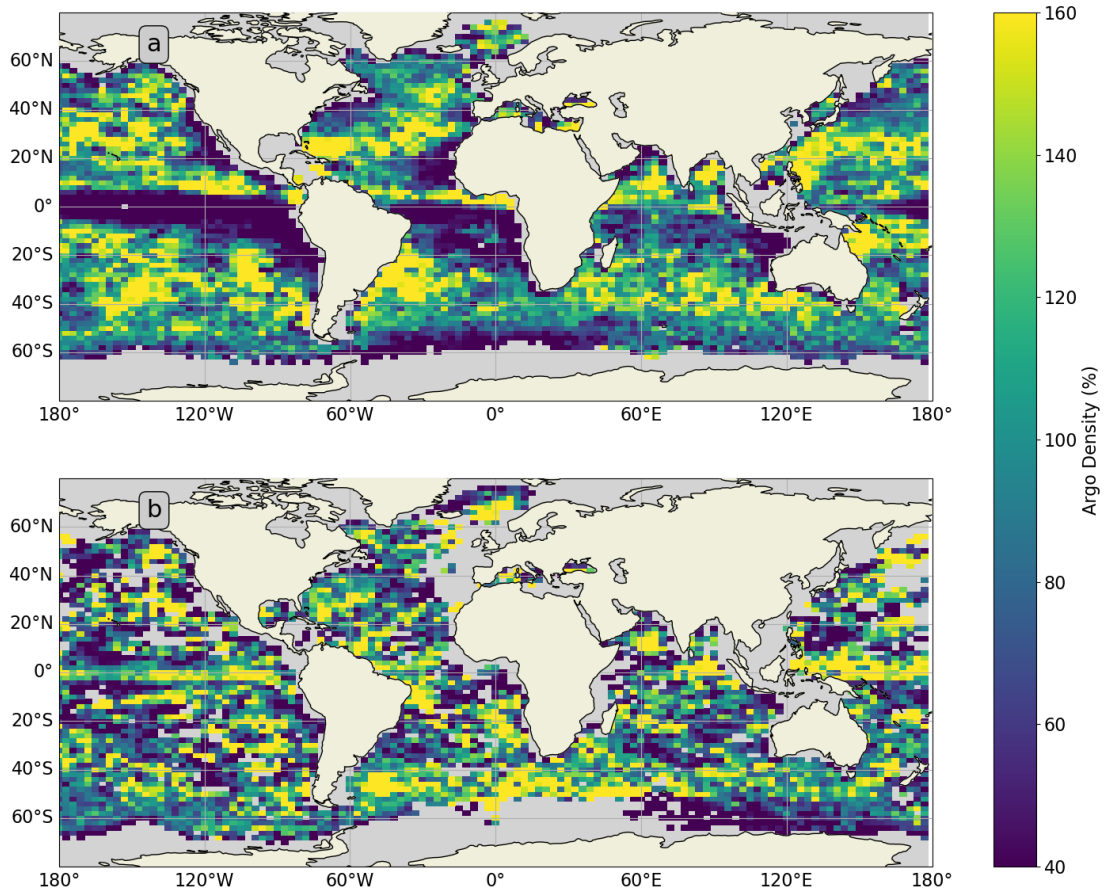


Figure 3.16. Comparison of future array density for (a) Argos System and (b) Iridium communications derived transition matrices at $2^\circ \times 3^\circ$ grid resolution and 180 day timestep. Transition matrices were propagated forward 8 years with initial array containing one float in each gridcell. Colormap represents future array density . Gray shading represents areas outside domain of the Transition Matrix; beige shading represents land.

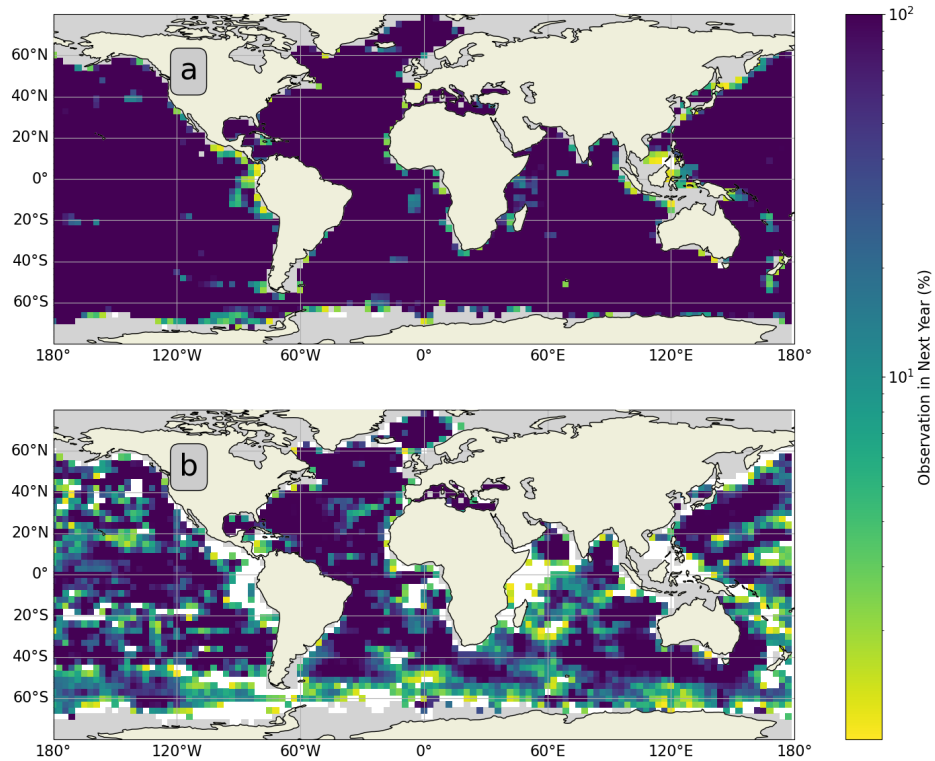


Figure 3.17. Chance of (a) any observation within the next year (Eq. 3.2) and (b) seasonal observation within the next year (Eq. 3.3) of temperature and salinity sensor equipped Argo floats. Argo distribution is taken from the May 10, 2021 snapshot and is comprised of 3262 floats. Colormap represents chance of observation; gray shading represents areas outside domain of the Transition Matrix; white shading indicates less than 1 % chance of observation; beige shading represents land. All projections are based on multiples of $3^\circ \times 3^\circ$ 90 day Transition Matrix.

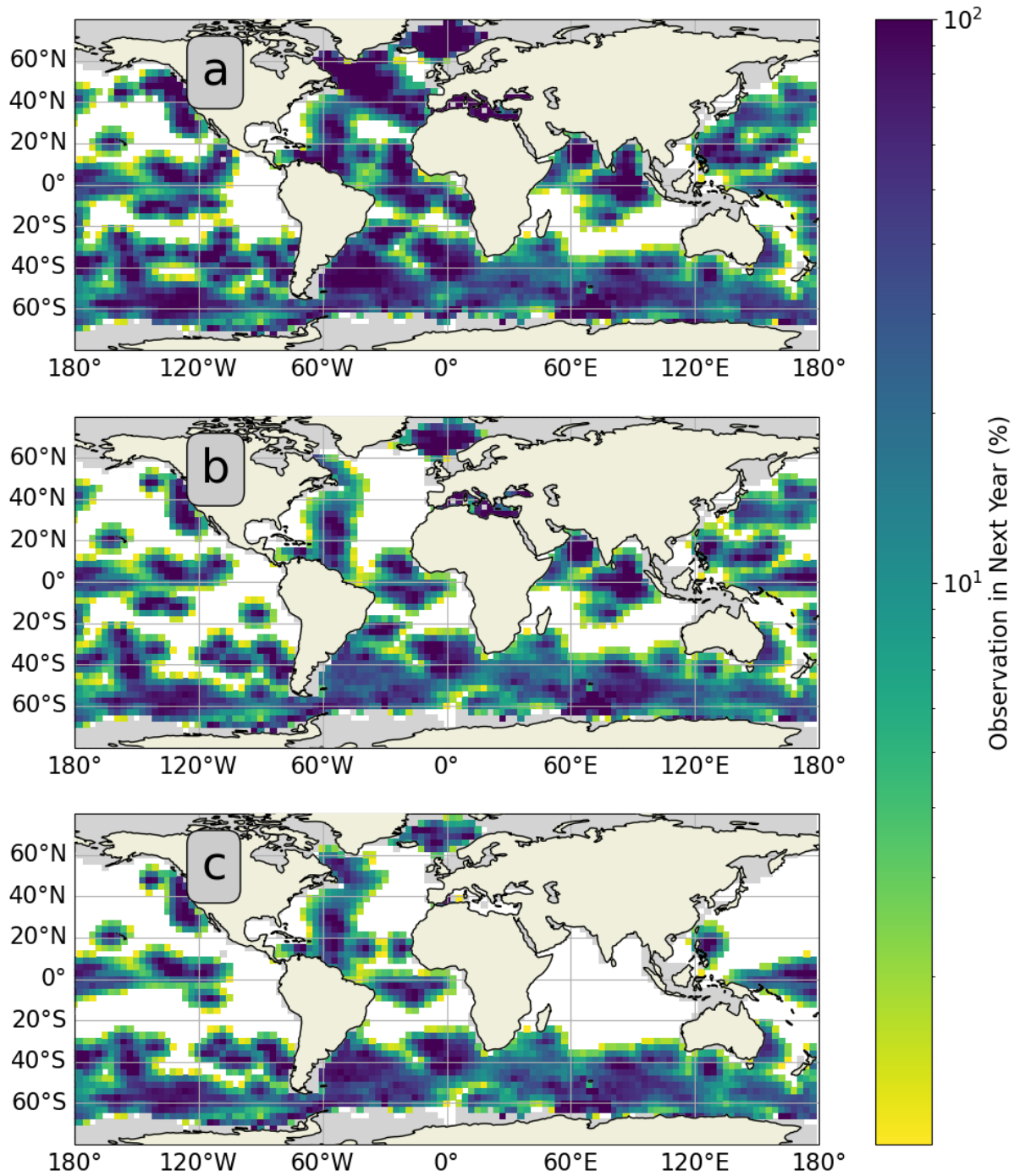


Figure 3.18. Chance of any observation within the next year (Eq. 3.2) of (a) oxygen sensor equipped Argo floats, (b) chlorophyll sensor equipped Argo floats, (c) pH sensor equipped Argo floats. Colormap represents chance of observation; gray shading represents areas outside domain of the Transition Matrix; white shading indicates less than 1 % chance of observation; beige shading represents land. All projections are based on multiples of $3^\circ \times 3^\circ$ 90 day Transition Matrix.

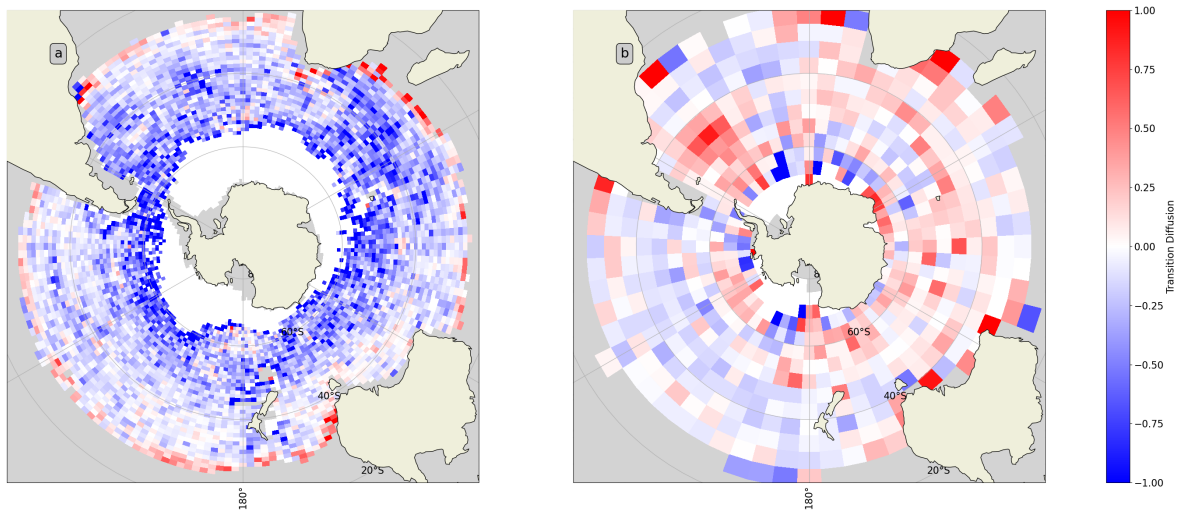


Figure 3.19. Difference of standard deviation around the mean of SOSE and Argo derived matrices for (a) $1^\circ \times 2^\circ$ and (b) $4^\circ \times 6^\circ$ grid cells with 180 day timestep. Shading represents SOSE - Argo standard deviation of transition.

Chapter 4

The Performance of Present, Future, and Optimal Argo Infrastructure

4.1 Abstract

The core Argo array has operated with the design goal of uniform spatial distribution of 3° in latitude and longitude. Recent studies have acknowledged that spatial and temporal scales of variability in some parts of the ocean are not resolved by 3° sampling and have recommended increased core Argo density in the equatorial waters, boundary currents, and marginal seas with an integrated vision of other Argo variants. Biogeochemical (BGC) Argo floats currently observe the ocean from a collection of pilot arrays, but recently funded proposals will transition these pilot arrays to a global array. The current BGC Argo implementation plan recommends uniform spatial distribution of BGC Argo floats. For the first time, we estimate the effectiveness of the existing BGC Argo array to resolve the anomaly from the mean using modeled, full-depth BGC fields. We also study the effectiveness of uniformly-distributed BGC Argo arrays at observing the ocean with varying float densities. Then, using previous Argo trajectories, we estimate the Argo array's future distribution and quantify how well it observes the ocean. Finally, using a novel technique for sequentially identifying the best deployment locations, we suggest the optimal array distribution for BGC Argo floats to minimize objective mapping uncertainty in BGC fields and best observe the anomaly from the mean.

4.2 Introduction

Once a distant prospect, the purchase and deployment of a global array of Biogeochemical (BGC) Argo has been funded. For the first time, nitrate, oxygen, chlorophyll, and pH will be measured on a global scale in near real time and will provide insight into how BGC variables flux and ventilate the ocean (Majkut et al., 2014; Landschützer et al., 2016; Bushinsky et al., 2019, 2017).

The core Argo array collects temperature and salinity profiles throughout most of the open ocean. For over 20 years, core Argo floats have been deployed at locations to achieve or exceed uniform spatial coverage of 3° latitude by 3° longitude (Roemmich et al., 1999). Recent Argo analysis has recognized there exists higher temperature and salinity variability in specific regions and has called for doubled Argo density in the tropics, marginal seas, and boundary currents as part of the new One Argo global design (Roemmich, Dean and Alford, Matthew H and Claustre, Hervé and Johnson, Kenneth and King, Brian and Moum, James and Oke, Peter and Owens, W Brechner and Pouliquen, Sylvie and Purkey, Sarah and others, 2019) .

One Argo consists of three components: core Argo, Deep Argo, and BGC Argo. The six BGC sensors specified for the newly-developing BGC Argo component are oxygen, nitrate, pH, fluorescence (converted to chlorophyll concentration), backscatter, and downwelling irradiance. BGC Argo floats in One Argo follow the same profiling mission as core Argo floats: profiling to 2000 m every 10 days and parking at 1000 m between profiles. BGC Argo float density has been specified at about one quarter the density of core Argo (Johnson and Claustre, 2016a), for a total of about 1000 floats globally. The growing global BGC Argo array is currently a collection of pilot arrays (Fig. 4.1). The largest of these is the Southern Ocean Carbon and Climate Observations and Modelling (SOCCOM) project, which maintains about 120 BGC floats in the Southern Ocean (Johnson, Kenneth S and Riser, Stephen C and Boss, Emmanuel S and Talley, Lynne D and Sarmiento, Jorge L and Swift, Dana D and Plant, Josh N and Maurer, Tanya L and Key, Robert M and Williams, Nancy L and others, 2017). To bridge the gaps between pilot

arrays, a new U.S. project called GO-BGC has begun to deploy 500 floats globally.

The BGC Argo Science and Implementation Plan (Johnson and Claustre, 2016a) guides the design goals of the global BGC array, with float numbers and coverage based primarily on Majkut et al.. After some analysis of the spatial and temporal variability of BGC fields, Johnson and Claustre state "It was, therefore, concluded that initial deployments and operations should begin with the premise that a relatively uniform distribution of floats was adequate." Similar to core Argo, this assumption will be tested as more experience is obtained.

In the time since Johnson and Claustre (2016a), several studies have considered BGC Argo array design. In a seminal BGC Argo study and motivating study for Johnson and Claustre, Majkut et al. (2014) estimated the uncertainty of CO₂ flux estimates in the Southern Ocean that can be inferred using modeled surface fields and a hypothetical, uniformly-distributed array of Argo floats. These estimates are surface restricted, do not consider the cross-covariance with other observations, and use stationary floats for calculating estimates. Johnson and Claustre (2016a) extended Majkut et al. (2014)'s work, estimating the amount of global CO₂ flux that a hypothetical, uniformly-distributed array of 500, 1000, and 2000 floats could constrain; the study considers other factors such as chlorophyll variability and decorrelation length scales and ultimately concludes that 1000 floats is an appropriate BGC Argo density. However, the Johnson and Claustre (2016a) analysis is subject to the same limitations of being surface restricted, not considering the full effects of all BGC sensors, and using stationary floats. Ford (2020) considered the improvements to BGC reanalysis using a full-depth multi-variable model. This study simulates initial float location and movement based on an amalgamation of actual float trajectories taken from 2009-2011, modifying their distribution to achieve the hypothetical design goals. This study found a synergistic effect of multiple BGC variables in improving assimilated model BGC performance (likely attributable to the covariance between BGC variables) and suggests a BGC Argo array larger than 1000 floats may be appropriate. Kamenkovich et al. (2017) advected floats using full-depth HYbrid Coordinate Ocean Model (HYCOM) reanalysis velocity fields from 2010-2014, with complete BGC fields, to study the impact of BGC floats on

Southern Ocean observing systems.

These studies can be incrementally improved to a greater or lesser degree in several ways: (i) include an estimate of float motion; (ii) quantify the impact of the BGC array at depths to 2000 m because an observing system designed for one depth level may not be suitable for all; (iii) consider the strong cross covariances that exist between BGC variables and temperature and salinity because the observation of one variable can constrain a significant amount of variance in another (Fig. 4.2). A float can travel a substantial distance over its lifespan. If not accounted for, this float motion can produce biases in the spatial distribution of the array and assimilation products that use these data (Kamenkovich et al., 2011). The spatial distribution of variability, the length scales, and the phase and amplitude of the seasonal cycles differ across BGC variables (Fig. 4.3). Designing an array to capture one variable may not adequately constrain all of the others. The spatial scales of BGC covariance are largest in the surface ocean (Figs. 4.2, 4.4, and 4.5). Many important and open climate monitoring results, like understanding the change of bulk inventories of oxygen or carbon at depth, need data of an appropriate spatial density to estimate processes and inventories at depth accurately.

In this study, we optimize the float array spatial distribution to constrain the maximum temporal variance of modeled variables over several depths using output from the Global Climate Model CM4 (Adcroft, Alistair and Anderson, Whit and Balaji, V and Blanton, Chris and Bushuk, Mitchell and Dufour, Carolina O and Dunne, John P and Griffies, Stephen M and Hallberg, Robert and Harrison, Matthew J and others, 2019) (see below). Observations and assumptions from the resulting float array are best suited to observe the anomaly from the mean given the criteria of the calculation. By construction, as compared to other float distributions, the observations from the optimized array can be used to create large-scale objective maps with the smallest uncertainty in the anomaly from the mean or to constrain data assimilating models with minimum error covariance. However, many criteria can define what is optimal. Previous observing system design experiments (Kamenkovich et al., 2017) have quantified how well arrays resolve the seasonal climatology of BGC variables. While seasonal variability is the

dominant mode of variability we observe, the optimal array we present may not be ideal for observing this signal. Time of emergence studies (Schlunegger, Sarah and Rodgers, Keith B and Sarmiento, Jorge L and Ilyina, Tatiana and Dunne, John P and Takano, Yohei and Christian, James R and Long, Matthew C and Frölicher, Thomas L and Slater, Richard and others, 2020) have estimated where, when, and how anthropogenic climate change will be detected. An array of floats could be designed to optimally quantify the anthropogenic signal; however, our method is not optimized for this, in that constraining the biogeochemical anomaly from the mean may not observe the effects of climate change as rapidly as an array designed to achieve that goal.

Argo floats sample at 10-day intervals; this is not ideal to observe high frequency surface fluxes (Monteiro et al., 2015). With the advent of efficient two-way satellite communication to Argo floats via Iridium, one can imagine a network of floats with regionally or seasonally adaptive temporal sampling to capture higher frequency signals in certain BGC provinces. Optimal temporal sampling is an important and open question. This study only addresses spatial sampling using spatial covariances and assumes that uncertainty or biases from sampling at too low a frequency can be represented by enhancing the assumed uncertainty of observations.

Finally, previous studies have documented unique BGC provinces (Fay and McKinley, 2014) and compelling BGC phenomena observed from BGC floats (Campbell et al., 2019; Prend et al., 2019). The proposed deployment methods are not optimized to observe these regional phenomena that have large-scale climate impacts. Skilled Argo deployment managers will always be required to tailor deployments to specific regional circumstances, but, like most machine learning methods, the optimization can provide a skilled initial estimate.

The observing system design method that we present has three components. First, we use a Transition Matrix operator to predict future float locations. Our Argo-specific Transition Matrix, documented in a companion publication (Chamberlain et al., 2022), is a statistical construction derived from Argo float trajectory histories that can be used to propagate an array into the future. Second, we use the coupled, full ocean depth climate model CM4 (Held, IM and Guo, H and Adcroft, A and Dunne, JP and Horowitz, LW and Krasting, J and Shevliakova, E and Winton,

M and Zhao, M and Bushuk, M and others, 2019; Adcroft, Alistair and Anderson, Whit and Balaji, V and Blanton, Chris and Bushuk, Mitchell and Dufour, Carolina O and Dunne, John P and Griffies, Stephen M and Hallberg, Robert and Harrison, Matthew J and others, 2019) in our observing system experiments. CM4 calculates temperature and salinity, chlorophyll, pH, and oxygen; BGC Argo floats measure these variables. Finally, we use BGC cross covariances calculated from CM4 to account for the additional constraint that the measurement of a co-varying variable has on the amount of BGC variance constrained by the observing system. In our calculations, we consider the variance constrained by both core and BGC Argo floats.

This study addresses the operational goal of optimal float deployment strategy for the newly integrated Core and BGC Argo arrays. We first quantify the amount of variance constrained by the existing core and BGC arrays. Next, we carry out several Monte-Carlo simulations to quantify the amount of variance constrained by different BGC Argo array densities. We then use the Argo Transition Matrix combined with the current Argo array locations to predict the variance constrained by that future float distribution. Argo floats are typically deployed from research vessels with goals that are independent of Argo array needs; we demonstrate new tools for optimizing deployment locations from such cruises of opportunity. Finally, we use computational models to quantify where the ocean needs increased observational density, accounting for the covariances of proposed and existing instrumentation; in so doing, we construct what we consider an optimal BGC array to observe the anomaly from the mean. We subject the proposed optimal array to a series of numerical experiments to test its efficacy.

We accept the challenge posed by Johnson and Claustre (2016a) to go beyond uniform float distribution and explore regionally-optimized float density. The analysis we show is just one possibility. It is difficult to predict the future scientific needs of the Argo program. Therefore, we present a framework for location selection that, through either models or community consensus, future bio-geochemical researchers can use to produce optimal float deployments. Bretherton et al. (1976), who provided the intellectual genesis for much of this work, said this more succinctly: "no refinement of analysis will eliminate the need for caution tempered by judgement

in the application of these methods to the designs of major programmes.” Since their work provided the intellectual foundation for this current chapter, we push forward inspired by their ethos.

4.3 Data

4.3.1 Argo float data

The analysis presented here requires Argo float locations and sensor suites. For this study, Argo float locations were taken from the May 2021 Argo Snapshot (Argo, 2021). Argo floats are intentionally staggered so that not all floats profile on the same day. We used the most recently reported positions of the active Argo floats; for this analysis, Argo floats were considered active if they had reported a position during the previous 6 months. With the advent of BGC Argo, not all Argo floats carry the same sensor suite. BGC Argo data are hosted by the Argo Global Data Acquisition Centers (GDACs), and the specific sensor makeup of each float was available in the downloaded GDAC snapshot (Figs. 4.1 and 4.3).

4.3.2 Biogeochemical Model

We used the CM4 coupled ocean-atmosphere model (Held, IM and Guo, H and Adcroft, A and Dunne, JP and Horowitz, LW and Krasting, J and Shevliakova, E and Winton, M and Zhao, M and Bushuk, M and others, 2019; Adcroft, Alistair and Anderson, Whit and Balaji, V and Blanton, Chris and Bushuk, Mitchell and Dufour, Carolina O and Dunne, John P and Griffies, Stephen M and Hallberg, Robert and Harrison, Matthew J and others, 2019) to estimate the spatial covariance of global ocean biogeochemistry. The CM4 ocean has a nominal grid spacing of $\frac{1}{4}^{\circ} \times \frac{1}{4}^{\circ}$ of latitude and longitude, and 75 depth levels with 2-m spacing at the surface and 200 m spacing at depth. CM4 ocean biogeochemistry was calculated using the Biology Light Iron Nutrient and Gas (BLING) model (Galbraith et al., 2010). These calculations used the daily averaged model temperature, salinity, oxygen, pH, and chlorophyll from 1850-2009. We

reduced the computational burden by subsampling CM4 to a grid spacing of $2^\circ \times 2^\circ$ of latitude and longitude where depths are greater than 2000 meters. Depth levels of 15 m, 40 m, 87.5 m, 137.5 m, 225 m, 350 m, 550 m, 750 m, 950 m, 1150 m, 1350 m, 1625 m, and 2250 m were used in these calculations. Chlorophyll was only calculated in the euphotic zone, which we define as all depths equal to or shallower than 137.5 m, and the log of the data was used in these calculations as is standard practice (Campbell, 1995). In total, the spatial domain of each depth level contained 9059 distinct gridcells of latitude and longitude extending from 76°S to 88°N . Over all depth levels and across all variables, the model data comprised 507,304 individual time series.

4.3.3 Transition Matrix

A Transition Matrix is an operator that propagates a state vector forward or backward in time. In this case, the Transition Matrix is calculated from previous Argo trajectories to propagate the Argo float array through time. The Argo float array is represented in these calculations as the Argo state vector, which exists in the spatial grid defined by the Argo state space. This spatial grid is a subset of the CM4 $2^\circ \times 2^\circ$ latitude and longitude spatial grid and defines all the locations in the ocean that an Argo float can occupy. (Some areas, like the Arctic, do not have many Argo trajectories and those grid cells were excluded from the Transition Matrix.) The Transition Matrix is a square matrix with rows and columns equal to the size of the Argo state space and defines the transitions of a discrete-time Markov Chain. The Transition Matrix we use has a 90-day time-step. The details of construction of this Transition Matrix and choices of this grid cell size and timestep can be found in chapter 3.

4.4 Methods

In this study, we fuse two established techniques: (i) a method that quantifies the amount of variance constrained by the full sensor suite of a BGC float, based on objective mapping (Bretherton et al., 1976) here using statistics generated from the CM4 model, and (ii) the

transition matrix approach that statistically predicts the future location of either an individual float or an entire float array computed using all previous observed Argo trajectories (Markov, 1906; Sevellec et al., 2017; Chamberlain et al., 2022). Our primary innovation is the combination of these ideas. Many of the scientific questions posed for BGC Argo arrays involve inventories and fluxes of BGC variables. Therefore, assessing the effect of a float observation has less practical utility if float planners do not know where the float will be, and, conversely, accurately predicting the observational density has less importance if the impact of observations to constrain models or budgets is unquantified (Chamberlain et al., 2018). This procedure is also applicable to core Argo properties, with of course the same transition matrix, and to other observing systems for which a transition matrix can be computed, whether from previous observations or from a model.

In section 4.4.1, we broadly explain the objective mapping and mapping error methods that are used to compute the results of this work. The literature on this topic is well developed and a summary is provided for convenience. Objective mapping depends on knowledge of the means and covariances of the mapped fields, which require a large amount of data to calculate accurately. In this case, we use the CM4 model output to estimate the covariances. Oceanic BGC variables have different variances and spatial and temporal scales of covariance (Fig. 4.3). To compare these variables, it is necessary to normalize them to be non-dimensional, with sizes reflecting their importance to the analysis. The normalization factors can vary with variable type and location.

In section 4.4.2, we describe the processing methods for the CM4 model data. We apparently mitigate spurious covariances and reduce the computational burden of these methods by applying a localization to the covariances calculated from the normalized data. A localization is a filter that restricts the regional extent that a specific grid cell can influence. The localization used in this work is described in section 4.4.3.

With the processed and localized data, the full covariance matrix in space is calculated for all points and variables and used to estimate mapping error for a given Argo float distribution.

In section 4.4.4 we describe the method to calculate the variance constrained by a static Argo array. We consider both existing Argo locations and hypothetical random distributions. Next, we propagate Argo floats into the future using the Transition Matrix, computed from historical Argo trajectories, and consider the amount of variance constrained by a future float distribution in section 4.4.5. Finally, in section 4.4.6, we explain our method for constructing an optimal array and the testing procedures for quantifying the array’s performance, using the notation of Ide et al. (1997). The processes and products described in this section are represented schematically in Figure 4.7.

4.4.1 Objective Mapping

Observations $\mathbf{y}(t)^o$ (length m) of a state vector $\mathbf{x}(t)$ are expressed as

$$\mathbf{y}(t)^o = \mathbf{H}\mathbf{x}(t) + \boldsymbol{\varepsilon} \quad (4.1)$$

where \mathbf{H} is the linearized observation operator, $\boldsymbol{\varepsilon}$ is the noise process, and the superscript ”o” refers to observations. The state vector, $\mathbf{x}(t)$, has dimension n and uncertainty covariance matrix \mathbf{P} . The noise process $\boldsymbol{\varepsilon}$ of length m is assumed to have zero mean and covariance matrix \mathbf{R} . The noise process is composed of instrumental and representation errors.

The state vector, $\mathbf{x}(t)$, has the values of all the physical BGC property variables from the CM4 model - temperature, salinity, oxygen, pH, and chlorophyll at shallower depths where it is non-zero. The state vector can be restricted to a single depth, or can be a combination of multiple depths, and is a subset of the model grid points. This means that the number of elements (n) in the state vector, $\mathbf{x}(t)$, is the number of grid points in the domain multiplied by the number of variables and depths considered: this can be many times longer than the total number of grid points in our domain. We use a time series of model state around its time mean to estimate the

Uncertainty Covariance Matrix (UCM), \mathbf{P} . This is defined as

$$\mathbf{P} = E[\mathbf{x}\mathbf{x}^T]. \quad (4.2)$$

The UCM contains the cross covariances between biogeochemical variables across depths and grid points (Fig. 4.2). We assume \mathbf{x} to be the true state of global biogeochemistry. Of course CM4 has biases and uncertainties (Held, IM and Guo, H and Adcroft, A and Dunne, JP and Horowitz, LW and Krasting, J and Shevliakova, E and Winton, M and Zhao, M and Bushuk, M and others, 2019), but the exact structure of these errors is outside the scope of this analysis.

Now we search for a linear estimate of \mathbf{x} from the observations, \mathbf{y}^o . Assume there exists a \mathbf{K} , termed the Kalman gain, such that

$$\hat{\mathbf{x}} = \mathbf{K}\mathbf{y}^o, \quad (4.3)$$

where $\hat{\mathbf{x}}$ is the state estimate. The Covariance of the Expected Error (CEE) of the estimate is termed $\hat{\mathbf{P}}$ and is defined as

$$\hat{\mathbf{P}} = E[(\mathbf{x} - \hat{\mathbf{x}})(\mathbf{x} - \hat{\mathbf{x}})^T] \quad (4.4)$$

$$\hat{\mathbf{P}} = E[(\mathbf{x} - \mathbf{K}\mathbf{y}^o)(\mathbf{x} - \mathbf{K}\mathbf{y}^o)^T] \quad (4.5)$$

$$\hat{\mathbf{P}} = \mathbf{K}\mathbf{P}_{yy}\mathbf{K}^T - \mathbf{P}_{xy}\mathbf{K}^T - \mathbf{K}\mathbf{P}_{xy} + \mathbf{P}_{xx}, \quad (4.6)$$

where \mathbf{P}_{xy} is the covariance between modeled locations and observed locations (model-data covariance) and \mathbf{P}_{yy} is the covariance between observed locations (data-data covariance). From Eq. 4.1 we have an expression for the observations, the covariance of which can be written

$$\mathbf{P}_{yy} = E[(\mathbf{H}\mathbf{x} + \boldsymbol{\varepsilon})(\mathbf{H}\mathbf{x} + \boldsymbol{\varepsilon})^T] = \mathbf{H}\mathbf{P}\mathbf{H}^T + \mathbf{R}. \quad (4.7)$$

Similarly,

$$\mathbf{P}_{xy} = E[\mathbf{x}(\mathbf{H}\mathbf{x} + \boldsymbol{\varepsilon})^T] = \mathbf{P}\mathbf{H}^T. \quad (4.8)$$

We complete the square by adding $\mathbf{P}_{xy}\mathbf{P}_{yy}^{-1}\mathbf{P}_{xy}^T$ to both sides of Equation 4.6, This gives

$$\hat{\mathbf{P}} = (\mathbf{K} - \mathbf{P}_{xy}\mathbf{P}_{yy}^{-1})\mathbf{P}_{yy}(\mathbf{K} - \mathbf{P}_{xy}\mathbf{P}_{yy}^{-1})^T + \mathbf{P} - \mathbf{P}_{xy}\mathbf{P}_{yy}^{-1}\mathbf{P}_{xy}^T. \quad (4.9)$$

If we assume the error, $\boldsymbol{\varepsilon}$, has zero mean, is stationary, and that the error of distinct points are uncorrelated with each other, then we can differentiate Equation 4.9 to find the Kalman gain, \mathbf{K} , that minimizes the variance of $\hat{\mathbf{P}}$. At an extremum,

$$\frac{\delta tr(\hat{\mathbf{P}})}{\delta \mathbf{K}} = 2(\mathbf{K} - \mathbf{P}_{xy}\mathbf{P}_{yy}^{-1})^T \mathbf{P}_{yy} = 0 \quad (4.10)$$

$$\mathbf{K} = \mathbf{P}_{xy}\mathbf{P}_{yy}^{-1} \quad (4.11)$$

and

$$\hat{\mathbf{P}} = \mathbf{P} - \mathbf{P}_{xy}\mathbf{P}_{yy}^{-1}\mathbf{P}_{xy}^T. \quad (4.12)$$

Substituting Eqs. 4.7 and 4.8 into Eqs. 4.11 and 4.12, we get

$$\mathbf{K} = \mathbf{P}\mathbf{H}^T(\mathbf{H}\mathbf{P}\mathbf{H}^T + \mathbf{R})^{-1}, \quad (4.13)$$

and, in terms of the Kalman gain,

$$\hat{\mathbf{P}} = [\mathbf{I} - \mathbf{K}\mathbf{H}]\mathbf{P}. \quad (4.14)$$

Intuitively, the Kalman gain (Eq. 4.13) is scaled by the size of the noise process covariance (\mathbf{R}) relative to the UCM projected into observation space ($\mathbf{H}\mathbf{P}\mathbf{H}^T$). The term $\mathbf{K}\mathbf{H}$ acts as an update term to reduce the UCM by an amount determined by the uncertainty and distribution of the observations.

Many of the following results quantify and minimize the diagonal elements of the CEE

($\hat{\mathbf{P}}$). Another metric, termed the Formal Mapping Error (FME), is the ratio of the diagonal elements of the CEE ($\hat{\mathbf{P}}$) to the UCM (\mathbf{P}) and is a vector. The i^{th} element of the FME is expressed as

$$E_i^{map} = \frac{\hat{\mathbf{P}}_{ii}}{\mathbf{P}_{ii}}. \quad (4.15)$$

FME (E^{map}) can be used to highlight regions where observations improve the estimate and reduce the CEE ($\hat{\mathbf{P}}$).

4.4.2 Variance Scaling

BGC properties have significantly different spatial and temporal variability (Fig. 4.3). The magnitude of the variability of these BGC signals also differs (by as much as 10 orders of magnitude, see appendix). Without scaling, variables with relatively large variance will dominate over variables with relatively smaller variance (see appendix). To provide equal treatment of the different properties and a reasonable representation of ocean variance, we scale the variance of individual BGC variables such that the scaled variances of all BGC variables are similar. The data scaling is a filter that imposes minimum and maximum temporal variance of each variable at each grid point.

For each variable, v , and depth k , we define $var_{kv}^{15^{th}}$ to be the 15th percentile of a dataset formed by the unscaled temporal variance of the timeseries, $\mathbf{x}(t)_{ijkv}$, at each gridpoint of longitude, i , and latitude, j . Then we impose a scaling, which we call σ_{ijkv} , on the data such that

$$var_{scaled}(\mathbf{x}(t)_{ijkv}) = \frac{var(\mathbf{x}(t)_{ijkv})}{\sigma_{ijkv}}, \quad (4.16)$$

where

$$\sigma_{ijkv} = \begin{cases} var(\mathbf{x}(t)_{ijkv}), & \text{if } var(\mathbf{x}(t)_{ijkv}) \leq var_{kv}^{15^{th}} \\ var_{kv}^{15^{th}}, & \text{if } var_{kv}^{15^{th}} < var(\mathbf{x}(t)_{ijkv}) \leq 15var_{kv}^{15^{th}} \\ \frac{var(\mathbf{x}(t)_{ijkv})}{15}, & \text{if } 15var_{kv}^{15^{th}} < var(\mathbf{x}(t)_{ijkv}), \end{cases} \quad (4.17)$$

and where σ is the scaling term and is a function of $var(\mathbf{x}(t)_{ijkv})$. A brief description of why the 15th percentile cutoff (and other tuning factors) were chosen can be found in the appendix. One can think of this scaling as a dynamic range limiter where small variances are amplified to the value of $var_{kv}^{15^{th}}$ and large variances saturate and are reduced to the value of $15var_{kv}^{15^{th}}$. This scaling has been tuned to reduce extremes in CM4 output without changing the spatial distribution of BGC variance.

The sum of the variance at the i^{th} longitude, j^{th} latitude gridpoint over depth and variable type can be written

$$var_{i,j}^{total} = \sum_k \sum_v var_{scaled}(x(t)_{ijkv}) \quad (4.18)$$

4.4.3 Localization

We expect observations at nearby grid points to be more correlated than distant observations. We hypothesize that these similarities decrease with distance and converge to a limit where grid points that are sufficiently far away are uncorrelated. However, for a variety of reasons (e.g. Cai et al., 2011), spuriously strong covariances may exist between gridpoints that are far apart. For this reason, imposing a filter that reduces correlations between distant points can be desirable.

Additionally, the UCM, \mathbf{P} , scales geometrically with the number of elements, n , in the state vector, \mathbf{x} . Necessary calculations on the UCM become exponentially more expensive with larger n . If we expect grid points at large distances to be uncorrelated, then much of the UCM is close to or equal to zero; this means that much of UCM does not contribute to these calculations and can be ignored. Imposing a filter to remove covariances at large distances makes the UCM a sparse matrix and significantly reduces the expense of calculations.

For these two reasons, we apply a localization filter to the UCM. The localization we use (Gaspari and Cohn, 1999) is a specially constructed piece-wise polynomial that does not introduce negative eigenvalues in the resulting localized matrix.

The Gaspari and Cohn localization filter contains a scaling term, s , that is defined as

$$s(r, c) = \begin{cases} -\frac{1}{4}\left(\frac{|r|}{c}\right)^5 + \frac{1}{2}\left(\frac{|r|}{c}\right)^4 + \frac{5}{8}\left(\frac{|r|}{c}\right)^3 - \frac{5}{3}\left(\frac{|r|}{c}\right)^2 + 1, & \text{if } 0 \leq |r| \leq c \\ \frac{1}{12}\left(\frac{|r|}{c}\right)^5 - \frac{1}{2}\left(\frac{|r|}{c}\right)^4 + \frac{5}{8}\left(\frac{|r|}{c}\right)^3 + \frac{5}{3}\left(\frac{|r|}{c}\right)^2 - 5\left(\frac{|r|}{c}\right) + 4 - \frac{2}{3}\left(\frac{c}{|r|}\right), & \text{if } c \leq |r| \leq 2c \\ 0, & \text{if } 2c \leq r \end{cases} \quad (4.19)$$

where $|r|$ is the magnitude of the distance between grid points, and c is the characteristic length scale of the localization. The localization is applied element-wise such that the resulting covariance matrix is calculated as

$$\mathbf{P} = \begin{bmatrix} p_{11}s(0, c) & p_{12}s(r_{12}, c) & \dots & p_{1K}s(r_{1K}, c) \\ p_{21}s(r_{21}, c) & p_{22}s(0, c) & & \\ \vdots & & \ddots & \\ p_{K1}s(r_{K1}, c) & & & p_{KK}s(0, c) \end{bmatrix} \quad (4.20)$$

where $p_{a,b}$ is the covariance between the a^{th} and b^{th} elements of the state vector \mathbf{x} , and r_{ab} is the horizontal distance between the a^{th} and b^{th} element of the state vector.

Ideally, the characteristic length scale, c , will be proportional to the length scale of the forcing that produces the covariance. We observe that the gravest eigenvectors of the covariance matrix (Figs. 4.4 and 4.5) correspond to either large-scale seasonal oscillations or waves, and higher eigenmodes of the covariance matrix (Fig. 4.4) appear to demonstrate finer mesoscale variability. For this reason, we chose to impose a scale separation on the 4 gravest eigenmodes of the covariance matrix. The localization applied to the gravest eigenmodes had a c value of 10.95 degrees of latitude and longitude, while localization applied to all higher modes had a c value of 3.65 of latitude and longitude. The localized covariances are represented as the blue square labeled "Cross Covariances" in Figure 4.7 .

4.4.4 Variance Constrained by Static Argo Arrays

Now that we have scaled and localized the UCM (\mathbf{P}), we focus on describing the calculation of the first of our three results - variance constrained by static distributions of Argo floats. We produce two results from the static arrays: variance constrained from an actual array of Argo floats at an example time, May 2021, which we term the “existing float array snapshot”, and variance constrained from randomly deployed floats, which we term the “Monte-Carlo snapshot” (Fig. 4.1). The CEE, $\hat{\mathbf{P}}$, is defined in Eqns. 4.13 and 4.14. This section describes the construction of the observation operator, \mathbf{H} , and the noise process covariance, \mathbf{R} , which are the two required matrices for the CEE calculation.

We will describe the construction of these matrices for the general float array and then explain the specifics of the existing float array snapshot and Monte-Carlo snapshot. The observation operator accounts for every float’s observational suite. Because \mathbf{x} includes multiple BGC variables at a grid cell, an individual Argo float profile must be considered as multiple distinct observations. The float array is binned to match the dimensions of the state vector \mathbf{x} . Let the list O of length m be the unique state vector index corresponding to every sensor of every float in the array. Multiple floats can occupy the same grid cell: for example, a core Argo and BGC Argo float could be located within approximately two hundred kilometers for $2^\circ \times 2^\circ$ grid spacing and farther for coarser resolutions. To account for the additional variance constrained by redundant sensors in a grid cell, we also record the number of measurements per element of \mathbf{x} and call this list N . List N is also of length m . From the fundamental observation equation (Eq. 4.1), we see that the observation operator \mathbf{H} is an $m \times n$ matrix, where n is the length of the state vector. The observation operator projects the state vector into the observation space in the observation equation. The observation operator is a sparse matrix composed of ones at the column indices defined in list O and zeros elsewhere. This can be written as the following:

$$\begin{aligned}
\mathbf{H}[1, O_1] &= 1 \\
\mathbf{H}[2, O_2] &= 1 \\
&\vdots \\
\mathbf{H}[m, O_m] &= 1.
\end{aligned} \tag{4.21}$$

To calculate \mathbf{R} in Eq. 4.13 we assume that the representation error of ε (Eq. 4.1) dominates the instrumentation error and is proportional to the uncertainty variance of the state vector for the observation location and variable type. We also assume that additional observations at a grid point reduce the representation error. \mathbf{R} is a diagonal $m \times m$ matrix with diagonal elements equal to four times the variance of the state vector element corresponding to the observation scaled by the number of observations. In matrix form, this is written as

$$\mathbf{R} = 4 \begin{bmatrix} \mathbf{P}(O_1, O_1)/N_1 & 0 & \dots & \dots & 0 \\ 0 & \mathbf{P}(O_2, O_2)/N_2 & & & \\ \vdots & & \ddots & & \\ \vdots & & & \ddots & \\ 0 & & & & \mathbf{P}(O_m, O_m)/N_m \end{bmatrix}. \tag{4.22}$$

Given the array distribution of the existing Argo floats (Fig. 4.1), it is straightforward to calculate the \mathbf{H} and \mathbf{R} matrices that correspond to the existing float array snapshot. The CEE, $\hat{\mathbf{P}}$ (Eq. 4.14), and FME, E^{map} (Eq. 4.15), were then calculated for all depth levels. Schematically, this is represented in Figure 4.7 as the combination of the existing float array and cross covariances to produce the present $\hat{\mathbf{P}}$.

Uniform float distribution has been a stated design goal of the Core Argo array and is a design goal of the BGC Argo array (Johnson and Claustre, 2016a). We examine whether non-uniform distribution might be more efficient, that is, reduce the numbers of floats required, by

first estimating the amount of variance the uniformly-distributed BGC Argo array will constrain by creating Monte-Carlo snapshots of many randomly distributed arrays of varying float densities and averaging the results together. Random arrays were constructed of hypothetical floats equipped with the full CM4 BGC sensor suite, and array sizes were calculated from 0 to 1000 floats in 50 float increments. We calculated Monte-Carlo variance snapshots for 50 random arrays at each array size and averaged the results. Schematically, this is represented in Figure 4.7 as the combination of the random float array and cross covariances to produce the designed $\hat{\mathbf{P}}$.

4.4.5 The Transition Matrix and Variance Constrained by Future Argo Arrays

Now that we have a quantifiable metric for assessing float performance for constraining the anomaly of a state vector, we consider the task of predicting future float distributions so that we can estimate how well the Argo array will observe the ocean at a future time. For these calculations, we assume that the statistics of the uncertainty covariance matrix, \mathbf{P} , are stationary. A $2^\circ \times 2^\circ$ spatially binned Transition Matrix with a 90-day time step, constructed from all existing Argo trajectories (Chamberlain et al., 2022) (Fig. 4.6), is used to estimate the evolving array distribution at later timesteps. The Transition Matrix acts on the Argo state vector ($\boldsymbol{\rho}$) which is defined as the probability of an Argo float in each grid cell, and propagates it into the future l time steps such that

$$\boldsymbol{\rho}(t+l) = \mathbf{M}^l \boldsymbol{\rho}(t) \quad (4.23)$$

where \mathbf{M} is the Transition Matrix. The vector $\boldsymbol{\rho}$ is $n^{tm} \times 1$, where the superscript tm indicates Transition Matrix. The Transition Matrix is a square $n^{tm} \times n^{tm}$ matrix that statistically predicts the future probability density of the Argo state vector as it evolves through time. Transition Matrix coverage is restricted to regions with a large amount of Argo trajectory data; therefore, while the Transition Matrix is on the same grid as CM4, the Transition Matrix grid is a subset of the CM4 grid.

The first statistical moment of the Transition Matrix can be expressed as

$$r_a = \sum_{b=1}^{n^m} \mathbf{M}_{ab}^l r_b \quad (4.24)$$

where r_b is the relative displacement vector from grid cell a to grid cell b , and \mathbf{M}_{ab}^l is the probability of transition from grid cell a to grid cell b . This first moment of the Transition Matrix probability distribution can be interpreted as the expected value of the transition. Using this equation, we can estimate the future location of an Argo float to any time step in the future. An example of the deployed Argo fleet from the May, 2021 snapshot projected from 90 days to 4 years in the future is seen as the colored curves in Figure 4.6.

Argo floats eventually fail, likely due to sensor failure or battery exhaustion. The lifespan of full float functionality is approximately 5 years. In our estimates of the future float distributions, we account for float age by removing floats from the distribution that are over 5 years old. For these examples, we do not include the ongoing replacements that maintain the global array at about 4000 floats.

Figure 4.7 represents the future float PDF as the existing float array operated on by the Transition Matrix; the future float PDF is combined with the UCM, \mathbf{P} , of CM4 to produce an estimate for future CEE, $\hat{\mathbf{P}}$.

4.4.6 Optimal Array Design

An optimal array utilizes the observations of every float to the greatest effect, that is, in this approach, to minimize the expected error variance for the estimated the anomaly of multiple BGC properties from the surface to the 2000 m depth. Our strategy to determine optimum deployment locations is iterative: placing floats in an ideal location one at a time. This means that every time a new float is added to the system, we must find the next best location to deploy a float, or, stated another way, the deployment location that constrains the most variance in the CEE, $\hat{\mathbf{P}}$. Naively, one might assume that deploying in the localized $\hat{\mathbf{P}}$ grid cell of most variance

is the best choice. However, this does not consider the spatial covariance or cross covariances of observations. An observation at one grid cell can constrain variance of the same or different variables many grid cells away. The structure of the CEE can be complicated and difficult to understand. The gravest eigenvector of the CEE will always contain the most variability in the eigenspectrum, and we assume the next best location is the maximum absolute value of this gravest eigenvector.

The iterative strategy is illustrated in Figure 4.7. Starting with an observation operator, \mathbf{H} , which is formed from a distribution of floats (\mathbf{H} can be the null matrix if there are no floats), we calculate a $\hat{\mathbf{P}}$ ($\hat{\mathbf{P}}$ will be \mathbf{P} if this is the first float in the array). Next, we calculate the gravest eigenvector of $\hat{\mathbf{P}}$ and find the location of the maximum sum of absolute value of the eigenvector weights (similar to Eq. 4.18). Finally, we add a float in the optimal array at this location and recalculate $\hat{\mathbf{P}}$. Floats are iteratively added until the maximum number of floats in the simulation has been reached.

The state vector, x , used in these calculations includes BGC variables from CM4 at depths 15 m, 87.5 m, 550 m, and 950 m sub-sampled to a $4^\circ \times 4^\circ$ grid of latitude and longitude. In previous results, we calculated CEE and FME on a single depth level, however because we wished to optimize observation over a wider range of depths, we chose the 4 depth levels to represent the surface, mixed layer, upper ocean, and deep ocean respectively. This method weights all variables, at all depths, equally. Equal weighting might not be the correct choice for all applications, as some variables (such as those related to the carbon cycle) may have more scientific or societal relevancy. Adjusting weights to the relative importance of these observations can easily be done by adjusting σ in Equation 4.17; however, it is outside the scope of this work to recommend alternate weightings.

4.5 Results

4.5.1 Estimates of Variance Constrained by the Current Argo Float Array

The ability of the combined core and BGC Argo float arrays from the May, 2021 snapshot (Argo, 2021) to observe the BGC anomaly fields is quantified here for the first time. Argo locations are used to create an observation operator (\mathbf{H} in Eq. 4.21). This \mathbf{H} is then used to calculate the CEE ($\hat{\mathbf{P}}$ in Eq. 4.14). Figure 4.8 shows the FME (Eq. 4.15) for temperature, salinity, pH, chlorophyll, and oxygen respectively. Figure 4.10 shows the zonal average of unconstrained variance for all variables.

FME depends on the correlation scales for the variables. Generally FME is larger at depth because spatial correlation scales are shorter (although temporal correlation scales may be longer) (Fig. 4.9). The largest FME occurs in the Arctic, where there are very few floats. The Southern Ocean is the region with the next largest mapping error, followed by the tropics. FME is smallest in the northern and southern mid-latitude surface waters. These regions tend to have very long spatial correlation scales.

Rather than minimizing mapping error (Eq. 4.15 and Fig. 4.9) we could choose to minimize CEE, $\hat{\mathbf{P}}$ (Fig 4.10). FME represents how well a region is observed, but even well-observed regions with high variance can have relatively high CEE; an example of this is seen in surface temperature in the northern mid-latitudes (Fig 4.10a). The Arctic shows high CEE in surface salinity and chlorophyll. As the Arctic is almost entirely unobserved by Argo, this means that Arctic variability of CEE and UCM are similar. Maximum pH and oxygen CEE are observed in the subsurface at northern mid-latitudes. The Southern Ocean and Southern Hemisphere mid-latitudes have relatively low FME and CEE. This is due to the impact of the SOCCOM project, which has deployed a substantial number of BGC floats in these regions.

4.5.2 Estimates of Variance Constrained by Monte-Carlo Distributions

Estimates for variance constrained by varying numbers of randomly deployed BGC Argo arrays of varying uniform densities have been calculated (Fig. 4.11). Random distributions of floats were used to create observation operators (\mathbf{H} in Eq. 4.21), which were used to calculate the CEE ($\hat{\mathbf{P}}$ in Eq. 4.14). Fifty Monte Carlo snapshots were calculated for each float density considered, and the results were averaged.

As expected, CEE is inversely proportional to float density for the 5 variables considered. Maximum CEE in temperature, salinity, and chlorophyll occurs in the surface layers, where pH and oxygen have high uncertainty at 100 m and oxygen has maximum uncertainty at depth (Fig. 4.11). High oxygen CEE at depth is due to large unobserved variance in the Sea of Japan. This area is known for bottom water formation (Talley et al., 2003).

The decrease in mapping error is not uniform across variables and depths. Salinity and oxygen have the slowest decrease in FME with increasing floats (hardest signals to constrain), and pH and chlorophyll have the steepest decrease in FME with increasing floats (easiest to constrain). pH has substantial covariance with temperature and oxygen and the FME of pH decreases an average of 12% faster than the mapping error of salinity with increasing floats. This work suggests that additional core Argo floats may need to be augmented with oxygen sensors in order to achieve a mapping error equivalent to that of pH.

When binned by depth, upper-ocean FME, averaged across variables and by depth, had a steeper decline than the deep-ocean with increasing floats; overall upper-ocean FME decreased an average of 6% faster. The upper-ocean is defined as everything shallower than 137.5 m and the deep ocean is defined as everything deeper than 137.5 m.

4.5.3 Estimates of Variance Constrained by Future Argo Floats

The ability of time-evolving Argo float arrays to observe BGC variance is quantified here for the first time. The future CEE, $\hat{\mathbf{P}}$, was calculated by propagating the current float distribution

into the future with the Argo trajectory-based Transition Matrix (Eq. 4.23). The first moment of the Transition Matrix (Eq. 4.24) was used to determine future float locations and construct a future observation operator (\mathbf{H} in Eq. 4.21). The future observation operator was then used to estimate $\hat{\mathbf{P}}$ (Eq. 4.14).

Similar to Section 4.5.2, the unconstrained BGC variance is inversely proportional to the array size. As the array is projected into the future, without replenishment, such that an increasing number of floats are removed due to age, the variance increases. Also, the distribution of highest variance is similar to the results shown in Section 4.5.2: namely, high unconstrained surface variability in temperature, salinity, and chlorophyll, and high unconstrained 100 m variability in pH and oxygen (Figs. 4.12 and 4.13).

To highlight the utility of this method, we deployed 2 hypothetical BGC Argo floats at the start (float 1) and end (float 2) of the GO-SHIP P1 transect that sailed in fall, 2021 (Fig. 4.14). Our method calculated the relative performance of these two hypothetical floats within the context of the natural BGC variability of the ocean (as realized by CM4) within the context of the surrounding float array from the May, 2021 Argo snapshot. The Transition Matrix evolved the position (and accompanying algorithm estimated death) of these and surrounding floats forward through time. $\hat{\mathbf{P}}$ was calculated for each float deployment, and their difference in CEE quantified their relative performance at each timestep. This calculation was done for all BGC variables in this study, from CM4. Float 1 convincingly outperforms float 2 in pH variance constrained in the entire water column and temperature variance constrained at depth throughout the experiment. In contrast, float 2 constrains more salinity and oxygen variance throughout the experiment. Changes in which one float constrains more variance also occur through time, particularly in chlorophyll at 200 m and salinity at the surface and 600 m. Skilled Argo managers are ultimately responsible for maximizing the relative value of observations collected by floats and this is a first step at quantifying the relative importance of potential deployment sites with respect to the assumption here of observing the anomaly from the mean.

4.5.4 Optimal Array Design

An optimal array based on BGC floats has been constructed to best constrain global BGC variability (Fig. 4.15). The method to calculate the optimal array takes an iterative approach by sequentially finding the next best float deployment. The best deployment location is approximated as the maximum absolute value of the sum of variances (Eq. 4.18) of the gravest eigenvector of the CEE ($\hat{\mathbf{P}}$ in Eq. 4.14). The new deployment location is then added to the observation operator (\mathbf{H} in Eq. 4.21), and a new $\hat{\mathbf{P}}$ is calculated. This iterative method is run until the entire array is constructed (Fig. 4.7).

The optimal float array was calculated for 1000 floats, which is the specification for the BGC Argo array (Johnson and Claustre, 2016a), and achieved global coverage (Fig. 4.15a). The meridionally binned optimal array (Fig. 4.15b) does not have a prominent structure; however, the zonally binned optimal array (Fig. 4.15c) has 4 distinct peaks in the distribution: 2 large peaks in the subtropical gyres around 45°N and S, and 2 smaller peaks in the Arctic and on the equator. The algorithm does not favor deployments in the boundaries that exist between the subtropical gyres, and the equator or the Arctic. We hypothesize this is due to the smaller correlation length scales and cross covariances in these regions. The algorithm also does not favor BGC Argo deployments in the western tropical Pacific. This is apparently because there is lower BGC variance in CM4 this region (see appendix).

The efficacy of the optimal array was tested in 2 ways. First, random and optimal arrays were used to constrain uncertainty covariance matrices degraded with Gaussian noise. Second, the optimal array was compared to random arrays of varying number of floats (Fig. 4.16). In the first test, we added gaussian noise with a scaling equal to that of the localization to the UCM and calculated the amount of unconstrained variance (diagonal of CEE) for both 1000 float random arrays and the 1000 float optimal array. The amount of noise added was scaled proportional to the variance at each grid point with signal-to-noise ratios (SNR) ranging from 10^3 to 10^{-2} . To encourage confidence in these results, these calculations were repeated with unique

Gaussian noise and random float arrays 50 times at every SNR. Figure 4.16 shows the optimal array outperformed the random arrays at all levels of SNR although the relative outperformance decreased by half in the noisier cases.

In the second test, the unconstrained variance (diagonal of CEE) was calculated for both the optimal and random arrays with an increasing number of floats. Again, these calculations were repeated with 50 unique random float distributions for each random float density. The 1000 float optimal array constrained an equivalent amount of variance as the mean 1100 float random array (Fig 4.16). Of course this idealized experiment does not take into account the reality that floats are mostly deployed from research ships of opportunity rather than along the most optimal tracks. This experiment does, however, offer insight into regional prioritization of BGC deployments.

4.6 Discussion

4.6.1 Expected Error Variance Structure

We have demonstrated a method to estimate the impact of present and future BGC Argo arrays on constraining variance in the float-observed BGC fields. The results show consistent structures in the CEE (covariance of the expected error) seen in the current, future (projected), and uniformly-distributed arrays. The consistent structure of CEE among these 3 distributions is not surprising because the design criteria for the current Argo fleet is a uniform distribution, so these reflect the same sampling strategy. We observe that the general structure of the CEE matches the structure of the UCM (uncertainty covariance matrix): higher temperature variability in the Northern Hemisphere mid-latitudes, higher salinity and chlorophyll variability in the Arctic, and higher pH and oxygen variability in the Northern Hemisphere mid-latitudes at a depth of 100 m.

The CEE estimate presented here only considered Argo floats. Additional observing platforms such as buoys, gliders, and satellites constrain additional variance that has not been

accounted for here. The largest moored buoy arrays (TAO, RAMA, and PIRATA) are located in the tropics and record high-frequency full-depth observations of temperature, salinity, and limited BGC variables. These observations constrain ocean variance in these regions, and the unconstrained variance in the tropics is undoubtedly lower than the results presented here. Additionally, satellite observations measure important ocean variables such as temperature, salinity, sea surface height, and chlorophyll; consequently, the unconstrained variance in the surface ocean of BGC variables is lower than presented here.

The BGC variance estimates presented are operationally idealized and ignore ice or the difficulty of deploying floats in remote regions. Some of this ocean variability may be unobservable in the real world with Argo floats. While the seasonal extent of the Southern Ocean sea ice cover offers many opportunities for floats to surface during the austral summer, a substantial area in the Arctic is continuously covered. Also, conventional Argo float ballasting has made them unsuitable for the Arctic, although this challenge is being overcome given the grave importance of Arctic monitoring. Because of this, innovations will be necessary for BGC Argo to be included in a viable Arctic observing strategy.

In this analysis, we have only considered the spatial correlation of observations, however, for use in many products like data assimilating models, quantifying the spatio-temporal impact of observations may be a better metric of observing design. At the surface, high temporal variability of surface fluxes is not captured in 10-day sampling and a larger observational uncertainty may be needed to realistically map these fields. At depth, forcing happens on much slower timescales (weeks to months), and information about the state of the deep may persist in the system longer than individual profiles. This means that the observations of multiple profiles could be combined into the same mapped product, similar to the widely used climatologies of Roemmich and Gilson (2009) or data assimilating models (Mazloff et al., 2010). The correlation of the state through time could be quantified in the UCM, $\hat{\mathbf{P}}$, but this would be substantially more computationally expensive.

4.6.2 Optimal Array Recommendations

The optimal array calculates the next best float deployment location for observing the anomaly from the mean. This method assumes the mean of BGC fields is already known. The algorithm prioritizes deployment of the first floats in the northern midlatitudes centered at 40°N and in the southern midlatitudes centered at 45°S . From this analysis, a large initial investment in Southern Ocean BGC deployments through the SOCCOM project was a wise first choice. Building on SOCCOM, the next latitude band this method recommends is centered at 45°N , then the Arctic (if possible), followed by the equator. These results also define which areas should be prioritized for replenishment. With a finite number of BGC floats each year and ships of opportunity to deploy from, the north and south mid-latitudes are prioritized over the tropics.

The relative unimportance of the tropics to BGC variability is not uniform and is concentrated in the western Pacific. In the depths considered, this region has the lowest combined scaled variance (Eq. 4.18) (see appendix). This low variability may be a result of the localization used to construct the UCM; the western tropical Pacific is a region that informs powerful, large scale teleconnections via the shape and extent of western boundary currents, the phase of Madden-Julian oscillations, and the ENSO cycle. This region highlights how array optimization methodologies can lead to different array distribution recommendations and is, in some respects, in contrast to Roemmich, Dean and Alford, Matthew H and Claustre, Hervé and Johnson, Kenneth and King, Brian and Moum, James and Oke, Peter and Owens, W Brechner and Pouliquen, Sylvie and Purkey, Sarah and others (2019) which calls for a doubling of Argo floats (which includes BGC floats) on the equator. We recommend BGC Argo managers carefully review the BGC signals they wish to observe before making a significant investment of BGC Argo floats in the western tropical Pacific.

The method employed to draw these conclusions about the optimal BGC float array has limitations: it inherits the biases and uncertainties of the CM4 model on which the prior covariances are based, as well as the narrower set of BGC variables in CM4 compared with

BGC Argo; additionally, we only consider 4 depth levels and use an approximate method to site floats. With more computing power, it would be possible to calculate full depth eigenvectors and covariances. These estimates only consider spatial covariances and could differ significantly if space and time covariances were used. Finally, sequential algorithms may not be the best way to identify the full array. Alternate algorithms exist that solve for the ideal distribution of floats simultaneously (Hastings, 1970) and may offer improvements to the amount of variance the optimal array can constrain, but are computationally more expensive and have not been investigated here.

4.7 Conclusion

The covariance of the expected error (CEE) of the existing, future, and uniformly-distributed BGC Argo float array has been quantified for the first time, and an optimal BGC Argo array is suggested. We find that the structure of unconstrained variance for the uniformly-distributed BGC Argo arrays as well as the May, 2021 snapshot both in static form and projected into the future all match the underlying structure of the of the prior variance: high surface temperature variance in the northern mid-latitudes, high surface chlorophyll and salinity variance in the Arctic, and high pH and oxygen variance at 100 m in the northern mid-latitudes. We also observe the spatial covariance length scales to be significantly longer at the surface than at depth; this results in subsurface maxima of formal mapping error (FME) for all variables and may be a result of not using the space-time covariance. The Monte-Carlo experiment found that pH and chlorophyll were relatively easy to constrain, and oxygen and salinity were relatively hard to constrain; salinity sensors are already deployed on all core and BGC Argo floats, while reducing oxygen variance may require additional deployment of oxygen sensors on core Argo floats.

A Transition Matrix, calculated from all existing Argo trajectories (Chamberlain et al., 2022), was combined with the model CM4 covariances to produce estimates of variance constrained in the future. This prediction was done for the existing full Argo array and also

demonstrated the relative variance constrained by two hypothetical floats in the Pacific in the context of surrounding Argo floats. These products and code are now publicly available for use by the broader Argo management community. In addition to an operational tool, we suggest that these maps of current and future Argo array performance are useful for communicating the importance of sustained investment in Argo to both funding agencies and the general public. By specifically quantifying the effectiveness of each float, the impact of each one is less abstract. The next logical step in this research is to translate the unconstrained variance into uncertainty in fluxes or bulk inventories of BGC variables, which would further quantify the direct impacts of BGC Argo observations.

The optimal array experiment identifies the Northern and Southern Hemisphere mid-latitudes as the best place to initially deploy BGC Argo floats and an area that should be prioritized for BGC Argo array maintenance. The western tropical Pacific was identified as a region of low BGC variability, requiring sparser BGC Argo coverage. Comparing the optimal array to random arrays, we found that the optimal array outperformed the random array by 100 floats or 10% on average, corresponding to obtaining equivalent mapping performance with a cost savings of more than \$7.5M over 5 years under current BGC Argo pricing.

As already noted, significant assumptions are made in developing these methods. This work is a first step toward an observations-driven approach to quantifying the effectiveness of present and future BGC Argo arrays.

4.8 Appendix

4.8.1 Comparison of Spatial Distribution of Sum of Variances

The result that the western tropical Pacific has less BGC variance is not fully supported in the figures presented in this paper. A potential criticism could be that the scaling, σ , we have applied to the data in Eq. 4.17 has skewed the results. Here we expand the justification.

We begin by showing the time series of the Black Sea and the western tropical Pacific: a

region of high combined variance and low combined variance respectively (Fig. 4.17). While salinity variance is relatively low in the Black Sea, temperature, pH, chlorophyll, and oxygen variance are orders of magnitude higher and the combined results are substantially larger than the western tropical Pacific BGC signal.

Scaling biogeochemical data is necessary in order to compare the relative importance of variables importance of observations. Section 4.8.3 illustrates this: the un-normalized variance of unconstrained variables covers 10 orders of magnitude from a minimum un-normalized variance of oxygen to a maximum un-normalized variance of temperature. A uniform scaling in Eq. 4.18 will be dominated by surface temperature variance.

To test the scaling used, we consider 2 alternate cases for σ : first, a scaling that is equal to the minimum or maximum value of the variance of each variable at each depth level, and, second, a scaling equal to the median of the variance at each depth level. After some testing (not demonstrated here), we realized that a scaling based on the extremes of the distribution produced suboptimal results, and we defaulted to the median. The field resulting from Eq. 4.18 with both the median σ and Eq. 4.17 σ are plotted in Figure 4.18. Comparing these 2 cases, we see that the largest effect of the scaling is to reduce the relative variance in the Black Sea (region of largest variability) and the Arctic (region of second largest variability) (Fig. 4.18). The reduced BGC variability in the western tropical Pacific is seen in both plots. From this, we can see that Eq. 4.17 σ reduces the dynamic range of variability and in so doing highlights a fundamental assumption about our analysis: all of the ocean is biogeochemically important to observe and no region should be singularly prioritized or ignored. This produces an optimal array that is more uniformly-distributed and not concentrated in the Black Sea and boundary currents.

The optimal array algorithm places a float in a location that constrains maximum variance. This is done by finding the maximum absolute value of the sum of the variances (Eq. 4.18) of the eigenvector. This is largely controlled by the variance at a grid point and the spatial and inter-variable cross covariances. The cross covariances are not obvious and can be significantly greater or smaller than expected. The length scale of spatial covariance appears to be largely

informed by variability in the mesoscale eddy structure and front locations. The inter-variable cross covariance seems to be largely informed by water mass properties or large scale physical forcing. The culmination of these two can manifest in unexpected ways, which is why we adopt the eigenvector scheme.

This analysis shows the combined variance in the western tropical Pacific is characteristically low. As this variance is a significant piece of where the algorithm chooses to deploy floats, it is not unreasonable to see an array with few floats deployed in this region.

4.8.2 Impact of scaling on the data

The raw and scaled data are plotted in Figure 4.19. The left side of the figure shows the variance of the raw data from the CM4 model. The right side of the figure shows the variance of the data after it has been scaled. The variance in the unscaled data can cover 4 orders of magnitude or more. The scaling imposes an artificial democratization where the relative importance of the gridpoint with the largest variance can, at most, be 15 times greater than the smallest. The scaling was tuned to remove the extremes of the variability distribution while preserving as much signal as possible. All the low variance extremes are removed by setting the minimum scaled variance of the system to the 15th percentile as described in the text. Setting the maximum scaled variance to be a multiple of the lower variance restricts the dynamic range of the variability so that different BGC variables at different depths can be meaningfully compared to one another. Salinity at 550 m is the most impacted by this upper limit with variability artificially capped at the 32nd percentile. The average upper bound over depths and variables exists at the 13th percentile of variances. This choice is not expected to be perfect, and can be adjusted to improve the optimization. The point here is to make the array design and evaluation reproducible.

4.8.3 Total Variance Before Observation

The total variance of the system is the diagonal elements of the uncertainty covariance \mathbf{P} , prior to observation. The zonally averaged variance of each variable can be seen in Figure 4.20.

4.9 Acknowledgements

This work was supported by the SOCCOM project under NSF Award PLR-1425989 and Global Ocean Biogeochemical Array (GO-BGC) under NSF Award OCE-1946578. We thank Dr. Matthias Morzfeld for many helpful conversations during the development of these methods. Chapter 4, in full, has been submitted for publication of the material as it may appear in Journal of Atmospheric and Oceanic Technology, 2022, Chamberlain, P. M., Talley, L. D., Cornuelle, B., Mazloff, M. R., & Gille, S. T., American Meteorological Society 2022. The dissertation author was the primary investigator and author of this paper.

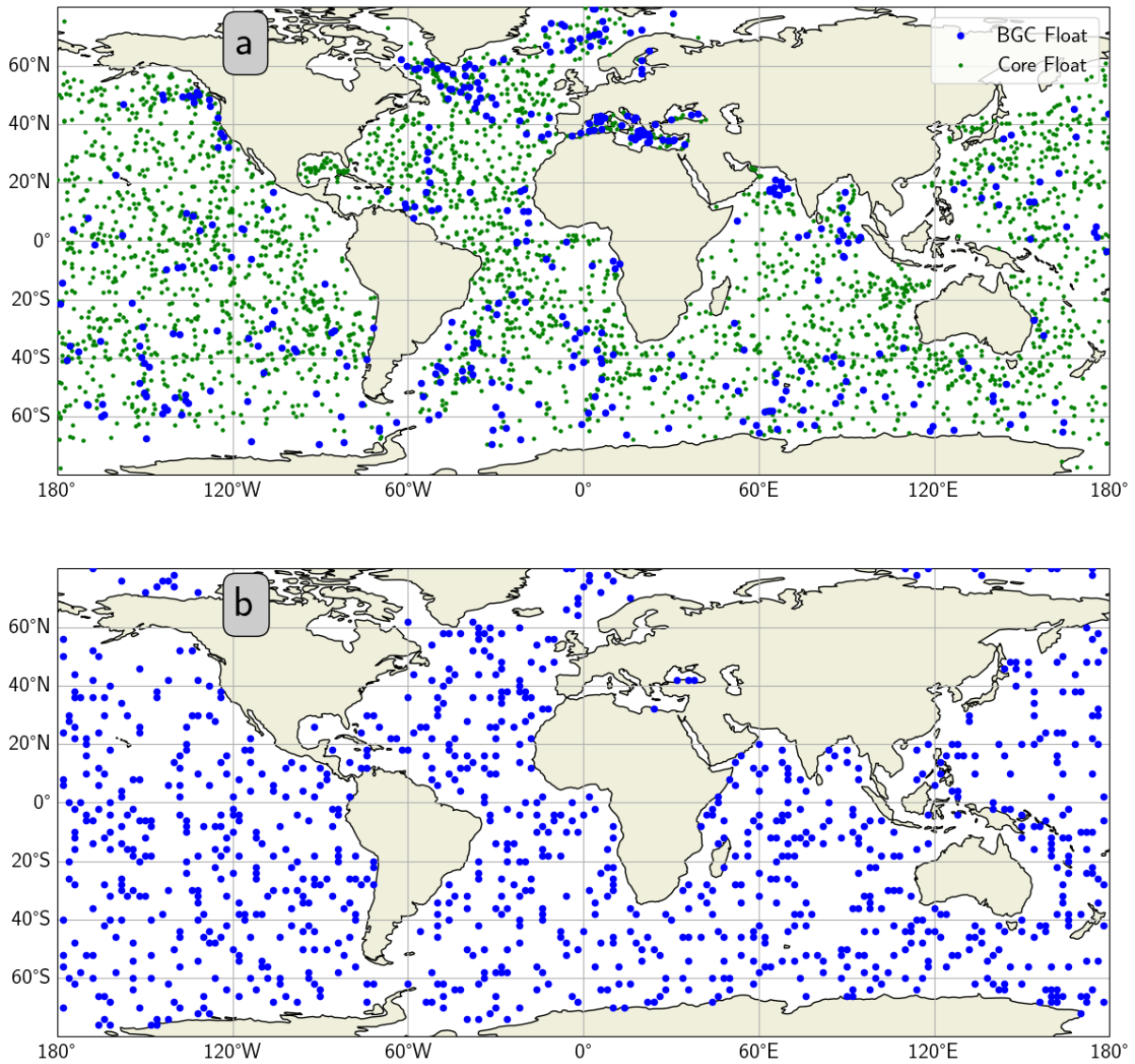


Figure 4.1. a) Map of May, 2021 snapshot Core and BGC Argo floats and b) example of random BGC float locations. Green dots are Core Argo floats, blue dots are BGC floats.

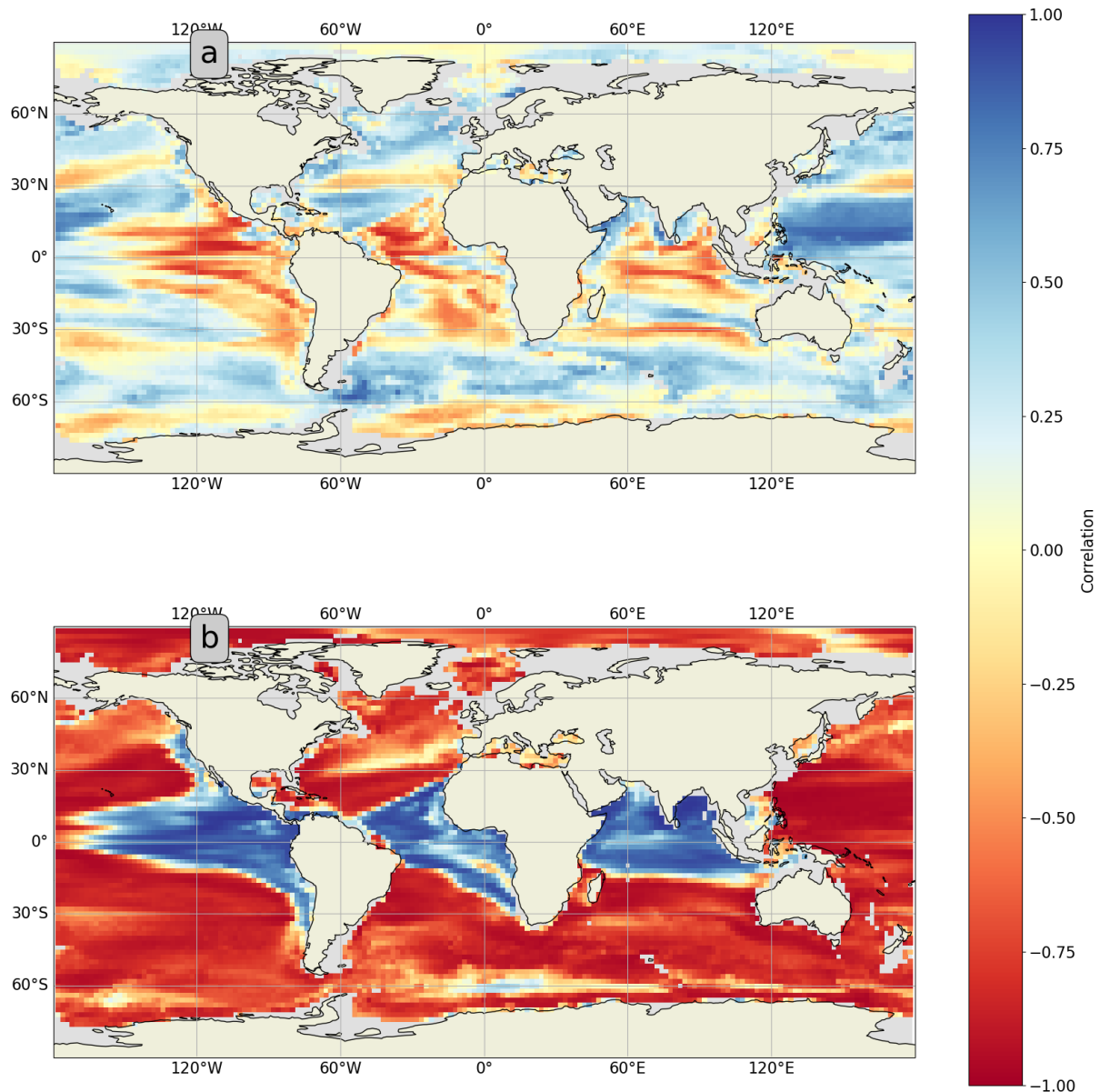


Figure 4.2. Global Climate Model (CM4) (Held, IM and Guo, H and Adcroft, A and Dunne, JP and Horowitz, LW and Krasting, J and Shevliakova, E and Winton, M and Zhao, M and Bushuk, M and others, 2019; Adcroft, Alistair and Anderson, Whit and Balaji, V and Blanton, Chris and Bushuk, Mitchell and Dufour, Carolina O and Dunne, John P and Griffies, Stephen M and Hallberg, Robert and Harrison, Matthew J and others, 2019) correlation maps of a) chlorophyll and oxygen and b) temperature and oxygen at a depth of 100 m. Colored shading represents strength of correlation. Beige shading represents land. Gray areas are too shallow to be calculated in simulations.

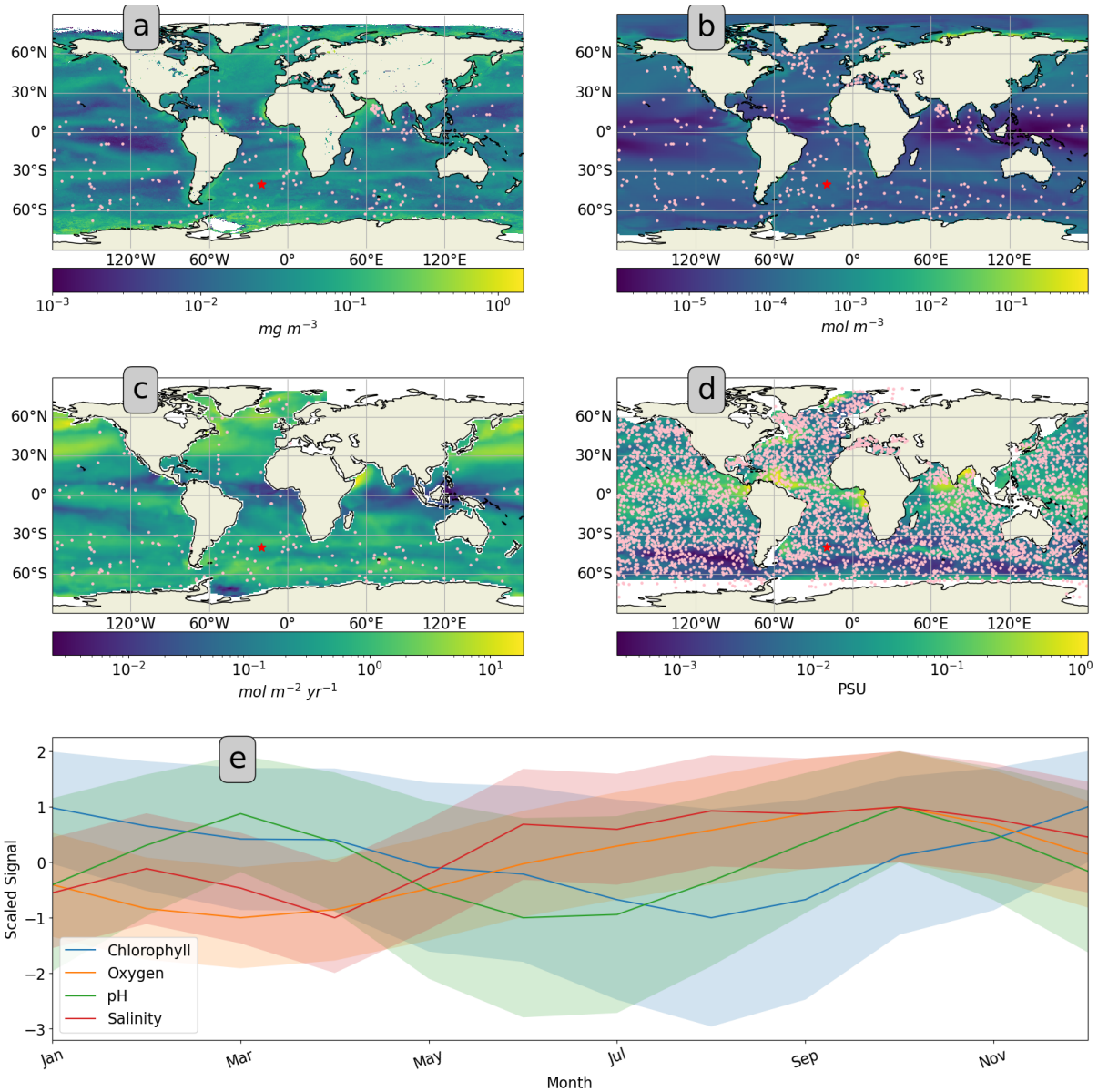


Figure 4.3. (a-d) Maps of standard deviation of a) chlorophyll (Data, 2022), b) oxygen (CM4), c) CO₂ flux (Landschützer et al., 2016), d) salinity (Roemmich and Gilson, 2009). Pink dots represent deployed floats with a sensor equipped to measure the plotted variable. Colored shading represents the standard deviation of the variable. Beige shading is land. e) Monthly mean and anomaly from annual mean normalized by standard deviation: chlorophyll (blue line), oxygen (orange line), pH (green line), and salinity (red line) at 40°S, 20°W (denoted by red star on all maps).

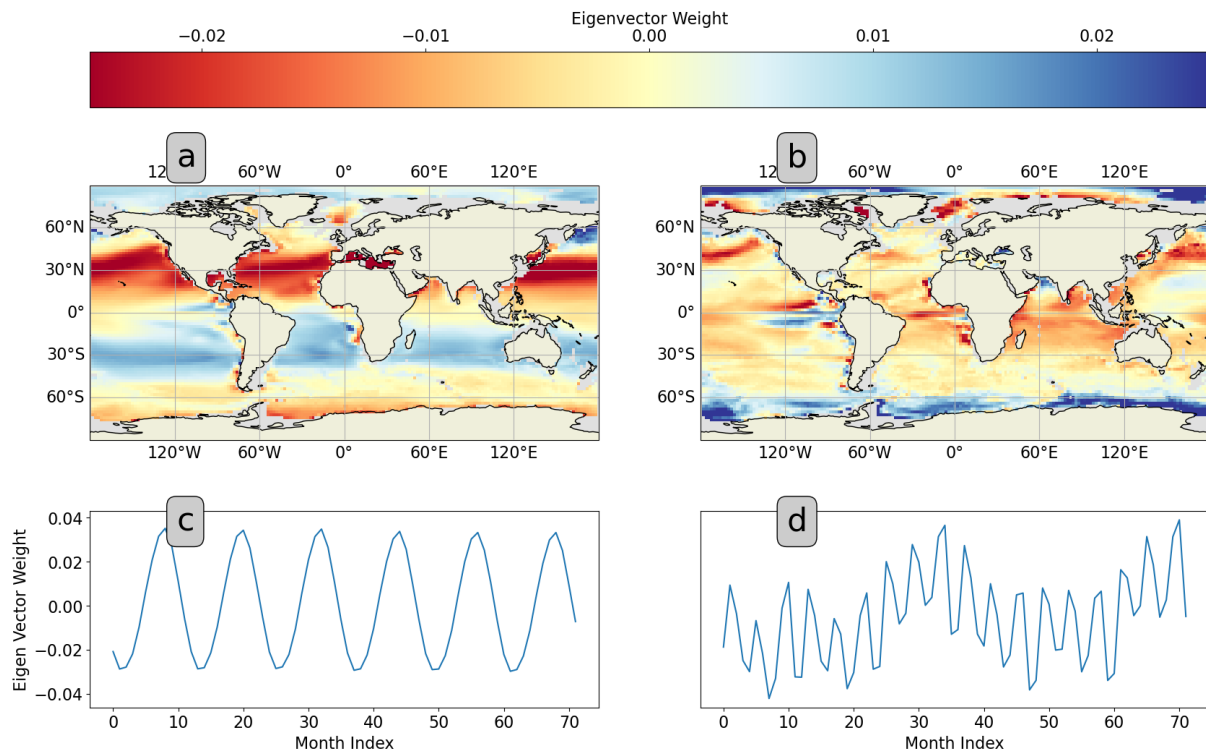


Figure 4.4. (a and b) CM4 maps of eigenvectors of spatial surface pH covariance for a) the gravest mode and b) the 7th eigenmode. Colored shading represents the covariance weighting, beige shading indicates land. (c and d) 72 month subsets of eigenvectors of temporal surface pH covariance for c) the gravest mode and d) the 7th eigenmode. Gravest mode explains 14.0% of the variance, 7th eigenmode explains 0.8 % of the variance.

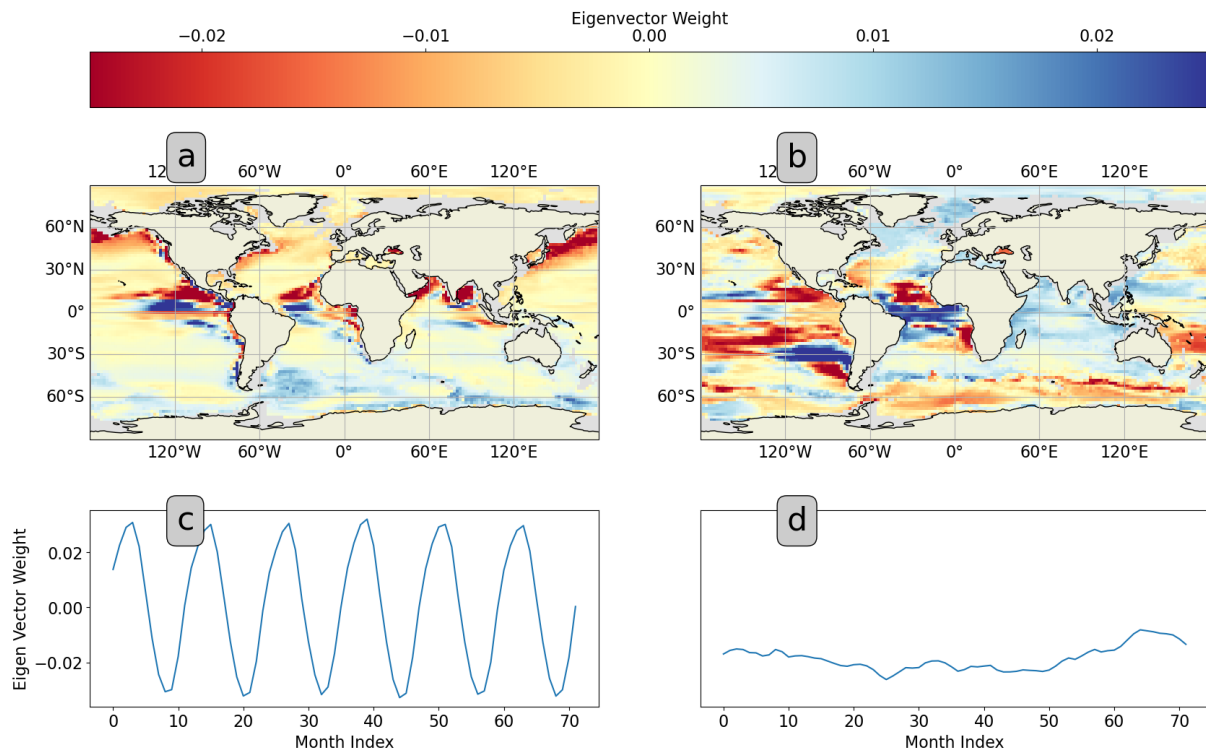


Figure 4.5. (a and b) CM4 maps of eigenvectors of spatial pH covariance for a) the gravest mode at 100 m depth and b) the gravest mode at 1000 m depth. Colored shading represents the covariance weighting, beige shading indicates land. (c and d) 72 month subsets of eigenvectors of temporal pH covariance for c) the gravest mode at 100 m depth and d) the gravest mode at 1000 m depth. Gravest mode at 100 m depth explains 15.5% of the variance, gravest mode at 1000 m depth explains 6.9 % of the variance.

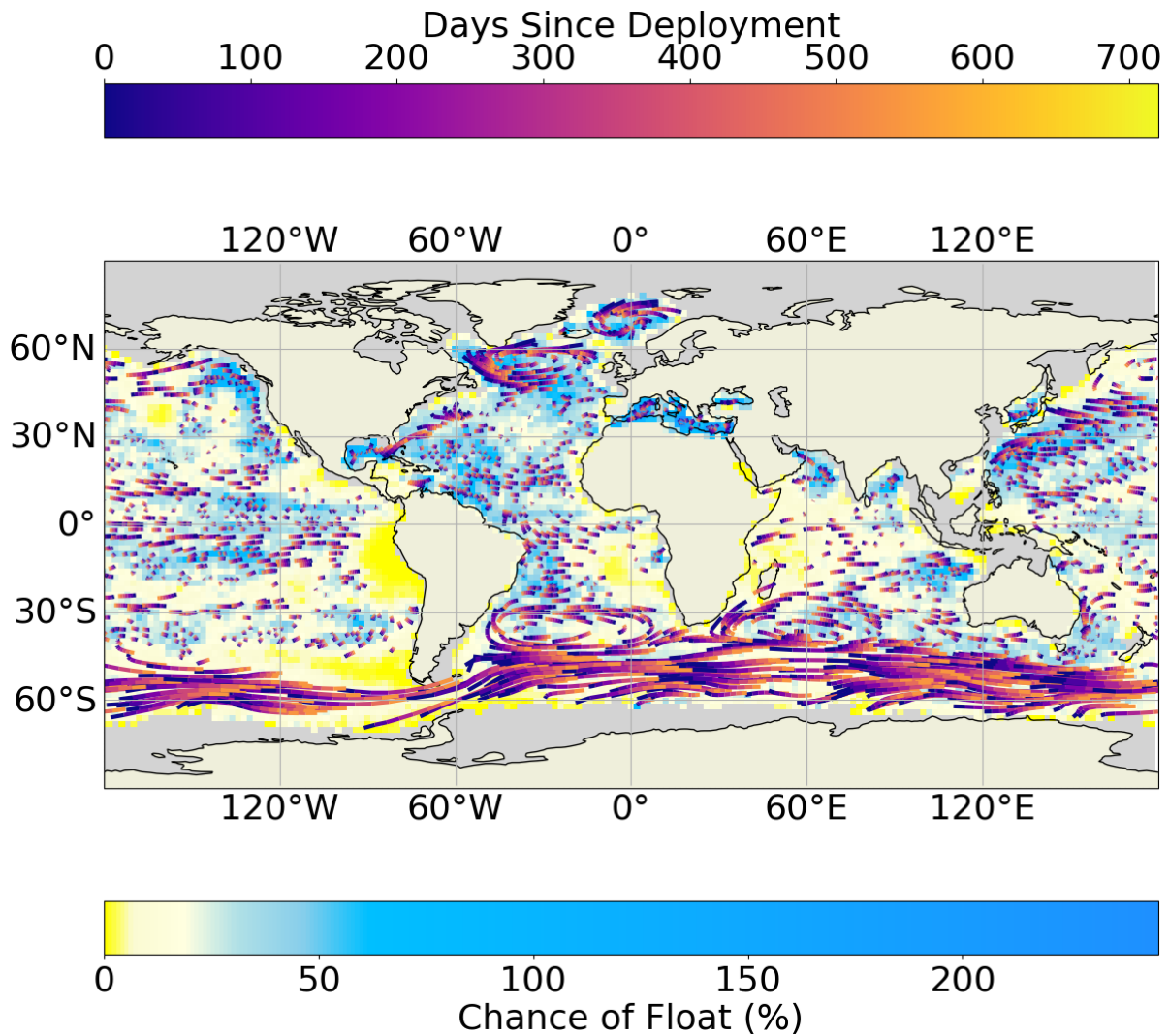


Figure 4.6. Two year prediction of array density of global Core Argo array. Argo array distribution is based on the May, 2021 snapshot (Argo, 2021) using the Transition Matrix (Chamberlain et al., 2022) (Eq. 4.23). Colored lines represent time of mean transition (t in Eq. 4.24). Grid cell shading represents estimated array density. Gray shading represents areas outside domain of the Transition Matrix; beige shading represents land.

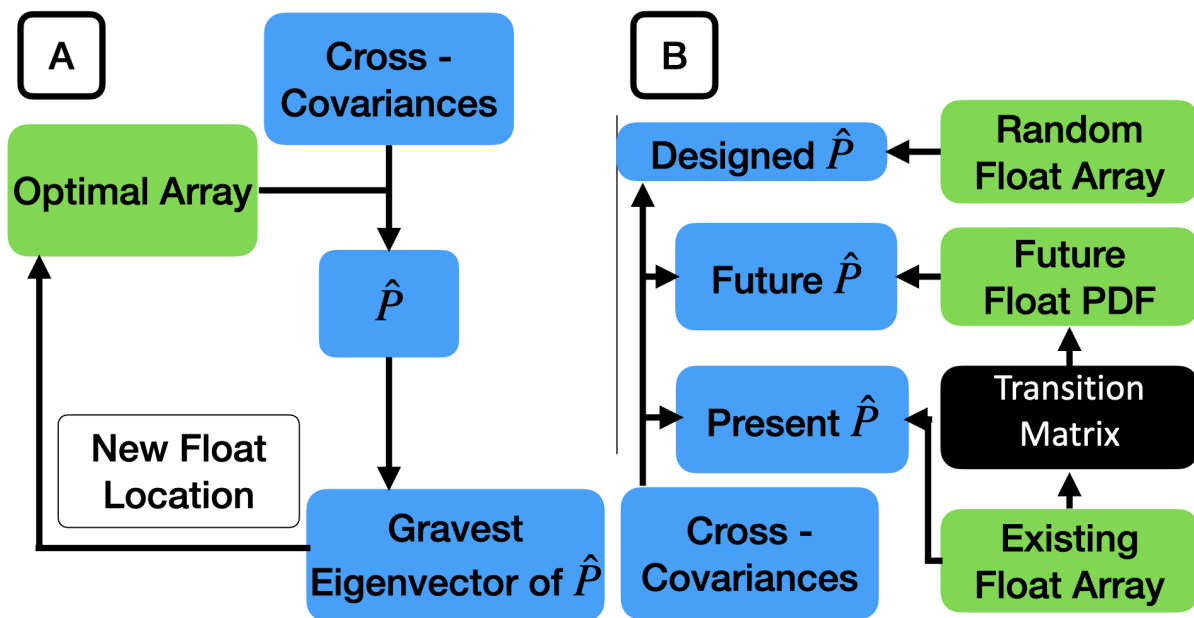


Figure 4.7. a) Flowchart of optimal deployment locations and b) organization of variance products. Covariance of the expected error (CEE), \hat{P} , is calculated from Equation 4.14, future float PDF is calculated from Equation 4.23.

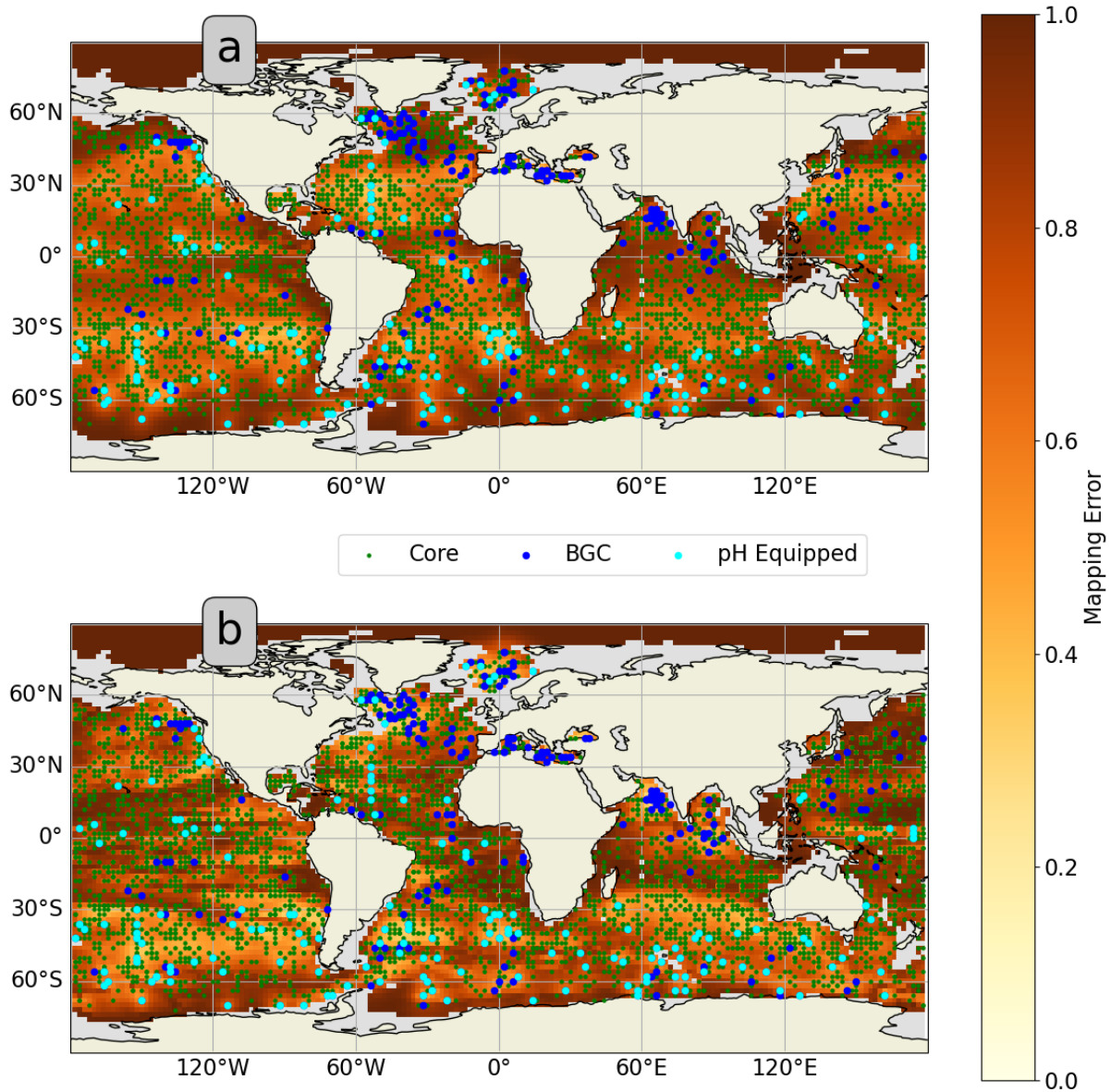


Figure 4.8. Scaled pH formal mapping error (FME) of existing core and BGC Argo float array taken from May, 2021 snapshot at a) the surface and b) 1000 meters. Colored shading represents amount of unconstrained variance. Beige shading represents land. Gray areas are too shallow. Green dots represent core Argo floats. Blue dots represent BGC Argo floats without pH sensors. Cyan dots represent BGC floats equipped with pH sensors.

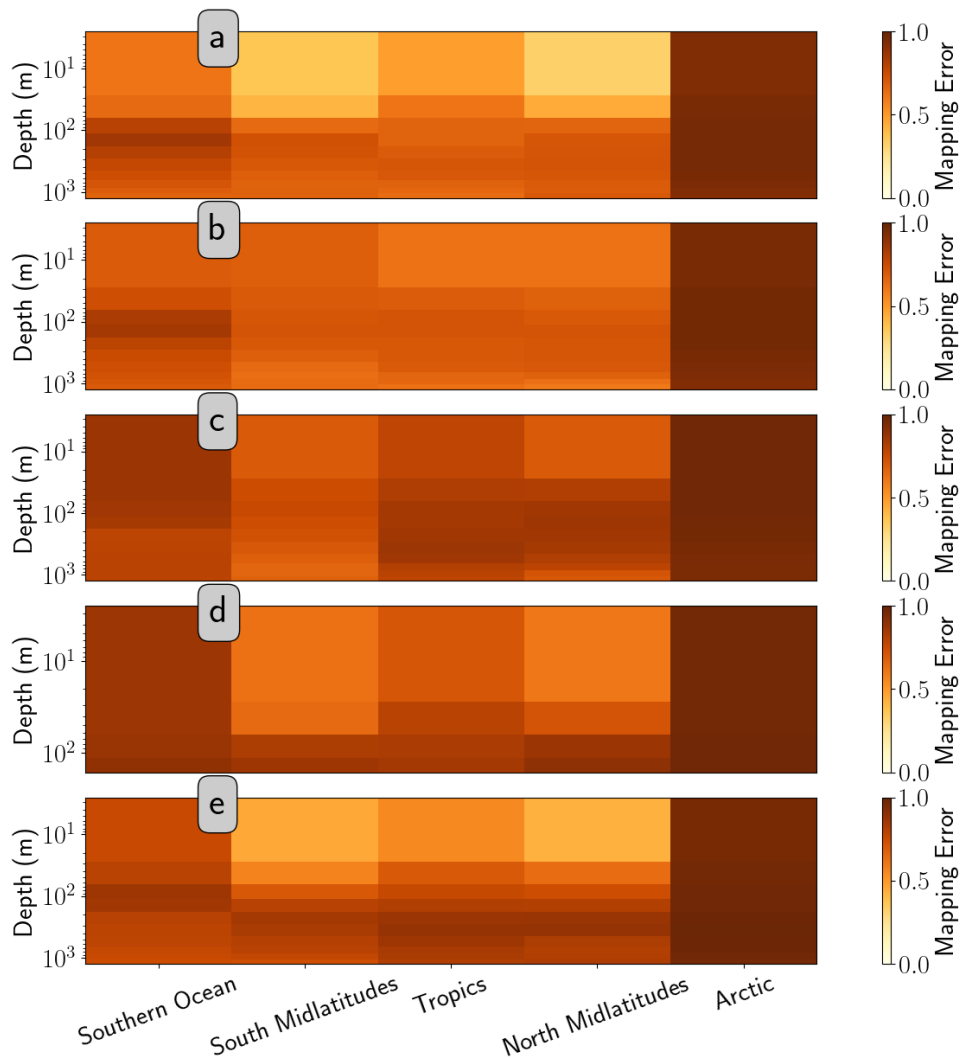


Figure 4.9. Zonal average formal mapping error (FME) of existing Argo core and BGC float array at all depths of a) temperature, b) salinity, c) pH, d) chlorophyll, and e) oxygen. (Zones are defined by Southern Ocean: south of 60°S, South Midlatitudes: 60°S - 20°S, Tropics: 20°S - 20°N, North Midlatitudes: 20°N - 60°N, Arctic: north of 60°N.)

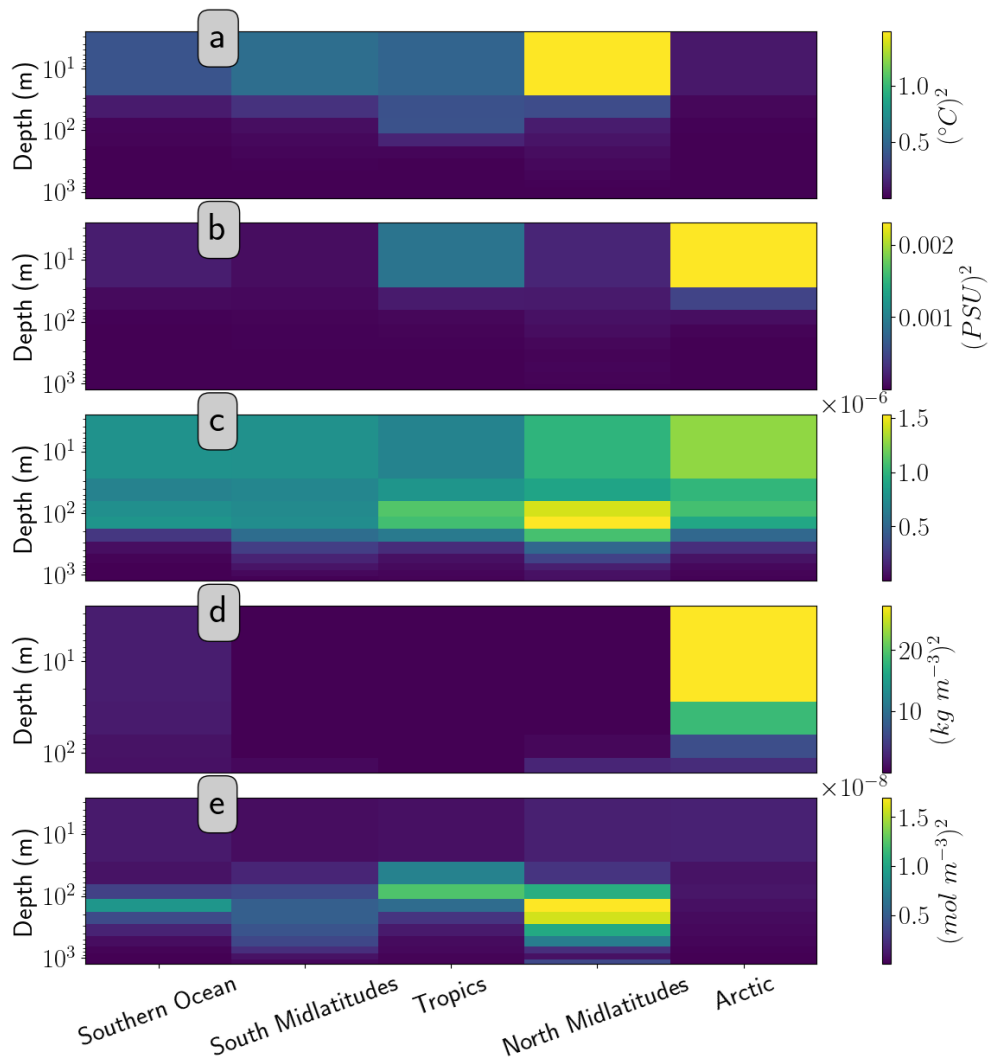


Figure 4.10. Zonal average covariance of the expected error (CEE) of existing Argo core and BGC float array at all depths, of a) temperature, b) salinity, c) pH, d) chlorophyll, and e) oxygen. (Zones are defined by Southern Ocean: south of 60°S , South Midlatitudes: $60^{\circ}\text{S} - 20^{\circ}\text{S}$, Tropics: $20^{\circ}\text{S} - 20^{\circ}\text{N}$, North Midlatitudes: $20^{\circ}\text{N} - 60^{\circ}\text{N}$, Arctic: north of 60°N .)

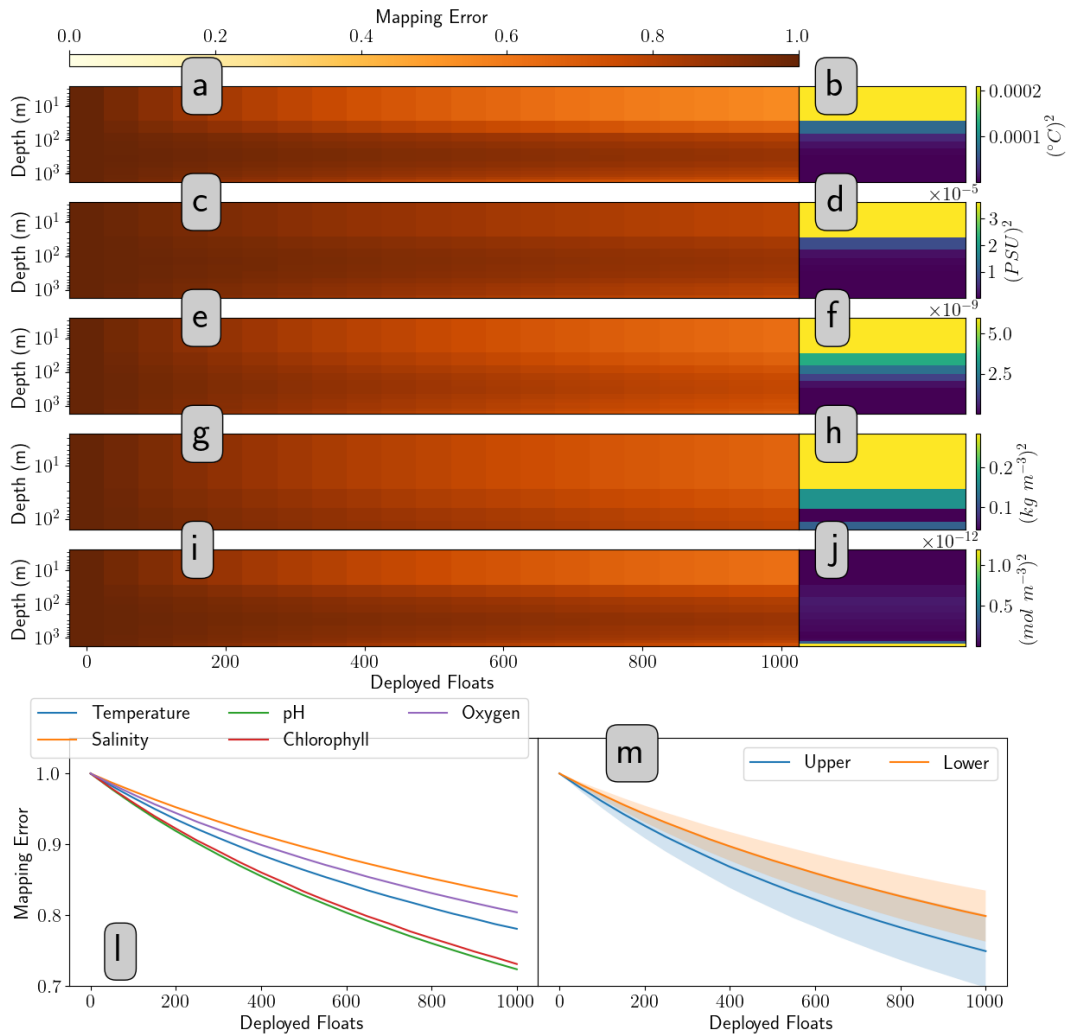


Figure 4.11. a-j) Global average of formal mapping error (FME) of randomly distributed Argo floats for increasing float density (left column), and covariance of the expected error (CEE) for 1000 BGC floats (right column) at all depths of a,b) temperature, c,d) salinity, d,e) pH, e,f) chlorophyll, and f,j) oxygen. l) Colored lines represent depth averaged FME by variable for increasing Argo float density. m) Colored lines represent variable averaged FME for upper and lower ocean depths. Upper ocean is defined as shallower than 137.5 m and deep is defined as deeper than 137.5 m. Shading represents standard deviation across all variables.

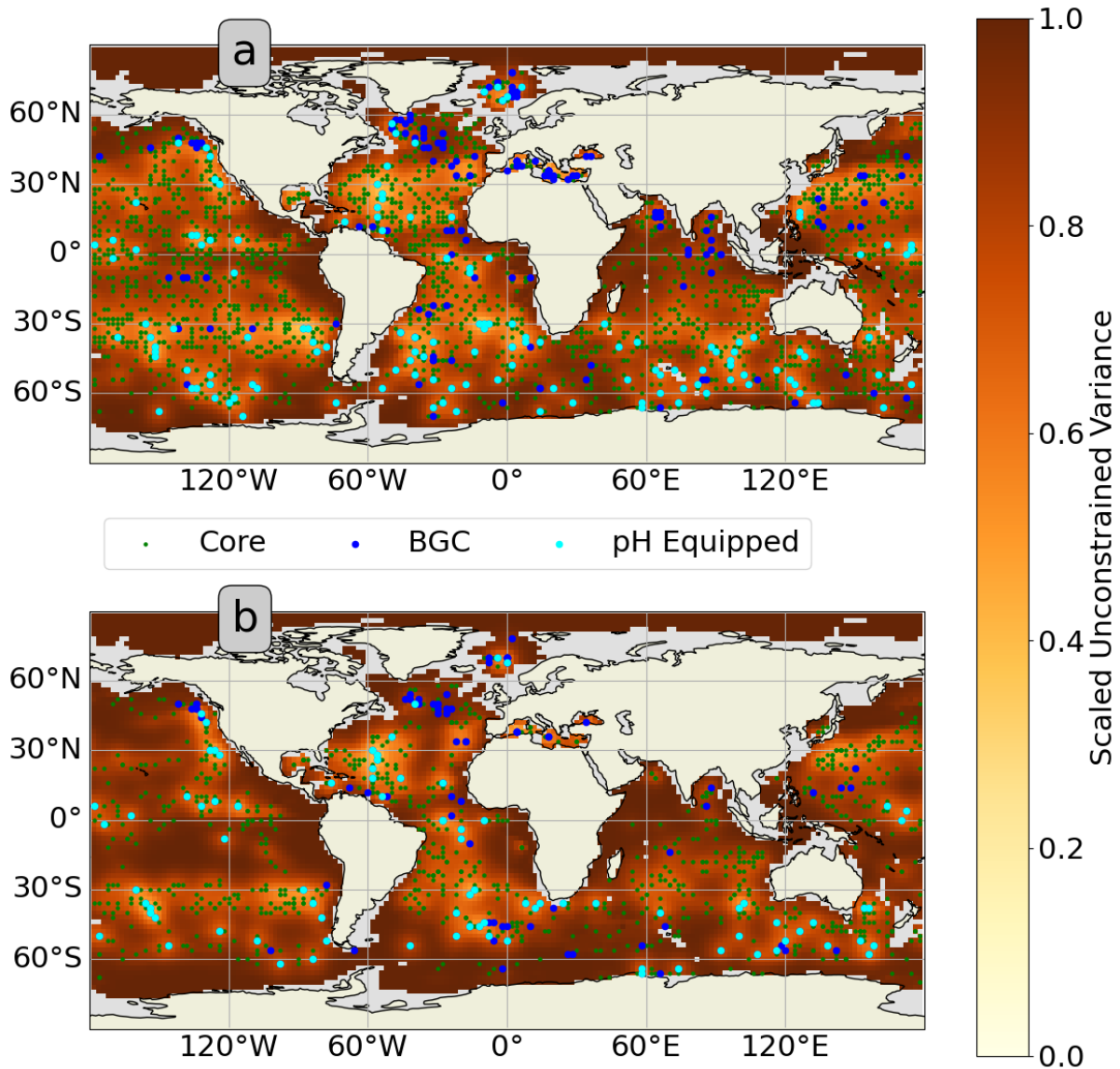


Figure 4.12. Scaled surface pH formal mapping error (FME) of the Argo float array of May, 2021, projected at a) one and b) two years into the future assuming floats are not replenished. Colored shading represents amount of FME. Beige shading represents land. Gray areas are too shallow to be calculated in simulations. Green dots represent location of existing core Argo floats. Blue dots represent location of existing BGC Argo floats. Cyan dots represent floats equipped with pH sensors.

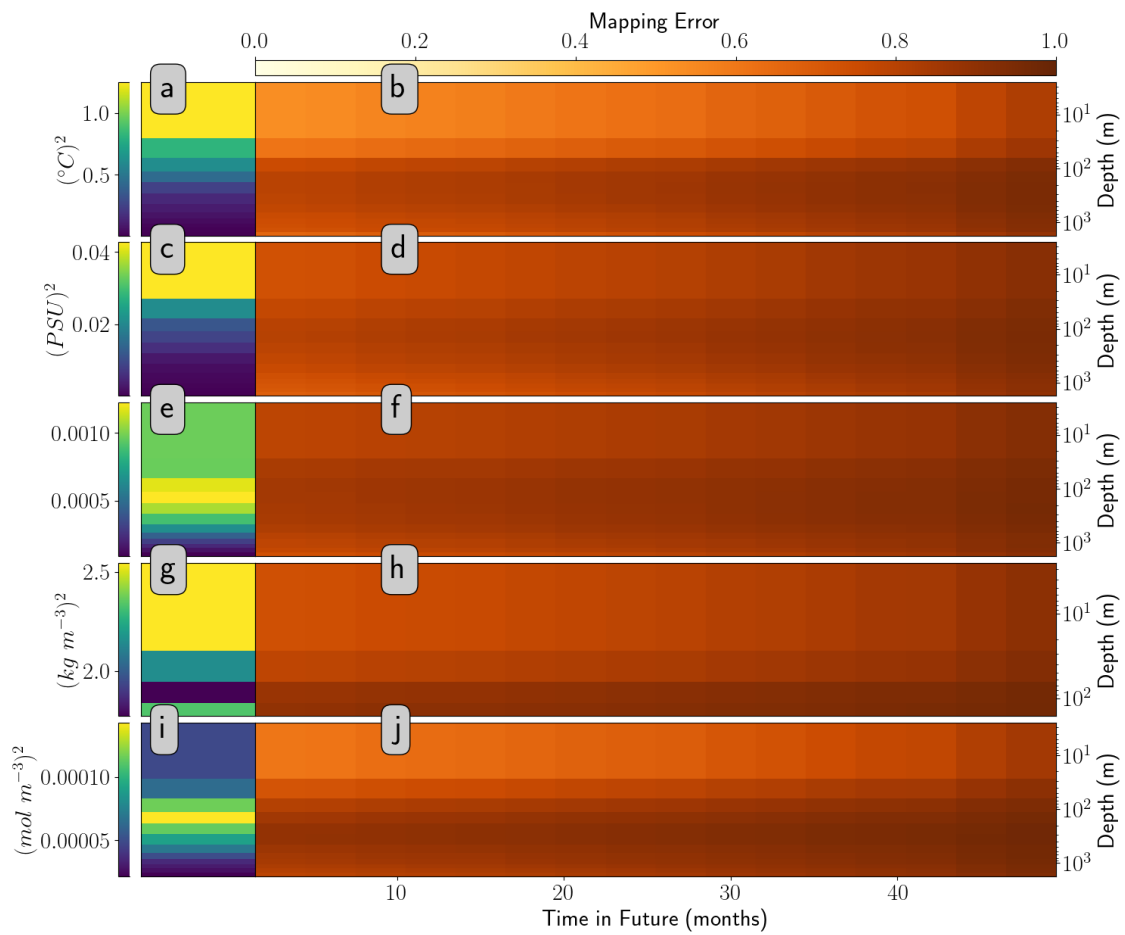


Figure 4.13. Global average of the covariance of the expected error (CEE) of the existing core and BGC Argo float array (left column) and formal mapping error (FME) of the predicted Argo array at all depths (right column): a,b) temperature, c,d) salinity, e,f) pH, g,h) chlorophyll, and i,j) oxygen

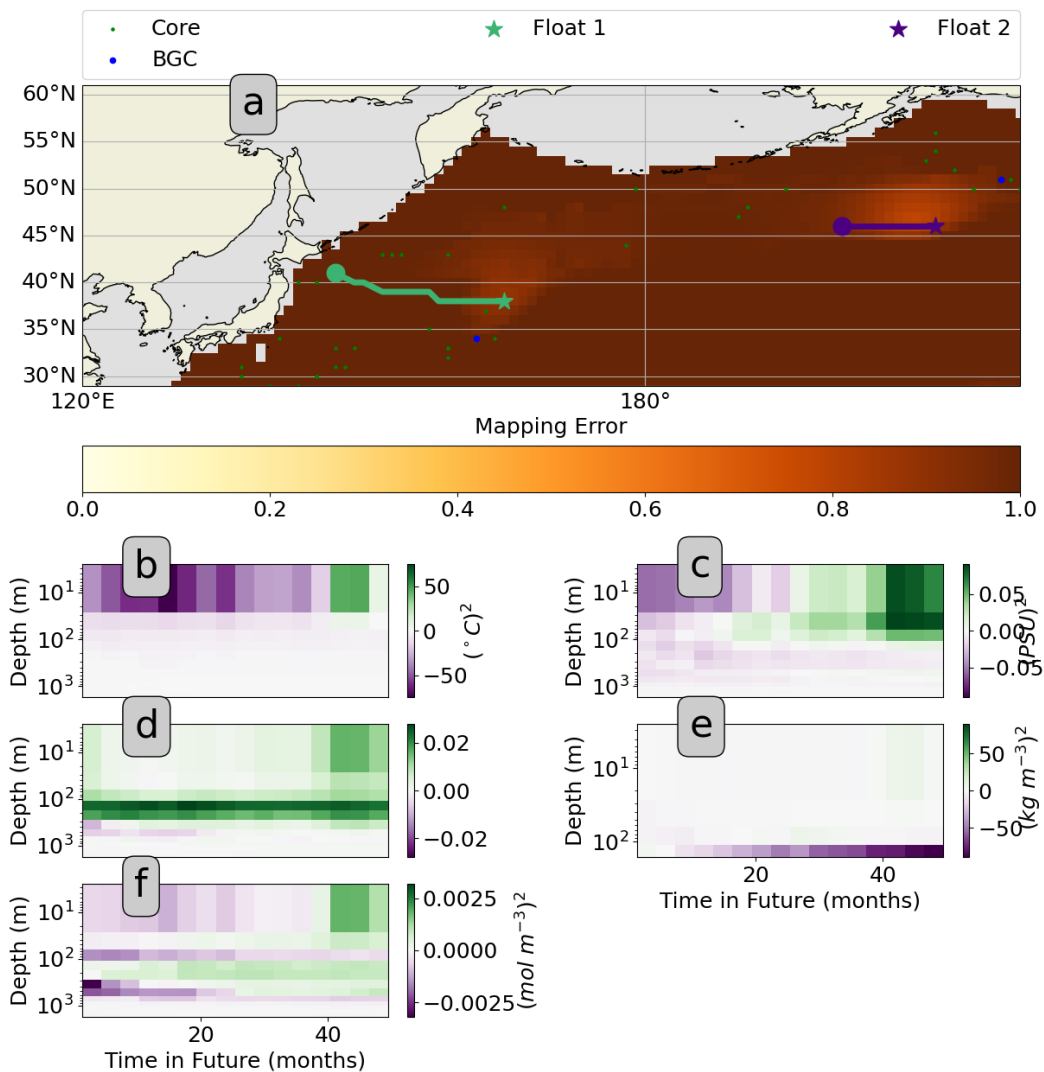


Figure 4.14. a) Formal mapping Error (FME) and tracklines of 2 hypothetical floats deployed along the P1 GO-SHIP line 48 months after deployment with surrounding Argo infrastructure as represented by the May, 2021 snapshot. All Argo floats (hypothetical and real) are propagated into future with Transition Matrix. Green dots represent core Argo floats, blue dots represent BGC Argo floats. Teal and purple circles represent deployment locations, teal and purple lines are tracklines, and teal and purple stars represent final locations of float 1 and float 2 respectively. Gray shading indicates region outside of model domain. Beige shading indicates land, colored shading indicates mapping error. b-f) Difference of float 1 and float 2 Expected Error Variance for b) temperature, c) salinity, d) pH, e) chlorophyll, and f) oxygen. Green shading indicates float 1 constrains more variance and purple shading indicates float 2 constrains more variance.

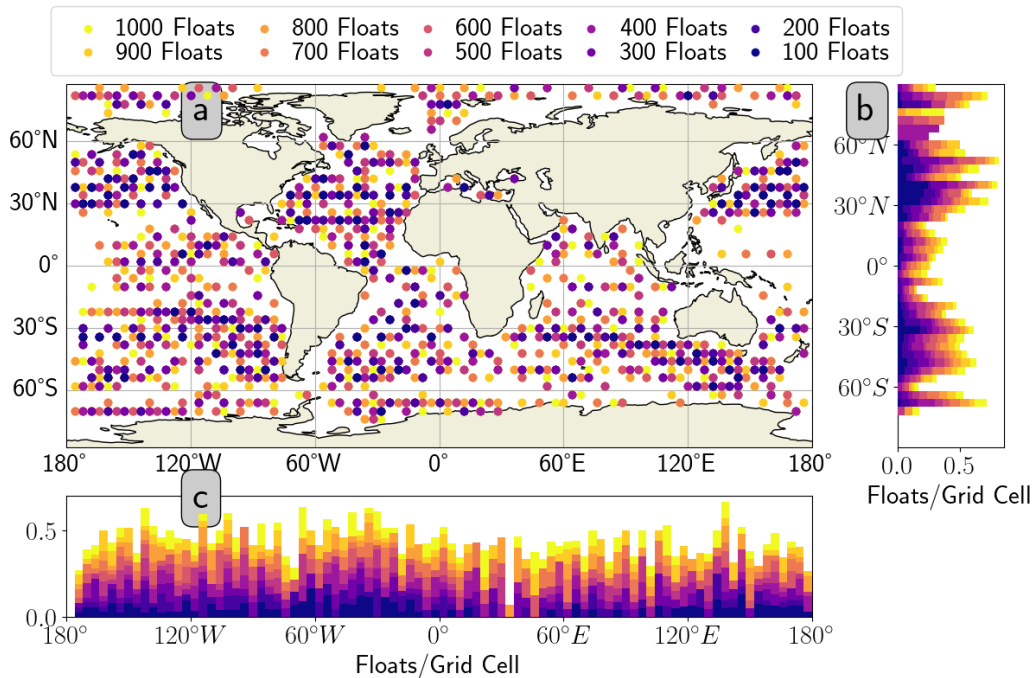


Figure 4.15. a) Map of the optimal distribution of 1000 BGC Argo floats with a grid spacing of approximately 6° in latitude and longitude. Dots represent ideal BGC Argo float locations for observing the BGC anomalies from the mean. State vector used for calculation is based on 4 depth levels (15 m, 87.5 m, 550 m, and 950 m) of CM4 BGC output at a grid spacing of 4° in latitude and longitude. Beige shading indicates land. b) Histogram of zonally binned optimal array. c) Histogram of meridionally binned optimal array. Both histograms binned in increments of 6° latitude and longitude respectively. Colored shading indicates when in the sequential calculation floats were deployed.

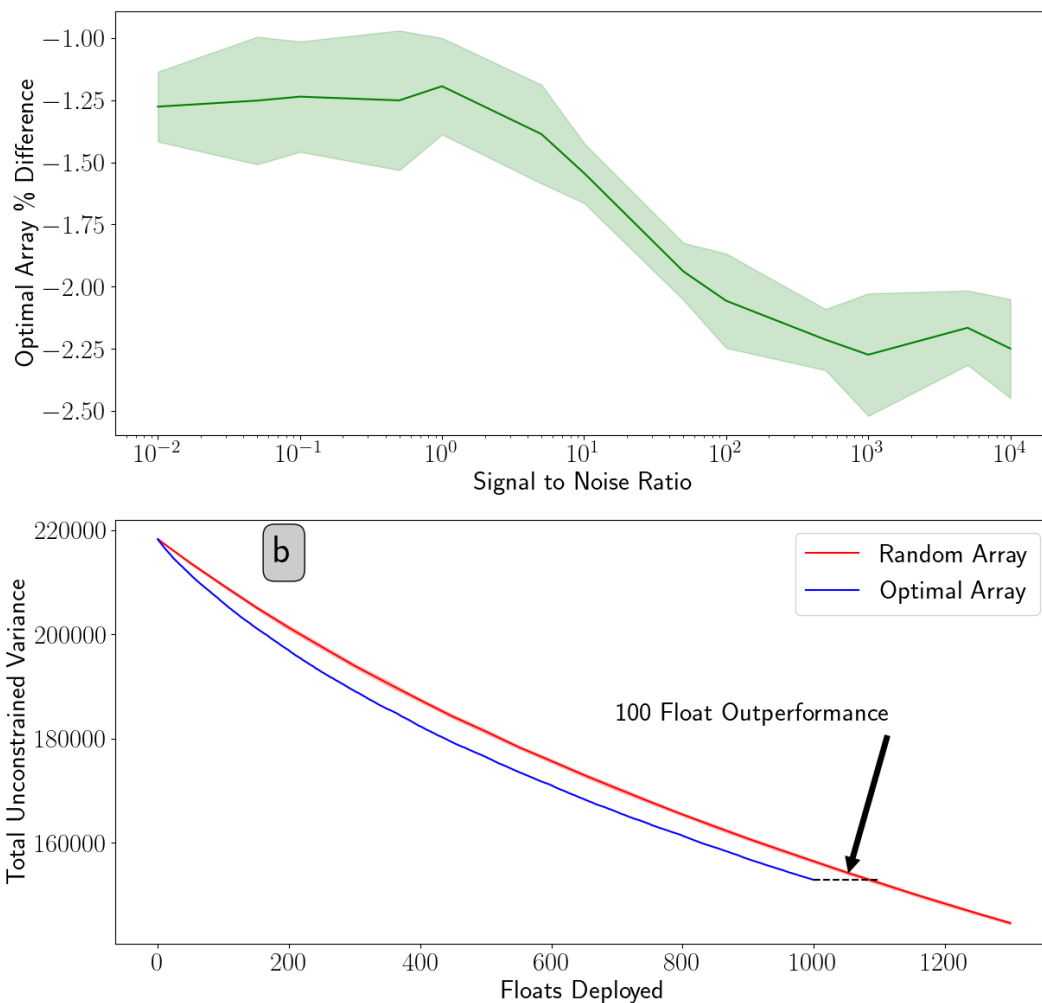


Figure 4.16. a) Relative unconstrained variance - diagonal of the covariance of the expected error (CEE) - of randomly distributed 1000 float arrays and the optimal 1000 float array with Gaussian noise added to the CEE at varying signal to noise ratios (SNRs). Calculations were repeated 50 times at each SNR. Green line represents mean of ensemble of calculations, green shading represents standard deviation of ensemble of calculations. b) Unconstrained variance - diagonal of CEE - of randomly distributed and optimal float arrays of increasing distributions. Blue line represents variance constrained by the optimal array, red line represents mean of variance constrained by random array.

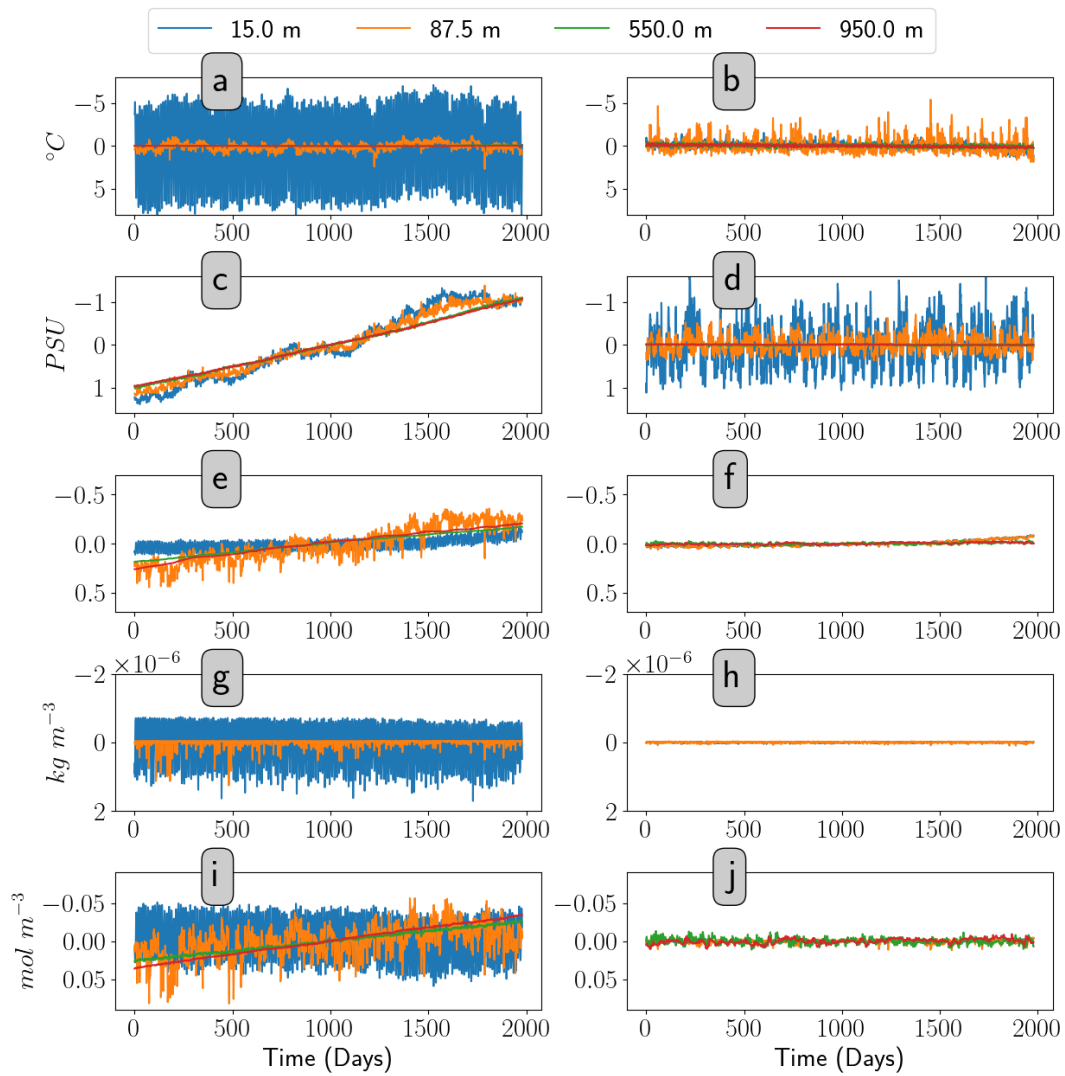


Figure 4.17. a,c,e,g,i) Raw CM4 time series in the Black Sea (location of very high variance) and b,d,f,h,j) raw CM4 time series in the western tropical Pacific (location of very low variance of temperature, salinity, pH, chlorophyll, and oxygen respectively). Mean removed from both timeseries.

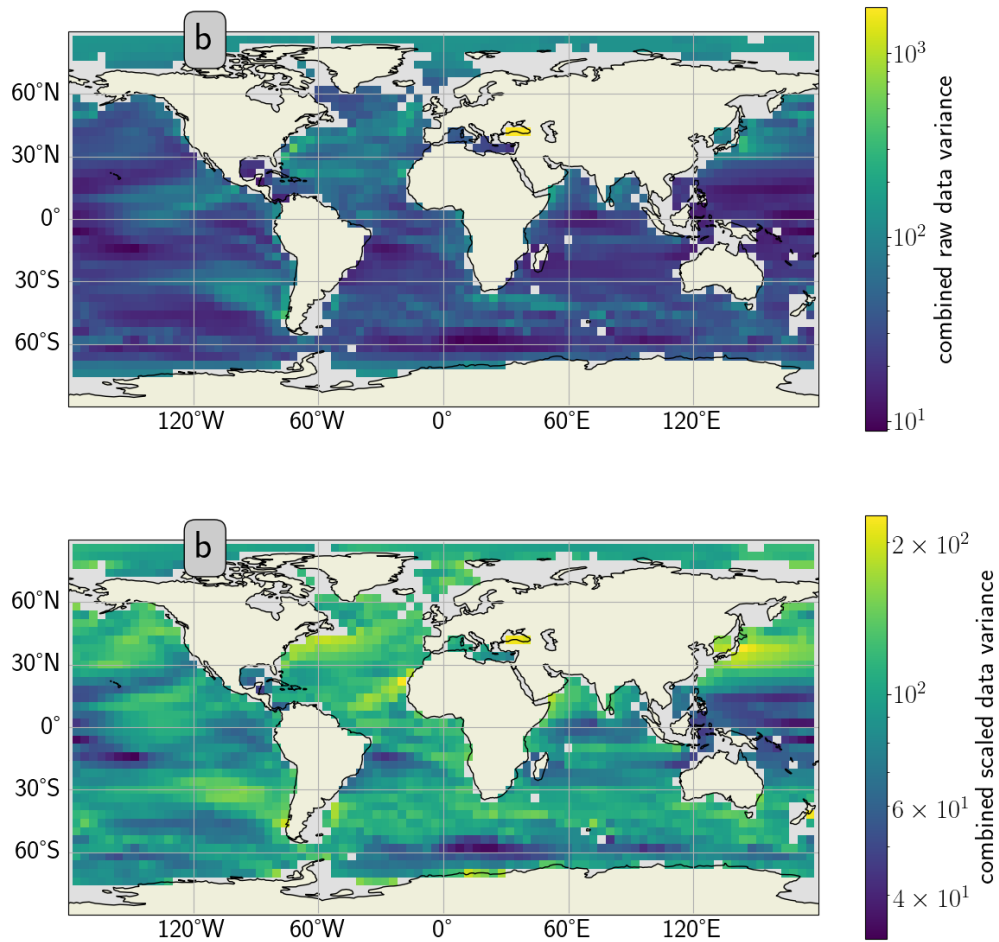


Figure 4.18. Sum of total variance at 4 depth levels considered in optimal array where individual variables are a) scaled by the median of the temporal standard deviation distribution, b) scaled as described in Eq. 4.17.

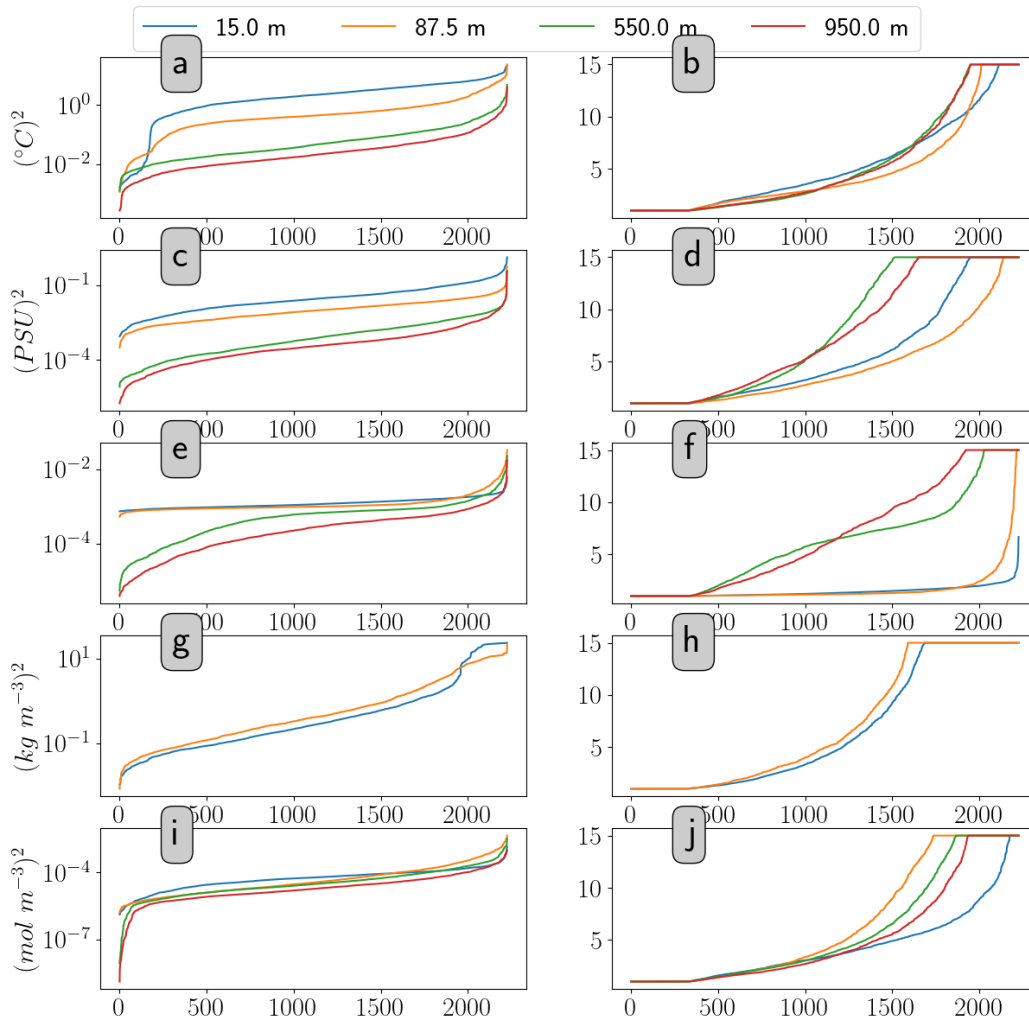


Figure 4.19. a,c,e,g,i) Raw CM4 data temporal variance and b,d,f,h,j) scaled CM4 temporal variance of temperature, salinity, pH, chlorophyll, and oxygen respectively. Variance was calculated at each of the 4 depth levels and sorted from smallest to largest in dataset.

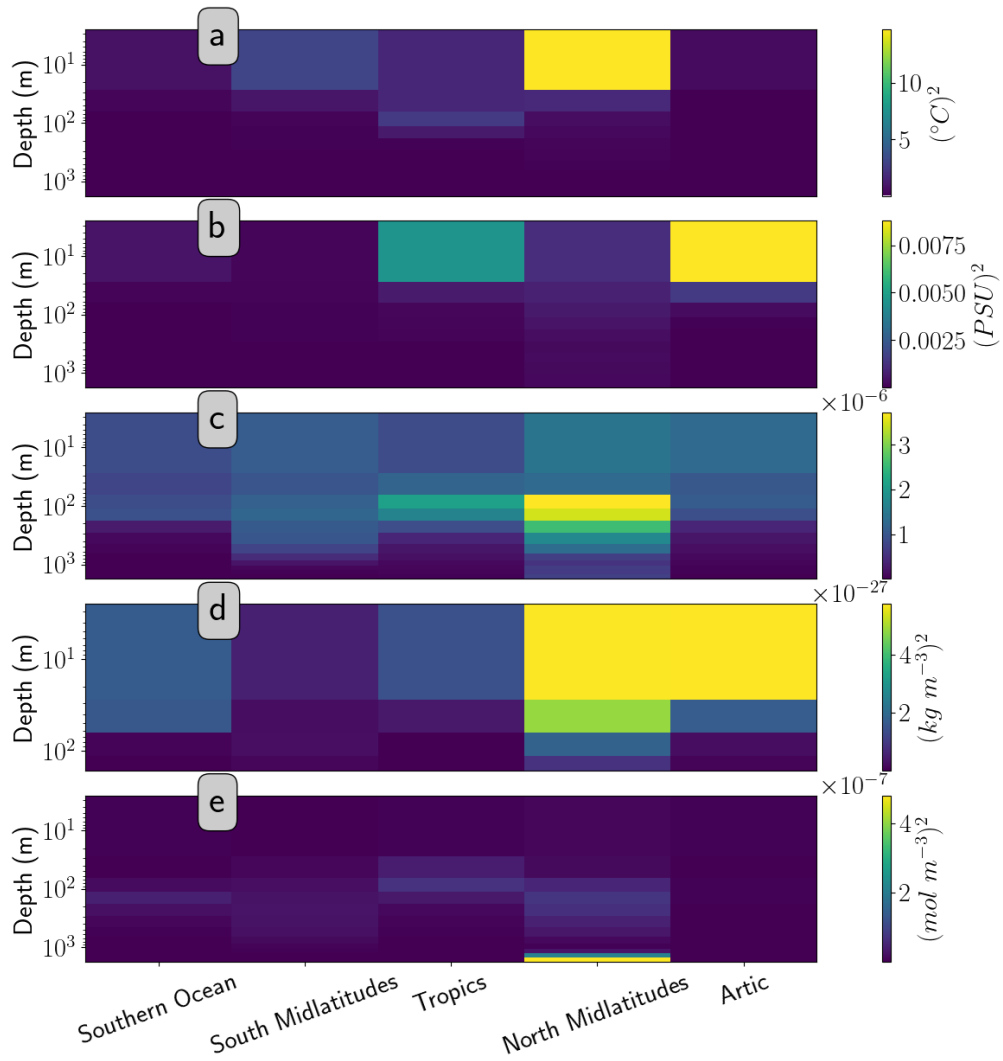


Figure 4.20. Zonal average of total variance for all variables and depths

Bibliography

Ryan P Abernathy, Ivana Cerovecki, Paul R Holland, Emily Newsom, Matt Mazloff, and Lynne D Talley. Water-mass transformation by sea ice in the upper branch of the southern ocean overturning. *Nature Geoscience*, 9(8):596, 2016.

Einar P Abrahamsen. Sustaining Observations in the Polar Oceans. *Philosophical Transactions of the Royal Society A: Mathematical, Physical and Engineering Sciences*, 372(2025):20130337, 2014.

Adcroft, Alistair and Anderson, Whit and Balaji, V and Blanton, Chris and Bushuk, Mitchell and Dufour, Carolina O and Dunne, John P and Griffies, Stephen M and Hallberg, Robert and Harrison, Matthew J and others. The GFDL global ocean and sea ice model OM4. 0: Model description and simulation features. *Journal of Advances in Modeling Earth Systems*, 11(10): 3167–3211, 2019.

C Amante and BW Eakins. ETOPO1 1 Arc-minute Global Relief Model: Procedures, Data Sources and Analysis. NOAA Technical Memorandum NESDIS NGDC-24. *National Geophysical Data Center, NOAA*, 10:V5C8276M, 2009.

J Antonov, D Seidov, T Boyer, R Locarnini, A Mishonov, H Garcia, O Baranova, M Zweng, and D Johnson. World Ocean Atlas 2009, Vol. 2, Salinity, edited by S. Levitus, 184 pp. *US Gov. Print. Off., Washington, DC*, 2010.

Argo. Argo Float Data and Metadata from Global Data Assembly Centre (Argo GDAC) - Snapshot of Argo GDAC of October 8th 2019. *SEANOE*, 2019. doi: <https://doi.org/10.17882/42182{\#}67548>.

Argo. Argo Float Data and Metadata from Global Data Assembly Centre (Argo GDAC) - Snapshot of Argo GDAC of May 10st 2021. *SEANOE*, 2021. doi: [10.17882/42182#83717](https://doi.org/10.17882/42182#83717).

ARTOA. ARTOA. <https://www.whoi.edu/instrument/rafos/artoa-float-tracking>, 2017. Accessed: 2017-9-12.

Dhruv Balwada, Kevin G Speer, Joseph H LaCasce, W Brechner Owens, John Marshall, and Raffaele Ferrari. Circulation and Stirring in the Southeast Pacific Ocean and the Scotia Sea

- Sectors of the Antarctic Circumpolar Current. *Journal of Physical Oceanography*, 46(7): 2005–2027, 2016.
- Dhruv Balwada, Joseph H LaCasce, Kevin G Speer, and Raffaele Ferrari. Relative Dispersion in the Antarctic Circumpolar Current. *Journal of Physical Oceanography*, 51(2):553–574, 2021.
- Andrew Barnard, Ronnie Van Dommelen, Emmanuel Boss, Burkhard Plache, Vlad Simontov, Cristina Orrico, Dave Walter, Marlon Lewis, and Daryl Carlson. A new paradigm for ocean color satellite calibration and validation: Accurate measurements of hyperspectral water leaving radiance from autonomous profiling floats (hypernav). *Earth and Space Science Open Archive*, page 10, 2018. doi: 10.1002/essoar.10500047.1.
- Olaf Boebel. The expedition of the research vessel” polarstern” to the antarctic in 2008/2009 (ant-xxv/2). *Berichte zur Polar-und Meeresforschung (Reports on Polar and Marine Research)*, 595, 2009.
- Olaf Boebel, Claudia Schmid, and Walter Zenk. Flow and Recirculation of Antarctic intermediate water Across the Rio Grande Rise. *Journal of Geophysical Research: Oceans*, 102(C9):20967–20986, 1997.
- Olaf Boebel, Johann Lutjeharms, Claudia Schmid, Walter Zenk, Tom Rossby, and Charlie Barron. The Cape Cauldron: A Regime of Turbulent Inter-Ocean Exchange. *Deep Sea Research Part II: Topical Studies in Oceanography*, 50(1):57–86, 2003.
- Francis P Bretherton, Russ E Davis, and CB Fandry. A technique for objective analysis and design of oceanographic experiments applied to mode-73. In *Deep Sea Research and Oceanographic Abstracts*, volume 23, pages 559–582. Elsevier, 1976.
- Seth M Bushinsky, Alison R Gray, Kenneth S Johnson, and Jorge L Sarmiento. Oxygen in the southern ocean from argo floats: Determination of processes driving air-sea fluxes. *Journal of Geophysical Research: Oceans*, 122(11):8661–8682, 2017.
- Seth M Bushinsky, Peter Landschützer, Christian Rödenbeck, Alison R Gray, David Baker, Matthew R Mazloff, Laure Resplandy, Kenneth S Johnson, and Jorge L Sarmiento. Re-assessing southern ocean air-sea co2 flux estimates with the addition of biogeochemical float observations. *Global Biogeochemical Cycles*, 33(11):1370–1388, 2019.
- Wenju Cai, Arnold Sullivan, and Tim Cowan. Interactions of ENSO, the IOD, and the SAM in CMIP3 models. *Journal of Climate*, 24(6):1688–1704, 2011.
- Ethan C Campbell, Earle A Wilson, GW Kent Moore, Stephen C Riser, Casey E Brayton, Matthew R Mazloff, and Lynne D Talley. Antarctic offshore polynyas linked to southern hemisphere climate anomalies. *Nature*, 570(7761):319–325, 2019.

- Janet W Campbell. The lognormal distribution as a model for bio-optical variability in the sea. *Journal of Geophysical Research: Oceans*, 100(C7):13237–13254, 1995.
- Carval, Thierry and Keeley, Robert and Takatsuki, Yasushi and Yoshida, Takashi and Schmid, Claudia and Goldsmith, Roger and Wong, Annie and Thresher, Ann and Tran, Anh and Loch, Stephen and others. Argo user’s manual v3. 2. 2015.
- Ivana Cerovečki and Matthew R Mazloff. The spatiotemporal structure of diabatic processes governing the evolution of SubAntarctic mode water in the Southern Ocean. *Journal of Physical Oceanography*, 46(2):683–710, 2016.
- Ivana Cerovečki, Lynne D Talley, and Matthew R Mazloff. A comparison of southern ocean air–sea buoyancy flux from an ocean state estimate with five other products. *Journal of climate*, 24(24):6283–6306, 2011.
- Ivana Cerovečki, Lynne D Talley, Matthew R Mazloff, and Guillaume Maze. Subantarctic mode water formation, destruction, and export in the eddy-permitting Southern Ocean state estimate. *Journal of Physical Oceanography*, 43(7):1485–1511, 2013.
- Paul Chamberlain, Talley L. D., Mazloff M., van Sebille E., Gille S. T., Tucker T., Scanderbeg M., and Robbins P. Using existing Argo trajectories to predict future float positions and determine optimal deployment locations. *JTECH*, 2022. submitted.
- Paul M Chamberlain, Lynne D Talley, Matthew R Mazloff, Stephen C Riser, Kevin Speer, Alison R Gray, and Armin Schwartzman. Observing the Ice-Covered Weddell Gyre with Profiling Floats: Position Uncertainties and Correlation Statistics. *Journal of Geophysical Research: Oceans*, 123(11):8383–8410, 2018.
- Data. NASA Goddard Space Flight Center, Ocean Ecology Laboratory, Ocean Biology Processing Group, 2022.
- RE Davis, LA Regier, J Dufour, and DC Webb. The autonomous lagrangian circulation explorer (alace). *Journal of atmospheric and oceanic technology*, 9(3):264–285, 1992.
- Russ E Davis. Observing the General Circulation with Floats. *Deep Sea Research Part A. Oceanographic Research Papers*, 38:S531–S571, 1991.
- Damien G Desbruyères, Sarah G Purkey, Elaine L McDonagh, Gregory C Johnson, and Brian A King. Deep and abyssal ocean warming from 35 years of repeat hydrography. *Geophysical Research Letters*, 43(19), 2016.
- Fabrizio D’Ortenzio, H el oise Lavigne, Florent Besson, Herv e Claustre, Laurent Coppola, Nicole Garcia, Agathe La es-Huon, Serge Le Reste, Damien Malard e, Christophe Mignon, et al. Observing mixed layer depth, nitrate and chlorophyll concentrations in the northwestern

- Mediterranean: A combined satellite and NO₃ profiling floats experiment. *Geophysical Research Letters*, 41(18):6443–6451, 2014.
- Timothy F Duda, Andrey K Morozov, Bruce M Howe, Michael G Brown, Kevin Speer, Peter Lazarevich, Peter F Worcester, and Bruce D Cornuelle. Evaluation of a Long-Range Joint Acoustic Navigation/Thermometry System. In *OCEANS 2006*, pages 1–6. IEEE, 2006.
- Eberhard Fahrbach and Hein de Baar. The expedition of the research vessel” polarstern” to the antarctic in 2008 (ant-xxiv/3). *Berichte zur Polar-und Meeresforschung (Reports on Polar and Marine Research)*, 606, 2010.
- Eberhard Fahrbach, M Hoppema, G Rohardt, O Boebel, O Klatt, and A Wisotzki. Warming of deep and abyssal water masses along the greenwich meridian on decadal time scales: The weddell gyre as a heat buffer. *Deep Sea Research Part II: Topical Studies in Oceanography*, 58(25):2509–2523, 2011.
- AR Fay and GA McKinley. Global open-ocean biomes: mean and temporal variability. *Earth System Science Data*, 6(2):273–284, 2014.
- F Fetterer, K Knowles, W Meier, and M Savoie. Sea Ice Index Version 2s. 2016. doi: <http://dx.doi.org/10.7265/N5736NV7>.
- D. Ford. Assimilating Synthetic Biogeochemical-Argo and Ocean Colour Observations into a Global Ocean Model to Inform Observing System Design. *Biogeosciences Discussions*, 2020:1–34, 2020. doi: 10.5194/bg-2020-152. URL <https://www.biogeosciences-discuss.net/bg-2020-152/>.
- HJ Freeland. Statistical Observations of the Trajectories of Neutrally Buoyant Floats in the North Atlantic. *J. Mar. Res.*, 33:383–404, 1975.
- Gary Froyland, Robyn M Stuart, and Erik van Sebille. How Well-Connected is the Surface of the Global Ocean? *Chaos: An Interdisciplinary Journal of Nonlinear Science*, 24(3):033126, 2014.
- Eric D Galbraith, Anand Gnanadesikan, John P Dunne, and Michael R Hiscock. Regional impacts of iron-light colimitation in a global biogeochemical model. *Biogeosciences*, 7(3): 1043–1064, 2010.
- Gregory Gaspari and Stephen E Cohn. Construction of correlation functions in two and three dimensions. *Quarterly Journal of the Royal Meteorological Society*, 125(554):723–757, 1999.
- Sarah T Gille and Kathryn A Kelly. Scales of spatial and temporal variability in the Southern Ocean. *Journal of Geophysical Research*, 101:8759–8773, 1996.

- Sarah T Gille and Leonel Romero. Statistical behavior of alace floats at the surface of the southern ocean. *Journal of Atmospheric and Oceanic Technology*, 20(11):1633–1640, 2003.
- Sarah T Gille, Kevin Speer, James R Ledwell, and Alberto C Naveira Garabato. Mixing and Stirring in the Southern Ocean. *Eos, Transactions American Geophysical Union*, 88(39):382–383, 2007.
- W John Gould. From Swallow Floats to Argo—The Development of Neutrally Buoyant Floats. *Deep Sea Research Part II: Topical Studies in Oceanography*, 52(3-4):529–543, 2005.
- Alison R Gray and Stephen C Riser. A Global Analysis of Sverdrup Balance Using Absolute Geostrophic Velocities from Argo. *Journal of Physical Oceanography*, 44(4):1213–1229, 2014.
- Alison R Gray, Kenneth S Johnson, Seth M Bushinsky, Stephen C Riser, Joellen L Russell, Lynne D Talley, Rik Wanninkhof, Nancy L Williams, and Jorge L Sarmiento. Autonomous Biogeochemical Floats Detect Significant Carbon Dioxide Outgassing in the High-Latitude Southern Ocean. *Geophysical Research Letters*, 45(17):9049–9057, 2018.
- W Keith Hastings. Monte carlo sampling methods using markov chains and their applications. 1970.
- F Alexander Haumann, Nicolas Gruber, Matthias Münnich, Ivy Frenger, and Stefan Kern. Sea-ice transport driving Southern Ocean salinity and its recent trends. *Nature*, 537(7618):89–92, 2016. doi: 10.1038/nature19101.
- Held, IM and Guo, H and Adcroft, A and Dunne, JP and Horowitz, LW and Krasting, J and Shevliakova, E and Winton, M and Zhao, M and Bushuk, M and others. Structure and performance of gfdl’s cm4. 0 climate model. *Journal of Advances in Modeling Earth Systems*, 11(11):3691–3727, 2019.
- Nelson G Hogg and W Brechner Owens. Direct Measurement of the Deep Circulation within the Brazil Basin. *Deep Sea Research Part II: Topical Studies in Oceanography*, 46(1-2):335–353, 1999.
- Kayo Ide, Philippe Courtier, Michael Ghil, and Andrew C Lorenc. Unified Notation for Data Assimilation: Operational, Sequential and Variational (Special Issue Data Assimilation in Meteorology and Oceanography: Theory and Practice). *Journal of the Meteorological Society of Japan. Ser. II*, 75(1B):181–189, 1997.
- Ali Jahan, Kevin L Edwards, and Marjan Bahraminasab. *Multi-criteria Decision Analysis for Supporting the Selection of Engineering Materials in Product Design*. Butterworth-Heinemann, 2016.

- Gregory C Johnson, Shigeki Hosoda, Steven R Jayne, Peter R Oke, Stephen C Riser, Dean Roemmich, Tohsio Suga, Virginie Thierry, Susan E Wijffels, and Jianping Xu. Argo—Two Decades: Global Oceanography, Revolutionized. *Annual review of marine science*, 14:379–403, 2022.
- K Johnson and H Claustre. The Scientific Rationale, Design, and Implementation Plan for a Biogeochemical-Argo Float Array. *Biogeochem.-Argo Plann. Group*, 58, 2016a.
- KS Johnson and H Claustre. Bringing biogeochemistry into the argo age. *Eos*, 97, 2016b.
- Johnson, Kenneth S and Plant, Joshua N and Coletti, Luke J and Jannasch, Hans W and Sakamoto, Carole M and Riser, Stephen C and Swift, Dana D and Williams, Nancy L and Boss, Emmanuel and Haëntjens, Nils and others. Biogeochemical Sensor Performance in the SOCCOM Profiling Float Array. *Journal of Geophysical Research: Oceans*, 2017.
- Johnson, Kenneth S and Riser, Stephen C and Boss, Emmanuel S and Talley, Lynne D and Sarmiento, Jorge L and Swift, Dana D and Plant, Josh N and Maurer, Tanya L and Key, Robert M and Williams, Nancy L and others. Southern ocean carbon and climate observations and modeling (soccom) float data archive. 2017. doi: <https://doi.org/10.6075/J0TX3C9X>.
- Elizabeth M Jones, Dorothee CE Bakker, Hugh J Venables, and Nick J Hardman-Mountford. Seasonal cycle of CO₂ from the sea ice edge to island blooms in the Scotia Sea, Southern Ocean. *Marine Chemistry*, 177:490–500, 2015.
- Igor Kamenkovich, Wei Cheng, Claudia Schmid, and DE Harrison. Effects of eddies on an ocean observing system with profiling floats: Idealized simulations of the argo array. *Journal of Geophysical Research: Oceans*, 116(C6), 2011.
- Igor Kamenkovich, Angelique Haza, Alison R Gray, Carolina O Dufour, and Zulema Garraffo. Observing System Simulation Experiments for an Array of Autonomous Biogeochemical Profiling Floats in the Southern Ocean. *Journal of Geophysical Research: Oceans*, 122(9): 7595–7611, 2017.
- Katsuro Katsumata and Hiroshi Yoshinari. Uncertainties in Global Mapping of Argo Drift Data at the Parking Level. *Journal of oceanography*, 66(4):553–569, 2010.
- Peter Kimball and Stephen Rock. Sonar-Based Iceberg-Relative Navigation for Autonomous Underwater Vehicles. *Deep Sea Research Part II: Topical Studies in Oceanography*, 58(11-12): 1301–1310, 2011.
- Olaf Klatt, Olaf Boebel, and Eberhard Fahrbach. A Profiling Float’s Sense of Ice. *Journal of Atmospheric and Oceanic Technology*, 24(7):1301–1308, 2007.
- JH LaCasce. Floats and f/H. *Journal of Marine Research*, 58(1):61–95, 2000.

- JH LaCasce and KG Speer. Lagrangian statistics in unforced barotropic flows. *Journal of marine research*, 57(2):245–274, 1999.
- JH LaCasce, R Ferrari, J Marshall, R Tulloch, D Balwada, and K Speer. Float-derived isopycnal diffusivities in the DIMES experiment. *Journal of Physical Oceanography*, 44(2):764–780, 2014. doi: <http://dx.doi.org/10.1175/JPO-D-13-0175.1>.
- Peter Landschützer, Nicolas Gruber, and Dorothee CE Bakker. Decadal variations and trends of the global ocean carbon sink. *Global Biogeochemical Cycles*, 30(10):1396–1417, 2016.
- Landschützer, Peter and Gruber, Nicolas and Haumann, F Alexander and Rödenbeck, Christian and Bakker, Dorothee CE and Van Heuven, Steven and Hoppema, Mario and Metzl, Nicolas and Sweeney, Colm and Takahashi, Taro and others. The reinvigoration of the southern ocean carbon sink. *Science*, 349(6253):1221–1224, 2015.
- Kitack Lee, Lan T Tong, Frank J Millero, Christopher L Sabine, Andrew G Dickson, Catherine Goyet, Geun-Ha Park, Rik Wanninkhof, Richard A Feely, and Robert M Key. Global relationships of total alkalinity with salinity and temperature in surface waters of the world’s oceans. *Geophysical Research Letters*, 33(19), 2006.
- Tianyang Li, Harsh H Pareek, Pradeep Ravikumar, Dhruv Balwada, and Kevin Speer. Tracking with Ranked Signals. In *UAI*, pages 474–483. Citeseer, 2015.
- RA Locarnini, AV Mishonov, JI Antonov, JP Boyer, HE Garcia, OK Baranova, M Zweng, CR Paver, JR Reagan, DR Johnson, et al. Temperature NOAA Atlas NESDIS 73. In *World Ocean Atlas*, volume 1, page 40. 2013.
- Locarnini, RA and Mishonov, AV and Antonov, JI and Boyer, TP and Garcia, HE and Baranova, OK and Zweng, MM and Johnson, DR. World Ocean Atlas 2009, Vol. 1. *Temperature, NOAA Atlas NESDIS*, 68, 2010.
- Rick Lumpkin, Luca Centurioni, and Renellys C Perez. Fulfilling Observing System Implementation Requirements with the Global Drifter Array. *Journal of Atmospheric and Oceanic Technology*, 33(4):685–695, 2016.
- Joseph D Majkut, Brendan R Carter, Thomas L Frölicher, Carolina O Dufour, Keith B Rodgers, and Jorge L Sarmiento. An observing system simulation for southern ocean carbon dioxide uptake. *Philosophical Transactions of the Royal Society A: Mathematical, Physical and Engineering Sciences*, 372(2019):20130046, 2014.
- Andrey Andreyevich Markov. Rasprostranenie Zakona Bol’shih Chisel na Velichiny, Zavisyaschie Drug ot Druga. *Izvestiya Fiziko-matematicheskogo obschestva pri Kazanskom universitete*, 15(135-156):18, 1906.

- Nikolai Maximenko, Jan Hafner, and Peter Niiler. Pathways of Marine Debris Derived from Trajectories of Lagrangian Drifters. *Marine pollution bulletin*, 65(1-3):51–62, 2012.
- Matthew R Mazloff, Patrick Heimbach, and Carl Wunsch. An eddy-permitting Southern Ocean State Estimate. *Journal of Physical Oceanography*, 40(5):880–899, 2010.
- Ronan McAdam and Erik van Sebille. Surface Connectivity and Inter-Ocean Exchanges From Drifter-Based Transition Matrices. *Journal of Geophysical Research: Oceans*, 2018.
- Trevor J McDougall and Paul M Barker. Getting Started with TEOS-10 and the Gibbs Seawater (GSW) Oceanographic Toolbox. *SCOR/IAPSO WG*, 127:1–28, 2011.
- Michael P Meredith, Andrew S Meijers, Alberto C Naveira Garabato, Peter J Brown, Hugh J Venables, E Povl Abrahamsen, Loïc Jullion, and Marie-José Messias. Circulation, retention, and mixing of waters within the w eddell-s cotia c onfluence, s outhern o cean: The role of stratified t aylor columns. *Journal of Geophysical Research: Oceans*, 120(1):547–562, 2015.
- P Miron, Francisco J Beron-Vera, Maria J Olascoaga, G Froyland, P Pérez-Brunius, and J Sheinbaum. Lagrangian Geography of the Deep Gulf of Mexico. *Journal of Physical Oceanography*, 49(1):269–290, 2019.
- Pedro MS Monteiro, Luke Gregor, Marina Lévy, Stacy Maenner, Christopher L Sabine, and Sebastiaan Swart. Intraseasonal variability linked to sampling alias in air-sea co₂ fluxes in the southern ocean. *Geophysical Research Letters*, 42(20):8507–8514, 2015.
- Adele K Morrison, Thomas L Frölicher, and Jorge L Sarmiento. Upwelling in the southern ocean. *Physics Today*, 68(1):27, 2015.
- An T Nguyen, Victor Ocaña, Vikram Garg, Patrick Heimbach, John M Toole, Richard A Krishfield, Craig M Lee, and Luc Rainville. On the benefit of current and future alps data for improving arctic coupled ocean-sea ice state estimation. *Oceanography*, 30(2):69–73, 2017.
- An T Nguyen, Patrick Heimbach, Vikram V Garg, Victor Ocaña, Craig Lee, and Luc Rainville. Impact of Synthetic Arctic Argo-Type Floats in a Aoupled Ocean–Sea Ice State Estimation Framework. *Journal of Atmospheric and Oceanic Technology*, 37(8):1477–1495, 2020.
- Floriane Ninove, P-Y Le Traon, E Remy, and S Guinehut. Spatial scales of temperature and salinity variability estimated from argo observations. *Ocean Science*, 12(1):1–7, 2016.
- Michel Ollitrault and Alain Colin de Verdière. The Ocean General Circulation Near 1000-m Depth. *Journal of Physical Oceanography*, 44(1):384–409, 2014.
- Michel Ollitrault and Jean-Philippe Rannou. ANDRO: An Argo-Based Deep Displacement Dataset. *Journal of Atmospheric and Oceanic Technology*, 30(4):759–788, 2013.

- Alejandro H Orsi, Worth D Nowlin, and Thomas Whitworth. On the circulation and stratification of the weddell gyre. *Deep Sea Research Part I: Oceanographic Research Papers*, 40(1): 169–203, 1993.
- Robert L Parker. *Geophysical Inverse Theory*, volume 1. Princeton university press, 1994. doi: 10.1515/9780691206837.
- Channing J Prend, Sarah T Gille, Lynne D Talley, B Greg Mitchell, Isabella Rosso, and Matthew R Mazloff. Physical drivers of phytoplankton bloom initiation in the southern ocean's scotia sea. *Journal of Geophysical Research: Oceans*, 124(8):5811–5826, 2019.
- Sarah G Purkey and Gregory C Johnson. Warming of global abyssal and deep Southern Ocean waters between the 1990s and 2000s: contributions to global heat and sea level rise budgets*. *Journal of Climate*, 23(23):6336–6351, 2010.
- Sarah G Purkey and Gregory C Johnson. Global contraction of Antarctic Bottom Water between the 1980s and 2000s*. *Journal of Climate*, 25(17):5830–5844, 2012.
- AL Ramsey, HH Furey, and AS Bower. Deep Floats Reveal Complex Ocean Circulation Patterns. *Eos*, 99, 2018. doi: 10.1029/2018EO105549.
- Herbert E Rauch, F Tung, and Charlotte T Striebel. Maximum Likelihood Estimates of Linear Dynamic Systems. *AIAA journal*, 3(8):1445–1450, 1965.
- KA Reeve, O Boebel, T Kanzow, V Strass, G Rohardt, and E Fahrbach. Objective mapping of argo data in the weddell gyre: a gridded dataset of upper ocean water properties. *Earth System Science Data Discussions*, 8(1), 2015.
- Krissy Reeve, Olaf Boebel, Torsten Kanzow, Volker Strass, Gerd Rohardt, and Eberhard Fahrbach. A Gridded Data Set of Upper-Ocean Hydrographic Properties in the Weddell Gyre Obtained By Objective Mapping of Argo Float Measurements. *Earth System Science Data*, 8(1):15–40, 2016.
- Daniel Revuz and Marc Yor. *Continuous martingales and Brownian motion*, volume 293. Springer Science & Business Media, 2013.
- Rhein, Met al and Rintoul, SR and Aoki, S and Campos, E and Chambers, D and Feely, RA and Gulev, S and Johnson, GC and Josey, SA and Kostianoy, A and others. Observations: ocean. *Climate Change*, pages 255–315, 2013.
- Stephen Riser. personal communication, 2022.
- Riser, Stephen C and Freeland, Howard J and Roemmich, Dean and Wijffels, Susan and Troisi, Ariel and Belbéoch, Mathieu and Gilbert, Denis and Xu, Jianping and Pouliquen, Sylvie and

- Thresher, Ann and others. Fifteen Years of Ocean Observations with the Global Argo Array. *Nature Climate Change*, 6(2):145–153, 2016.
- Pelle Robbins. personal communication, 2021.
- Dean Roemmich and John Gilson. The 2004–2008 mean and annual cycle of temperature, salinity, and steric height in the global ocean from the Argo Program. *Progress in Oceanography*, 82 (2):81–100, 2009.
- Dean Roemmich, Olaf Boebel, Howard Freeland, Brian King, PY LeTraon, Robert Molinari, W Brechner Owens, Stephen Riser, Uwe Send, Kensuke Takeuchi, et al. On the design and implementation of Argo: A global array of profiling floats. *Argo Science Team*, 1999. URL <https://argo.ucsd.edu/wp-content/uploads/sites/361/2020/05/argo-design.pdf>.
- Roemmich, D and Boebel, O and Freeland, H and King, B and LeTraon, PY and Molinari, R and Brechner Owens, W and Riser, S and Send, U and Takeuchi, K and others. On the Design and Implementation of Argo: an Initial Plan for a Global Array of Profiling Floats. *International CLIVAR Project Office Report*, 21, 1998.
- Roemmich, Dean and Alford, Matthew H and Claustre, Hervé and Johnson, Kenneth and King, Brian and Moum, James and Oke, Peter and Owens, W Brechner and Pouliquen, Sylvie and Purkey, Sarah and others. On the Future of Argo: A Global, Full-Depth, Multi-Disciplinary Array. *Frontiers in Marine Science*, 6, 2019.
- T Rossby, D Dorson, and J Fontaine. The RAFOS System. *Journal of atmospheric and oceanic technology*, 3(4):672–679, 1986.
- J L Sarmiento, N Gruber, MA Brzezinski, and JP Dunne. High-Latitude Controls of Thermocline Nutrients and Low Latitude Biological Productivity. *Nature*, 427(6969):56, 2004.
- Schlunegger, Sarah and Rodgers, Keith B and Sarmiento, Jorge L and Ilyina, Tatiana and Dunne, John P and Takano, Yohei and Christian, James R and Long, Matthew C and Frölicher, Thomas L and Slater, Richard and others. Time of emergence and large ensemble intercomparison for ocean biogeochemical trends. *Global biogeochemical cycles*, 34(8):e2019GB006453, 2020.
- SEANOE. Argo float data and metadata from Global Data Assembly Centre (Argo GDAC). 2000. doi: 10.17882/42182.
- Florian Sevellec, Alain Colin de Verdière, and Michel Ollitraul. Evolution of Intermediate Water Masses Based on Argo Float Displacements. *Journal of Physical Oceanography*, 47(7): 1569–1586, 2017.
- Stefanie Spiesecke. *Analysis and Modelling of RAFOS Signal Propagation Under the Antarctic Sea-Ice for Positioning Argo Floats*. PhD thesis, Alfred Wegener Institut, 2018.

- John C Swallow. A Neutral-Buoyancy Float for Measuring Deep Currents. *Deep Sea Research (1953)*, 3(1):74–81, 1955.
- Lynne D Talley, Vyacheslav Lobanov, Vladimir Ponomarev, Anatoly Salyuk, Pavel Tishchenko, Igor Zhabin, and S Riser. Deep convection and brine rejection in the japan sea. *Geophysical Research Letters*, 30(4), 2003.
- Talley, LD and Rosso, I and Kamenkovich, Igor and Mazloff, MR and Wang, J and Boss, E and Gray, AR and Johnson, KS and Key, RM and Riser, SC and others. Southern Ocean Biogeochemical Float Deployment Strategy, With Example From the Greenwich Meridian Line (GO-SHIP A12). *Journal of Geophysical Research: Oceans*, 124(1):403–431, 2019.
- Tamsitt, Veronica and Drake, Henri F and Morrison, Adele K and Talley, Lynne D and Dufour, Carolina O and Gray, Alison R and Griffies, Stephen M and Mazloff, Matthew R and Sarmiento, Jorge L and Wang, Jinbo and others. Spiraling Pathways of Global Deep Waters to the Surface of the Southern Ocean. *Nature communications*, 8(1):1–10, 2017.
- Tyler Tucker, Donata Giglio, Megan Scanderbeg, and Samuel SP Shen. Argovis: a web application for fast delivery, visualization, and analysis of argo data. *Journal of Atmospheric and Oceanic Technology*, 37(3):401–416, 2020.
- Erik Van Sebille, Peter Jan Van Leeuwen, Arne Biastoch, and Wilhelmus PM de Ruijter. On The Fast Decay of Agulhas Rings. *Journal of Geophysical Research: Oceans*, 115(C3), 2010.
- Erik Van Sebille, Matthew H England, and Gary Froyland. Origin, Dynamics and Evolution of Ocean Garbage Patches from Observed Surface Drifters. *Environmental Research Letters*, 7(4):044040, 2012.
- Van Sebille, Erik and Griffies, Stephen M and Abernathey, Ryan and Adams, Thomas P and Berloff, Pavel and Biastoch, Arne and Blanke, Bruno and Chassignet, Eric P and Cheng, Yu and Cotter, Colin J and others. Lagrangian Ocean Analysis: Fundamentals and Practices. *Ocean Modelling*, 121:49–75, 2018.
- LO Wallace, EM Van Wijk, SR Rintoul, and B Hally. Bathymetry-Constrained Navigation of Argo Floats Under Sea Ice on the Antarctic Continental Shelf. *Geophysical Research Letters*, 47(11):e2020GL087019, 2020.
- Jinbo Wang, Matthew R. Mazloff, and Sarah T. Gille. Pathways of the Agulhas waters poleward of 29° S. *Journal of Geophysical Research: Oceans*, 119(7):4234–4250, 2014. ISSN 2169-9291. doi: 10.1002/2014JC010049. URL <http://dx.doi.org/10.1002/2014JC010049>.
- Sarah E Webster, Lee E Freitag, Craig M Lee, and Jason I Gobat. Towards Real-Time Under-Ice Acoustic Navigation at Mesoscale Ranges. In *2015 IEEE International Conference on Robotics and Automation (ICRA)*, pages 537–544. IEEE, 2015.

- Annie PS Wong and Stephen C Riser. Profiling Float Observations of the Upper Ocean Under Sea Ice Off the Wilkes Land Coast of Antarctica. *Journal of Physical Oceanography*, 41(6): 1102–1115, 2011.
- Wong, Annie PS and Wijffels, Susan E and Riser, Stephen C and Pouliquen, Sylvie and Hosoda, Shigeki and Roemmich, Dean and Gilson, John and Johnson, Gregory C and Martini, Kim and Murphy, David J and others. Argo data 1999–2019: two million temperature-salinity profiles and subsurface velocity observations from a global array of profiling floats. *Frontiers in Marine Science*, page 700, 2020.
- Christine M Wooding, Heather H Furey, and Marguerite A Pachece. RAFOS Float Processing at the Woods Hole Oceanographic Institution. Technical report, Woods Hole Oceanographic Institution, 2005.
- Carl Wunsch. *Discrete Inverse and State Estimation Problems: with Geophysical Fluid Applications*. Cambridge University Press, 2006. doi: 10.1017/CBO9780511535949.
- Kaihe Yamazaki, Shigeru Aoki, Keishi Shimada, Taiyo Kobayashi, and Yujiro Kitade. Structure of the Subpolar Gyre in the Australian-Antarctic Basin Derived From Argo Floats. *Journal of Geophysical Research: Oceans*, 125, 07 2020. doi: 10.1029/2019JC015406.
- MM Zweng, JR Reagan, JI Antonov, RA Locarnini, AV Mishonov, TP Boyer, HE Garcia, OK Baranova, DR Johnson, D Seidov, et al. World Ocean Atlas 2013, Volume 2: Salinity. *NOAA Atlas NESDIS*, 74:39, 2013.